Doctoral Dissertation

Intrinsic and extrinsic control of Eu luminescence in Eu,O-codoped GaN

Takenori Iwaya

December 2023

Graduate School of Engineering

Osaka University

Abstract

With the development of smart society, there is a growing interest in developing high-resolution displays for smart phones, smart watches, and augmented reality and visual reality (AR and VR) that provide us with beautiful experiences of truly immersive real-world sensation. To achieve such devices, micro-LED (μ -LED) display is the best technology candidates, where micrometer-sized LEDs are densely integrated. Conventional red LEDs are made from $Al_xGa_yIn_{1-x-y}P$-based materials, while blue and green LEDs are made utilizing III-nitride materials. Therefore, the fabrication process is complex because different color LEDs are cut out from substrate and placed on a wafer, leading to high fabrication cost. Development of III-nitride-based red LEDs is demanded for the monolithic integration of three primary colors LEDs, however, conventional $In_xGa_{1-x}N$-based red LEDs remain issues in various aspects, including the color stability and color purity, as well as the luminescence efficiency. In this context, Eu,O-codoped GaN (GaN:Eu,O) has been in a spotlight, due to its high color stability and color purity which originate from 4*f*-intra transition of Eu^{3+} ions. The light output of GaN:Eu,O-based LEDs has been increasing, however it is still relatively low as compared to $In_xGa_{1-x}N$-based blue and green LEDs. Therefore, "intrinsic control" is essential to selectively form Eu^{3+} luminescent sites with high excitation efficiencies.

Furthermore, GaN;Eu,O is expected to be utilized as a laser source for next-generation laser display application, and as a quantum light source for quantum information technology and quantum computing, due to its noteworthy luminescence properties. In order to achieve such light sources, "extrinsic control" of Eu^{3+} luminescence by optical cavities with high *Q*-factors is crucial to modulate the radiative properties of Eu^{3+}.

In this thesis, we perform "intrinsic" and "extrinsic" control of Eu^{3+} emission in GaN:Eu,O grown using the organometallic vapor-phase epitaxy (OMVPE) method. As the "intrinsic" control, we perform thermal annealing to selectively form luminescent sites with high excitation efficiencies. In terms of the "extrinsic" control, we investigate the design of two-dimensional photonic crystal (2D-PhC) cavity structures which achieve high *Q*-factors even with structural disorder (fabrication error).

In Chapter2, we investigate the effect of thermal annealing on optical properties of GaN:Eu,O. GaN:Eu,O grown using the OMVPE method typically has eight unique luminescent sites with different local atomic structures (OMVPE1-8). Particularly, OMVPE1 and OMVPE2, which are

considered to be Eu clusters, have a large existing ratio in GaN:Eu,O when a relatively low growth temperature (960 °C) is utilized. However, their low excitation efficiencies limit the output of GaN:Eu,O. To dissociate the Eu clusters (OMVPE1 and OMVPE2), we perform post-growth thermal annealing. As results, we exhibit that annealing at high temperatures (> 1000 °C) effectively converts OMVPE1 and OMVPE2 into sites with much higher excitation efficiencies (OMVPE7, OMVP8 and OMVPE-X), leading to reasonably enhanced photoluminescence (PL) intensities.

In Chapter 3, we focus on OMVPE-X, with an emission peak at ~2.004 eV which shows a strong emission under low excitation power region. This peak has been tentatively assigned as OMVPE8 so far, because it is excited at the similar resonant excitation energy of OMVPE8. Using combined excitation-emission spectroscopy (CEES) and time-resolved PL measurement, we reveal that OMVPE-X is an independent site. Furthermore, temperature and excitation power dependent PL exhibit that OMVPE-X is a noteworthy luminescent site due to its small thermal quenching ratio and high excitation efficiency. Furthermore, we introduce the annealing technique to LED fabrication process to investigate the impact of annealing on the electrical and optical properties of LEDs. As results, optimized annealing process enable fabrication of an LED with good rectification property. Moreover, the annealed LED exhibit a reasonably stronger electroluminescence (EL) intensity as compared to a conventional LED. The annealed LED exhibits a dominant emission associated with OMVPE-X at low current injection regime. These results indicate that OVMPE~X has a quite high excitation efficiency also under current injection, and annealing is an effective method to selectively form such beneficial sites and to improve EL intensity.

In Chapter 4, to extrinsically control Eu^{3+} emission by utilizing outer optical cavities, we perform a study on design of nanocavities to achieve high *Q*-factors. Especially, we focus on 2D-PhC cavities, because high-*Q* 2D-PhC cavities have a potential to significantly modify the radiative probability of Eu^{3+} emission, which could lead to lasing in this material. However, *Q*-factors of III-nitride-based 2D-PhC cavities have been limited up to ~5000 in the ultraviolet-visible range. This is mainly due to the small device size designed for short wavelength range, and the chemical and physical stability that hinders accurate dry- and wet-etching process. In order to improve *Q*-factors of III-nitride-based 2D-PhC cavities, we reproduce experimentally introduced structural disorder in 3D-FDTD simulations and investigate the impact of such disorder on *Q*-factors. As a result, we demonstrate that H*N* cavities, particularly an H3-type cavity exhibits high robustness to structural disorder, and can maintain high *Q*-factors even when large structural disorder is introduced.

In Chapter 5, we fabricate H3 cavities to validate the simulation results and to explore the dominant optical loss that limits *Q*-factors with the aim of further enhancement. As a result, the maximum experimental *Q*-factor of 7900 is demonstrated, which is reasonably higher than earlier reported values, confirming our suggestion that the H3 cavity is a promising structure to achieve high *Q*-factors. For an even further improvement of *Q*-factors, we explore the dominant optical loss of H3 cavities through the combination of experimental and simulation studies. As a result, the designed *Q*-factor itself (12000) is derived as the most important limitation. Based on this knowledge we design 2D-heterostructure type of cavity, which strongly confine light by appropriately modulated photonic band gap. Through a proper cavity design, we show that a high design *Q*-factors beyond 1.1×10^5 can be attained using this structure. Furthermore, electromagnetic simulations reveal that this cavity can maintain the high *Q*-factor even large structural disorder is introduced. Based on this design we show a much higher experimental *Q*-factor of 10500. These results clearly suggest the high potential of this type of cavity, and even higher *Q*-factors are expected through a further optimization of design parameters.

Finally in Chapter 6, we summarize the obtained results and discuss several future prospects.

Acknowledgments

In my Ph.D. life at Osaka University, I was fortunate to receive support from numerous people. I would like to Express my gratitude to all of them here.

First and foremost, I want to extend my heartfelt gratitude to Professor Yasufumi Fujiwara. In addition to supervising the laboratory, he held various responsibilities such as committee memberships of several academic societies, Nevertheless, he provided me with support and guidance in my research. He emphasized the importance of conducting unique and innovative research as a researcher. He also offered valuable insights into giving impactful research presentations and papers. Being a part of his research group allowed me to discover the joy and fulfillment of research, ultimately led me to pursue a Ph.D. degree. I am deeply grateful to him for giving me great opportunities to determine the direction of my life.

I am also thankful to Professor Hiromi Yamashita and Professor Ryoichi Nakatani for their valuable advice during the dissertation process. The meaningful discussions greatly assisted me in completing the Ph.D. thesis.

Associate Professor Jun Tatebayashi provided me with extensive guidance and support. He assisted my research in various aspects of running the laboratory, including equipment maintenance. During conferences, he introduced me to many distinguished researchers, greatly expanding my network. I am deeply grateful for his supports.

I am particularly grateful to Assistant Professor Shuhei Ichikawa. When I was an undergraduate student, he patiently taught me experimental and analytical techniques, as well as the fundamentals of creating research presentation slides and structuring research papers. Even after he moved to a different department, he continued to provide frequent opportunities for discussion and offered substantial support in the direction of research. He also gave me invaluable life advice, sometimes over drinks. My admiration for him was a decisive factor in decision to enter a doctoral program. I am deeply thankful for the significant role he has played in shaping my life. Thank you for taking time out of your precious time.

Former Assistant Professor Dolf Timmerman offered guidance on research, paper structure, writing and presentations in English. I am grateful that the conversation with him provided me with excellent opportunities to practice English.

Professors Dierolf Volkmar and Brandon Mitchell provided numerous opportunities for fruitful discussions. Their assistance was substantial and memorable, particularly during my

overseas research in the United States. Thanks to them, I had a wonderful experience.

I have also greatly benefited from Professor Masaaki Ashida. He was significantly instrumental in optical experiments using pulse lasers and cathodoluminescence measurements. His expertise in superfluorescence and superradiance was very helpful to gain deep insights into fundamental optics.

I would like to Express my special appreciation to Professor Hajime Ishihara, Associate Professor Kazunori Sato, and Assistant Professor Katsuhiro Suzuki. They offered valuable insights, particularly from a theoretical perspective. Thanks to them, I have deepened my understanding of fundamental physics and computational science.

I would also like to acknowledge Professor Ryuji Katayama, Dr. Atsushi Nishikawa, Dr. Shin-ichiro Sato, Associate Professor Hiroto Sekiguchi, Associate Professor Momoko Deura, Associate Professor Tomoyuki Tanikawa, Assistant Professor Ryota Ishii, Lecturer Kanako Shojiki, Associate Professor Kenjiro Uesugi for valuable advice in conferences on nitride semiconductors. They provided me with opportunities to understand the significance and position of my research.

Assistant Professor Shigeyoshi Usami, Specific Assistant Professor Yoshinobu Matsuda, and Lecturer Takuya Maeda offered not only advice on my research, but also valuable insights on career development in the field of academia. These conversations provided me a wonderful opportunity to consider my future path. I am grateful to all of them for kind support.

I also appreciate meaningful discussions I had with Dr. Tomoaki Nambu, Mr. Ryosuke Noro, Mr. Hanqiao Ye, Mr. Fumikazu Murakami, Ms. Meguru Endo, Mr. Hiroto Honda, Mr. Yuki Murata, and Mr. Shogo Washida during conferences. I appreciate the opportunity to interact with all of them.

Dr. Hayley Austin supported me in research, as well as in my daily life during my stay in the United States. Her kindness made the time we had there fruitful and memorable.

I would like to thank Mr. Fang Zhidong for his support and valuable time during my Ph.D. life in Professor Fujiwara’s laboratory. It was very meaningful for my English skill to have opportunities to talk with him, I really appreciate it. I will never forget the conversations we had during our difficult time writing our Ph.D. theses.

My deepest acknowledgement goes to Mr. Atushi Takeo for sharing pleasant time. We frequently went out together, that was an excellent opportunity to refresh my mind. I have

unforgettable memories of international/domestic conferences and overseas research we experienced together.

I also would like to give thanks to Mr. Masato Murakami, who was a mentor in my early days in the lab. He told me basics of research, including fabrication process of photonic crystal and optical characterization. We also had a great time in our private time.

Mr. Shuhei Kobayashi, Mr. Ryota Komai, Mr. Naoto Nishiyama, Mr. Reo Saito, and Mr. Ken Higuchi shared enjoyable moments and discussions as colleagues. The time we spent together is very memorable.

I extend my gratitude to Dr. Masayuki Ogawa, Mr. Takaya Morikawa, Mr. Masao Mishina, Mr. Ryoma Higashi, Mr. Yoji Matsude, Mr. Shunya Hasegawa, Mr. Naoki Yoshioka, Mr. Ryohei Homi, Mr. Shogo Maeda, Mr. Tomohiro Hirate, Mr. Kazuto Nishimura, Mr. Teruki Taniguchi, Mr. Takaya Otabara, Mr. Wataru Ichimiya, Mr. Toshihiro Ishihara, Mr. Sotaro Nakagawa, Mr. Hibiki Komatsu, Mr. Raiki Hada, Mr. Shunsuke Yamazaki, Mr. Kaito Yamada, Mr. Reo Yamato, Mr. Takuma Yoshimura, Mr. Takumi Ueda, Mr. Masato Ida, Mr. Kaito Kitaura, Mr. Genki Tanaka, Mr. Akihiro Miyaji, Mr. Ryo Yoshida, Mr. Iori Nakata, Mr. Shuma Asai, Mr. Kouki Ueno, Mr. Noritaka Sakabe, Mr. Taketo Shimada, Mr. Haruya Naganawa, Mr. Katsuya Hyodo, Mr. Riko Masuda, and Mr. Kazuki Mori, who spent memorable time with me in Professor Fujiwara's laboratory.

I am thankful for the support and assistance from Ms. Akiko Sugimoto, Ms. Chizuru Eitoku, and Ms. Chikako Umeda in my research activities.

This work was partially supported by Osaka University Fellowship "Quantum Leader Recourses" (QLEAR Fellowship) and the Japan Society for the Promotion of Science (JSPS) through the Grant-in-Aid for Research Fellow. I Express my deep gratitude to Professor Akira Ooiwa, Associate Professor Shigehiko Hasegawa, and Ms. Yoko Yoshida for their significant support within the QLEAR Fellowship.

I would like to extend my heartfelt appreciation to all of my friends I have met during my student life at Osaka University.

Finally, the most gratitude has to go to my parents for their understanding my decision, and for their constant support.

最後に、博士後期課程への進学に理解を示し、大阪大学での学生生活において精神的・金銭的に支えてくれた両親に心より感謝申し上げます。

Takenori Iwaya

Contents

Chapter 1. Introduction

1.1 Background of light emitting devices

Artificial light sources have evolved along with modern human civilization. Fluorescent lamps have been in use for a long time and are still widely used because of the high light emission efficiency as compared to the conventional incandescent lamps. In a fluorescent lamp, accelerated electrons excite mercury vapor, generating ultra-violet (UV) light that excites the phosphors coated inside the lamp. Rare-earth (RE) ions are widely used as the component of the phosphors because of the efficient light emitting properties that originate from the intra-4*f* transitions.

In recent years, light-emitting diodes (LEDs) and laser diodes (LDs) have emerged; they show high luminous efficiency which originates from band-to-band transitions in semiconductors. As the three primarily colors LEDs and LDs, $Al_xGa_yIn_{1-x-y}P$ alloy is used for the red light source and $In_xGa_{1-x}N$ is used for blue and green light sources with quantum well (QW) structures. The combination of blue LED and yellow phosphors enabled high-efficient white light sources [1,2], which have replaced conventional fluorescent lamps.

In the field of displays, thin film transistor liquid crystal displays (TFT-LCDs) and organic light-emitting diode (OLED) displays have emerged and delivered high-resolution and high-efficient displays for a broad range of applications (e.g., smartphones, televisions, handheld gaming consoles).

The evolution of human light sources has enriched our lives and played a vital role in the reduction of energy loss. However, with the further evolved human civilization, next generation light sources are required for a variety of applications including ultrahigh resolution displays, quantum computing and quantum information communication, which are difficult to achieve using conventional lighting technology.

1.2 Candidate materials for high-resolution μ-LED displays

There is a growing interest in developing high-resolution displays for smart phones, smart watches, and augmented reality and visual reality (AR and VR) devices. In order to experience a truly immersive real-world sensation using AR and VR devices, ultra-high-resolution of 5000 pixels per inch (PPI) is required, with each pixel being as small as ~5 μm. Candidate display techniques are TFT-LCDs, OLED displays, and micro-LED (μ-LED) displays. TFT-LCDs typically consist of color-filters, polarizers, a liquid crystal layer, and a backlight. The transmittance can be adjusted by applying voltage, allowing for the modulation of light output from the backlight. Images are produced by blocking light, therefore the luminescence efficiency is inevitably limited. Besides, enhancing the contrast ratio (the ratio of luminescence between the brightest and the darkest state) is challenging due to the difficulty to minimize the transmittance when no voltage is applied. This is because of several issues, such as light diffraction, scattering, and misalignment of optical components [3–7].

In contrast, OLEDs are self-light-emissive devices, and they have achieved high luminous efficiency and high color contrast. However, the device lifetime is typically shorter than LCDs because of several degradation mechanisms including the deterioration of the organic/metal interface [8,9] and trap formation [10].

Another noteworthy display technique is μ-LED display, where LEDs with dimensions ranging from several to hundreds of micrometers are integrated. μ-LED displays can achieve higher efficiency than LCDs and OLEDs [2,11–13], as well as the great color contrast ratio and extended device lifetime. One of the primary bottlenecks for the implementation of μ-LED display is the cost of fabrication. Currently, commercial three-primary color LEDs utilize $Al_xGa_yIn_{1-x-y}P$ for red LEDs and $In_xGa_{1-x}N$ for blue and green LEDs. While full-color LED displays have been demonstrated using a pick-and-place method [14,15], there is still room for improvement in this process. It remains time-consuming, expensive, and there are challenges creating small pixels (~ 5 μm for 5000 PPI).

Furthermore, with the reduction of device size, $Al_xGa_yIn_{1-x-y}P$-based red LEDs strongly suffer from the internal quantum efficiency (IQE) degradation due to their long carrier diffusion length and high surface recombination rate [16,17]. In contrast, it is widely known that $In_xGa_{1-x}N$-based

blue and green LEDs demonstrate better size dependent characteristics because of the carrier localization effect caused by composition fluctuations leading to a relatively small surface recombination rate [18–20].

For these reasons, there is an urgent need for monolithic integration of three primary colors μ-LEDs based on III-nitride-semiconductors. However, efficient $In_xGa_{1-x}N$-based green and red LEDs remain to be realized because high indium composition leads to degradation of the crystal quality and strong internal electric fields in the well layers [21–32]. Besides, with increasing current injection level, the emission wavelength inevitably blueshifts due to screening of the quantum confined Stark effect [33]. Additionally, the influence of well-width fluctuations, alloy-disorder, and compositional fluctuations significantly contributes to the linewidth broadening [34–36]. As a result, the typical linewidth of the present planar $In_xGa_{1-x}N$-based red LEDs exceeds 50 nm [37], leading to a poor color impurity. Moreover, it is essential to note that human eyes exhibit a significant reduction in spectral sensitivity at wavelengths beyond approximately 650 nm. Hence, achieving emissions with a narrow linewidth at the central wavelength of 620-630 nm is of utmost importance for brightness and color rendering quality of displays.

Furthermore, monolithic integration of three primary colors LEDs is technically challenging. Several monolithic integration techniques using $In_xGa_{1-x}N$-based material have been proposed. Kishino *et al*. has demonstrated $In_xGa_{1-x}N$ nanocolumn structure for III-nitride-based full-color μ-LEDs [38], which can relax the strain in QWs even for high indium component. However, nanocolumn structures with high color purity remain to be realized because of the challenge of precisely controlling the uniformity of nanocolumn structures, particularly when the indium composition is high. Furthermore, electron-beam lithography process is indispensable prior to the growth to achieve desired emission wavelength, which would lower the productivity in the mass production process.

Color-conversion technique is another candidate for the monolithic integration. Quantum dots (QDs) or phosphors are used for the color conversion by exciting with $In_xGa_{1-x}N$-based UV-blue LEDs, however the color-conversion efficiency remains to be improved [39–41]. Furthermore, to mitigate crosstalk between LEDs of different colors and to improve color purity and pixel contrast, black partitions need to be applied between subpixels [41], which complicates the fabrication process, making it difficult to improve display resolution.

If a high-efficient III-nitride-based planer red LED is achieved, it enables vertical stacking integration of three primary colors LEDs [42–45]. The technique allows the wafer to be prepared

by a single epitaxial process. Besides, μ-LED displays can be fabricated using conventional lithography and etching techniques. The pixel pitch is primarily constrained by the accuracy of mechanical alignment in flip-chip integration. However, it is feasible to achieve μ-LED displays with high resolution exceeding 5000 PPI using current technologies [42,44].

As the material candidate of III-nitride-semiconductor-based planer red LED, Eu-doped GaN (GaN:Eu) has been in the spotlight. GaN:Eu shows high efficient red light emission (~622 nm), and the operation of GaN:Eu-based LEDs has been demonstrated [46–48] by combining with p-type and n-type layers. Emission from GaN:Eu originates from intra 4*f*-shell of Eu^{3+} ions, which is shielded by the closed-shell 5*s* and 5*p* electrons, therefore the emission wavelength is less sensitive to ambient temperature and current injection level. The intra 4*f*-transitions are parity forbidden by the Laporte selection rule, however, within the GaN host, local crystal fields reduce the symmetry around Eu ions and relax the selectin rule [49,50]. Nevertheless, the forbidden nature of the transition results in a considerably long radiative lifetime. The typical lifetime of red emission originating from the $^5D_0$-$^7F_2$ transition is ~ 250 μs [51], that often limits the quantum efficiency of GaN:Eu. The long lifetime, however, has an advantage for optical device applications. The emission linewidth of GaN:Eu is narrow due to the long lifetime of the excited state, thus the color purity is much higher than that of emission originating from band-to-band transitions. In addition, it was shown that the luminous efficiency of GaN:Eu does not decrease as the device size is reduced [52], which is an important characteristic for μ-LED applications. This nature stems from the large carrier capture cross section of Eu^{3+} ions. In this contribution, III-nitride-based monolithic integration of three primary colors of μ-LEDs is expected using GaN:Eu red LEDs and conventional $In_xGa_{1-x}N$-based blue and green LEDs.

Schematic of the monolithically integrated three primary colors planar μ-LEDs that we propose is illustrated in Fig. 1. 1. The typical growth temperature of GaN:Eu(,O) layer is ~960 °C, which is considerably higher than those for $In_xGa_{1-x}N$/GaN blue and green QWs (~ 650-850 °C), hence the GaN:Eu layer is thermally stable at those temperatures. This allows for the growth of subsequent n-type and p-type layers at a relatively high temperature, enabling high crystallinity. From this perspective, GaN:Eu-based red LEDs are more suitable for vertically stacked integration as compared to $In_xGa_{1-x}N$/GaN-based red LEDs, which are prone to In-desorption at high temperatures [53].

In most of the early reports, GaN:Eu samples were fabricated utilizing ion implantation techniques [54,55]. Ion implantation is attractive because of the relatively easy procedures, and it

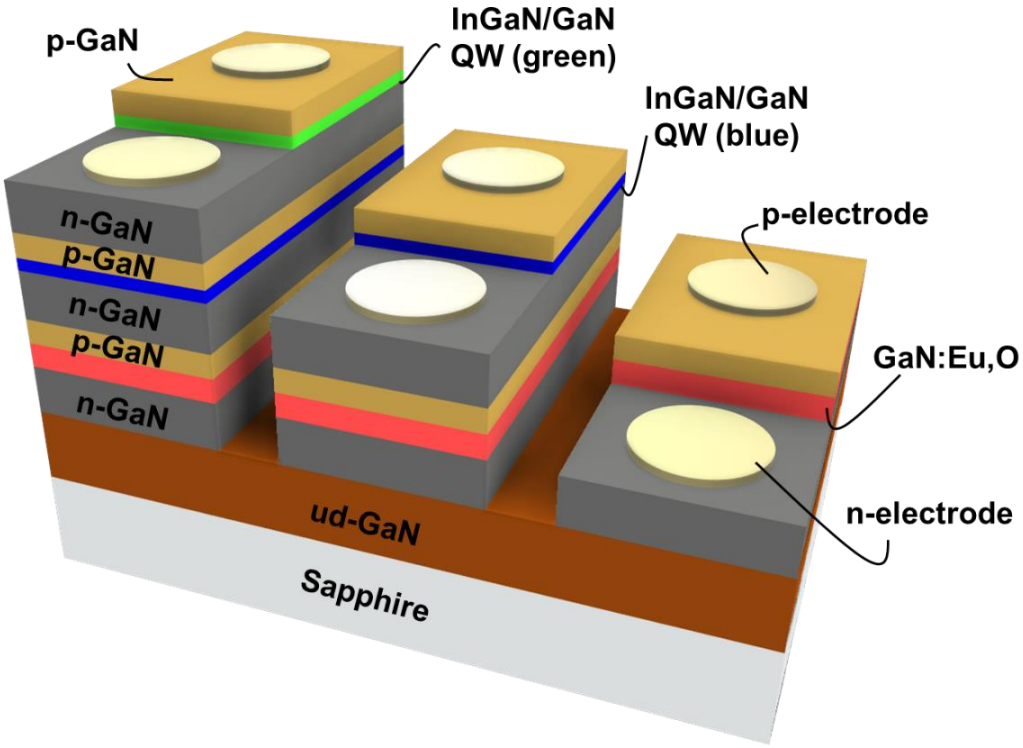

Fig. 1. 1 Schematic of the proposed structure for the monolithic integration of three primary colors planar μ-LEDs.

allows for accurate control of the implantation area and ion concentration. However, this technique introduces point defects (e.g., vacancies and interstitials) due to energetic collision cascades of ions, and strongly degrades optical and electrical properties [56]. Such damages can be partially recovered by thermal annealing [57], however, high temperatures beyond ~900 °C introduces additional challenges with the thermodynamic stability of GaN at atmospheric pressure. Ultra-high pressure annealing (UHPA) is recently employed to solve this issue, nevertheless, the luminescence efficiency is still limited due to the relatively poor crystal quality [58,59] . Molecular beam epitaxy (MBE) is a method for in-situ doping of Eu into GaN during an epitaxial growth process [46,47,60–62]. This epitaxial method enables high crystallinity, however, it requires high vacuum conditions, thus is not practical for the mass production.

Organometallic vapor-phase epitaxy (OMVPE) is a method that is widely used for the mass production of semiconductor devices. It enables simultaneous growth on multiple substrates without the need for a high vacuum. Using the OMVPE method, Eu ions can be *in-situ* doped into GaN under nearly thermal equilibrium condition, leading to a high crystallinity [63,64].

We have fabricated GaN:Eu samples using the OMVPE method and demonstrated LED operation [48]. In order to achieve high efficient GaN:Eu-based LED devices, methods to selectively form luminescent sites with high luminescence efficiencies has been intensely studied. The radiative lifetime of Eu^{3+} ions does not significantly depend on the kind of luminescent site, therefore the luminescence efficiency is greatly determined by carrier-mediated excitation efficiency, including free carrier capture rate and energy transfer rate to Eu^{3+} ions. Therefore, the formation of luminescent sites with high excitation efficiencies is crucial to improve the external quantum efficiency (EQE).

It has been reported that GaN:Eu grown using the OMVPE method has mainly eight luminescent sites labeled as OMVPE1-8 [51], and each site has different local atomic structure. Especially, OMVPE7 (Eu2) and OMVPE8 ($Eu2^{*}$), which are believed to be charge states of the same local atomic structure [65], have large excitation cross section that is two-three order of magnitude larger than those of other sites [66]. Ishii *et al*. has investigated the local potential around Eu^{3+} luminescent site of GaN:Eu grown by the OMPVE method using the site-selective pulse-driven emission spectroscopy method, and has suggested that OMVPE7 and OMVPE8 has larger carrier capture cross section as compared to OMVPE4, which has the largest abundance [51,67]. Consequently, OMVPE7 and OMVPE8 show dominant emission under current injection [66,67]. However, these two sites typically account for less than 10% of the total amount of Eu^{3+} ions doped

in GaN [51]; therefore it is highly important to increase the number of luminescent sites with high excitation efficiencies such as OMVPE7 and OMVPE8 for the realization of high efficient GaN:Eu-based LEDs.

In the research history of RE-doped semiconductors [68–70], co-doping of other ions has been recognized as an effective method to form luminescent sites with high excitation efficiencies. It is reported that oxygen co-doped into Er-doped Si optically activates Er^{3+} ions leading to a significant increase in the luminescence intensity [71]. In addition, oxygen co-doping into Er-doped GaAs selectively forms one specific luminescent site, where an Er atom locates at the Ga sublattice with two neighboring O atoms and two As atoms, resulting in a significant enhancement in the luminescent intensity [72,73].

For GaN:Eu, Mg-codoping has been intensely studied because it leads to the formation of Mg-related Eu luminescent sites, which is much more efficient than Eu sites found in Mg-free GaN:Eu [74–79]. However, the enhanced PL intensity was severely reduced after thermal annealing process [80], which is required for the activation of Mg-doped p-type GaN layers [81]. The Mg-related Eu luminescent sites with high excitation efficiencies are believed to be formed by Eu-Mg-H complex. Thermal annealing effectively dissociates the Mg-H complex [82], resulting in a significant quenching in the PL intensity associated with that complex. Si-codoping into GaN:Eu,Mg was investigated to control the local structure around Eu^{3+} ions, however, it did not result in an increase in the luminescence efficiency [83].

However, these studies on co-doping have suggested that the formation of donor-acceptor pairs (DAPs) in the vicinity of Eu^{3+} ions may be beneficial because they facilitate free carrier capture and energy transfer processes [84]. In the case of GaN:Eu,Mg, it is believed that a nitrogen vacancy (V_N) acts as a donor and form a DAP with a Mg acceptor around an Eu^{3+} ion [84]. This knowledge is an important guideline for the formation of luminescent sites with high excitation efficiencies.

Co-doping of oxygen into GaN:Eu has also been intensely studied. Early GaN:Eu samples grown using the OMVPE method were fabricated using tris(dipivaroylmethanate)-europium [$Eu(DPM)_3$] as the Eu precursor. $Eu(DPM)_3$ contains a high concentration of oxygen in its molecular structure, hence oxygen was spontaneously incorporated into GaN:Eu during growth on the order of 10^{20} cm^{-3}, which is much higher as compared to conventional GaN-based optoelectronic devices. Because a high oxygen concentration can lead to the degradation of GaN-based devices [48], an oxygen-free Eu source, bis(n-propyl-tetramethylcyclopentadienyl)-europium [$Eu(Cp^{pm}_2)$] was developed. However, for samples grown using $Eu(Cp^{pm}_2)$, Eu precipitation was observed on the

samples surface [85]. In addition, the linewidth of Eu^{3+} emission was much broader than those of GaN:Eu samples grown with $Eu(DPM)_3$. As a result of intentional codoping of oxygen using argon-diluted oxygen, it was found that oxygen plays an important role in the incorporation of Eu atoms into GaN. Besides, Rutherford backscattering/channeling measurements revealed that substantial oxygen leads to a homogeneous Eu incorporation into Ga site and an increased Eu concentration [85]. Furthermore, it was suggested that the OMVPE7 and OMVPE8 have oxygen atoms in the vicinity of Eu^{3+}. The oxygen acts as a donor and form a DAP with a V_{Ga} acceptor [86,87], leading to a quite high excitation efficiency [84]. Based on these results, luminescence efficiency of Eu^{3+} emission from GaN:Eu,O using $Eu(Cp^{pm}_2)$ precursor has been improved by controlling the oxygen concentration by the flow rate of argon-diluted oxygen.

Furthermore, it has been found that multi-layer structure (MLS) samples with alternating layers of Eu,O-codoped and undoped-GaN significantly enhance the luminescence efficiency of Eu^{3+} [85,88]. Terahertz spectroscopy revealed that Eu-doping into GaN effectively decreases the bandgap while increasing the refractive index. These effects contribute to an efficient confinement of carrier and light in the GaN:Eu,O layers, leading to an enhanced luminescence intensity [89]. A GaN:Eu,O-based MLS LED exhibited a high light output of 1.25 mW at 20 mA operation with the maximum EQE of 9.2% [90], which is significantly improved comparing to the EQE of LEDs in the early years of research (~1×10^{-3}%) [48].

However, for the future implementation of III-nitride-based monolithic LED displays using GaN:Eu, it is crucial to improve the EQE of GaN:Eu-based LEDs, because it is still one order of magnitude lower than that of $In_xGa_{1-x}N$-based blue and green LEDs [2,11].

EQE is proportional to the product of IQE × LEE, where LEE is light extraction efficiency. Enhanced light output of GaN:Eu,O-based devices by utilizing microcavities [91,92] and the localized surface plasmon effect [93] have been demonstrated. A thorough investigation of their optical properties revealed that these methods are effective to enhance the LEE, while has a relatively minor impact on the IQE. Therefore, intrinsic approach to enhance the IQE is required for even higher EQEs.

In order to further improve IQEs, it is imminent to develop methods to selectively form luminescent sites with high excitation efficiencies such as OMVPE7 and OMVPE8. In this thesis, we perform post-growth thermal annealing to selectively form efficient sites, aiming to develop highly efficient and bright GaN:Eu,O-based LEDs for the implementation of III-nitride-based μ-LED displays.

1.3 Towards GaN:Eu,O-based LDs

In addition to the monolithic integration of three primary colors LEDs, the integration of LDs is also of great interest for wide applications including high-definition laser displays, head-up displays and ultra-small projectors due to the high scanning performance, high brightness and high quantum efficiency of LDs. Therefore, there is considerable interest in exploring the possibility of achieving lasing in GaN:Eu,O within optical cavities for the realization of III-nitride-based red LDs.

Besides, with the recent development of an advanced smart society, there is an urgent need to simplify and reduce the power consumption of data centers. On-chip optical communications are attracting attentions for low-power, compact and fast communications. Conventional optical communication systems have utilized RE-doped fiber lasers for decades, which excite RE ions doped in a long fiber with an excitation source. However compact lasers using RE ions are required for the future on-chip optical communication devices. In this regard, RE-doped-semiconductor-based LDs are promising candidates.

Park *et al*. have reported laser action in GaN:Eu at room temperature by photoexcitation [60,61]. They have provided evidence of lasing action through the analysis of emission polarization, spectral line narrowing and the quick increase in the integrated PL intensity at a lasing threshold. However, regarding the emission polarization, they have not investigated the excitation power dependence of the polarization. The polarization of GaN:Eu intrinsic emission is determined by atomic structure and group theory [84], therefore more detailed analysis is required to confirm the occurrence of lasing action. Furthermore, the emission spectrum for GaN:Eu is highly complicated because it is composed of emission peaks originating from several luminescent sites. Each luminescent site has different efficiency to be excited [66], therefore a careful attention should be paid when investigating the spectral linewidth, as well as the integrated PL intensity.

To evaluate the possibility of lasing in GaN:Eu,O, optical cavities with high-quality factors (*Q*-factors) are required because of the relatively low optical gain of GaN:Eu,O (6.6-14 cm^{-1}) [94–96]. Especially, two-dimensional photonic crystal (2D-PhC) [97] cavities are promising because they enable high *Q*-factors and wavelength-scale small modal volumes. 2D-PhC cavities have been intensely investigated in the infrared (IR) range utilizing mature semiconductors such as Si and InP, and high *Q*-factors exceeding 1×10^6 have been reported [98,99].

We have previously reported strongly enhanced light output of GaN:Eu,O using microdisk cavities with a maximum *Q*-factor of 3680 [100,101], however, 2D-PhC cavities have the potential to offer even higher *Q*-factors and much smaller modal volumes.

Recently, III-nitride-based 2D-PhC cavities have attracted attention for various applications including nonlinear wavelength conversion devices [102,103]. *Q*-factors exceeding 10000 have been reported in the IR region [102–104]. However, *Q*-factors in the ultraviolet-visible regime are still limited to about 5000, because *Q*-factors are greatly dependent on resonant wavelength as shown in Fig. 1. 2 [102–116]. Contrarily to cavities designed for the IR-red range, *Q*-factors of III-nitride-based cavities designed for the visible range are significantly limited by various optical losses. Previous studies have suggested that the *Q*-factor of III-nitride-based cavities are predominantly limited by light absorption of bulk [117], gain medium (QW) [118] and surface [119] for microdisk cavities, structural disorder originating from fabrication imperfections [120], and scattering losses due to surface roughness [120,121] for 1D-nanobeam cavities. Based on these studies, various techniques have been utilized to reduce such losses, for example, surface passivation [119] and suppression of light absorption by coupling resonant peaks to longer wavelength region of QW emission [120]. Due to these contributions, a high *Q*-factor of 7950 for a 1D-nanobeam cavity [119], and 10200 for a microdisk cavity [122] have been demonstrated in the visible range. However, the dominant optical loss of III-nitride-based 2D-PhC cavity has yet to be clarified. In order to improve *Q*-factors of 2D-PhC cavities for the realization of GaN:Eu,O-based lasers, it is thus essential to determine the dominant loss process and consider measures to suppress it.

Furthermore, based on the knowledge on the dominant optical loss, it is crucial to design cavities which can effectively suppress such losses. In these contributions, we reproduce experimentally introduced in-plane structural disorder in electromagnetic simulations, and discuss the impact of such disorder on *Q*-factors. In addition, by combining experimental results, we discuss the dominant optical loss which limits *Q*-factors. Subsequently, we design cavity structures to suppress the dominant optical loss for III-nitride-based 2D-PhC high-*Q* cavities.

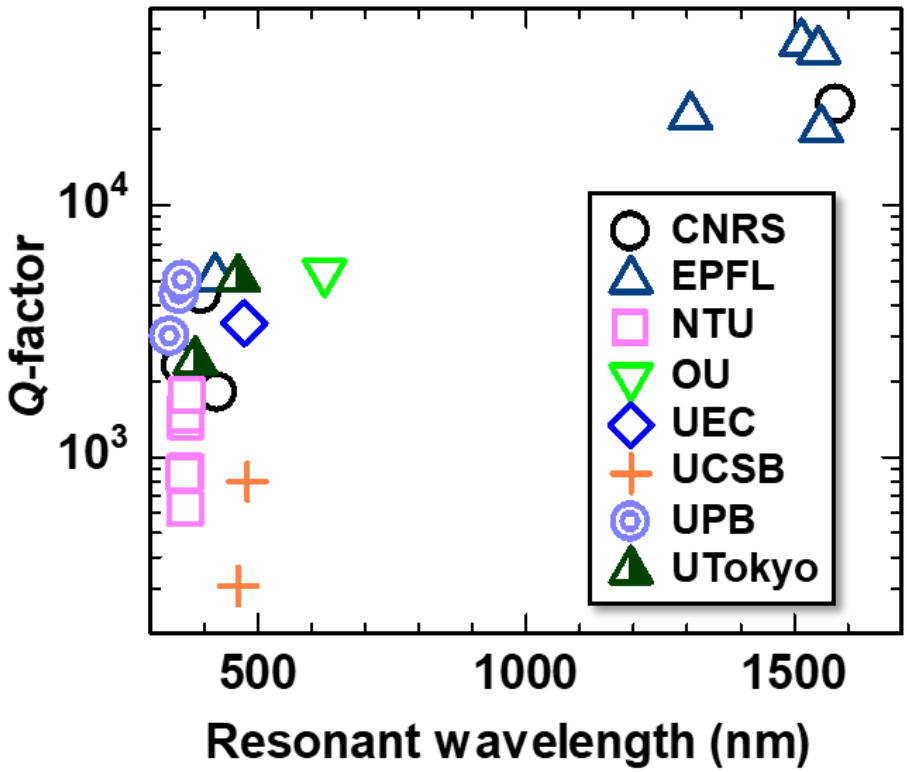

Fig. 1. 2 Reported *Q*-factors of III-nitride-based 2D-PhC cavities as a function of resonant wavelength [102–116].

1.4 Candidate materials for quantum information technologies

With the development of "smart society", the demand for quantum technologies is rapidly increasing for secure communication and ultrafast quantum computation. Further development of these technologies requires reliable quantum material systems such as single photon emitters with high reproducibility and probability. Atomic and atom-like point defect in solids is the most prominent candidate, especially nitrogen vacancy (NV) center in diamond has been intensely studied because it provides long spin relaxation lifetimes even at room temperature [123,124]. Silicon-vacancy center in diamond, which has very narrow emission lines distinguishable from the broad-band NV center emission, is also a promising material system [125]. In addition, quantum dots made from III-nitrides are attractive because it offers adequate exciton confinement at high temperatures [126–130]. However, for an even wider range of applications, other material systems should be investigated to give more choices of emission wavelength and optical and spin coherence properties. RE-doped materials are promising candidate because it offers long spin coherence time [131] in addition to the narrow linewidth and stable emission wavelength. Besides, it is possible to cover the whole visible regime as well as the IR regime using transition of different RE ions, making it useful for wide applications. For example, for a large-scale communication, Er^{3+} ion is the best candidate because the emission wavelength is at the telecom band (~1.5 μm), where the signal losses in optical fibers is as low as 0.2 dB/km [132] (for NV centers in diamond at 637 nm; 8 dB/km [133]).

So far, crystals such as YAG, YBO and YSO have been the main focus of study as host materials for doping RE ions in the field of quantum technology [131,133–141], taking advantage of the expertise cultivated in the development of laser gain media. For such materials, inhomogeneous line broadening can be well controlled by applying electric and magnetic fields [142,143] and the low-spin crystal hosts can minimize optical decoherence [144,145]. Even though the precise nano fabrication to form nanocavities possesses technical challenges because of fabrication errors primary caused by ion beam drift during the focused ion beam (FIB) milling process, Bayn *et al*. and Zhong *et al*. has proposed triangular nanobeams to solve this issue. These structures show high robustness against such fabrication errors and have demonstrated relatively high *Q*-factors in the visible-IR regime [146,147]. However, the operation of the devices based on RE-doped crystals requires an excitation laser source, limiting miniaturization and power

consumption reduction. Furthermore, for advanced systems such as quantum computers using RE ions as qubits, a highly complex optical system is needed to individually excite and detect signals from each qubit.

In this contribution, RE-doped semiconductor is a promising material system for quantum information technologies, because it can be driven under current injection making it easy to access each RE ion. For the host material, semiconductor transparent to emitted photons is preferable, III-nitrides are the most encouraging candidate because of the most matured growth and device fabrication technologies among wide-band gap semiconductors at this stage.

One issue of using RE ions for quantum information technologies is the small radiative recombination rate which limits the photon emission rate, that needs to be enhanced using optical cavities with high Purcell factors [100,133,141,148–150]. Especially, 2D-PhC cavities with high *Q*-factors have a large potential for applications, because the integration with 2D-PhC-based optical waveguides enables integrated circuits with a small footprint. Furthermore, the emission directionality can be well controlled by using band-edge modes near the Γ point in the photonic band diagram [151–155], which has a great potential to increase the extraction and detection efficiency.

In addition, it is essential to selectively form efficient luminescent sites with high excitation efficiencies such as OMVPE7 and OMVPE8. For the application in quantum information technologies such as single photon emitters, it is essential to keep the number of RE ions within a device sufficiently low. Assuming that the size of the active layer of a single photon emitter is 100 nm × 1 μm × 1 μm, the concentration of the Eu^{3+} ions should be less than 1×10^{19} cm^{-3} to achieve single photon generation from the device. However, for GaN:Eu,O samples, emission from defect levels in GaN becomes dominant with the reduction of RE ion concentration. In Fig. 1. 3, photoluminescence (PL) spectra are depicted for GaN:Eu,O films grown by OMVPE method with Eu precursor ($EuCp^{pm}_2$) flow rate of 1.1×10^{-2}, 5.7×10^{-2}, 5.9×10^{-1} μmol/min, with an estimated Eu concentration of 4.4×10^{20}, 4.2×10^{19} and 8.3×10^{18} cm^{-3}, respectively. The samples grown with $EuCp^{pm}_2$ flow rate larger than or equal to 5.7×10^{-2} show clear Eu^{3+} emission, however, the sample with further diluted Eu^{3+} concentration dominantly shows a broad emission which originates from defect levels in GaN.

Therefore, to achieve clear Eu^{3+} emission from samples with diluted Eu^{3+} ion concentration while suppressing emission from defect levels, luminescent sites with high excitation efficiency need to be selectively formed.

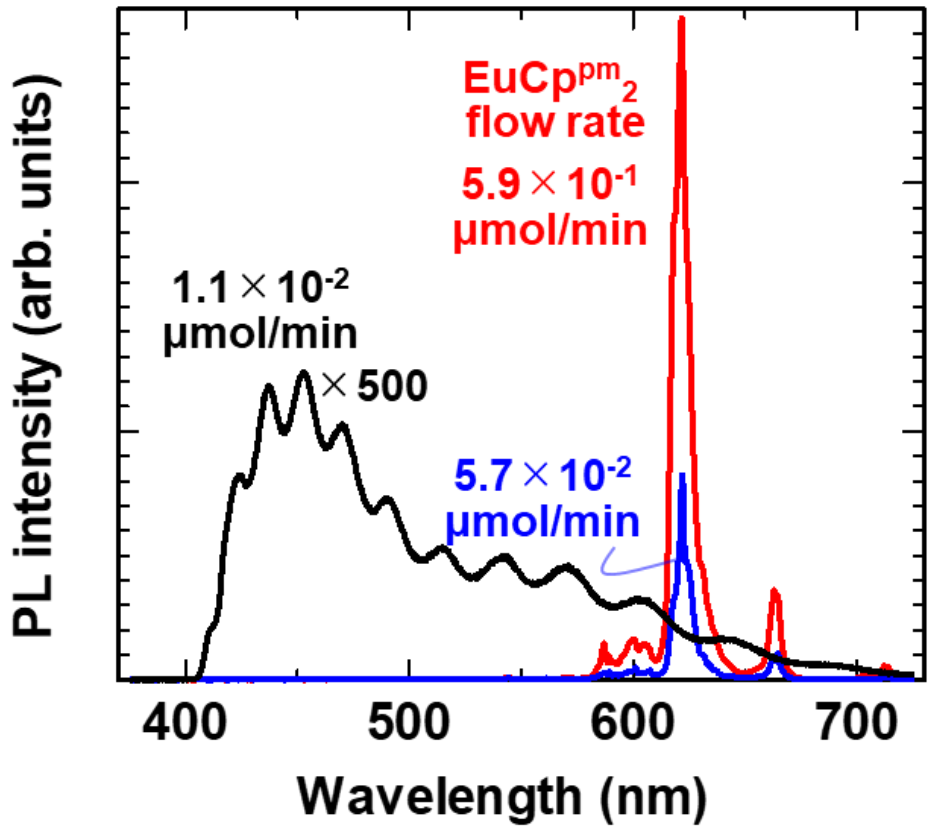

Fig. 1. 3 PL spectra for GaN:Eu,O films grown with EuCp$^{pm}_2$ flow rate of 1.1×10^{-2}, 5.7×10^{-2}, 5.9×10^{-1} μmol/min measured at room temperature.

1.5 Aims and outline of this research

In this research, we investigate intrinsic and extrinsic control of Eu^{3+} emission in GaN:Eu,O for wide applications including high efficient LEDs, LDs and quantum information technologies. For the intrinsic control, we aim to selectively form efficient luminescent sites with high excitation efficiencies through optimization of growth parameters and utilizing post-growth thermal annealing process. Furthermore, as the extrinsic control of Eu^{3+} emission, we investigate on high-*Q* 2D-PhC cavities to modify the local density of states of photons and to improve luminous efficiency of Eu^{3+}.

In Chapter 2, we study the impact of post-growth thermal annealing at high temperatures on the optical properties of GaN:Eu,O. The results clarify that thermal annealing at temperature above 1000 °C effectively eliminates inefficient Eu clusters and converts them into efficient luminescent sites with high excitation efficiencies. These sites can efficiently capture free carriers and compete with non-radiative traps, thus the formation of them results in a great improvement in luminescence efficiency especially at low excitation power region, where μ-LED displays are expected to be utilized.

In Chapter 3, we focus on a specific luminescent site (OMVPE-X), which is preferentially formed by the annealing process. We conduct PL measurements and report that this site has a quite high excitation efficiency. Furthermore, we apply the annealing technique to LED fabrication process, and report that the OMVPE-X shows a dominant emission under low current injection density region, suggesting it has a high excitation efficiency even under current injection.

In Chapter 4, we focus on 2D-PhC cavities to extrinsically control the optical transition probability of Eu^{3+}, and investigate on proper cavity design to achieve high *Q*-factors even with III-nitride semiconductors. To numerically examine the impact of structural disorder on *Q*-factors, we reproduce experimentally found disorder in simulations. We demonstrate the importance of cavity design to achieve high *Q*-factors when a large degree of structural disorder is introduced. We suggest that hexagonal-defect cavities, particularly an H3 cavity shows a great robust stability of *Q*-factors against structural disorder.

In Chapter 5, we fabricate H3 cavities to validate the simulation results and to explore the dominant optical loss that limits *Q*-factors with the aim of further enhancement. As a result, we show that the most important limitation is the theoretical value of the design *Q*-factor itself. Based on this knowledge, a 2D photonic heterostructure, which exhibits a band-edge mode with higher

theoretical *Q*-factor, is introduced. Consequently, we find that such type of cavity structure is promising to achieve high *Q*-factors for III-nitride semiconductors.

Finally in Chapter 6, we summarize the obtained results and discuss several future prospects.

References

[1] K. Bando, K. Sakano, Y. Noguchi, and Y. Shimizu, *J. Light Vis. Environ.* **22**, 2 (1998).

[2] Y. Narukawa, M. Ichikawa, D. Sanga, M. Sano, and T. Mukai, *J. Phys. D Appl. Phys.* **43**, 354002 (2010).

[3] Y. Utsumi, I. Hiyama, Y. Tomioka, K. Kondo, and S. Matsuyama, *Jpn. J. Appl. Phys*. **46**, 1047 (2007).

[4] Y. Utsumi, S. Takeda, I. Hiyama, Y. Tomioka, M. Ishii, and K. Ono, *Jpn. J. Appl. Phys*. **47**, 2144 (2008).

[5] J.S. Hsu, Y.H. Lin, H.C. Lin, and K.H. Yang, *J. Appl. Phys*. **105**, 033503 (2009).

[6] M. Ishiguro, M. Sekiguchi, and Y. Saitoh, *Jpn. J. Appl. Phys*. **49**, 030208 (2010).

[7] H. Chen, G. Tan, M.-C. Li, S.-L. Lee, and S.-T. Wu, *Opt. Express* **25**, 11315 (2017).

[8] T.Y. Chu, Y.H. Lee, and O.K. Song, *Appl. Phys. Lett.* **91**, 223509 (2007).

[9] R. Phatak, T.Y. Tsui, and H. Aziz, *J. Appl. Phys.* **111**, 054512 (2012).

[10] D.Y. Kondakov, J.R. Sandifer, C.W. Tang, and R.H. Young, *J. Appl. Phys.* **93**, 1108–1119 (2003).

[11] S. Saito, R. Hashimoto, J. Hwang, and S. Nunoue, *Appl. Phys. Express* **6**, 111004 (2013).

[12] B. Zhao, T. Zhang, B. Chu, W. Li, Z. Su, H. Wu, X. Yan, F. Jin, Y. Gao, and C. Liu, *Sci. Rep.* **5**, 10697 (2015).

[13] M.Y. Wong and E. Zysman-Colman, *Adv. Mater.* **29**, 1605444 (2017).

[14] B.H. Kim, S. Nam, N. Oh, S.Y. Cho, K.J. Yu, C.H. Lee, J. Zhang, K. Deshpande, P. Trefonas, J.H. Kim, J. Lee, J.H. Shin, Y. Yu, J. Bin Lim, S.M. Won, Y.K. Cho, N.H. Kim, K.J. Seo, H. Lee, et al., *ACS Nano.* **10**, 4920–4925 (2016).

[15] J. Xiao, R.R. Chaudhuri, and S.W. Seo, *IEEE Trans. Compon. Packaging Manuf. Technol.* **6**, 1283–1289 (2016).

[16] J. Kou, C.-C. Shen, H. Shao, J. Che, X. Hou, C. Chu, K. Tian, Y. Zhang, Z.-H. Zhang, and H.-C. Kuo, *Opt. Express* **27**, A643 (2019).

[17] J.-I. Shim, J.H. Moon, C. Oh, Y.-T. Moon, K.Y. Song, J.-T. Oh, T.-Y. Seong, S.-Y. Lee, J.-O. Song, S. Park, H.-H. Jeong, K.Y. Hong, and H. Amano, *Opt. Express* **26**, 11194–11200 (2018).

[18] Y. Narukawa, Y. Kawakami, M. Funato, S. Fujita, S. Fujita, and S. Nakamura, *Appl. Phys. Lett.* **70**, 981–983 (1997).

[19] S. Chichibu, K. Wada, and S. Nakamura, *Appl. Phys. Lett.* **71**, 2346–2348 (1997).

[20] S. Nakamura, *Science*, **281**, 956–961 (1998).

[21] T. Takeuchi, S. Sota, M. Katsuragawa, M. Komori, H. Takeuchi, H.A.H. Amano, and I.A.I. Akasaki, *Jpn. J. Appl. Phys.* **36**, L382 (1997).

[22] M.B. Nardelli, K. Rapcewicz, and J. Bernholc, *Appl. Phys. Lett.* **71**, 3135 (1997).

[23] R. Singh, D. Doppalapudi, T.D. Moustakas, and L.T. Romano, *Appl. Phys. Lett.* **70**, 1089–1091 (1997).

[24] M. Auf Der Maur, A. Pecchia, G. Penazzi, W. Rodrigues, and A. Di Carlo, *Phys. Rev. Lett.* **116**, 027401 (2016).

[25] S. Nakamura, M. Senoh, N. Iwasa, and S.I. Nagahama, *Jpn. J. Appl. Phys.* **34**, L797–L799 (1995).

[26] M. Funato, M. Ueda, Y. Kawakami, Y. Narukawa, T. Kosugi, M. Takahashi, and T. Mukai, *Jpn. J. Appl. Phys.* **45**, L659 (2006).

[27] K. Ohkawa, T. Watanabe, M. Sakamoto, A. Hirako, and M. Deura, *J. Cryst. Growth* **343**, 13–16 (2012).

[28] Y. Kawaguchi, C.Y. Huang, Y.R. Wu, Y. Zhao, S.P. DenBaars, and S. Nakamura, *Jpn. J. Appl. Phys.* **52**, 08JC08 (2013).

[29] J. Il Hwang, R. Hashimoto, S. Saito, and S. Nunoue, *Appl. Phys. Express* **7**, 071003 (2014).

[30] K. Kishino, A. Yanagihara, K. Ikeda, and K. Yamano, *Electron. Lett.* **51**, 852–854 (2015).

[31] D. Iida, K. Niwa, S. Kamiyama, and K. Ohkawa, *Appl. Phys. Express* **9**, 111003 (2016).

[32] T. Ozaki, M. Funato, and Y. Kawakami, *Appl. Phys. Express* **12**, 011007 (2019).

[33] D.A. B Miller, D.S. Chemla, T.C. Damen, A.C. Gossard and, T.H. Wood, C.A. Burrus, D.A.B. Miller, D.S. Chemla, T.C. Damen, A.C. Gossard, W. Wiegmann, T.H. Wood, and C.A. Burrus, *Phys. Rev. Lett.* **53**, 2173–2176 (1984).

[34] O. Goede, L. John, and D. Henning, *Phys. Status Solidi B* **89**, K183 (1978).

[35] E.F. Schubert, E.O. Göbel, Y. Horikoshi, K. Ploog, and H.J. Queisser, *Phys. Rev. B* **30**, 813–820 (1984).

[36] G. Coli, K.K. Bajaj, J. Li, J.Y. Lin, and H.X. Jiang, *Appl. Phys. Lett.* **78**, 1829–1831 (2001).

[37] D. Iida and K. Ohkawa, *Semicond. Sci. Technol.* **37**, 013001 (2022).

[38] K. Kishino, N. Sakakibara, K. Narita, and T. Oto, *Appl. Phys. Express* **13**, 014003 (2020).

[39] D.C. Chen, Z.G. Liu, Z.H. Deng, C. Wang, Y.G. Cao, and Q.L. Liu, *Rare Met.* **33**, 348–352 (2014).

[40] H.-V.H. Han, H.-Y. Lin, C.C.-C.C. Lin, W.-C.C. Chong, J.-R. Li, K.-J.J.K. Chen, P. Yu, T.-M.T. Chen, H.C.H.-M. Chen, K.-M.M. Lau, and H.-C.H. Kuo, *Opt. Express* **23**, 32504 (2015).

[41] G.S. Chen, B.Y. Wei, C.T. Lee, and H.Y. Lee, *IEEE Photon. Technol. Lett.* **30**, 262–265 (2018).

[42] D.M. Geum, S.K. Kim, C.M. Kang, S.H. Moon, J. Kyhm, J. Han, D.S. Lee, and S. Kim, *Nanoscale*, **11**, 23139–23148 (2019).

[43] R.M.M. Hasan and X. Luo, *Nanomanuf. Metrol.* **1**, 67–81 (2018).

[44] L. Zhang, F. Ou, W.C. Chong, Y. Chen, and Q. Li, *J. Soc. Inf. Disp.* **26**, 137–145 (2018).

[45] S. Ichikawa, K. Shiomi, T. Morikawa, D. Timmerman, Y. Sasaki, J. Tatebayashi, and Y. Fujiwara, *Appl. Phys. Express* **14**, 031008 (2021).

[46] S. Morishima, T. Maruyama, M. Tanaka, Y. Masumoto, and K. Akimoto, *Phys. Status Solidi A, Appl. Res.* **176**, 113–117 (1999).

[47] J. Heikenfeld, M. Garter, D.S. Lee, R. Birkhahn, and A.J. Steckl, *Appl. Phys. Lett.* **75**, 1189–1191 (1999).

[48] A. Nishikawa, T. Kawasaki, N. Furukawa, Y. Terai, and Y. Fujiwara, *Appl. Phys. Express* **2**, 071004 (2009).

[49] B.R. Judd, *Phys. Rev.* **127**, 750–761 (1962).

[50] G.S. Ofelt, *J. Chem. Phys.* **37**, 511–520 (1962).

[51] R. Wakamatsu, D.G. Lee, A. Koizumi, V. Dierolf, and Y. Fujiwara, *J. Appl. Phys.* **114**, 043501 (2013).

[52] D. Denier van der Gon, D. Timmerman, Y. Matsude, S. Ichikawa, M. Ashida, P. Schall, and Y. Fujiwara, *Opt. Lett.* **45**, 3973 (2020).

[53] H.P.D. Schenk, P. De Mierry, M. Laügt, F. Omnès, M. Leroux, B. Beaumont, and P. Gibart, *Appl. Phys. Lett.* **75**, 2587–2589 (1999).

[54] H.J. Lozykowski, W.M. Jadwisienczak, J. Han, and I.G. Brown, *Appl. Phys. Lett.* **77**, 767–769 (2000).

[55] V. Katchkanov, K.P. O'Donnell, S. Dalmasso, R.W. Martin, A. Braud, Y. Nakanishi, A. Wakahara, and A. Yoshida, *Phys. Status Solidi B, Basic Res.* **242**, 1491–1496 (2005).

[56] D.N. Faye, M. Fialho, S. Magalhães, E. Alves, N. Ben Sedrine, J. Rodrigues, M.R. Correia, T. Monteiro, M. Boćkowski, V. Hoffmann, M. Weyers, and K. Lorenz, *Nucl. Instrum. Methods. Phys. Res. B* **379**, 251–254 (2016).

[57] L. Bodiou, A. Oussif, A. Braud, J.L. Doualan, R. Moncorgé, K. Lorenz, and E. Alves, *Opt. Mater.* **28**, 780–784 (2006).

[58] K. Lorenz, S.M.C. Miranda, E. Alves, I.S. Roqan, K.P. O'Donnell, and M. Bokowski, *Proc. SPIE* **8262**, 82620C (2012).

[59] P. Jaroszynski, E. Grzanka, M. Grabowski, G. Staszczak, I. Prozheev, R. Jakiela, F. Tuomisto, and M. Bockowski, *Appl. Surf. Sci.* **625**, 157188 (2023).

[60] J.H. Park and A.J. Steckl, *Appl. Phys. Lett.* **85**, 4588–4590 (2004).

[61] J.H. Park and A.J. Steckl, *J. Appl. Phys.* **98**, 056108 (2005).

[62] U. Hömmerich, E.E. Nyein, D.S. Lee, J. Heikenfeld, A.J. Steckl, and J.M. Zavada, *Mater. Sci. Eng. B: Solid-State Mater. Adv. Technol.* **105**, 91–96 (2003).

[63] M. Pan and A.J. Steckl, *Appl. Phys. Lett.* **83**, 9–11 (2003).

[64] K. Wang, R.W. Martin, K.P. O'Donnell, V. Katchkanov, E. Nogales, K. Lorenz, E. Alves, S. Ruffenach, and O. Briot, *Appl. Phys. Lett.* **87**, 112107 (2005).

[65] B. Mitchell, N. Hernandez, D. Lee, A. Koizumi, Y. Fujiwara, and V. Dierolf, *Phys. Rev. B* **96**, 064308 (2017).

[66] D. Timmerman, B. Mitchell, S. Ichikawa, J. Tatebayashi, M. Ashida, and Y. Fujiwara, *Phys. Rev. Appl.* **13**, 014044 (2020).

[67] M. Ishii, A. Koizumi, and Y. Fujiwara, *J. Appl. Phys.* **117**, 155307 (2015).

[68] H. Ennen, U. Kaufmann, G. Pomrenke, J. Schneider, J. Windscheif, and A. Axmann, *J. Cryst. Growth* **64**, 165–168 (1983).

[69] H. Ennen, J. Schneider, G. Pomrenke, and A. Axmann, *Appl. Phys. Lett.* **43**, 943–945 (1983).

[70] H. Ennen, G. Pomrenke, A. Axmann, K. Eisele, W. Haydl, and J. Schneider, *Appl. Phys. Lett.* **46**, 381–383 (1985).

[71] P.N. Favennec, H. L'Haridon, D. Moutonnet, M. Salvi, and M. Gauneau, *Jpn. J. Appl. Phys.* **29**, L524–L526 (1990).

[72] K. Takahei and A. Taguchi, *J. Appl. Phys.* **74**, 1979–1982 (1993).

[73] K. Takahei, A. Taguchi, Y. Horikoshi, and J. Nakata, *J. Appl. Phys.* **76**, 4332–4339 (1994).

[74] Y. Takagi, T. Suwa, H. Sekiguchi, H. Okada, and A. Wakahara, *Appl. Phys. Lett.* **99**, 97–100 (2011).

[75] D.G. Lee, A. Nishikawa, Y. Terai, and Y. Fujiwara, *Appl. Phys. Lett.* **100**, 2010–2013 (2012).

[76] H. Sekiguchi, Y. Takagi, T. Otani, H. Okada, and A. Wakahara, *J. Appl. Phys.* **113**, 013105 (2013).

[77] H. Sekiguchi, M. Sakai, T. Kamada, H. Tateishi, A. Syouji, and A. Wakahara, *Appl. Phys. Lett.* **109**, 151106 (2016).

[78] K.P. O'Donnell, P.R. Edwards, M. Yamaga, K. Lorenz, M.J. Kappers, and M. Boćkowski, *Appl. Phys. Lett.* **108**, 022102 (2016).

[79] H. Sekiguchi, M. Sakai, T. Kamada, K. Yamane, H. Okada, and A. Wakahara, *J. Appl. Phys.* **125**, 175702 (2019).

[80] D.G. Lee, R. Wakamatsu, A. Koizumi, Y. Terai, J.D. Poplawsky, V. Dierolf, and Y. Fujiwara, *Appl. Phys. Lett.* **102**, 141904 (2013).

[81] S. Nakamura, T. Mukai, M. Senoh, and N. Iwasa, *Jpn. J. Appl. Phys.* **31**, 139–142 (1992).

[82] W. Götz, N.M. Johnson, D.P. Bour, M.D. McCluskey, and E.E. Haller, *Appl. Phys. Lett.* **69**, 3725–3727 (1996).

[83] D.G. Lee, R. Wakamatsu, A. Koizumi, Y. Terai, and Y. Fujiwara, *Jpn. J. Appl. Phys.* **52**, 08JM01 (2013).

[84] B. Mitchell, J. Poplawsky, D. Lee, A. Koizumi, Y. Fujiwara, and V. Dierolf, *J. Appl. Phys.* **115**, 204501 (2014).

[85] B. Mitchell, D. Timmerman, J. Poplawsky, W. Zhu, D. Lee, R. Wakamatsu, J. Takatsu, M. Matsuda, W. Guo, K. Lorenz, E. Alves, A. Koizumi, V. Dierolf, and Y. Fujiwara, *Sci. Rep.* **6**, 18808 (2016).

[86] J. Neugebauer and C.G. Van de Walle, *Appl. Phys. Lett.* **69**, 503–505 (1996).

[87] N.T. Son, C.G. Hemmingsson, T. Paskova, K.R. Evans, A. Usui, N. Morishita, T. Ohshima, J. Isoya, B. Monemar, and E. Janzén, *Phys. Rev. B* **80**, 153202 (2009).

[88] W. Zhu, B. Mitchell, D. Timmerman, A. Koizumi, T. Gregorkiewicz, and Y. Fujiwara, *MRS Adv.* **1**, 159 (2017).

[89] F. Murakami, A. Takeo, B. Mitchell, V. Dierolf, Y. Fujiwara, and M. Tonouchi, *Commun. Mater.* **4**, 100 (2023).

[90] B. Mitchell, V. Dierolf, T. Gregorkiewicz, and Y. Fujiwara, *J. Appl. Phys.* **123**, 160901 (2018).

[91] T. Inaba, D.G. Lee, R. Wakamatsu, T. Kojima, B. Mitchell, A. Capretti, T. Gregorkiewicz, A. Koizumi, and Y. Fujiwara, *AIP Adv.* **6**, 045105 (2016).

[92] T. Inaba, J. Tatebayashi, K. Shiomi, D. Timmerman, S. Ichikawa, and Y. Fujiwara, *ACS Appl. Electron. Mater.* **2**, 732–738 (2020).

[93] J. Tatebayashi, T. Yamada, T. Inaba, D. Timmerman, S. Ichikawa, and Y. Fujiwara, *Appl. Phys. Express* **12**, 095003 (2019).

[94] A. Takeo, S. Ichikawa, S. Maeda, D. Timmerman, J. Tatebayashi, and Y. Fujiwara, *Jpn. J. Appl. Phys.* **60**, 120905 (2021).

[95] N.N. Ha, A. Nishikawa, Y. Fujiwara, and T. Gregorkiewicz, *Journal of Science: J. Sci.: Adv. Mater. Devices* **1**, 220 (2016).

[96] T. Iwaya, S. Ichikawa, M. Murakami, D. Timmerman, J. Tatebayashi, and Y. Fujiwara, *Appl. Phys. Express* **14**, 122002 (2021).

[97] E. Yablonovitch, *Phys. Rev. Lett.* **58**, 2059 (1987).

[98] E. Kuramochi, E. Grossman, K. Nozaki, K. Takeda, A. Shinya, H. Taniyama, and M. Notomi, *Opt. Lett.* **39**, 5780 (2014).

[99] Y. Lai, S. Pirotta, G. Urbinati, D. Gerace, M. Minkov, V. Savona, A. Badolato, and M. Galli, *Appl. Phys. Lett.* **104**, 241101 (2014).

[100] D. Timmerman, Y. Matsude, Y. Sasaki, S. Ichikawa, J. Tatebayashi, and Y. Fujiwara, *Phys. Rev. Appl.* **14**, 064059 (2020).

[101] T. Taniguchi, D. Timmerman, S. Ichikawa, J. Tatebayashi, and Y. Fujiwara, *Opt. Lett.* **48**, 4590 (2023).

[102] M.S. Mohamed, A. Simbula, J.F. Carlin, M. Minkov, D. Gerace, V. Savona, N. Grandjean, M. Galli, and R. Houdré, *APL Photonics* **2**, 031301 (2017).

[103] Y. Zeng, I. Roland, X. Checoury, Z. Han, M. El Kurdi, S. Sauvage, B. Gayral, C. Brimont, T. Guillet, M. Mexis, F. Semond, and P. Boucaud, *Appl. Phys. Lett.* **106**, 081105 (2015).

[104] N.V. Triviño, M. Minkov, G. Urbinati, M. Galli, J.F. Carlin, R. Butté, V. Savona, and N. Grandjean, *Appl. Phys. Lett.* **105**, 231119 (2014).

[105] D. Néel, S. Sergent, M. Mexis, D. Sam-Giao, T. Guillet, C. Brimont, T. Bretagnon, F. Semond, B. Gayral, S. David, X. Checoury, and P. Boucaud, *Appl. Phys. Lett.* **98**, 261106 (2011).

[106] D. Sam-Giao, D. Néel, S. Sergent, B. Gayral, M.J. Rashid, F. Semond, J.Y. Duboz, M. Mexis, T. Guillet, C. Brimont, S. David, X. Checoury, and P. Boucaud, *Appl. Phys. Lett.* **100**, 191104 (2012).

[107] N. Vico Triviño, G. Rossbach, U. Dharanipathy, J. Levrat, A. Castiglia, J.F. Carlin, K.A. Atlasov, R. Butté, R. Houdré, and N. Grandjean, *Appl. Phys. Lett.* **100**, 071103 (2012).

[108] C.H. Lin, J.Y. Wang, C.Y. Chen, K.C. Shen, D.M. Yeh, Y.W. Kiang, and C.C. Yang, *Nanotechnology* **22**, 025201 (2011).

[109] S. Ichikawa, Y. Sasaki, T. Iwaya, M. Murakami, M. Ashida, D. Timmerman, J. Tatebayashi, and Y. Fujiwara, *Phys. Rev. Appl.* **15**, 034086 (2021).

[110] T. Tajiri, M. Yoshida, S. Sosumi, K. Shimoyoshi, and K. Uchida, *Jpn. J. Appl. Phys.* **62**, SG1019 (2023).

[111] Y.S. Choi, K. Hennessy, R. Sharma, E. Haberer, Y. Gao, S.P. Denbaars, S. Nakamura, E.L. Hu, and C. Meier, *Appl. Phys. Lett.* **87**, 243101 (2005).

[112] C. Meier, K. Hennessy, E.D. Haberer, R. Sharma, Y.S. Choi, K. McGroddy, S. Keller, S.P. DenBaars, S. Nakamura, and E.L. Hu, *Appl. Phys. Lett.* **88**, 031111 (2006).

[113] S. Blumenthal, M. Bürger, A. Hildebrandt, J. Förstner, N. Weber, C. Meier, D. Reuter, and D.J. As, *Phys. Status Solidi C* **13**, 292–296 (2016).

[114] M. Arita, S. Kako, S. Iwamoto, and Y. Arakawa, *Appl. Phys. Express* **5**, 126502 (2012).

[115] M. Arita, S. Ishida, S. Kako, S. Iwamoto, and Y. Arakawa, *Appl. Phys. Lett.* **91**, 051106 (2007).

[116] J. Wang, M. Clementi, M. Minkov, A. Barone, J.-F. Carlin, N. Grandjean, D. Gerace, S. Fan, M. Galli, and R. Houdré, *Optica* **7**, 1126 (2020).

[117] T.J. Puchtler, A. Woolf, T. Zhu, D. Gachet, E.L. Hu, and R.A. Oliver, *ACS Photonics* **2**, 137 (2015).

[118] D. Simeonov, E. Feltin, A. Altoukhov, A. Castiglia, J.F. Carlin, R. Butt́, and N. Grandjean, *Appl. Phys. Lett.* **92**, 171102 (2008).

[119] I. Rousseau, G. Callsen, G. Jacopin, J.F. Carlin, R. Butté, and N. Grandjean, *J. Appl. Phys.* **123** (2018).

[120] I. Rousseau, I. Sánchez-Arribas, K. Shojiki, J.F. Carlin, R. Butté, and N. Grandjean, *Phys. Rev. B* **95**, 125313 (2017).

[121] S. Sergent, M. Arita, S. Iwamoto, and Y. Arakawa, *Appl. Phys. Lett.* **100**, 121103 (2012).

[122] I.M. Rousseau, *Ph.D. thesis. EPFL* (2018).

[123] A. Jarmola, V.M. Acosta, K. Jensen, S. Chemerisov, and D. Budker, *Phys. Rev. Lett.* **108**, 197601 (2012).

[124] T. Rosskopf, A. Dussaux, K. Ohashi, M. Loretz, R. Schirhagl, H. Watanabe, S. Shikata, K.M. Itoh, and C.L. Degen, *Phys. Rev. Lett.* **112**, 147602 (2014).

[125] E. Neu, D. Steinmetz, J. Riedrich-Möller, S. Gsell, M. Fischer, M. Schreck, and C. Becher, *New J. Phys.* **13**, 025012 (2011).

[126] S. Kako, C. Santori, K. Hoshino, S. Götzinger, Y. Yamamoto, and Y. Arakawa, *Nat. Mater*. **5**, 887–892 (2006).

[127] Y. Arakawa and S. Kako, *Phys. Status Solidi A, Appl. Mater. Sci.* **203**, 3512–3522 (2006).

[128] M.J. Holmes, K. Choi, S. Kako, M. Arita, and Y. Arakawa, *Nano Lett.* **14**, 982–986 (2014).

[129] Y. Arakawa and M.J. Holmes, *Appl. Phys. Rev*. **7**, 021309 (2020).

[130] S. Xia, T. Aoki, K. Gao, M. Arita, Y. Arakawa, and M.J. Holmes, *ACS Photonics*, **8**, 1656–1661 (2021).

[131] M. Zhong, M.P. Hedges, R.L. Ahlefeldt, J.G. Bartholomew, S.E. Beavan, S.M. Wittig, J.J. Longdell, and M.J. Sellars, *Nature* **517**, 177–180 (2015).

[132] G. P. Agrawal, “Fiber-Optic Communications Systems, 4th ed.”, John Wiley & Sons, Inc., New York, (2011).

[133] A.M. Dibos, M. Raha, C.M. Phenicie, and J.D. Thompson, *Phys. Rev. Lett.* **120**, 243601 (2018).

[134] R. Yano, M. Mitsunaga, and N. Uesugi, *J. Opt. Soc. Am. B* **9**, 992 (1992).

[135] J.J. Longdell, M.J. Sellars, and N.B. Manson, *Phys. Rev. Lett.* **93**, 130503 (2004).

[136] J.J. Longdell, E. Fraval, M.J. Sellars, and N.B. Manson, *Phys. Rev. Lett.* **95**, 063601 (2005).

[137] H. De Riedmatten, M. Afzelius, M.U. Staudt, C. Simon, and N. Gisin, *Nature* **456**, 773–777 (2008).

[138] C. Clausen, I. Usmani, F. Bussiéres, N. Sangouard, M. Afzelius, H. De Riedmatten, and N. Gisin, *Nature* **469**, 508–512 (2011).

[139] M. Raha, S. Chen, C.M. Phenicie, S. Ourari, A.M. Dibos, and J.D. Thompson, *Nat. Commun.* **11**, 1605 (2020).

[140] I. Aharonovich, D. Englund, and M. Toth, *Nat. Photonics*, **10**, 631–641 (2016).

[141] T. Zhong, J.M. Kindem, J.G. Bartholomew, J. Rochman, I. Craiciu, E. Miyazono, M. Bettinelli, E. Cavalli, V. Verma, S.W. Nam, F. Marsili, M.D. Shaw, A.D. Beyer, and A. Faraon, *Science* **357**, 1392–1395 (2017).

[142] R.M. Macfarlane, *J. Lumin.* **100**, 1–20 (2002).

[143] R.M. Macfarlane, *J. Lumin.* **125**, 156–174 (2007).

[144] T. Böttger, C.W. Thiel, R.L. Cone, and Y. Sun, *Phys. Rev. B* **79**, 115104 (2009).

[145] E. Fraval, M.J. Sellars, and J.J. Longdell, *Phys. Rev. Lett.* **95**, 030506 (2005).

[146] I. Bayn, B. Meyler, J. Salzman, and R. Kalish, *New J. Phys.* **13**, 025018 (2011).

[147] T. Zhong, J. Rochman, J.M. Kindem, E. Miyazono, and A. Faraon, *Opt. Express* **24**, 536 (2016).

[148] E.M. Purcell, *Phys. Rev.* **69**, 681 (1946).

[149] T. Zhong, J.M. Kindem, J.G. Bartholomew, J. Rochman, I. Craiciu, V. Verma, S.W. Nam, F. Marsili, M.D. Shaw, A.D. Beyer, and A. Faraon, *Phys. Rev. Lett.* **121**, 183603 (2018).

[150] T. Zhong, J.M. Kindem, E. Miyazono, and A. Faraon, *Nat. Commun.* **6**, 8206 (2015).

[151] M. Imada, S. Noda, A. Chutinan, T. Tokuda, M. Murata, and G. Sasaki, *Appl. Phys. Lett.* **75**, 316–318 (1999).

[152] M. Imada, A. Chutinan, S. Noda, and M. Mochizuki, *Phys. Rev. B* **65**, 195306 (2002).

[153] S. Noda, K. Kitamura, T. Okino, D. Yasuda, and Y. Tanaka, *IEEE J. Sel. Top. Quantum Electron.* **23**, (2017).

[154] X. Ge, M. Minkov, S. Fan, X. Li, and W. Zhou, *Appl. Phys. Lett.* **112**, 141105 (2018).

[155] X. Ge, M. Minkov, S. Fan, X. Li, and W. Zhou, *NPJ 2D Mater. Appl.* **3**, 2–6 (2019).

Chapter 2. Enhanced red emission of GaN:Eu,O caused by reconfiguration of luminescent site during post-growth thermal annealing

2. 1 Introduction

As we have mentioned in Chapter 1, current EQE of GaN:Eu,O-based LEDs is one order of magnitude lower than those of $In_xGa_{1-x}N$-based blue and green LEDs and further improvement of luminescence efficiency is highly desirable for future application in III-nitride-based monolithically integrated RGB LED devices.

Schematic diagram of the luminescence process of Eu^{3+} ions in GaN is illustrated in Fig. 2. 1; (1) For photoexcitation, free carriers are created in the conduction band (CB) and valance band (VB) by above-bandgap excitation of the GaN host. For current injection, free carriers are transported into the CB and VB. An electron (hole) from the CB (VB) is captured by an acceptor- (donor-) like trap levels associated with (2) defects and impurities, and (3) Eu^{3+} ions. By Coulomb attraction, the trapped electron (hole) attracts hole (electron) from the VB (CB), forming bound excitons (BE). (4) The BE captured by a defect associated with an Eu^{3+} ion recombines, and the recombination energy is non-radiatively transferred to the Eu^{3+} ion. (5) The Eu^{3+} ion is excited into the $^5D_0$ state or into one of the higher ^5D_J (J = 1, 2, 3) excited states [1,2]. (6) If the Eu^{3+} ion is excited into the higher excited states, it relaxes to the $^5D_0$ state through multiple phonon relaxation process [1,3,4]. Radiative recombination from the $^5D_0$ state to the $^7F_2$ state generates a photon at ~621 nm, which is the main emission peak of GaN:Eu.

The carrier capture is a competitive process between trap levels associated with defect and impurities and those related to Eu^{3+} ions. Therefore, selective formation of luminescent sites with high excitation efficiency is of great importance to efficiently distribute carries to Eu^{3+} ions for efficient GaN:Eu-based light emitting devices.

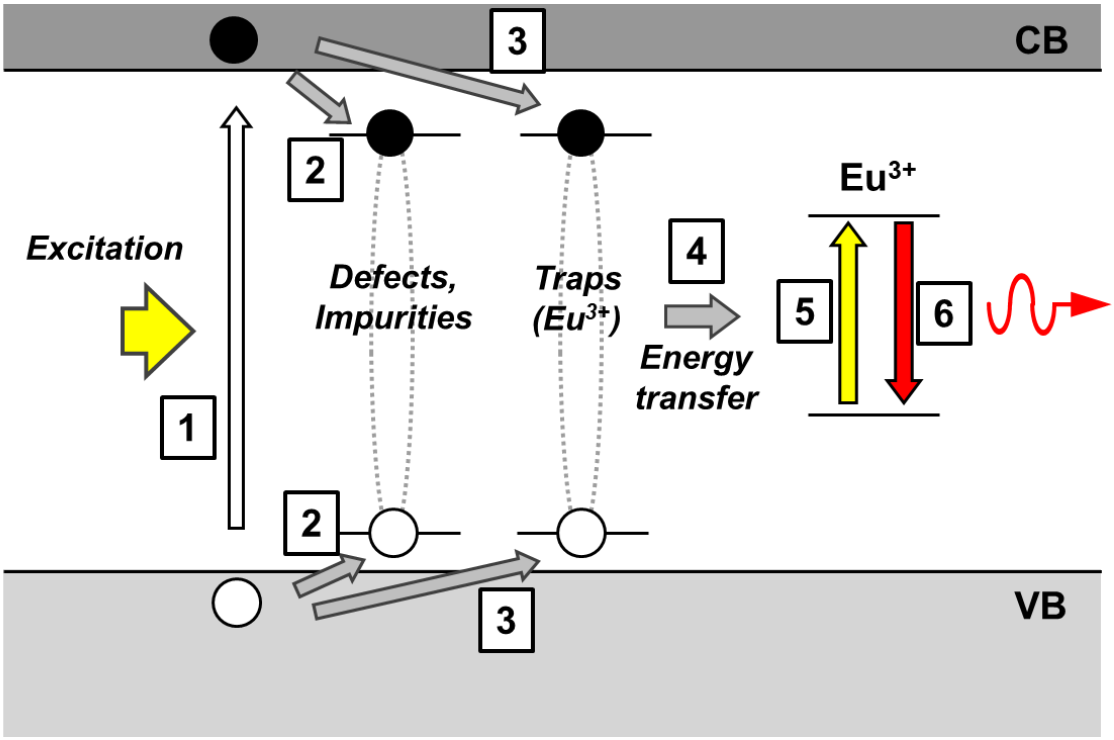

Fig. 2. 1 Schematic of the luminescence process of Eu^{3+} ions in GaN.

It is reported that the excitation cross section of OMVPE7 and OMVPE8 is about two-three order larger than that of other sites. However, these two sites typically account for less than 10% of the total amount of Eu^{3+} ions doped in GaN; therefore, to improve the luminescence efficiency, it is desirable to increase the number of such luminescent sites with high excitation efficiencies while suppressing the formation of other sites.

For the growth of GaN:Eu,O by the OMVPE method, a relatively low growth temperature (960 °C) is employed as compared to typical growth conditions for undoped GaN because high temperature growth (> ~1000 °C) results in a limited Eu incorporation and decreased luminescence intensity, because large amounts of Eu precipitates out as EuN [5]. Furthermore, the EuN adheres to surface and degrades surface morphology. However, such a low temperature growth preferentially creates luminescent sites with low excitation efficiencies under carrier injection (designated as OMVPE1 and OMVPE2) among the eight unique Eu^{3+} luminescent sites labeled as OMVPE1-8 [5,6]. OMVPE1 and OMVPE2 have been suggested to be Eu diatomic cluster [7], and are predominantly created at relatively low growth temperatures, where atomic diffusion length is limited, and Eu atom clustering is likely to occur [8].

In this chapter, to improve the luminous efficiency of GaN:Eu,O, we perform post-growth thermal annealing for promoting diffusion of Eu atoms in order to dissociate OMVPE1 and OMVPE2 sites, and convert them into other sites with higher excitation efficiencies. We investigate the site distribution using the combined excitation-emission spectroscopy (CEES) technique. Furthermore, we conduct excitation power and temperature dependence PL measurements to clarify the change in optical properties caused by thermal annealing.

2. 2 Experimental procedures

2. 2. 1 Sample fabrication

All of the epitaxial films were fabricated using the OMVPE method on a (0001) sapphire substrate in this study. Trimethylgallium (TMG), trimethylindium (TMI), trimethylaluminum (TMA) and ammonia (NH_3) were used as precursors of Ga, In, Al, and N, respectively. For the GaN:Eu,O layers, $EuCp^{pm}_2$ and argon-diluted oxygen were used as the Eu and O sources, respectively. The sample growth was initiated with a low-temperature GaN buffer layer, followed by a 2-μm-thick

undoped GaN layer, a 600-nm-thick $Al_{0.19}In_{0.81}N$ layer, a 220-nm-thick GaN:Eu,O layer, and a 10-nm-thick GaN capping layer. The growth temperature of the GaN:Eu,O layer was 960 °C, which can effectively suppress EuN precipitation [5]. This layer structure is typically used when a strong vertical light confinement is required such as in optical resonators [9–12], because the $Al_{0.19}In_{0.81}N$ layer can be selectively etched in hot nitric acid, which can be utilized as "air-clad" layer [13]. It is typically difficult to achieve thick (> 100 nm) $Al_xIn_{1-x}N$ with high crystalline due to In droplet and V-pits [14–21]. To achieve a thick $Al_xIn_{1-x}N$ layer with high crystalline and high In composition uniformity, we employed an original growth method, as we discuss the detail in Chapter 4.

After the crystal growth, a 50-nm-thick SiO_2 film was deposited on samples using an electron-beam evaporator in order to prevent thermal decomposition. Thermal annealing was performed at T_A = 800-1200 °C in N_2+NH_3 atmosphere at 100 kPa for 10 minutes, and finally, the SiO_2 films were removed using HF solution.

2. 2. 2 PL measurements

To characterize the optical properties of samples, PL spectroscopy was performed. The PL setups are shown in Fig. 2. 2. For macroscopic PL measurements [Fig. 2. 2 (a)], excitation laser was guided by mirrors to a sample in a cryostat. The irradiated light was corrected by lenses, then spectrally dispersed by a 50-cm-spectrometer, and detected by a Peltier-cooled CCD camera. For microscopic PL spectroscopy [Fig. 2. 2 (b)], excitation laser was focused on a sample with a spot diameter of 1.6 μm through an objective lens (50×, NA = 0.42). The luminescence was collected by the same objective, dispersed by a 50-cm-spectrometer and detected by a Peltier-cooled CCD camera. The excitation laser and corrected light was separated using a dichroic mirror. Both measurement setups used a closed-cycle He cryostat to control temperature ranging from ~5 K to room temperature (RT).

Two excitation methods were used to gain deep insight into the optical properties of GaN:Eu,O. For the indirect excitation that excites GaN host (as illustrated in Fig. 2. 1), a continuous-wave He-Cd (λ = 325 nm) laser was used as an above-bandgap light source. On the other hand, an wavelength-tunable dye laser was used for resonantly exciting Eu^{3+} ions ($^7F_0 \rightarrow {}^5D_0$). Especially, we utilized the CEES technique which allow us to selectively excite specific luminescence sites by resonantly exciting them. The PL intensity under resonant excitation is not

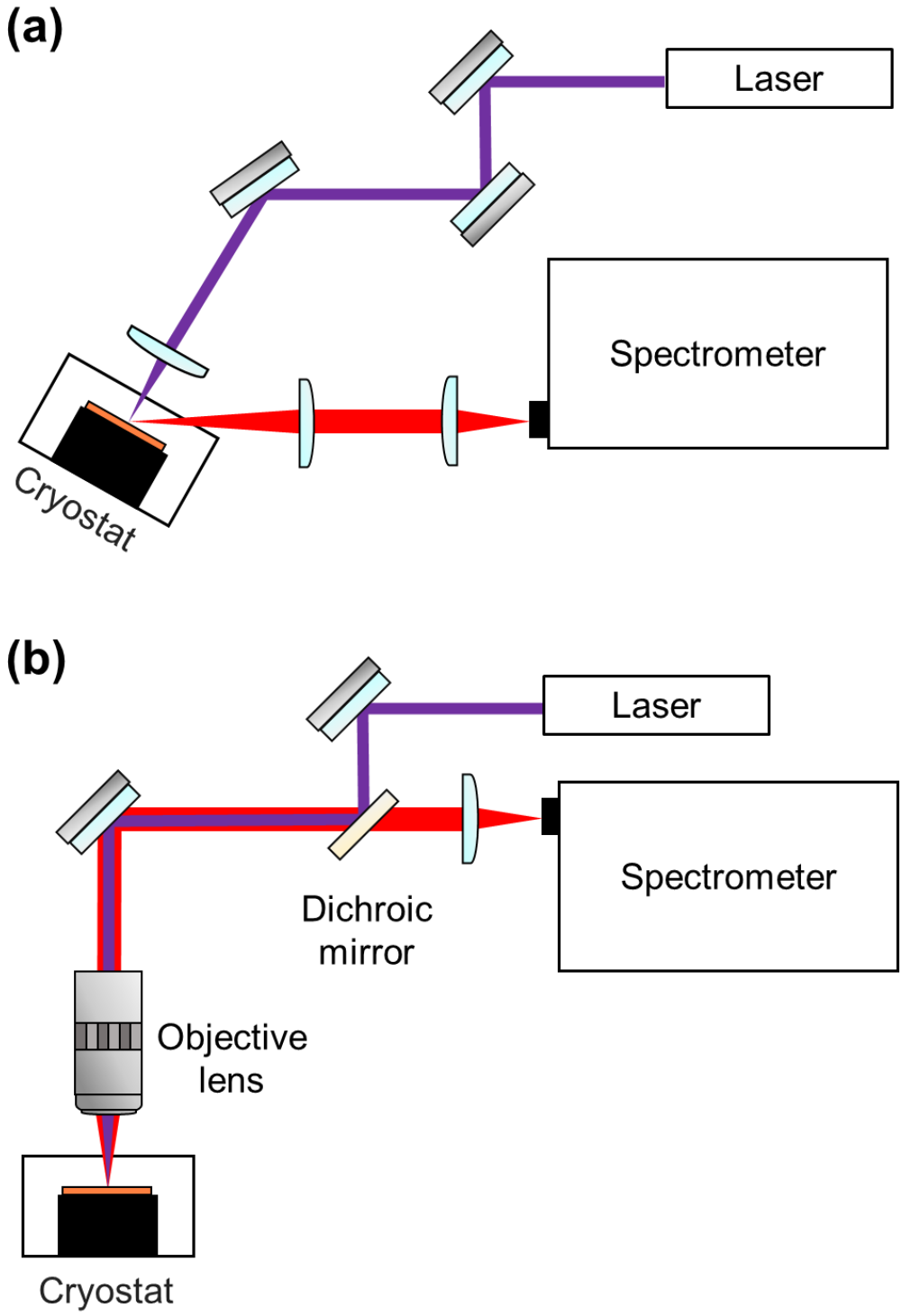

Fig. 2. 2 Schematic of PL measurement setup for (a) macroscopic and (b) microscopic spectroscopy.

affected by the difference in the efficiencies of carrier capture and energy transfer, thus it makes possible to quantify the number of each luminescent site [22–24]. Rhodamine 59 Chloride and an $In_xGa_{1-x}N$ green laser were used as dye and excitation laser source, respectively.

2. 3 Results and discussions

2. 3. 1 Surface morphology

Nomarski microscopy revealed that samples annealed up to 1100 °C show smooth surfaces like the as-grown sample (Fig. 2. 3). This result indicates that the lower growth temperature resulted in good Eu incorporation and that annealing did not cause Eu precipitation nor the formation of EuN at the surface. However, the sample annealed at 1200 °C demonstrated a very rough surface morphology due to the decomposition of the GaN:Eu,O layer. For this reason, under the annealing conditions utilized in this chapter, 1100 °C was the maximum temperature capable of preventing decomposition.

We note that an 80-nm-thick SiO_2 mask evaporated using radio frequency (RF) sputtering technique enabled annealing at 1200 °C maintaining a good surface morphology. This is likely due to the higher film density of the SiO_2 mask fabricated by sputtering. Optimization of the mask evaporation process or exploring alternative materials for the mask (e.g., AlN) would allow us for annealing at even higher temperatures without thermal decomposition.

2. 3. 2 Secondary ion mass spectroscopy

Next, we conducted secondary ion mass (SIMS) spectroscopy for the as-grown sample and the sample annealed at 1100 °C to gain insight into the change in the atomic distribution during annealing. As a result, the estimated Eu concentration in the GaN:Eu,O layer was identical (1×10^{20} cm^{-3}) for the two samples. On the contrary, the O concentration in the GaN:Eu,O layer has increased from 1×10^{18} to 2×10^{19} cm^{-3} after annealing at 1100 °C, which is likely due to the O diffusion from SiO_2 mask [25].

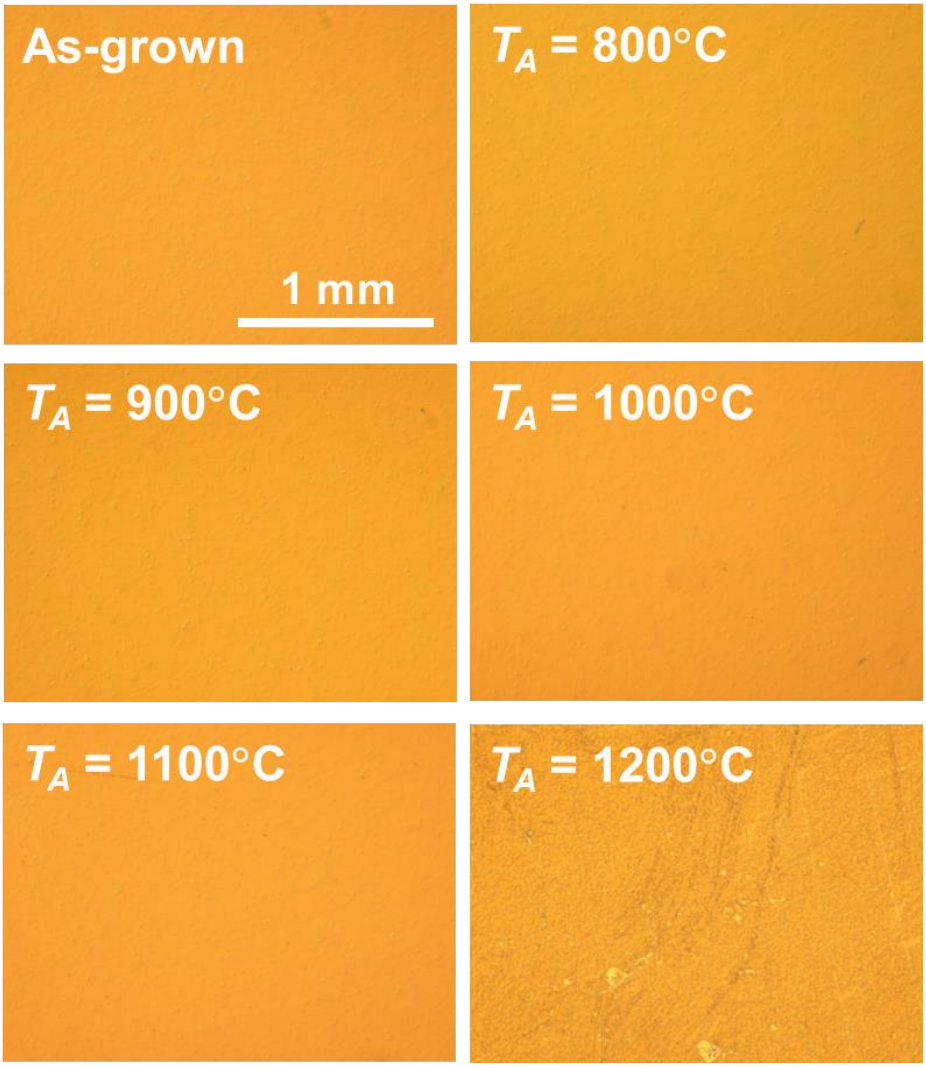

Fig. 2. 3 Nomarski microscope image of the as-grown and annealed samples.

2. 3. 3 PL measurements

Subsequently, the samples (as-grown, T_A = 800-1100 °C) were evaluated by PL spectroscopy at 10 K using a continuous-wave He-Cd laser. As illustrated in Fig. 2. 4 (a), the samples annealed up to 900 °C show almost identical spectra to the as-grown sample. However, the spectral shape dramatically changes after annealing at 1000 °C or higher. The PL intensity related to OMVPE1 and OMVPE2 decreases, while those related to OMVPE4, OMVPE7 and OMVPE8 increase strongly, suggesting the transformation to more beneficial sites at high temperatures. The growth temperature of GaN:Eu,O layer is 960 °C, hence the result suggests that temperatures higher than the growth temperature is required for luminescent site transformation.

Normalized PL spectra are shown in Fig. 2. 4 (b). The relative contribution of OMVPE1 and OMVPE2 strongly decreases with increasing annealing temperature and reduces the full-width at half-maximum (FWHM) of the entire Eu^{3+} emission spectrum. The FWHM of each sample is determined as 5.66 nm (As-grown), 5.16 nm (T_A = 800 °C), 5.97 nm, (T_A = 900 °C), 1.54 nm (T_A = 1000 °C), and 1.36 nm (T_A = 1100 °C).

2. 3. 4 CEES measurements

To gain further insight into the site distribution of Eu^{3+} ions, the CEES technique was performed at 10 K on the as-grown sample and the sample annealed at 1100 °C. The CEES results are shown in Fig. 2. 5. For the as-grown sample, the emission from OMVPE1 and OMVPE2 is dominant, while that from OMVPE7 and OMVPE8 is negligible. In contrast, for the sample annealed at 1100 °C, the emission from OMVPE1 and OMVPE2 almost disappears, while that from OMVPE4 and OMVPE7 becomes dominant. The increment factor of the number of each luminescent site is plotted in Fig. 2. 6. The number of OMVPE4, OMVPE7 and OMVPE8 was increased by factors of 2.2, 7.7, 9.8, respectively, while that of OMVPE1 and OMVPE2 was decreased by a factor of 0.1. This large change in the distribution of luminescent sites clearly demonstrates the site reconfiguration that occurs during annealing. The decrease in luminescence intensity from OMVPE1 and OMVPE2 indicates that the diatomic Eu agglomerates are dissociated and the Eu atoms form complexes with nitrogen vacancies (N_V), N_V and O, or other point defects to create OMVPE4, OMVPE7 and OMVPE8, or other luminescent sites, respectively [26].

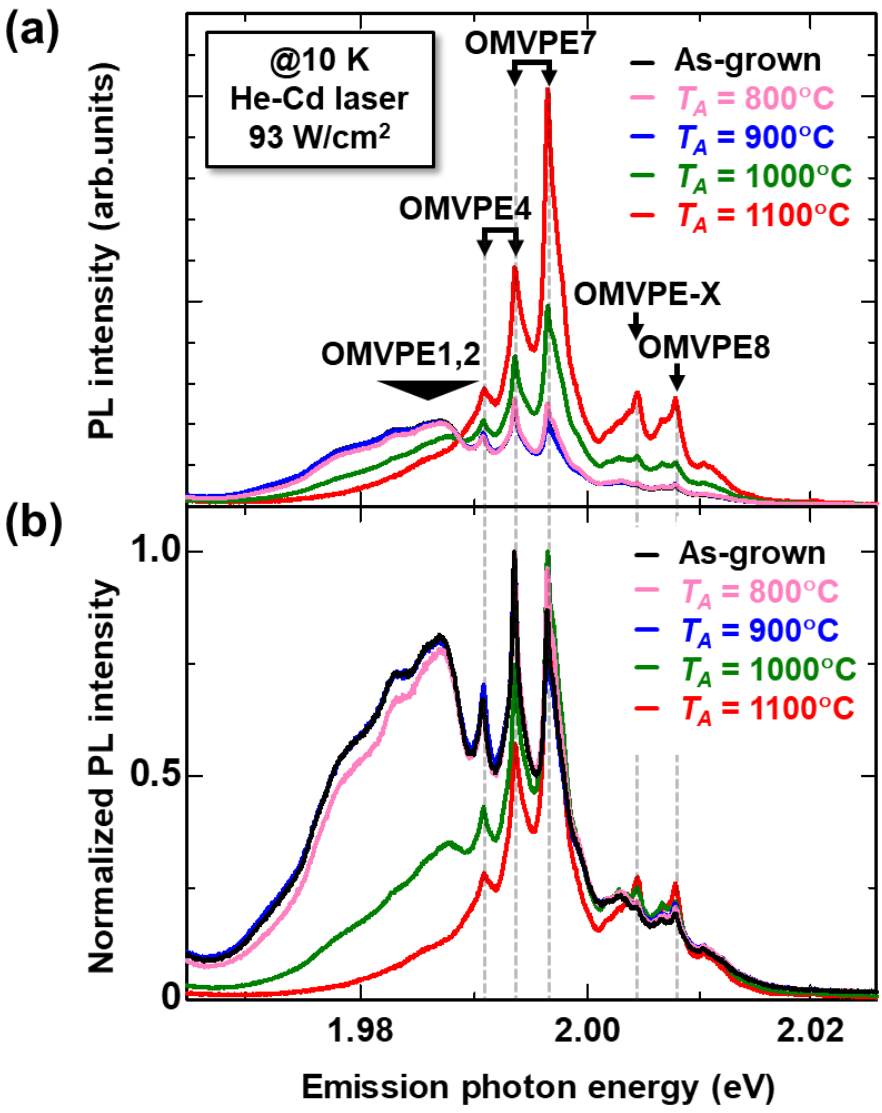

Fig. 2. 4 (a) PL spectra for the as-grown sample and samples annealed at 800-1100 °C measured at 10 K. (b) Normalized PL spectra for the as-grown sample and samples annealed at 800-1100 °C.

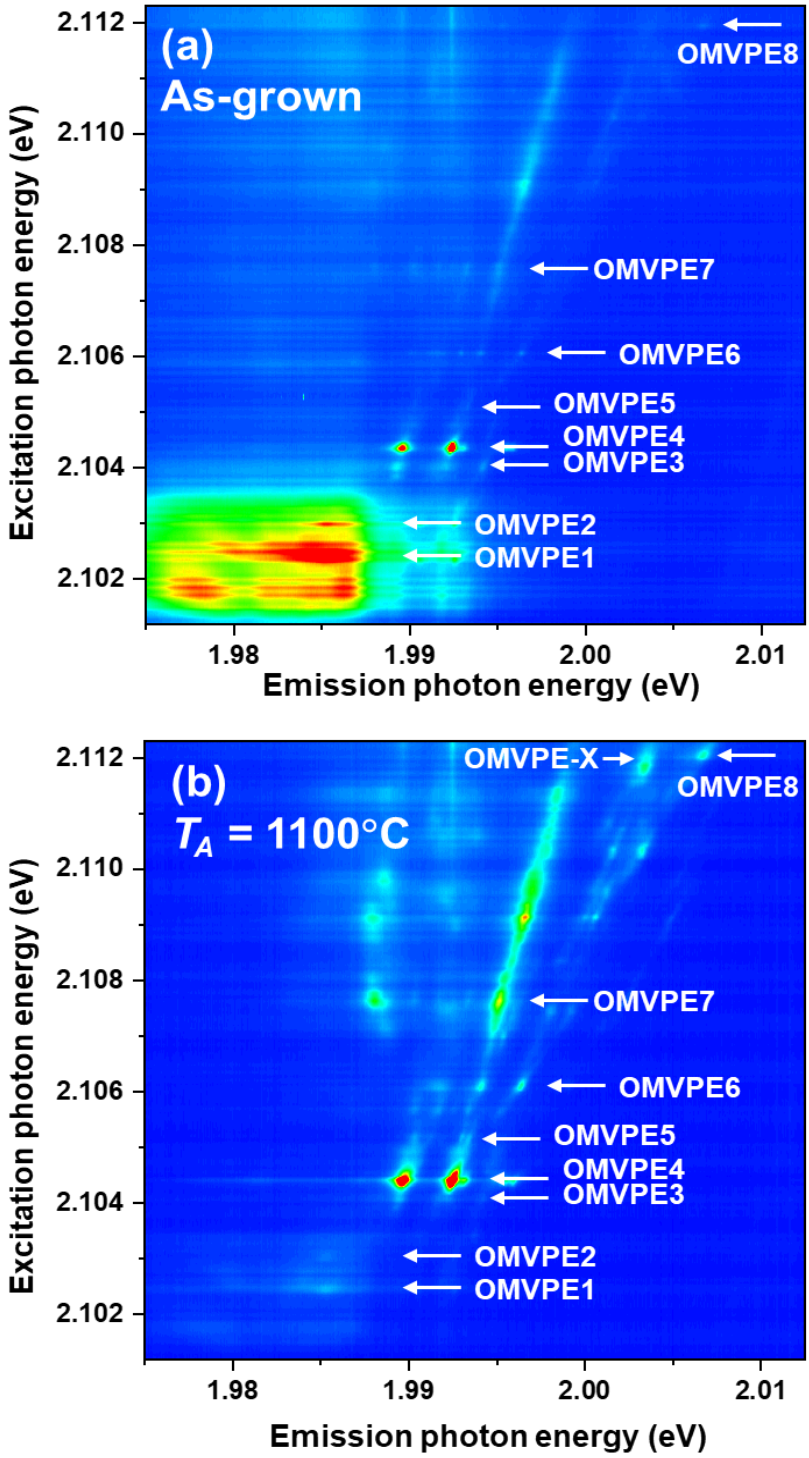

Fig. 2. 5 CEES map for the (a) as-grown sample and (b) the sample annealed at 1100 °C measured at 10 K.

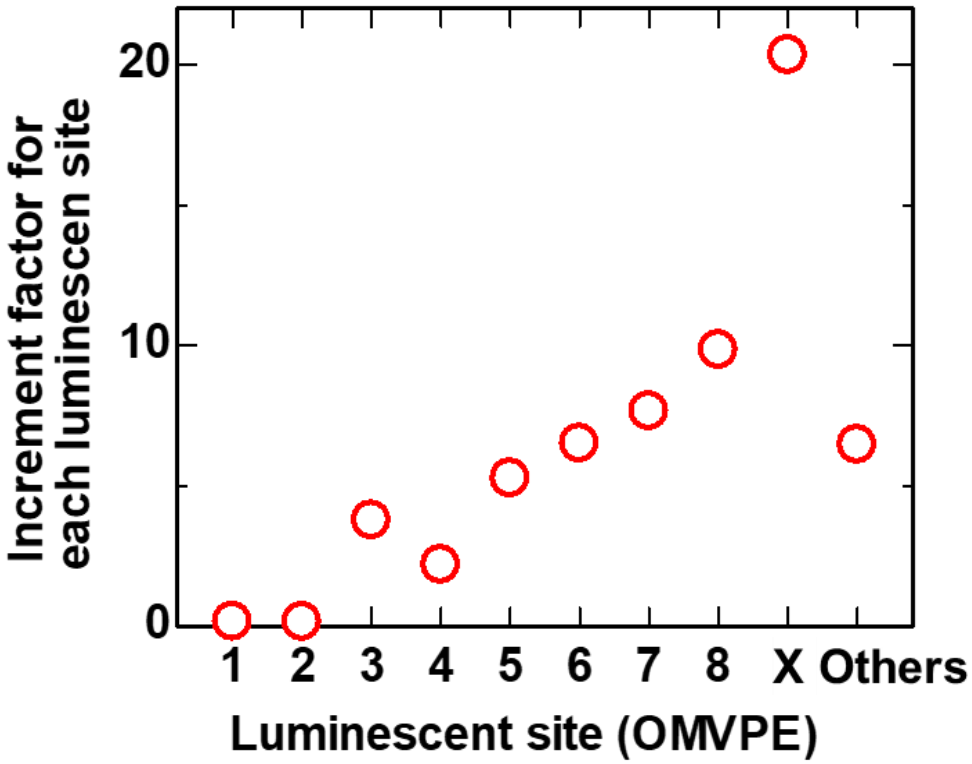

Fig. 2. 6 Increment factor for each luminescent site caused by annealing at 1100 °C.

Furthermore, a luminescent site that shows a emission peak at ~2.004 eV has greatly increased. Although this site has been tentatively assigned as a part of OMVPE8 [27,28], we have found that it is a different site, as mainly discussed in Chapter 3. We label this site as OMVPE-X in this study, the number of OMPVE-X was increased 20.3-fold after annealing at 1100 °C.

2. 3. 5 Excitation power dependent PL measurements

In order to evaluate the change in the luminescent efficiency associated with the site reconfiguration, we performed PL measurements under varied excitation power at room temperature. Integrated PL intensities (I_{em}, integrated over the emission photon energy from 1.97 to 2.02 eV) as a function of excitation power for the as-grown sample and the sample annealed at 1000 °C and 1100 °C are illustrated in Fig. 2. 7. Annealed samples show higher integrated PL intensities compared to the as-grown sample. Especially, the sample annealed at 1100 °C shows the highest integrated PL intensity among samples studied in this Chapter. The maximum enhancement factor of 5.1 compared to the as-grown sample is achieved at an excitation power of 0.18 mW/cm^2. Because the Eu^{3+} concentration is unchanged by the annealing process, this PL intensity enhancement demonstrates an improved luminescence efficiency.

In addition to the site reconfiguration, it is conceivable that the emission lifetime of Eu^{3+} has been changed with modified strain or point-defect distribution in the GaN:Eu,O layer [29], and contributes to enhancing the luminescence efficiency. In this point of view, we conducted time-resolved PL (TR-PL) measurements at 10 K. As excitations source, we used a He-Cd laser (λ = 325 nm) pulsed by an acousto-optic modulator. Luminescence was detected by a streak camera equipped with a 30-cm-spectrometer. TR-PL signals of OMVPE7 are plotted in Fig. 2. 8. Fitting with single-exponential functions revealed lifetimes of 213±2 μs for the as-grown sample and 235±2 μs for the sample annealed at 1100 °C. Although the details of the change in the lifetime are under investigation, the lifetime difference (~10%) is much smaller than the observed emission enhancement (×5.1) and has only a minor impact on the luminescence efficiency.

Subsequently, we evaluated relative quantum efficiencies (QE) by dividing E_{em} by the excitation power (E_{ex}) at room temperature. It has been reported that the luminescence efficiency of Eu^{3+} is typically low under low excitation power conditions because free carriers are captured by efficient traps that are competing with Eu^{3+}, such as H1hole trap [30–32]. Under moderate excitation power conditions where such traps are filled, more carriers are distributed to trap levels associated

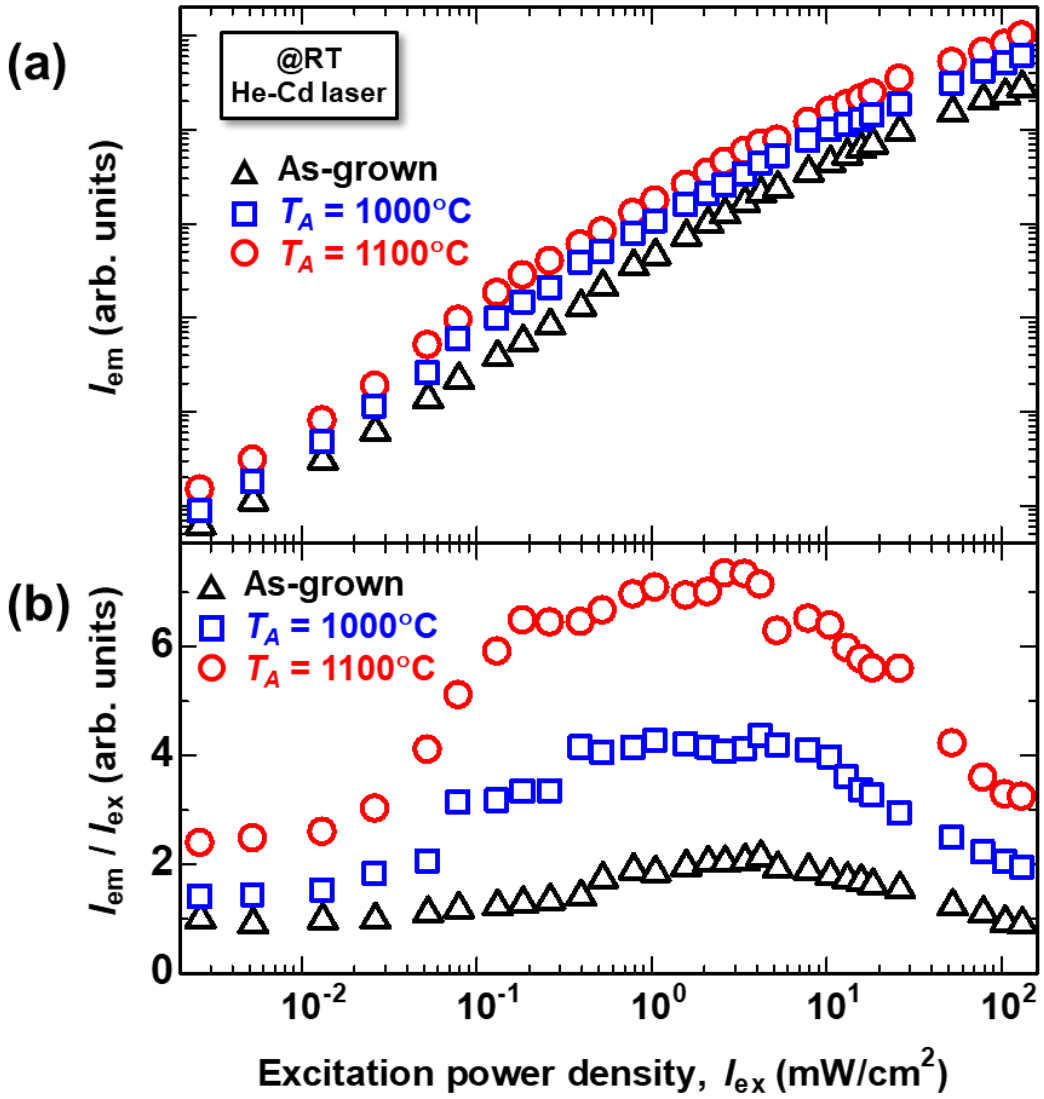

Fig. 2. 7 (a) Excitation power (I_{ex}) dependence of the integrated PL intensities (I_{em}) measured at room temperature for the as-grown sample and the samples annealed at 1100 °C and 1100 °C. (b) The ratio of I_{em} and I_{ex} as a function of I_{ex}.

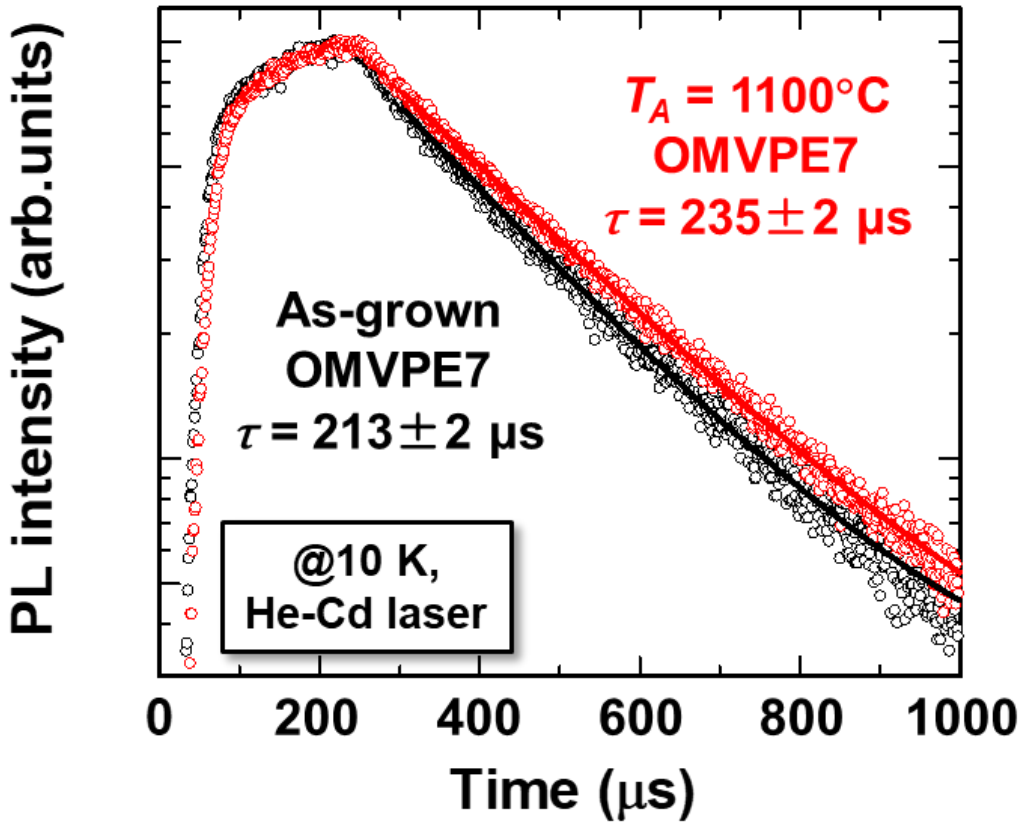

Fig. 2. 8 PL decay transient of OMVPE7 and fits for the as-grown sample and the sample annealed at 1100 °C.

with Eu^{3+} ions, leading to an improved QE. The QE lowers again for even higher excitation powers due to saturation effect in which most of the Eu^{3+} ions are excited [32]. As shown in Fig. 2. 7 (b), the relative QEs for annealed samples show reasonably higher QE even under low excitation power density (< 10^{-2} mW/cm^2). Moreover, QEs of the annealed samples quickly rise with increasing excitation power around ~3×10^{-2} mW/cm^2 and show much larger QE values than the as-grown sample.

PL spectra for the as-grown sample and samples annealed at 1000 °C and 1100 °C at room temperature under an I_{ex} of 0.18 mW/cm^2 are illustrated in Fig. 2. 9 (a). Although it is difficult to distinguish the emission from each luminescent site due to the broad linewidth at room temperature, it is possible to isolate the peak of OMVPE-X (~2.004 eV). For the annealed samples, OMVPE-X shows a predominant emission (Note: as discussed in Chapter 3, this site is thermally activated like reported for OMVPE8 [33], which explains the large difference in relative intensity at room temperature compared to the low-temperature spectra of Fig. 2. 4.). The PL intensity ratio of OMVPE-X decreases with increasing I_{ex} [Fig. 2. 9 (b)] due to its high excitation efficiency and small existing ratio (~3% of the total amount of Eu^{3+} ions doped in GaN), and the most of OMVPE-X is in the excited states under high excitation power. These results indicate that the fast initial increase of QE for annealed samples is primarily due to OMVPE-X as well as OMVPE7 and OMVPE8 centers formed by the annealing process. These can efficiently capture free carriers and compete with non-radiative traps, even at relatively low excitation power conditions, and are also responsible for the improvement of the QE of Eu^{3+} luminescence for a wide range of I_{ex} [Fig. 2. 7 (b)].

The luminescent efficiency of the sample annealed at 1100 °C is maximized for a laser power density of ~18 mW/cm^2, where the laser flux corresponds to a current flux of ~5 mA/cm^2. This is nearly the minimum current density required for μ-LED applications, where current densities of 20-2000 mA/cm^2 are typically employed [34]. Further optimized growth and annealing conditions that lead to increased OMVPE7, OMVPE8 and OMVPE-X concentrations, will improve the luminous efficiency at further higher current densities.

2. 4 Summary

In this chapter, we have performed post-growth thermal annealing to convert inefficient Eu^{3+}

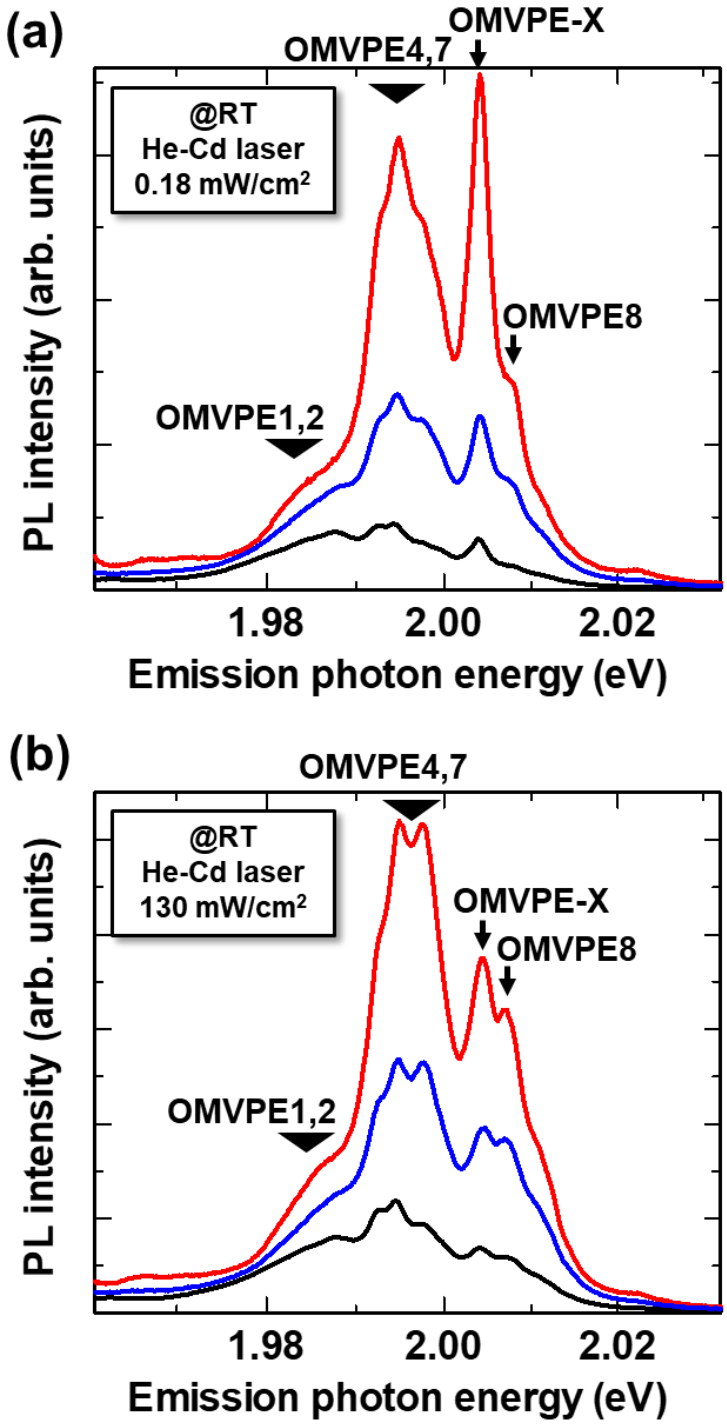

Fig. 2. 9 PL spectra for the as-grown samples and samples annealed at 1000 °C and1100 °C measured at room temperature with an excitation power density of (a) 0.18 mW/cm^2 and (b) 130 mW/cm^2.

luminescent sites into efficient ones and, in this way, enhance the light output of GaN:Eu,O grown by the OMVPE method. Thermal annealing at high temperatures (≥ 1000 °C) effectively drives the reconfiguration of luminescent sites. By site-selective excitation, we confirmed that the number of sites with lower excitation efficiencies under current injection (OMVPE1 and OMVPE2) remarkably decreased, while the number of sites with higher excitation efficiencies (OMVPE7, OMVPE8 and OMVPE-X) strongly increased. Because the OMVPE7, OMVPE8 and OMVPE-X centers can be excited efficiently by free carriers even at room temperature, the sample annealed at 1100 °C showed up to a 5.1-times improved luminescence efficiency as compared to the as-grown sample. These results show the potential of improving the efficiency of GaN:Eu,O-based LEDs using thermal annealing techniques to realize III-nitride-based monolithic RGB LED displays. Additionally, the preferential formation of luminescent sites with high excitation efficiencies by the annealing process is expected to enhance the optical gain of GaN:Eu,O [35] and could pave the way toward III-nitride-based red laser sources.

References

[1] C.W. Lee, H.O. Everitt, D.S. Lee, A.J. Steckl, and J.M. Zavada, *J. Appl. Phys.* **95**, 7717–7724 (2004).

[2] K. Binnemans, *Coord. Chem. Rev.* **295**, 1–45 (2015).

[3] H. Peng, C.W. Lee, H.O. Everitt, C. Munasinghe, D.S. Lee, and A.J. Steckl, *J. Appl. Phys.* **102**, 073520 (2007).

[4] W. Zhu, R. Wei, D. Timmerman, T. Gregorkiewicz, B. Mitchell, Y. Fujiwara, and V. Dierolf, *ACS Photonics* **5**, 875–880 (2018).

[5] W. Zhu, B. Mitchell, D. Timmerman, A. Uedono, A. Koizumi, and Y. Fujiwara, *APL. Mater.* **4**, 056103 (2016).

[6] T. Kawasaki, A. Nishikawa, N. Furukawa, Y. Terai, and Y. Fujiwara, *Phys. Status Solidi C* **7**, 2040–2042 (2010).

[7] N. Woodward, A. Nishikawa, Y. Fujiwara, and V. Dierolf, *Opt. Mater.* **33**, 1050–1054 (2011).

[8] R. Wakamatsu, D.G. Lee, A. Koizumi, V. Dierolf, and Y. Fujiwara, *J. Appl. Phys.* **114**, 043501 (2013).

[9] S. Ichikawa, Y. Sasaki, T. Iwaya, M. Murakami, M. Ashida, D. Timmerman, J. Tatebayashi, and Y. Fujiwara, *Phys. Rev. Appl.* **15**, 034086 (2021).

[10] D. Timmerman, Y. Matsude, Y. Sasaki, S. Ichikawa, J. Tatebayashi, and Y. Fujiwara, *Phys. Rev. Appl.* **14**, 064059 (2020).

[11] T. Iwaya, S. Ichikawa, M. Murakami, D. Timmerman, J. Tatebayashi, and Y. Fujiwara, *Appl. Phys. Express* **14**, 122002 (2021).

[12] T. Iwaya, S. Ichikawa, D. Timmerman, J. Tatebayashi, and Y. Fujiwara, *Opt. Express* **30**, 28853–28864 (2022).

[13] C. Xiong, P.R. Edwards, G. Christmann, E. Gu, M.D. Dawson, J.J. Baumberg, R.W. Martin, and I.M. Watson, *Semicond. Sci. Technol.* **25**, 032001 (2010).

[14] S. Zhang, B. Liu, J.Y. Yin, H.H. Sun, Z.H. Feng, and L.C. Zhao, *J. Phys. D Appl. Phys.* **44**, 075405 (2011).

[15] Q.Y. Wei, T. Li, Y. Huang, J.Y. Huang, Z.T. Chen, T. Egawa, and F.A. Ponce, *Appl. Phys. Lett.* **100**, 092101 (2012).

[16] G. Perillat-Merceroz, G. Cosendey, J.F. Carlin, R. Butté, and N. Grandjean, *J. Appl. Phys.* **113**, 063506 (2013).

[17] M. Miyoshi, M. Yamanaka, T. Egawa, and T. Takeuchi, *Appl. Phys. Express* **11**, 051001 (2018).

[18] M. Miyoshi, M. Yamanaka, T. Egawa, and T. Takeuchi, *J. Cryst. Growth* **506**, 40–44 (2019).

[19] Z.T. Chen, K. Fujita, J. Ichikawa, and T. Egawa, *J. Appl. Phys.* **111**, 053535 (2012).

[20] J.F. Carlin, C. Zellweger, J. Dorsaz, S. Nicolay, G. Christmann, E. Feltin, R. Butté, and N. Grandjean, *Phys. Status Solidi B* **242**, 2326–2344 (2005).

[21] T.S. Oh, J.O. Kim, H. Jeong, Y.S. Lee, S. Nagarajan, K.Y. Lim, C.H. Hong, and E.K. Suh, *J. Phys. D Appl. Phys.* **41**, 095402 (2008).

[22] V. Dierolf, C. Sandmann, J. Zavada, P. Chow, and B. Hertog, *J. Appl. Phys.* **95**, 5464 (2004).

[23] G.D. Metcalfe, E.D. Readinger, H. Shen, N.T. Woodward, V. Dierolf, and M. Wraback, *J. Appl. Phys.* **105**, 053101 (2009).

[24] Z. Fleischman, C. Munasinghe, A.J. Steckl, A. Wakahara, J. Zavada, and V. Dierolf, *Appl. Phys. B*, **97**, 607 (2009).

[25] S.J. Pearton, H. Cho, J.R. LaRoche, F. Ren, R.G. Wilson, and J.W. Lee, *Appl. Phys. Lett.* **75**, 2939–2941 (1999).

[26] B. Mitchell, V. Dierolf, T. Gregorkiewicz, and Y. Fujiwara, *J. Appl. Phys.* **123**, 160901 (2018).

[27] B. Mitchell, N. Hernandez, D. Lee, A. Koizumi, Y. Fujiwara, and V. Dierolf, *Phys. Rev. B* **96**, 064308 (2017).

[28] T. Iwaya, S. Ichikawa, D. Timmerman, J. Tatebayashi, and Y. Fujiwara, *Appl. Phys. Lett.* **122**, 032102 (2023).

[29] T. Inaba, B. Mitchell, A. Koizumi, and Y. Fujiwara, *Opt. Mater. Express* **7**, 1381 (2017).

[30] F.D. Auret, W.E. Meyer, L. Wu, M. Hayes, M.J. Legodi, B. Beaumont, and P. Gibart, *Phys. Status Solidi A*, **201**, 2271–2276 (2004).

[31] U. Honda, Y. Yamada, Y. Tokuda, and K. Shiojima, *Jpn. J. Appl. Phys.* **51**, 04DF04 (2012).

[32] D. Timmerman, B. Mitchell, S. Ichikawa, J. Tatebayashi, M. Ashida, and Y. Fujiwara, *Phys. Rev. Appl.* **13**, 014044 (2020).

[33] R. Wakamatsu, D. Timmerman, D. Lee, A. Koizumi, and Y. Fujiwara, *J. Appl. Phys.* **116**, 043515 (2014).

[34] X. Jia, Y. Zhou, B. Liu, H. Lu, Z. Xie, R. Zhang, and Y. Zheng, *Mater. Res. Express* **6**, 105915 (2019).

[35] A. Takeo, S. Ichikawa, S. Maeda, D. Timmerman, J. Tatebayashi, and Y. Fujiwara, *Jpn. J. Appl. Phys.* **60**, 120905 (2021).

Chapter 3. An efficiently excited Eu^{3+} luminescent site formed in Eu,O-codoped GaN

3. 1 Introduction

As discussed in Chapter 2, OMVPE7 and OMVPE8, which are assumed to have an oxygen atom in the vicinity of Eu^{3+} ion, play a key role to enhance the light output of LEDs due to their much higher excitation efficiencies as compared to other sites. OMVPE7 and OMVPE8 are believed to be charged states of the same local atomic structure [1]. OMVPE8 is considered to have an additional electron compared to OMVPE7, it shows low luminescence intensity at a cryogenic temperature, however the intensity increases with elevating temperature [2]. This behavior is considered to be caused by a change in the charge state of intrinsic defects in GaN (e.g., V_N, V_{Ga} and their complexes) with increasing temperature, and a part of OMVPE7 is converted into OMVPE8 [1,3,4]. TR-PL measurements have revealed that OMVPE8 shows "afterglow" behavior, where the emission intensity from OMVPE8 increases after the excitation laser pulse is terminated [2]. We have suggested a possibility that this afterglow behavior comes from the conversion of OMVPE7 into OMVPE8 [1].

In Chapter 2, we have performed post-growth thermal annealing and observed a strongly enhanced PL emission from Eu^{3+}. This PL intensity enhancement was accomplished by luminescent site reconfiguration, where high temperature annealing decreases the amount of OMVPE1 and OMVPE2, whereas increases that of OMVPE7, OMVPE8 and OMVPE-X. OMVPE-X has been tentatively assigned as OMVPE8 so far [1,5] due to their almost identical resonant excitation energies. This site shows a quite high excitation efficiency as compared to other sites, therefore it is worth studying the detailed optical properties. Furthermore, to improve the light output of GaN:Eu,O-based LEDs, it is highly important to elucidate the optical properties of OMVPE-X under current injection. Several peaks have also been observed in Eu-implanted GaN in the similar

emission energy region to OMVPE-X [6]. The emission energies of GaN:Eu fabricated by different methods slightly vary, therefore a more careful analysis, such as the CEES measurements [7], is needed to identify the sites, however, it is possible that this site also can be formed when other growth methods are used.

In this chapter, we conduct CEES and TR-PL measurements to demonstrate that OMVPE-X is a previously unidentified independent site. Additionally, we perform excitation power and temperature dependent PL measurements to investigate the optical properties of OMVPE-X. Furthermore, we investigate on processes to apply the annealing technique to LED fabrication, and study the optical properties of OMVPE-X under current injection for even efficient and bright GaN:Eu,O-based LEDs..

3. 2 Optical properties of OMVPE-X under photoexcitation

We investigated the detailed optical properties of a sample annealed at 1100 °C, that was studied in Chapter 2. A macroscopic PL setup was utilized.

3. 2. 1 CEES measurements

To begin with, we performed CEES measurement in the excitation region of phonon-assisted absorption at 10 K and 150 K [7,8]. As shown in the CEES map measured at 10 K [Fig. 3. 1 (a)], each luminescent site can be clearly observed. The resonant excitation energies of OMVPE8 and OMVPE-X are almost identical, which is why OMVPE-X has been assigned initially to be a part of OMVPE8 [1,5]. For the CEES map measured at 150 K [Fig. 3. 1 (b)], emission from OMVPE8 is observed at the resonant excitation energies of OMVPE7 (~2.1735, 2.1751 eV) as previously reported [1]. However, at these excitation energies, OMVPE-X is not excited, suggesting that OMVPE-X is a different luminescent site from OMVPE8. We note that OMVPE-X is also excited at multiple excitation energies at 150 K (~2.1738, 2.1757 eV). This implies the presence of an Eu^{3+} site associated with OMVPE-X, similar to the relationship between OMVPE7 and OMVPE8, although emission from that site was not observed.

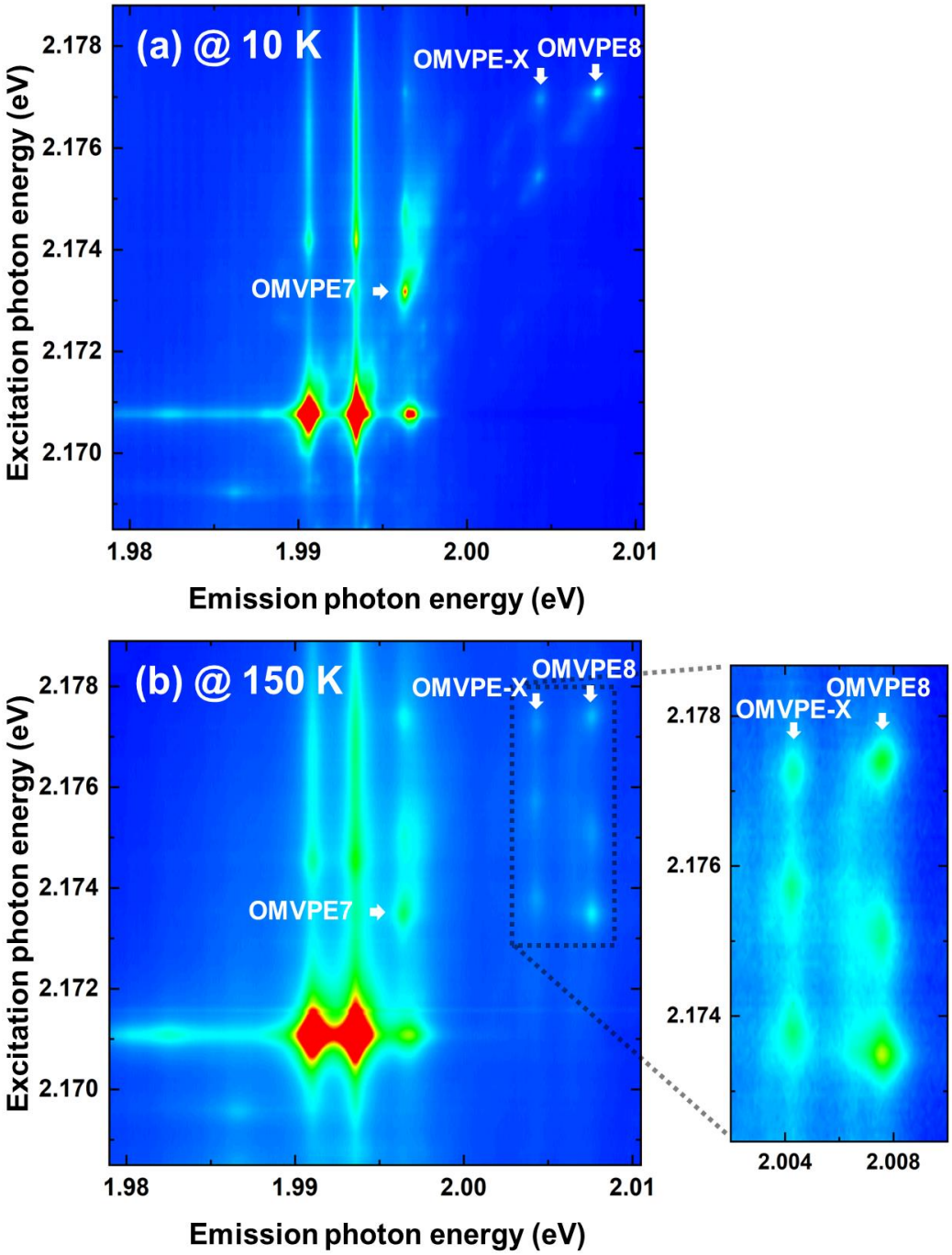

Fig. 3. 1 CEES map measured at (a) 10 K and (b) 150 K. The right panel shows the enlarged CEES map.

3. 2. 2 TR-PL measurements

Subsequently, TR-PL was performed at 180 K to investigate the detailed optical properties of OMVPE8 and OMVPE-X. We used a He-Cd laser (λ = 325 nm) pulsed by an acousto-optic modulator. Luminescence was detected by a streak camera equipped with a 30-cm-spectrometer. Figure 3. 2 shows TR-PL signal for OMVPE8 and OMVPE-X. OMVPE8 shows afterglow behavior as it has been reported [2]. Contrary to OMVPE8, emission from OMVPE-X monotonically decreases after the laser pulse with a single-exponential function, confirming that OMVPE-X is not a part of OMVPE8.

3. 2. 3 Temperature dependent PL measurements

Now that OMVPE-X has been identified as a distinct luminescent site, we investigate the optical properties in detail. First, we conducted temperature dependent PL using a He-Cd laser. Figure 3. 3 shows PL intensity at the emission peak energy for each luminescent site. As it has been reported, PL intensity from OMVPE8 rises with increasing temperature, and reaches the maximum intensity at ~150 K.

OMVPE-X also exhibited an increase in PL intensity with the rise in temperature (< ~150 K), which indicates that the local atomic structure of OMVPE-X stabilizes with increasing temperature. Due to its thermally activated characteristics, the thermal quenching ratio of the integrated PL intensity of OMVPE-X is smaller compared to other luminescent sites. Similar "anti-thermal-quenching" behavior has been observed for Eu-implanted Mg-codoped GaN [9–11], though a hysteric behavior was not observed for OMVPE8 and OMVPE-X in this study. The authors have suggested the existence of two unique metastable states with different acceptor states. These results imply the presence of a metastable state related to OMVPE-X as well as OMVPE8. In the case of OMVPE8, the metastable state can be OMVPE7 [1].

3. 2. 4 Excitation power dependent PL measurements

Then, we performed excitation power density dependent PL at room temperature to evaluate the luminescence properties of OMVPE-X. As shown in Fig. 3. 4, OMVPE-X shows a predominant emission at low excitation power region.

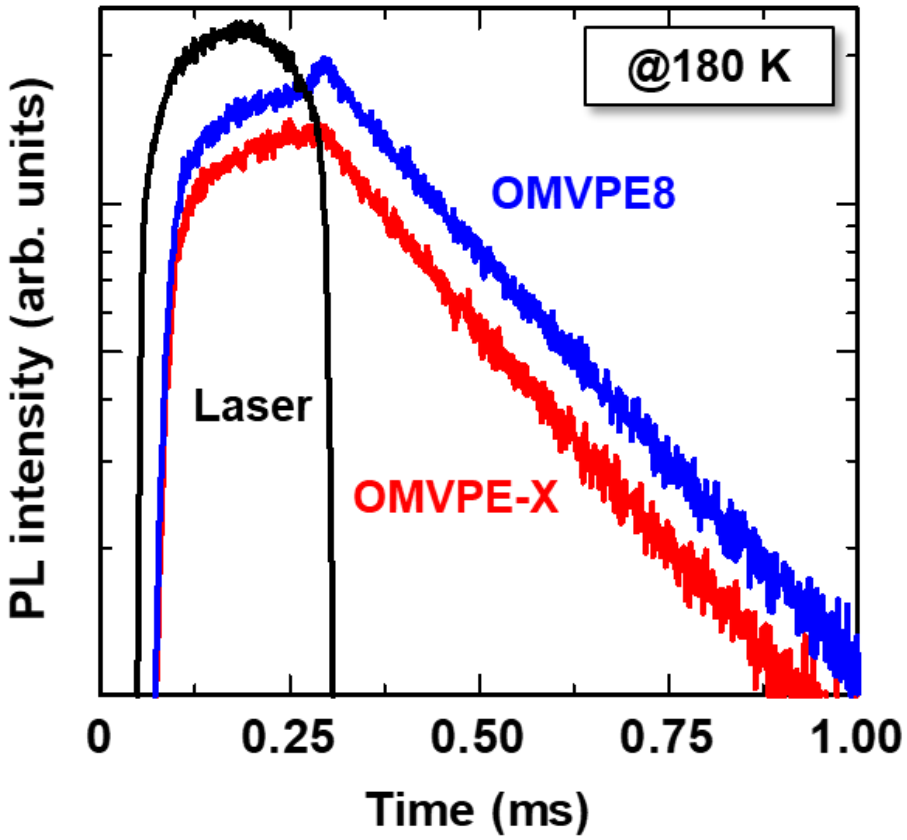

Fig. 3. 2 TR-PL profile for OMVPE8 and OMVPE-X measured at 180 K.

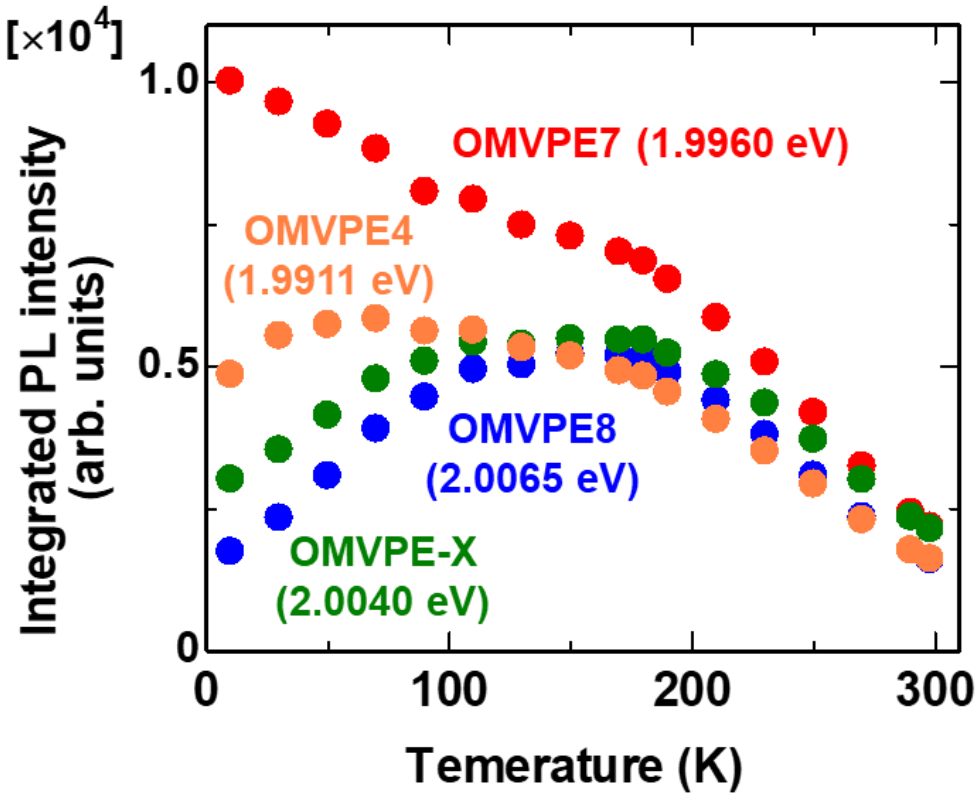

Fig. 3. 3 Temperature dependent integrated PL intensity ranging from 10 K to room temperature.

To discuss the relative luminescence efficiency of OMVPE-X, we roughly estimated the existing ratio of OMVPE-X from the CEES map measured at 10 K in the excitation region of zero-phonon-assisted region [Fig. 2. 5 (b)] using the following equation [12].

$$N_{\mathrm{Eu}_i} \propto \frac{\sigma_i \Phi \tau_{\mathrm{rad}_i} + 1}{\sigma_i \phi} I_i, \tag{3.1}$$

where N_{Eu_i} is the number of a luminescent site i, σ_i is the excitation cross section under resonant excitation, Φ is the photon flux, τ_{rad_i} is the radiative lifetime and I_i is the PL intensity. For calculation, we used reported values of σ_i and τ_{rad_i} for OMVPE1-8 [12]. For OMVPE-X and other unidentified sites, we utilized the average values of OMVPE1-8. As a result, the existing ratio of OMVPE-X was roughly estimated to be ~3%. The fact that OMVPE-X shows a predominant emission in spite of its small existing ratio suggests its quite high excitation efficiency.

As discussed in Chapter 2, it is known that the luminescence efficiency of GaN:Eu,O is typically low under low excitation power condition because free carriers are captured by efficient non-radiative traps with large carrier capture cross section [5,13]. Hence, the creation of Eu^{3+} luminescent sites with high excitation efficiencies is highly important to compete with non-radiative traps in the carrier capture process and to improve the luminescence efficiency at low current injection density region, where μ-LED displays are commonly utilized.

The approximate concentration of OMVPE-X for the as-grown state was estimated to be ~1×10^{-1}%, indicating that the concentration was greatly increased by annealing at 1100 °C. Thus, it is expected that the relative abundance of OMVPE-X can be further increased through future optimizations of growth and annealing condition, leading to higher-efficient GaN:Eu,O luminescence even under high excitation power condition. Despite being a minority site, OMVPE-X showed a predominant PL emission. It would be challenging to make OMVPE-X a majority site, however a small increase in the concentration of OMVPE-X is likely to lead a large increase in PL intensity due to the high excitation efficiency.

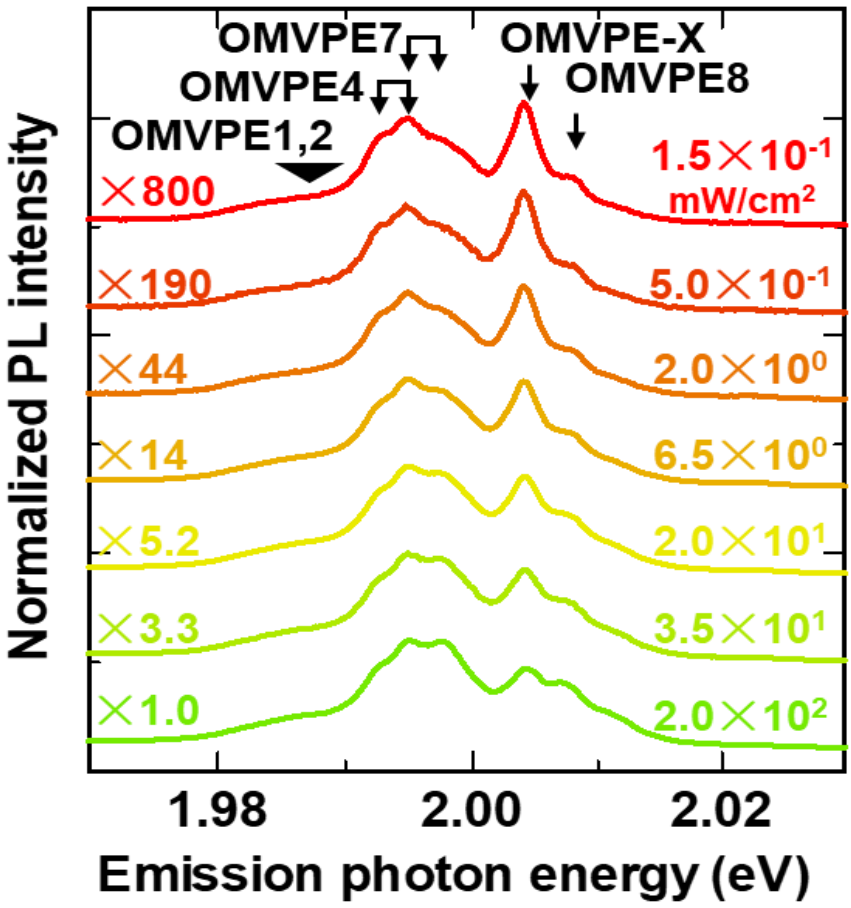

Fig. 3. 4 Normalized excitation power density dependent PL spectra.

3. 3 Optical and electrical properties of LEDs fabricated with annealing treatment

Finally, we fabricated GaN:Eu,O-based LED with annealing treatment to investigate the optical properties of OMVPE-X under current injection. In order to apply the annealing techniques to LED fabrication processes, we have to care about the damage introduction to p-type layers, which leads to compensation of Mg acceptors and high electrical resistivity. Therefore, we investigate proper LED fabrication processes which can suppress damage introduction and discuss the optoelectrical properties of LEDs.

3. 3. 1 LED fabrication process

To mitigate damage introduction to p-type GaN, annealing should be performed before the growth of p-GaN layer. First, we conducted annealing after carrying out the sample from the reactor, with subsequent regrowth of p-type GaN. The growth of LED was initiated with a low-temperature GaN buffer layer grown on a (0001) sapphire substrate, followed by an undoped GaN layer, an n-type GaN layer and a GaN:Eu,O active layer. The growth temperature of the active layer was 960 °C. The sample was carried out from the reactor after the growth of GaN:Eu,O, and an 80-nm-thick SiO_2 mask was deposited using RF-sputtering method. After annealing in N_2+NH_3 atmosphere, the SiO_2 mask was removed using HF solution, and the sample was placed back into the reactor. Then, p-GaN and p^+-GaN layers were regrown at 1050 °C. To control the n-type and p-type conductivity, we used monomethyl silane (CH_3SiH_3) and bis-cyclopentadienyl magnesium (Cp_2Mg) to dope Si and Mg, respectively.

The current-voltage (*I-V*) characteristic of the annealed LED is displayed in Fig. 3. 5. The red curve shows the *I-V* curve of the annealed LED, while the black curve shows that of a reference LED in which that the p-GaN layer was regrown without annealing process. The annealed LED does not exhibit rectification characteristic. The reference LED, on the other hand, shows a rectification characteristic, however it has a quite large leakage current density. It is reported that a high concentration of Si is incorporated at the regrown interface when the sample is removed from a reactor before the regrowth process [14–16]. Particularly, the sample annealed with a SiO_2 mask is expected to have higher Si concentration at the regrown interface owing to Si diffusion

from the SiO_2 mask. It is known that the presence of Si at the interface often leads to the deterioration of electrical properties [14–18]. Besides, the electroluminescence (EL) spectrum for the annealed exhibited a pronounced yellow luminescence, which is likely attributed to the damage and contamination introduced into the GaN:Eu,O and p-GaN layers.

Then, to minimize such damage and contamination introduced during the regrowth process, we fabricate an LED continuously annealed after the growth of GaN:Eu,O layer without carrying out from the reactor. After the growth of a 280-nm-thick GaN:Eu,O active layer, annealing was conducted at 1100 °C for 20 minutes at 100 kPa in H_2+NH_3 atmosphere. *In-situ* reflectivity monitoring system revealed that approximately 90 nm of the active layer was thermally decomposed during the annealing. Afterwards, p-GaN and p^+-GaN layers were grown. As the reference, we prepared a conventional LED without annealing treatment with a 190-nm-thick GaN:Eu,O active layer.

In Fig. 3. 6, the blue curves show the *I-V* characteristics of the annealed LED, whereas the black curves show those of the conventional LED. Both LEDs present good rectification properties, with similar turn-on voltages and series resistances [Fig. 3. 6 (a)]. The annealed LED shows a slightly higher leakage current density [Fig. 3. 6 (b)], that is expected to be a result of damage introduction to the GaN:Eu,O layer during the annealing process. However, the electrical properties were greatly improved by the *in-situ* annealing process without carrying out the sample from the reactor.

3. 3. 2 CEES measurements

The growth temperature of p-type GaN layers is 1050 °C, therefore even for the conventional LED without an intentional annealing process, the GaN:Eu,O active layer is effectively annealed at 1050 °C. This suggests that the distribution of luminescent sites is likely to be similar between the conventional LED and the annealed LED. In this contribution, we conducted CEES measurement to get insight into the luminescent site distribution. CEES maps measured at 150 K for the conventional LED and the annealed LED are depicted in Fig. 3. 7. For the conventional LED, some amount of OMVPE1 and OMVPE2 still exist, though the existing ratio is much smaller than the as-grown state [Fig. 2. 5 (a)]. Contrary to this, PL intensities from OMVPE1 and OMVPE2 are almost the background level for the annealed LED. Besides, the annealed LED shows brighter emission from OMVPE4, OMVPE7, OMVPE8 and OMVPE-X. These results

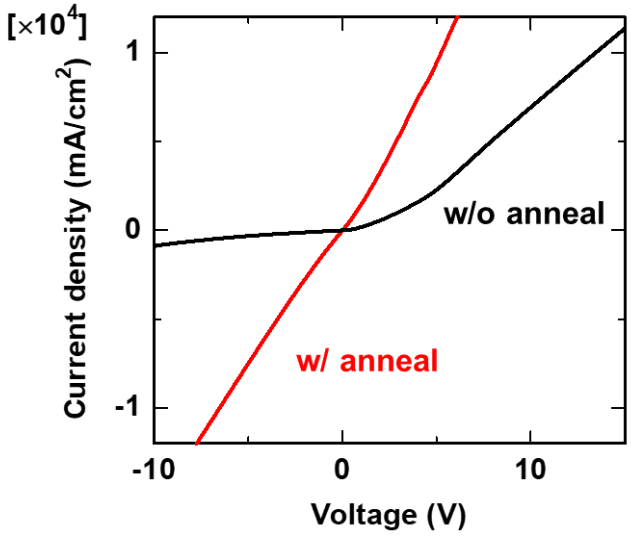

Fig. 3. 5 *I-V* characteristics of LEDs. Red curve: The LED annealed after carrying out from the reactor. Black curve: The reference LED that the p-GaN layer was regrown without annealing process.

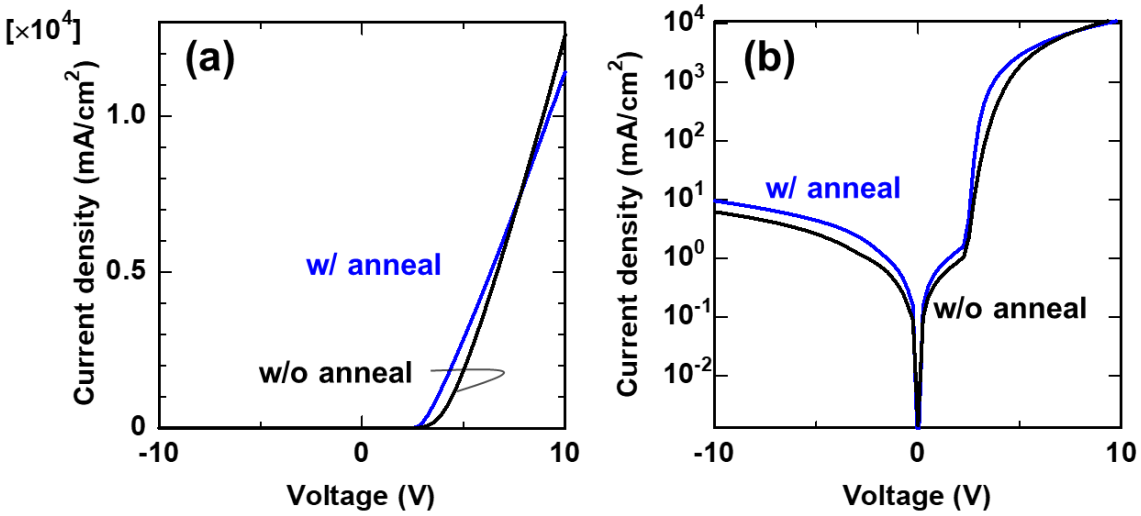

Fig. 3. 6 *I-V* characteristics of LEDs in (a) linear scale and (b) logarithmic scale. Blue curves: The LED annealed continuously in the reactor. Black curve: The reference LED without annealing process.

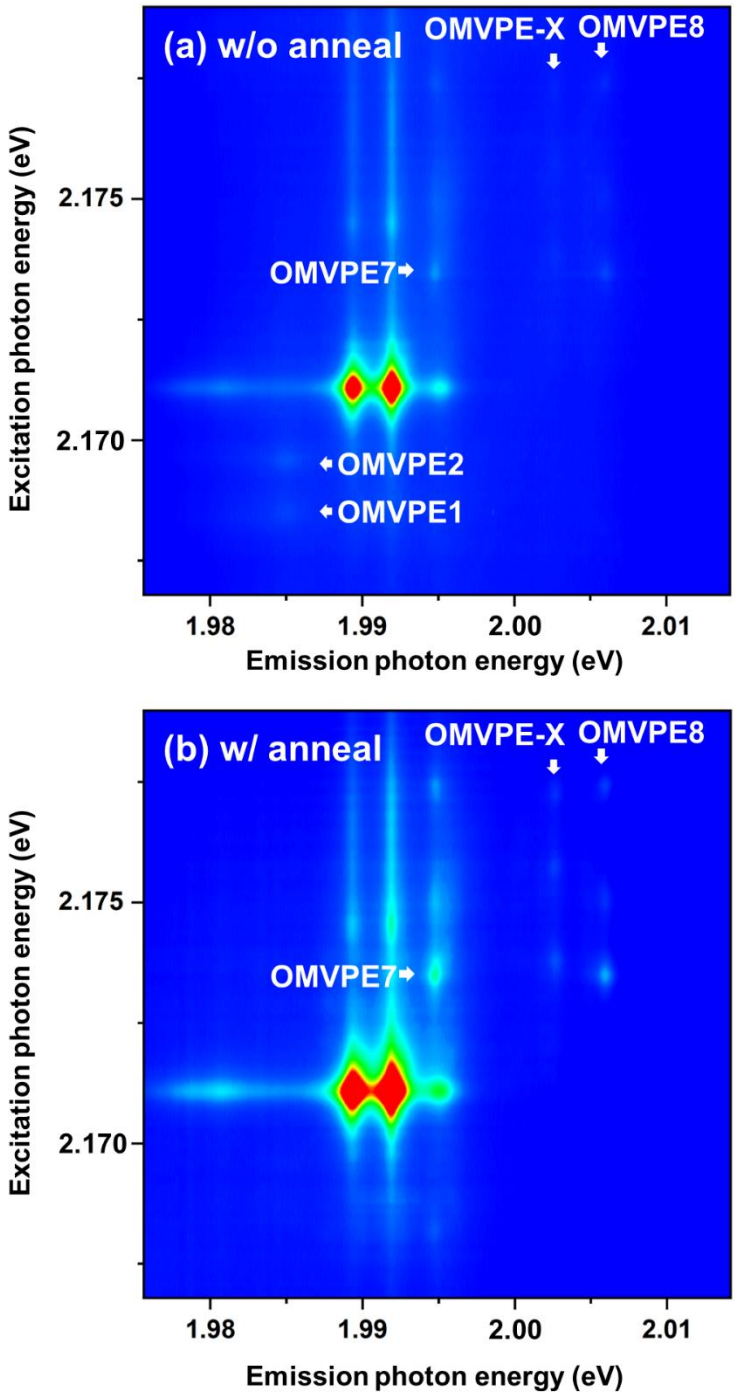

Fig. 3. 7 CEES map for (a) the conventional LED and (b) the annealed LED measured at 150 K.

suggest that annealing at 1100 °C effectively dissociated OMVPE1 and OMVPE2 and converted them into other beneficial sites. The PL intensities revealed that the annealed LED contains approximately three-times more OMVPE-X as compared to the conventional LED.

3. 3. 3 EL measurements

Normalized EL spectra are displayed in Fig. 3. 8 (a). Similar to the PL spectra, OMVPE-X exhibits a dominant emission especially at low injection current density region for the annealed LED. This indicates that OMVPE-X has a high excitation efficiency even under current injection, which is an essential characteristic for the implementation of μ-LED displays. The conventional LED (w/o anneal) shows much smaller EL intensity related to OMVPE-X even under low current density region, implying the relatively low abundance of OMVPE-X. EQEs of LEDs measured using an integrating sphere are displayed in Fig. 3. 8 (b). The annealed LED exhibits higher EQE due to the formation of luminescent sites with high excitation efficiency, including OMVPE-X. These results clearly indicate that annealing is an effective method to enhance the light output of GaN:Eu,O-based LEDs.

The EQE demonstrated in this research is smaller than previously reported values [19]. Optimization of LED structure (e.g., introducing electron blocking layer, increasing the thickness of the active layer) is important to improve the output power. Especially, MLS is crucial to be employed because it greatly improves the luminescence efficiency of GaN:Eu,O-based LEDs [19,20]. In terms of the annealing process, annealing time, temperature, atmosphere, and pressure should be optimized to suppress thermal decomposition and Eu desorption during the process.

3. 4 Investigation on the local atomic structure of OMVPE-X

These results clearly indicate the importance of increasing the amount of OMVPE-X to achieve even brighter and efficient GaN:Eu,O-based LEDs in the future. For this purpose, it is crucial to elucidate the atomic structure of OMVPE-X. OMVPE7 and OMVPE8, which have high excitation efficiencies, are considered to have an oxygen atom around Eu^{3+}. Oxygen works as a

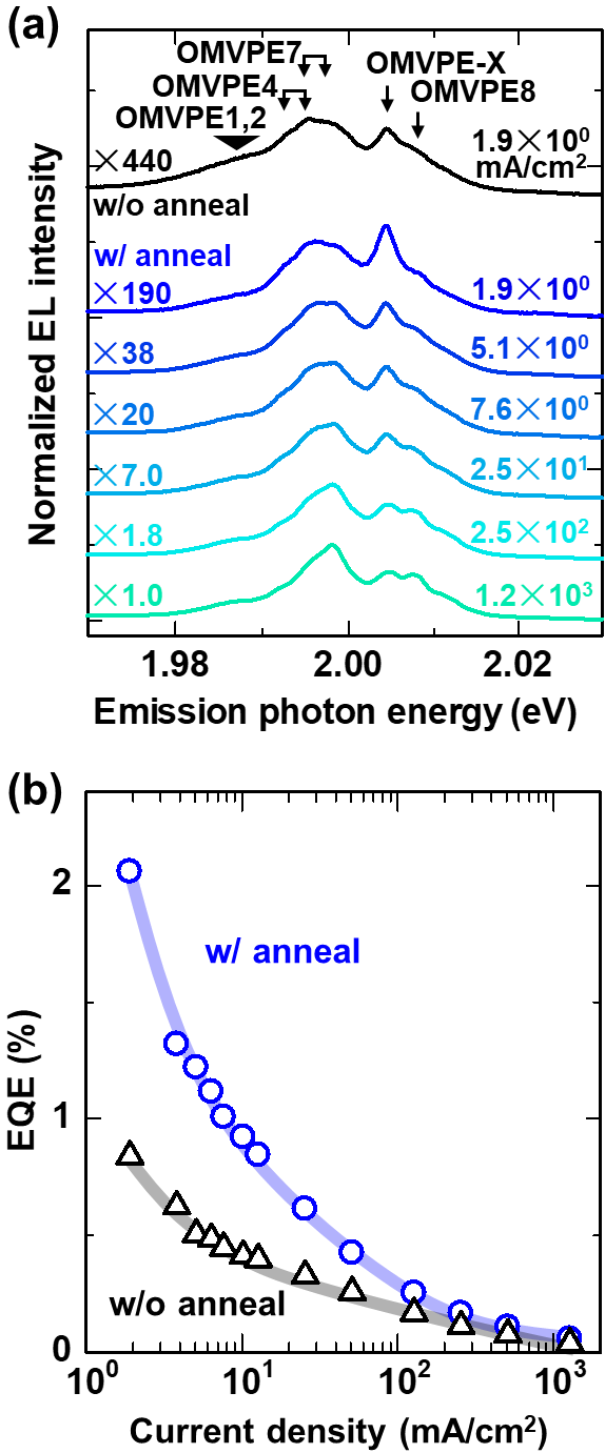

Fig. 3. 8 (a) Normalized injection current density dependent EL spectra for the annealed LED. The black line shows the EL spectrum of the conventional LED as the reference. (b) EQE as a function of injection current density for the annealed LED and the conventional LED.

donor-like defect in GaN:Eu,O and is believed to pair with V_{Ga} acceptor-like defect, thereby enhancing the efficiency of carrier capture and energy transfer to Eu^{3+} ions [21]. Therefore, certain impurities such as oxygen may be associated with OMVPE-X. In order to provide hints for the identification of the atomic structure of OMVPE-X, we prepared two samples with different oxygen concentration. The oxygen concentration was controlled by the flow rate of Ar-diluted oxygen.

As shown in Fig. 3. 9 (a), for the as-grown state, the sample grown with conventional Ar-diluted oxygen flow rate shows higher PL intensity. We expect this is due to the degraded crystal quality with an increased oxygen concentration. However, after annealing at 1200 °C, the sample grown with increased flow rate exhibits larger PL intensity associated with OMVPE-X [Fig. 3. 9 (b)]. This result suggests that oxygen plays a key role in the formation of OMVPE-X. This is an important knowledge to selectively form OMVPE-X in the future for the implementation of GaN:Eu,O-based light emitting devices.

In order to determine the local atomic structure of OMVPE-X, first-principles calculations should be employed [22,23] with sufficient supporting experimental data. Recently, Yamaga *et al.* have demonstrated crystal-field analysis of Eu^{3+} for Mg-codoped GaN:Eu grown by molecular beam epitaxy method [24]. They have determined local symmetry of Eu^{3+} for some specific luminescent sites. However, GaN:Eu,O grown by OMVPE method has more kinds of luminescent sites and the spectrum is highly complicated, making accurate evaluation difficult using this method. We have reported polarization dependent CEES measurements to study the local symmetry of sites, and found that OMVPE-X has a similar symmetry as OMVPE7 and OMVPE8, which have the highest degree of C_{3v}-like symmetry [25]. However, OMVPE-X is likely to have several point defects in the vicinity including an oxygen atom, thus further experimental and theoretical investigations are required to determine the local atomic structure of OMVPE-X. X-ray fluorescence holography should serve as a powerful solution to directly determine the location of Eu^{3+} in GaN:Eu,O [26–28].

3. 5 Summary

In this chapter, we have revealed that the luminescent site with a peak at ~2.004 eV (referred to as OMVPE-X), which can be preferentially formed by annealing, is an independent site using CEES

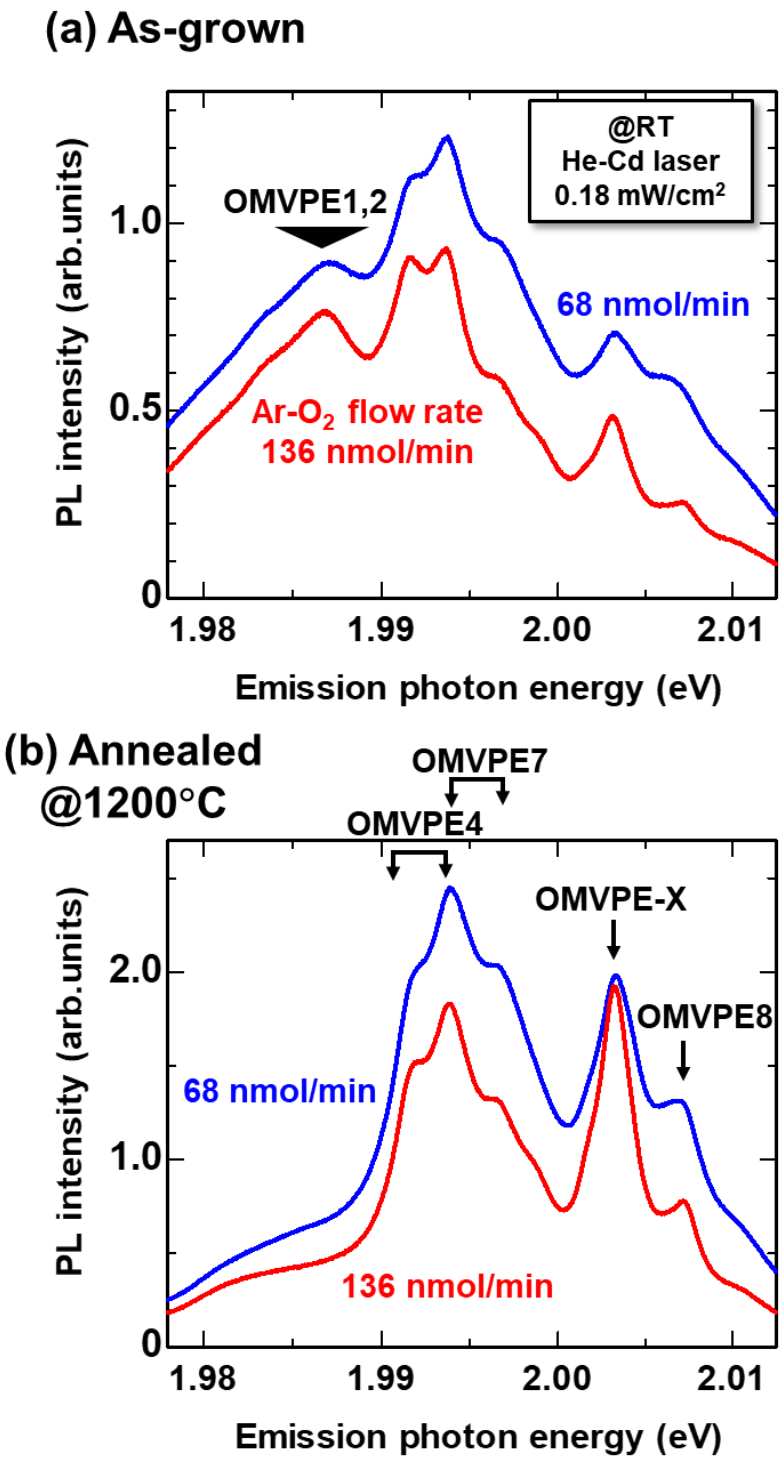

Fig. 3. 9 PL spectra for samples grown with different Ar-diluted oxygen flow rate (a) before and (b) after annealing at 1200 °C.

and TR-PL measurements. OMVPE-X exhibits a thermally activated characteristic, which is likely due to the stabilization of the local atomic structure of OMVPE-X with increasing temperature. OMVPE-X shows a predominant emission under both photoexcitation and current injection when the free carrier density is small (weak excitation region). These results demonstrate that OMVPE-X has a high excitation efficiency, and is a noteworthy luminescent site for even brighter and efficient GaN:Eu,O-based μ-LEDs. In addition, selective formation of a site with high excitation efficiency is essential to for a wide variety of applications including LDs and quantum information technologies.

References

[1] B. Mitchell, N. Hernandez, D. Lee, A. Koizumi, Y. Fujiwara, and V. Dierolf, Phys. Rev. B 96, 064308 (2017).

[2] R. Wakamatsu, D. Timmerman, D. Lee, A. Koizumi, and Y. Fujiwara, J. Appl. Phys. 116, 043515 (2014).

[3] C.G. van de Walle and J. Neugebauer, J. Appl. Phys. 95, 3851–3879 (2004).

[4] I.C. Diallo and D.O. Demchenko, Phys. Rev. Appl. 6, 064002 (2016).

[5] T. Iwaya, S. Ichikawa, D. Timmerman, J. Tatebayashi, and Y. Fujiwara, Appl. Phys. Lett. 122, 032102 (2023).

[6] V. Katchkanov, K.P. O'Donnell, S. Dalmasso, R.W. Martin, A. Braud, Y. Nakanishi, A. Wakahara, and A. Yoshida, *Phys. Status Solidi B Basic Res.* **242**, 1491 (2005).

[7] V. Dierolf, C. Sandmann, J. Zavada, P. Chow, and B. Hertog, *J. Appl. Phys.* **95**, 5464 (2004).

[8] N. Woodward, A. Nishikawa, Y. Fujiwara, and V. Dierolf, *Opt. Mate.* **33**, 1050–1054 (2011).

[9] K.P. O'Donnell, P.R. Edwards, M.J. Kappers, K. Lorenz, E. Alves, and M. Boćkowski, *Phys. Status Solidi C* **11**, 662–665 (2014).

[10] A.K. Singh, K.P. O'Donnell, P.R. Edwards, K. Lorenz, M.J. Kappers, and M. Boćkowski, *Sci. Rep.* **7**, 41982 (2017).

[11] D. Cameron, K.P. O'Donnell, P.R. Edwards, M. Peres, K. Lorenz, M.J. Kappers, and M. Boćkowski, *Appl. Phys. Lett.* **116**, 102105 (2020).

[12] R. Wakamatsu, D.G. Lee, A. Koizumi, V. Dierolf, and Y. Fujiwara, *J. Appl. Phys.* **114**, 043501 (2013).

[13] D. Timmerman, B. Mitchell, S. Ichikawa, J. Tatebayashi, M. Ashida, and Y. Fujiwara, *Phys. Rev. Appl.* **13**, 014044 (2020).

[14] W. Lee, J.H. Ryou, D. Yoo, J. Limb, R.D. Dupuis, D. Hanser, E. Preble, N.M. Williams, and K. Evans, *Appl. Phys. Lett.* **90**, 093509 (2007).

[15] J.P. Liu, J.H. Ryou, D. Yoo, Y. Zhang, J. Limb, C.A. Horne, S.C. Shen, R.D. Dupuis, A.D. Hanser, E.A. Preble, and K.R. Evans, *Appl. Phys. Lett.* **92**, 133513 (2008).

[16] G. Koblmuller, R.M. Chu, A. Raman, U.K. Mishra, and J.S. Speck, *J. Appl. Phys.* **107**, (2010).

[17] M. Azize, Z. Bougrioua, and P. Gibart, *J. Cryst. Growth.* **299**, 103 (2007).

[18] G.W. Pickrell, A.M. Armstrong, A.A. Allerman, M.H. Crawford, K.C. Cross, C.E. Glaser,

and V.M. Abate, *J. Electron. Mater.* **48**, 3311 (2019).

[19] B. Mitchell, V. Dierolf, T. Gregorkiewicz, and Y. Fujiwara, *J. Appl. Phys*. **123**, 160901 (2018).

[20] W. Zhu, B. Mitchell, D. Timmerman, A. Koizumi, T. Gregorkiewicz, and Y. Fujiwara, *MRS Adv.* **1**, 159 (2017).

[21] B. Mitchell, J. Poplawsky, D. Lee, A. Koizumi, Y. Fujiwara, and V. Dierolf, *J. Appl. Phys.* **115**, 204501 (2014).

[22] K. Hoang, *Phys. Status Solidi RRL* **10**, 915 (2016).

[23] K. Hoang, *Phys. Rev. Mater.* **5**, 034601 (2021).

[24] M. Yamaga, K.P. O'Donnell, H. Sekiguchi, and A. Wakahara, *J. Lumin.* **262**, 119953 (2023).

[25] S. Copelman, H. Austin, D. Timmerman, J.D. Poplawsky, M.M. Waite, J. Tatebayashi, S. Ichikawa, Y. Fujiwara, V. Dierolf, and B.J. Mitchell, *Proc. SPIE* **11302**, 113021Z (2020).

[26] P.M. Len, S. Thevuthasan, C.S. Fadley, A.P. Kaduwela, and M.A. Van Hove, *Phys. Rev. B* **50**, 11275 (1994).

[27] T. Gog, P.M. Len, G. Materlik, D. Bahr, C.S. Fadley, and C. Sanchez-Hanke, *Phys. Rev. Lett.* **76**, 3132 (1996).

[28] M. Tegze and G. Faigel, *Nature* **380**, 49 (1996).

Chapter 4. Design considerations of III-nitride-based two-dimensional photonic crystal cavities with crystallographically induced disorder

4. 1 Introduction

In Chapter 2 and 3, we have provided studies about *intrinsic* control of Eu^{3+} emission, and mainly discussed on the impact of post-growth thermal annealing on optical properties of GaN:Eu,O. The light output from GaN:Eu,O was reasonably improved as a result of luminescent site reconfigurations.

In Chapter 4 and 5, for even wider potential applications of GaN:Eu,O-based light emitting devices including LDs and quantum light sources, we investigate the method of *extrinsic* control of Eu^{3+} emission using optical nanocavities. As we have mentioned in Chapter 1, high-Q nanocavities can greatly modify the density of states of photons resulting in a significant change in the radiative properties of light emitters [1]. Particularly, we mainly focus on 2D-PhC cavities, which have been recognized for their ultrahigh Q-factors [2,3].

However, Q-factors of III-nitride-based 2D-PhC cavities have been limited up to ~5000 in the UV-visible range [4–16]. This is mainly due to the small device size designed for short wavelength range, and the chemical and physical stability that hinders accurate dry- and wet-etching process. Cl-based reactive ion etching (RIE) also transforms circular air-holes into rounded hexagons [17]. Therefore, fabrication of accurate circular holes is highly challenging for III-nitrides, especially for applications in the visible range where the air-holes are typically small. However, 2D-PhCs with hexagonal holes have a great potential for photonic band engineering, such as the formation of a large absolute bandgap, or a flexibly modulated band diagram by rotating air-holes [18]. Thus, 2D-PhC cavities with hexagonal air-holes should be further investigated considering the present fabrication techniques and potential applications.

In this chapter, we investigate the impact of disorder on the Q-factor of 2D-PhC cavities by introducing structural disorder into the 2D-PhC cavities in the 3D finite-difference time-domain (FDTD) simulations, and discuss the cavity structures tolerant to disorder.

4. 2 Theory of photonic crystal and cavity quantum electrodynamics

4. 2. 1 Theory of photonic crystal

A semiconductor has an energy gap that forbids electrons with specific range of energies to propagate in specific directions. This gap is formed by periodically located lattice potential, and if the potential is large enough, a complete band gap is formed between the valence band and the conduction band. The optical analogy is PhC, in which photonic band gap (PBG) is formed that prohibits photons with specific range of frequencies to propagate and exist [19].

According to the dimension of the periodicity, 1-, 2-, and 3-dimension (1D, 2D, 3D) PhCs are defined. Especially, 2D-PhCs, formed by a periodic array of cylindric vertical dielectric rods, or of air rods (air-holes) in a dielectric slab, have been widely investigated because of the relatively easy fabrication process and the strong light confinement effect. In this study, we focus on 2D-PhCs formed by a GaN slab with etched air-holes as the schematic is illustrated in Fig. 4. 1 (a). Such 2D-PhCs are known to form a PBG for the transverse-electric (TE) mode because of a large frequency jump between the fundamental mode and higher order modes [Fig. 4. 1 (b)]. A structural defect formed into a 2D-PhC [Fig. 4. 1 (c)] introduces a peak of density of states of photons (defect mode) within the photonic band as depicted in Fig. 4. 1 (d). The defect mode cannot propagate into outside of the defect and is confined inside the defect, because it has a frequency in the PBG.

A PBG map is shown in Fig. 4. 1 (e) for a GaN-based 2D-PhC with a triangular lattice pattern of hexagonal air-holes for the TE polarized light, where r is the radius of air-holes (a side length of a hexagon) and a is the periodicity of 2D-PhC. It is found that the PBG is formed with r/a ranging from 0.2 to 0.55. The PBG width was maximized with r/a of 0.44; the PBG was formed in the range of normalized angular frequency ($\omega a/2\pi c$) of 0.38-0.51, where ω is the angular frequency of light, and c is the speed of light. The PBG width ($\Delta\omega/\omega_{med}$) normalized by the angular frequency at the center of the PBG (ω_{med}) was calculated as 29%. On the other hand, the maximum

PBG width of a 2D-PhC formed with circular air-holes was 27% with *r*/*a* of 0.38. This result indicates 2D-PhCs formed with hexagonal air-holes can achieve PBG widths comparable to those formed with circular air-holes.

4. 2. 2 Theory of cavity quantum electrodynamics

The ability of optical cavities to confine light is evaluated by cavity Q-factors, which is defined by the following equation;

$$Q = \omega_{\mathrm{res}} \frac{U(t)}{-\frac{\mathrm{d}U(t)}{\mathrm{d}t}}, \tag{4.1}$$

where ω_{res} is the resonant angular frequency and U is the energy confined in a cavity. Q-factor can also be determined by using the linewidth of a cavity mode ($\Delta\lambda$) and the resonant wavelength (λ_{r}) as

$$Q = \frac{\lambda_r}{\Delta\lambda}. \tag{4.2}$$

The modal volume *V*, which indicates the volume where the electromagnetic field of a resonant mode is distributed, is defined as [20]

$$V = \frac{\int_V \epsilon(r)|E(r)|^2 dr^3}{\{\epsilon(r)|E(r)|^2\}_{MAX}}, \tag{4.3}$$

where $\epsilon(r)$ is the dielectric constant, $|E(r)|$ is the electric field strength.

In a nano-microcavity like 2D-PhC cavities with small modal volume (V), the spontaneous emission rate of an emitter which couple to a cavity mode is enhanced by a Purcell factor (F_p) as following the well-known equation [1]:

$$F_p = \frac{3Q}{4\pi V}\left(\frac{\lambda_r}{n}\right)^3, \tag{4.4}$$

where *n* indicates the refractive index of material. Strictly, F_p is limited by the linewidth of emitter (Δf_e) and that of cavity mode (Δf_r), spectral and polarization overlap, that is given by [21,22]

$$F_p = \frac{3}{4\pi V}\left(\frac{\lambda_r}{n}\right)^3 \frac{f_e \Delta f_r + f_r \Delta f_e}{4(f_e - f_r)^2 + (\Delta f_e + \Delta f_r)^2}\xi^2, \tag{4.5}$$

where f_e, f_r is the central frequency of the emitter and resonant mode, respectively, ξ^2 the polarization overlap factor which is less than one. When emitters have random polarization, ξ^2 is equal to 1/3.

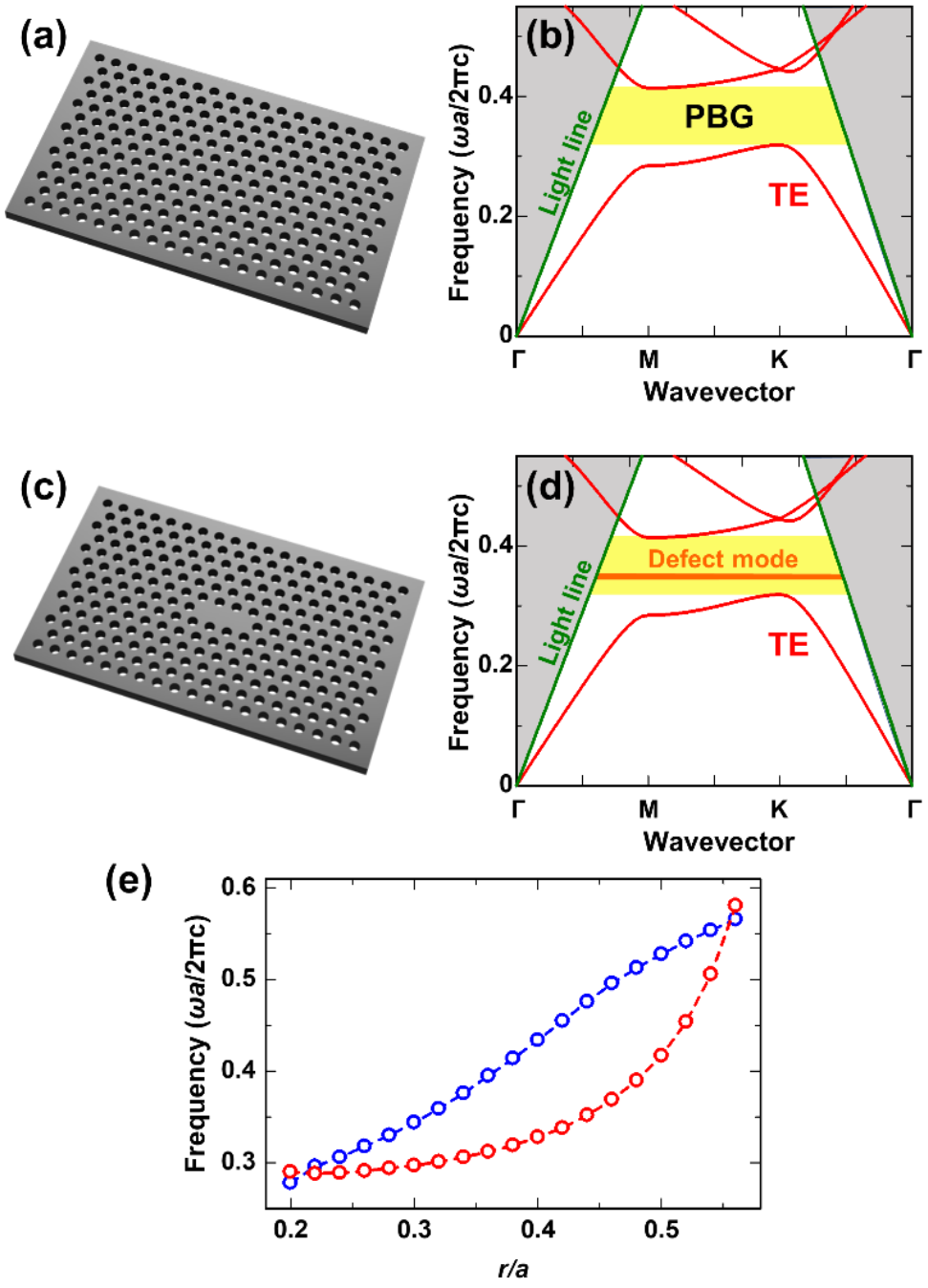

Fig. 4. 1 Schematic of a (a) 2D-PhC and (c) 2D-PhC cavity. Photonic band diagram of a GaN-based (b) 2D-PhC and (d) 2D-PhC cavity with a triangular lattice pattern of hexagonal air holes with *r*/*a* of 0.38 for TE polarized light. The shaded area indicates the light cone. (e) Photonic band gap map for a GaN-based 2D-PhC with a triangular lattice pattern of hexagonal air holes.

4. 3 Reproducing experimentally introduced structural disorder in 3D-FDTD simulations

We employed 3D-FDTD simulations to calculate the time evolution of the electromagnetic field. All simulations were conducted using the perfectly matched layer boundary conditions applied to all four sides normal to the membrane, and symmetric boundary applied along the membrane. The 2D-PhC slab was composed of GaN with a thickness of 220 nm. The refractive index of GaN was set to 2.35, which is a typical value in the red region (615-630 nm) [23]. A point dipole source with TE polarization was put at the center of each cavity. Defect-type cavities were surrounded by triangular-lattice PhCs with 48 rows and columns, which are large enough to obtain a strong light confinement effect.

It is well-known that 2D-PhCs are highly sensitive to disorder, and the impact of disorder on 2D-PhCs has been intensely investigated experimentally [24–28]. Theoretically, the experimental disorder has been reproduced in calculations by introducing variations of size [26] and position [28]. Although these studies were conducted for conventional 2D-PhCs with circular air-holes, we utilize 2D-PhCs with hexagonal holes in this study. From the observation of a 2D-PhC using scanning electron microscopy (SEM) [Fig. 4. 2 (a)], we conclude that the most dominant disorder for III-nitride-based PhCs is the shape variation of hexagonal air-holes. Note that the shape variation of hexagonal air-holes actually contributes to variations in both size and centroid position of air-holes.

As shown in Fig. 4. 2 (a), hexagonal air-holes fabricated in III-nitride slabs consist of flat $\{1\bar{1}00\}$ side walls. In order to accurately reproduce the crystallographically induced structural disorder in FDTD simulations, we changed the distance between the center of the hexagons and each hexagonal side in the radial direction with a Gaussian distribution with a standard deviation of $\sqrt{3}\sigma r/2$. Note that all the following FDTD calculations considering the disorders are repeated 10 times, and we show the averaged results. A typical disorder-induced 2D-PhC structure simulated with σ of 0.1 [Fig. 4. 2 (b)] demonstrates that the shapes of air-holes are reliably reproduced.

We note that limitations in the fabrication accuracy more strongly affects smaller air-holes. From SEM observations, we concluded that the experimental value of σ degraded from 0.05 to 0.18 when r was decreased from 81 nm to 28 nm as shown in Fig. 4. 2 (c).

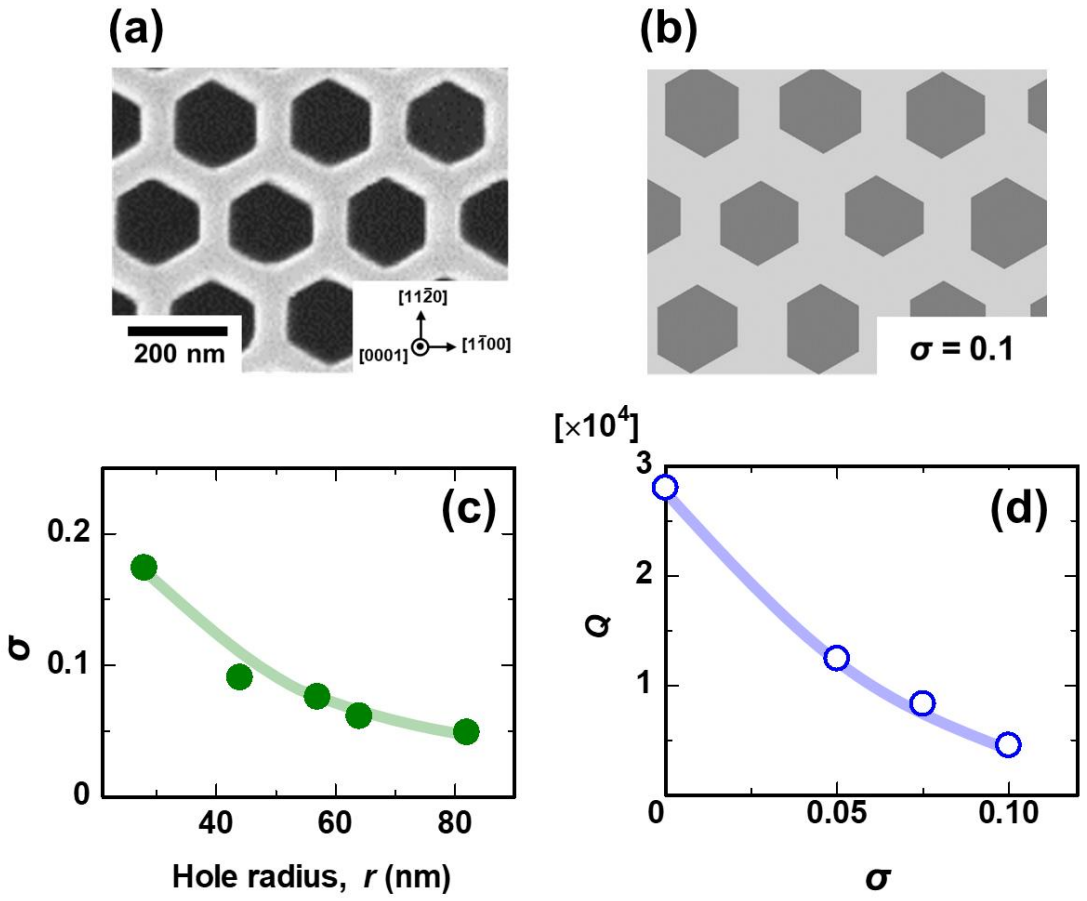

Fig. 4. 2 (a) A SEM image of a GaN:Eu-based PhC with hexagonal holes. (b) Disorder-induced air-holes with σ = 0.1. (c) Experimentally introduced degree of disorder (σ) as a function of hole radius of 2D-PhCs. (d) Q-factor of an L7 cavity as a function of σ.

Calculated Q-factors of an L7 cavity as a function of σ are plotted in Fig. 4. 2 (d). Note that σ was varied by changing r and a while maintaining the ratio of r/a. Q-factors at resonant wavelengths monotonically decrease with increasing σ, and the calculated degradation of the Q-factors reproduced the tendency in actual experiments. In our previous report, the experimental Q-factor of an L7 cavity was 5400, considerably lower than the calculated ideal Q-factor of 28000 ($\lambda \sim 620$ nm, $r \sim 67$ nm, $r/a = 0.32$) [7]. In the calculations, this experimental Q-factor was reproduced for $\sigma \sim 0.09$, which well corresponds to the experimentally introduced σ of 0.07 [Fig. 4. 2 (c)]. This suggests that the dominant optical loss for the GaN:Eu,O-based L7 cavity is the experimentally introduced in-plane structural disorder. Hence, studying the impact of such structural disorder on the optical properties of III-nitrides-based 2D-PhC cavities is of utmost importance.

4. 4 The impact of *Q*-factors on the lasing possibilities

In order to investigate the impact of degraded Q-factors on the lasing possibilities, we estimated the optical gain threshold g_{th}, which is the minimum optical gain (g_{opt}) required for lasing. It is possible to consider optical gain in FDTD simulations by introducing a negative value of the extinction coefficient (k), as g_{opt} can be Expressed as $k = \lambda g_{opt}/4\pi$. In FDTD simulations, when the optical gain of an active layer is larger than the g_{th}, the electromagnetic field intensity of a cavity mode increases with time [29,30], corresponding to numerical lasing.

We calculated the time evolution of the electromagnetic field varying g_{opt} as a parameter, and estimated g_{th} of each cavity structure. To appropriately calculate the optical gain threshold (g_{th}) of a cavity mode, it is necessary to extract the time evolution of the resonant frequency. Therefore, we selected the resonant mode in the frequency domain using a Fourier transformation, and then applied an inverse Fourier transformation on them to characterize the time evolution. The extracted signals of the resonant mode of an L7 cavity for optical gain (g_{opt}) of 5, 10 and 15 cm^{-1} are shown in Fig. 4. 3 (a).

Subsequently, we determined the slope (m) of the time evolution of the field intensity $I(t)$ by using $\log_{10}[I(t)] = mt$, where t is time in simulations. The derived m for each value of g_{opt} is shown

in Fig. 4. 3 (b). Note that m and g_{opt} have a linear relationship, and positive m means laser oscillation occurs. Finally, g_{th} is given by the intersection of the fitting line and the horizontal axis (g_{th} = 9.2 cm^{-1}, when σ = 0.1 and r/a = 0.35), as m = 0 when $g_{opt} = g_{th}$.

In this study, we set optical gain in the entire area of the membrane for the simplicity. In experimental situations, however, 2D-PhCs are pumped with lasers (or by current injection), and the area with optical gain might be limited in the vicinity of the excitation spot. To ensure the accuracy of calculated value of g_{th}, we also conducted simulations with limited gain area. Herein, we limited the gain area assuming a typical laser spot with radius of 1.5 μm at the center of 2D-PhC cavities. The calculated g_{th} for a L7 cavity (r/a = 0.35) was 8.7 cm^{-1}, which well corresponds to the value calculated with setting optical gain in the entire area of membrane (9.2 cm^{-1}). This result indicates that the optical gain outside a cavity has less impact on g_{th} as the electric field of a resonant mode is well confined inside the cavity [31].

Typically, g_{opt} depends on the excitation power density and current density for optical and electrical pumping, respectively. Therefore, g_{th} in the FDTD simulations is closely related to the lasing threshold. Hence, a cavity structure with a low g_{th} is a promising structure to achieve lasing in GaN:Eu,O, considering its limited optical gain.

We do note that in the GaN:Eu,O material we work with the Purcell effect that could modulate the transition rate of emitters and might affect g_{th} at room temperature [22]. However, due to the variability of this effect to emitters with different polarization, location, and spectral overlap between emitter and cavity, we ignore here in order to generalize the discussion to the cavity design.

In order to investigate suitable structures for III-nitrides using above-mentioned simulation methods, we compared LN (N = 3, 5, 7, 9) cavities and HN (N = 2, 3) cavities, which are widely used for PhC lasers (Fig. 4. 4) [32,33]. The N of LN corresponds to the number of linearly missing air-holes. Regarding the HN cavities, H2 and H3 consist of 7 and 19 hexagonally missing holes, respectively.

Calculated g_{th} and Q-factors are shown in Fig. 4. 5 (a), the red and blue dots indicate the results for ideal (non-disordered, σ = 0) and disordered structures (σ = 0.1), respectively. The ratio of r/a was fixed to 0.35.

As shown in Fig. 4. 5 (a), the Q-factors of all the structures are degraded due to the introduced disorders. Furthermore, g_{th} linearly decreases with an increase of the Q-factor. Therefore, g_{th} is almost uniquely determined by the Q-factor independently of the cavity

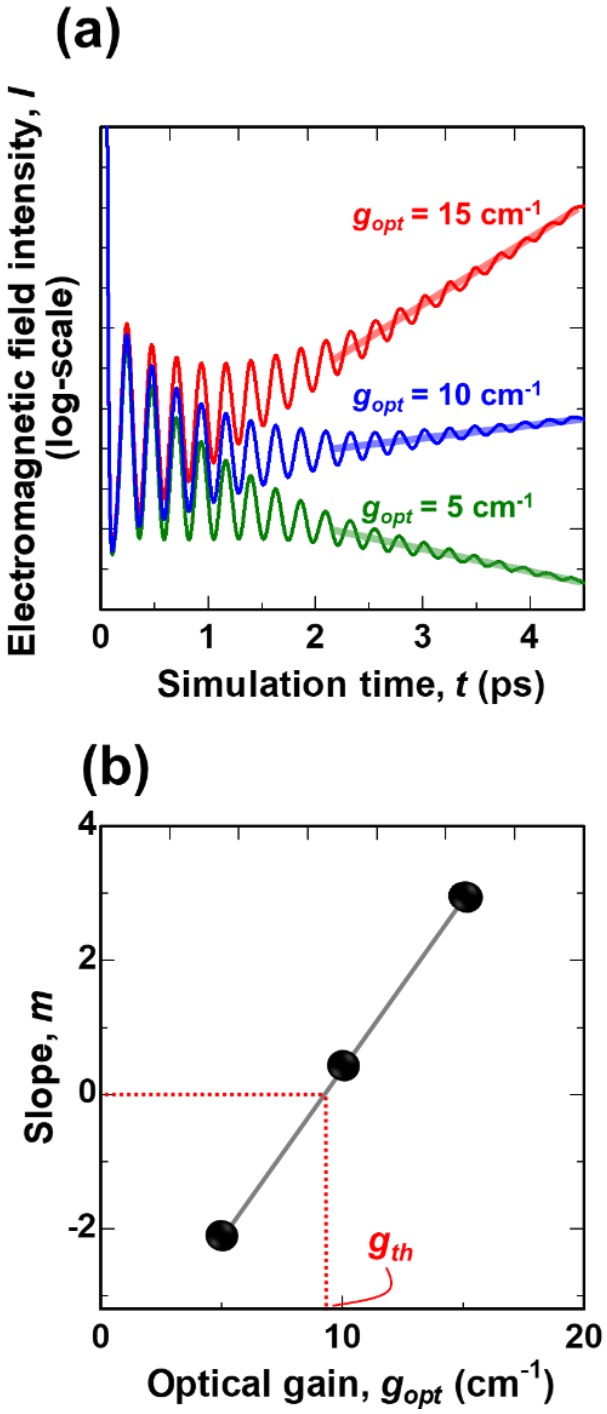

Fig. 4. 3 (a) Time evolution of the electromagnetic field of an L7 cavity mode for values of the optical gain of 5, 10 and 15cm^{-1}. (b) The slope of the time evolution of the electromagnetic field as a function of optical gain.

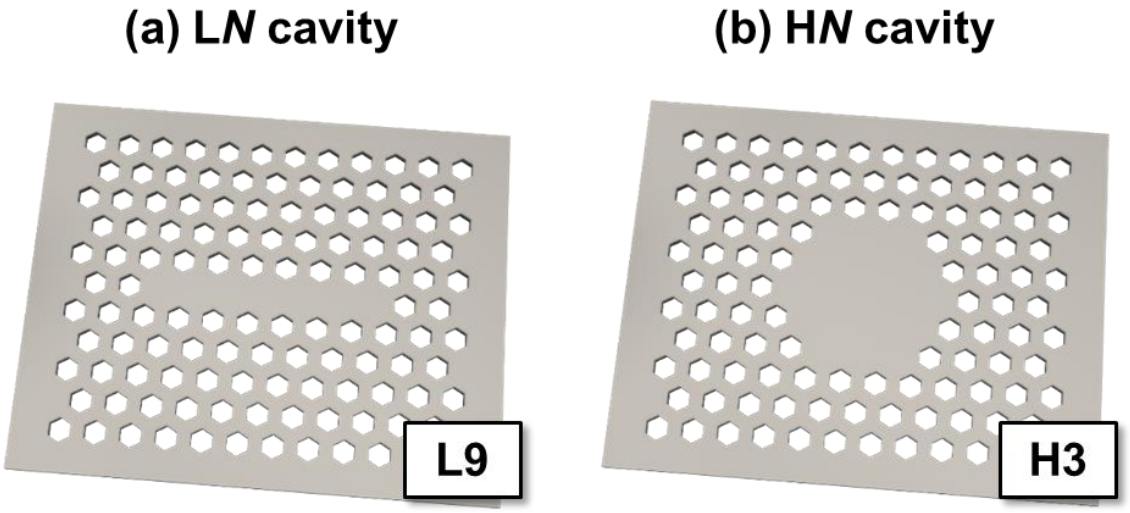

Fig. 4. 4 Schematic of a (a) L*N* cavity (L9 cavity) and (b) H*N* cavity (H3 cavity).

structures. This is a direct confirmation of the fact that g_{th} is inversely proportional to Q-factors when the spontaneous mission coupling factor (β) is constant [34]. This result clearly indicates that Q-factor is one of the most crucial parameter to achieve lasing in GaN:Eu,O.

4. 5 Investigation on suitable cavity structure to achieve high *Q*-factors for III-nitride semiconductors

Ideal Q-factors (Q_{id}) and degraded Q-factors (Q) due to disorder are shown in Fig. 4. 5 (b). For a value of σ = 0.05, Q monotonically increases along with Q_{id}, indicating that when disorder is suppressed in the order of σ of 0.05, high Q-factors can be realized by employing cavities with high-Q_{id}. However, for large disorder (σ = 0.1) that corresponds to the degree of experimentally introduced disorder, Q unexpectedly saturates even for high-Q_{id} designs. This saturation trend can be described by the following equation;

$$Q^{-1} = Q_{id}^{-1} + Q_{in}^{-1} \ , \tag{4. 6}$$

where Q_{in} corresponds to in-plane-disorder-induced losses. This equation means that, even if Q_{id}

is sufficiently high, the low Q_{in} limits the Q. Therefore, design of cavities that are robust to structural disorder, and that exhibit high Q_{in} is crucial to achieve high Q-factors with large disorder.

We firstly calculated Q_{id} as a function of *r/a* for all cavity structures. As shown in Fig. 4. 6 (a), Q-factors are maximized at different values of *r/a* for each cavity. Q-factors of smaller (shorter) cavities were maximized with relatively small *r/a* values. This is likely due to that for small cavities where the cavity length is short, smaller air-holes leads to a longer effective cavity length, effectively suppressing the out-of-plane optical loss caused at the interface between the PhC region and the cavity [35,36]. By using values of *r/a* at the maximum Q_{id} for each structure, we calculated Q and estimated Q_{in} with Eq. (4. 1). Although the resonant wavelengths of cavities with their respective optimal *r/a* are slightly different (650 ± 30 nm with *a* of 220 nm), we consider the variation is small enough to neglect the impact on our main discussion.

In Fig. 4. 6 (b), Q of L*N* cavities saturates with increasing *N*, even for the optimized values of *r/a*. This is especially clear for large L*N* cavities (L7, L9) where Q is dominated by Q_{in} as its value approaches ~7000, independent of the value of Q_{id}. This result numerically supports the idea that experimental Q-factors of III-nitride-based L*N* cavities (~up to 5500) are limited by the crystallographically induced disorders [4–14]. Based on the optical gain of $In_xGa_{1-x}N$ active layers in the red region (up to ~35 cm^{-1}) [37], a Q-factor larger than 8000 is required for laser oscillation [see Fig. 4. 5 (a)]. In addition, for lasing in GaN:Eu,O, Q-factors of 20000-30000 is necessary assuming the optical gain (6.6-14 cm^{-1}) [38,39]. However, the limited Q-factors induced by the disorders increase g_{th} and prevent lasing in these materials. Because it is difficult for wurtzite crystals to avoid this type of disorder from a crystallographic perspective, a more accurate fabrication of nanoscale structures is technically challenging. Therefore, in order to improve Q-factors and to achieve laser oscillation at long wavelengths, a suitable design of cavities tolerant to disorder is essential for GaN:Eu,O as well as $In_xGa_{1-x}N$-based devices.

It should be noted that III-nitride-based 2D-PhC L*N* cavities with high experimental Q-factor of 22500 has been reported in the infrared region (λ ~ 1300 nm, *r* ~ 120 nm) by proper modification of the cavity structure [35,40]. These results demonstrate that such cavity modifications are effective to achieve high Q-factors, as reported for matured semiconductor systems. In order to investigate the tolerance to disorder for such modified L*N* cavity in the UV-visible regime, where large structural disorder is introduced, we additionally calculated Q_{id} and Q of a properly designed L3 cavity.

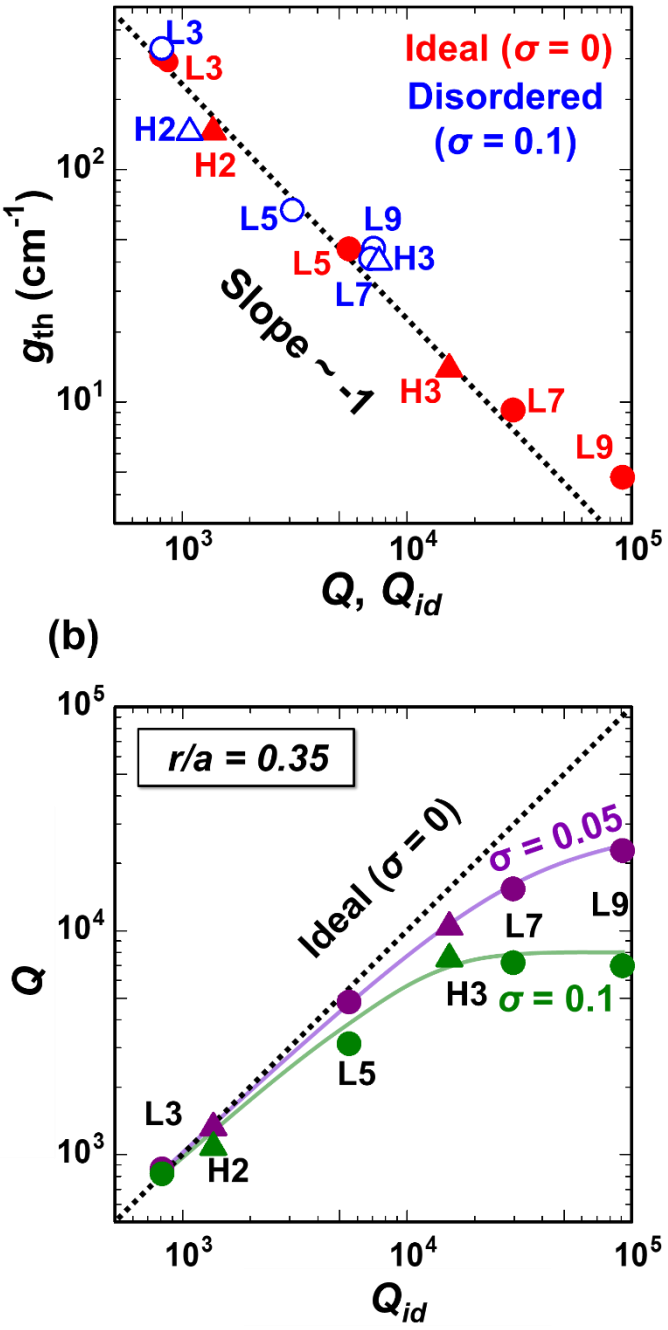

Fig. 4. 5 (a) Calculated Q-factors and g_{th} for L*N* and H*N* cavities. The red and blue dots indicate the results for ideal (non-disordered) and disordered structures, respectively. (b) Ideal and degraded Q-factors with disorder (σ = 0.05, 0.1).

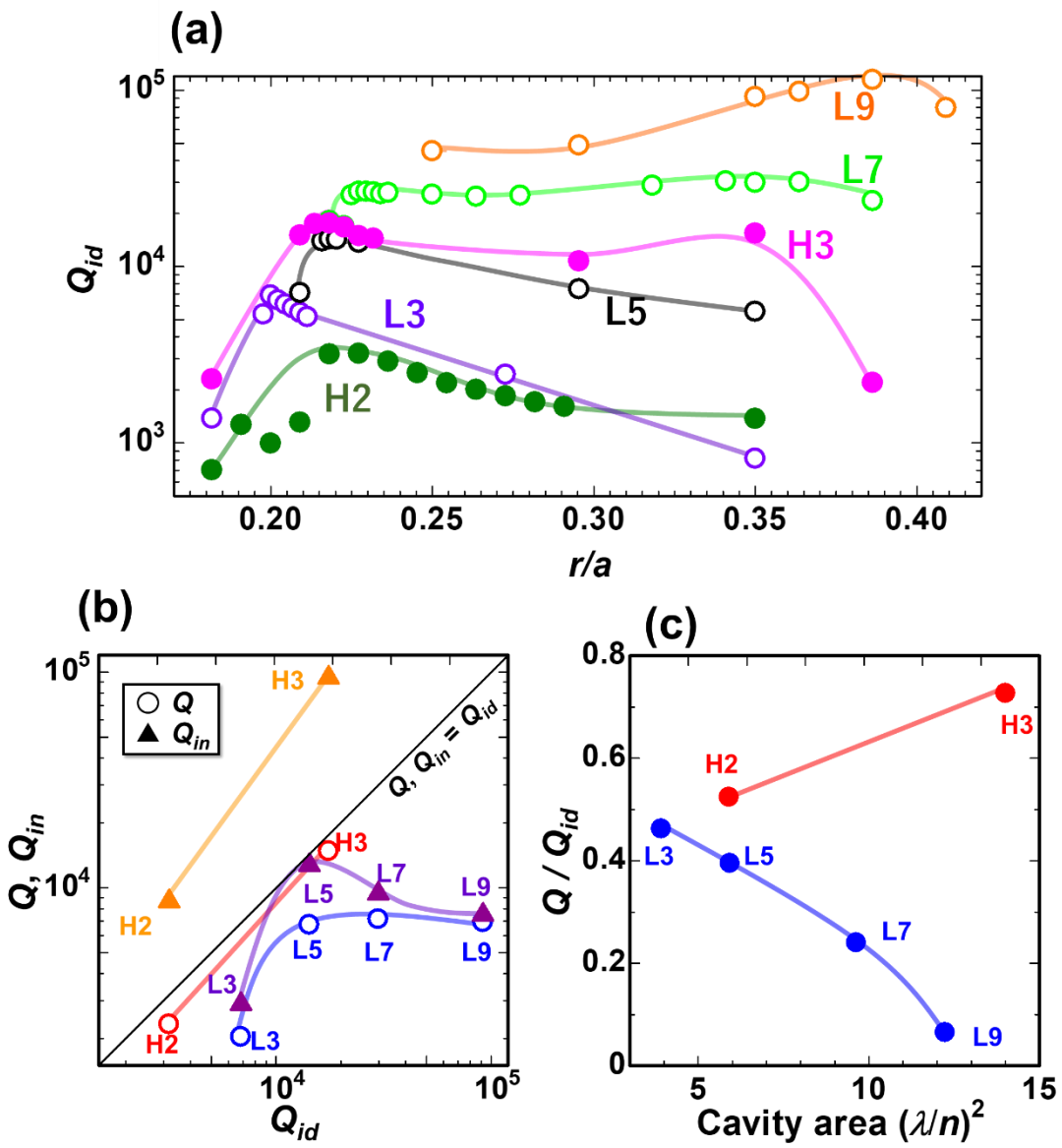

Fig. 4. 6 (a) Calculated ideal Q-factors (Q_{id}) as a function of *r/a* for L*N* and H*N* cavities. (b) Q and Q_{in} as a function of Q_{id}. (c) Ratios of Q to Q_{id} as a function of cavity area. Values of *r/a* are optimized to maximize Q_{id} in (b) and (c).

In general, air-holes at both edges of a cavity are displaced outwards to improve Q-factors in L3 cavities, because out-of-plane losses are significantly suppressed [35]. We confirmed that Q_{id} of an L3 cavity with *r*/*a* of 0.23 was improved from 4200 to 45700 by properly displacing the air-holes outwards by 0.25*a*. For this structure, *r* of 50 nm was chosen to tune the resonant wavelength to the red range (λ ~ 680 nm) with a corresponding σ of 0.15. By utilizing our disorder model to this structure, it was clarified that the calculated Q strongly degraded to 9700, which corresponds to the upper limit of the Q-factors for L*N* cavities with disorder as shown in Fig. 4. 6 (b).

In the infrared range (λ~1300 nm), on the other hand, σ decreases to 0.08 because the optimal value of *r* increases to 96 nm under the same *r/a* of 0.23. Due to the smaller value of σ, the calculated *Q* was as high as 26000, which well reproduces the experimental Q-factor of 22500 demonstrated in Ref. [40]. The results clearly indicate that L*N* cavities are highly sensitive to structural disorder particularly in the visible ranges, and their Q-factors are strongly limited by Q_{in} even after appropriate displacement of air-holes. Thus, in order to realize high Q-factors in the visible range, a robust fundamental cavity design is prerequisite.

In contrast to L*N* cavities, values of Q_{in} of H*N* cavities are much higher than their Q_{id}, indicating that the disorder-induced degradation of Q is negligible ($Q^{-1} = Q_{in}^{-1} + Q_{id}^{-1} \cong Q_{id}^{-1}$) [Fig. 4. 6 (b)]. In particular, Q_{in} of H3 is about one order of magnitude higher than Q_{id}. It is noteworthy that the Q_{in} strongly depends on the cavity structure even though the same value of disorder is induced into 2D-PhC cavities.

In Fig. 4. 7, calculated Q-factors of H3 (*r/a* = 0.22), L5 (*r/a* = 0.22) and L7 (*r/a* = 0.35) cavities are shown as a function of σ. Note that *r/a* of each cavity is optimized to maximize its Q-factor. σ was varied by changing *r* and *a* while maintaining the ratio of *r/a*. The Q-factors of the L5 and L7 cavities drastically decrease with increasing σ, indicating that L*N* cavities are quite sensitive to the degree of disorder. On the contrary, the H3 cavity shows a great robustness against σ, and its Q-factor hardly changes.

These results indicate that H*N* cavities are highly tolerant to disorder, independently of the magnitude of σ, and more suitable for III-nitride-based 2D-PhC cavities rather than conventional L*N* cavities.

In order to investigate the reason why H*N* cavities are more tolerant to disorder than L*N* cavities, we focused on the cavity area, which is the physical space where a cavity exists. Generally, we can realize both high Q_{id} and a high tolerance of Q-factors to disorder by using cavities with a large cavity area, because the ratio of the sidewall surface of air-holes to cavity volume decreases.

However, as shown in Fig. 4. 6 (c), the ratios of Q to Q_{id} of L*N* cavities drastically decreases as *N* increases. Particularly, the Q of an L9 cavity was only 6.5% of Q_{id}. This is a result of the cavity mode localization shown in Fig. 4. 8 (c), leading to a large degradation of the Q-factor [41].

Although Q_{id} of L*N* cavities can be improved by increasing the cavity size, Q is strongly limited by the mode localization when structural disorder is introduced. In contrast, in Fig. 4. 6 (c), the ratio of Q to Q_{id} of H*N* cavities increases with *N*. For these structures, the cavity modes do not localize even with disorder, as shown in Fig. 4. 8 (d). To evaluate the degree of cavity mode localization, we compared the modal volume with and without disorder (V_d and V_{id}, respectively). The modal volume of an H3 cavity hardly changed with a ratio of V_d/V_{id} of 1.01, while that of the L9 cavity was only 0.85.

These results suggest that H3 is a highly promising structure for the realization of high-Q-factors with III-nitride-based 2D-PhC cavities.

4. 6 Summary

In summary, we have investigated the impact of crystallographically induced disorder on the Q-factor of L*N* and H*N* 2D-PhC cavities by FDTD simulations. We found that the Q-factor and g_{th} have an inverse linear-relationship, implying that it is necessary to improve the Q-factor in order to achieve laser oscillation in GaN:Eu,O as well as red $In_xGa_{1-x}N$/GaN-QWs. Although high-Q-factors are usually obtained by introducing large cavity structures, the value for large L*N* cavities dramatically decreases due to the cavity mode localization. In contrast, an H3 cavity exhibits a high Q-factor even with disorder. These results indicate that H3 cavities can overcome the general problem of Q-factor-degradation of III-nitride-based PhC cavities.

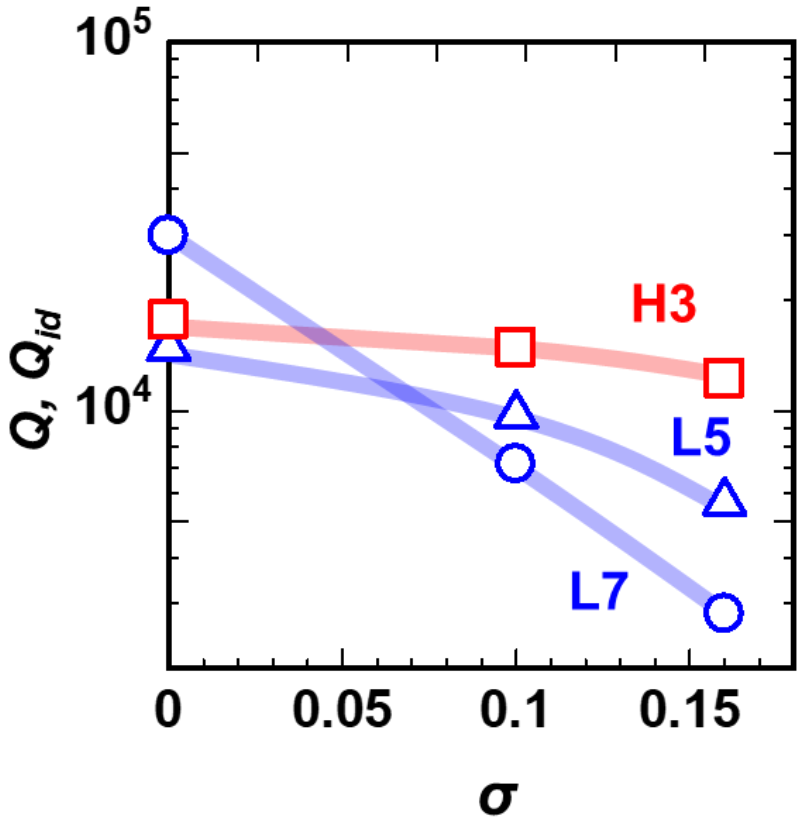

Fig. 4. 7 Calculated Q-factors of H3 (r/a = 0.22), L5 (r/a = 0.22) and L7 (r/a = 0.35) cavities as a function of σ.

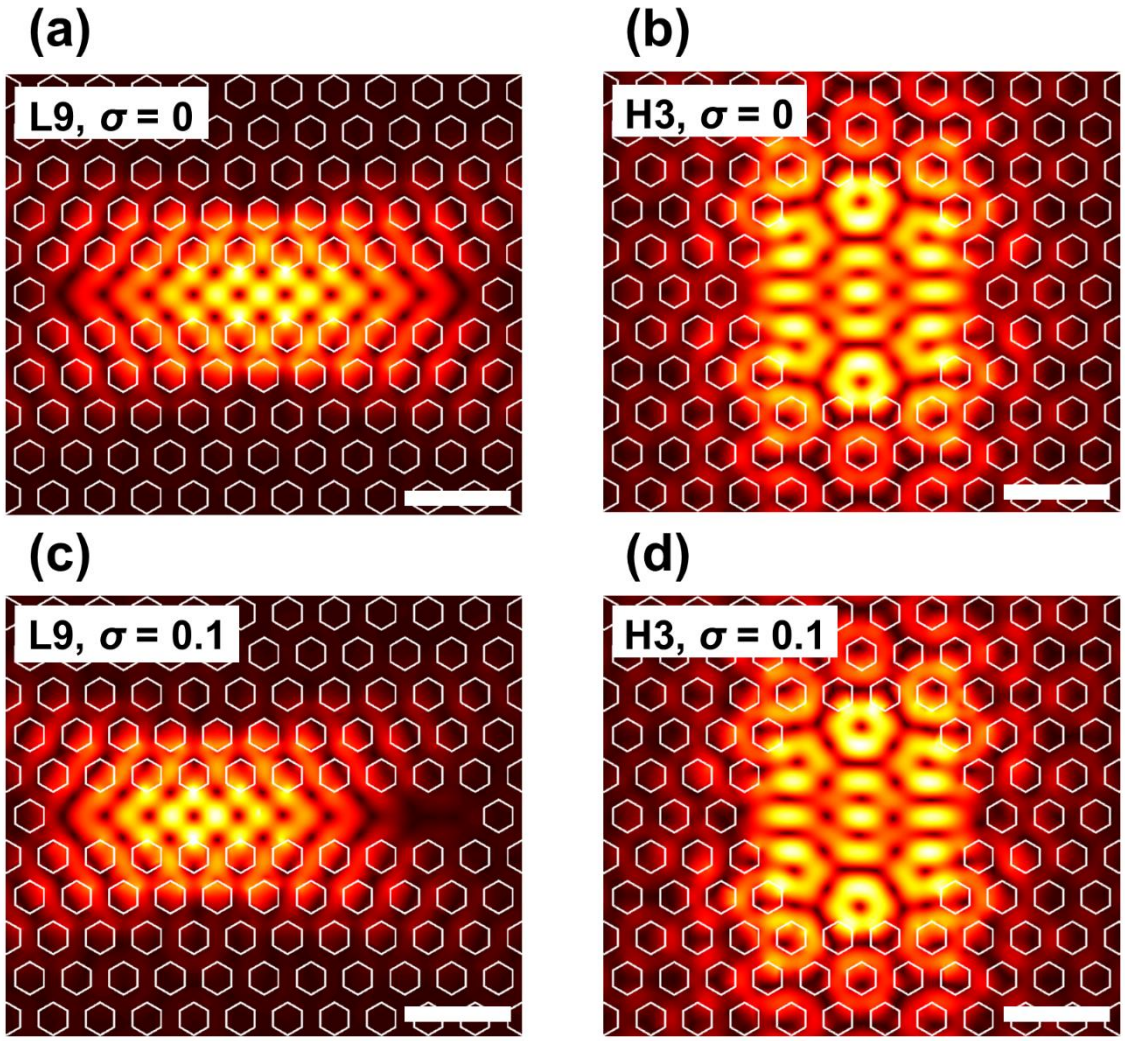

Fig. 4. 8 Electric field distribution of (a) a non-disordered L9, (b) a non-disordered H3, (c) a disordered L9 and (d) a disordered H3 cavity mode, with *r/a* of 0.35. The scale bars correspond to 500 nm.

References

[1] E.M. Purcell, *Phys. Rev.* **69**, 681 (1946).

[2] E. Kuramochi, E. Grossman, K. Nozaki, K. Takeda, A. Shinya, H. Taniyama, and M. Notomi, *Opt. Lett.* **39**, 5780 (2014).

[3] Y. Lai, S. Pirotta, G. Urbinati, D. Gerace, M. Minkov, V. Savona, A. Badolato, and M. Galli, *Appl. Phys. Lett.* **104**, 241101 (2014).

[4] Y.S. Choi, K. Hennessy, R. Sharma, E. Haberer, Y. Gao, S.P. Denbaars, S. Nakamura, E.L. Hu, and C. Meier, *Appl. Phys. Lett.* **87**, 243101 (2005).

[5] C. Meier, K. Hennessy, E.D. Haberer, R. Sharma, Y.S. Choi, K. McGroddy, S. Keller, S.P. DenBaars, S. Nakamura, and E.L. Hu, *Appl. Phys. Lett.* **88**, 031111 (2006).

[6] M. Arita, S. Kako, S. Iwamoto, and Y. Arakawa, *Appl. Phys. Express* **5**, 126502 (2012).

[7] S. Ichikawa, Y. Sasaki, T. Iwaya, M. Murakami, M. Ashida, D. Timmerman, J. Tatebayashi, and Y. Fujiwara, *Phys. Rev. Appl.* **15**, 034086 (2021).

[8] M. Arita, S. Ishida, S. Kako, S. Iwamoto, and Y. Arakawa, *Appl. Phys. Lett.* **91**, 051106 (2007).

[9] D. Néel, S. Sergent, M. Mexis, D. Sam-Giao, T. Guillet, C. Brimont, T. Bretagnon, F. Semond, B. Gayral, S. David, X. Checoury, and P. Boucaud, *Appl. Phys. Lett.* **98**, 261106 (2011).

[10] N. Vico Triviño, G. Rossbach, U. Dharanipathy, J. Levrat, A. Castiglia, J.F. Carlin, K.A. Atlasov, R. Butté, R. Houdré, and N. Grandjean, *Appl. Phys. Lett.* **100**, 071103 (2012).

[11] S. Blumenthal, M. Bürger, A. Hildebrandt, J. Förstner, N. Weber, C. Meier, D. Reuter, and D.J. As, *Phys. Status Solidi C* **13**, 292–296 (2016).

[12] T.T. Wu, P.H. Weng, Y.J. Hou, and T.C. Lu, *Appl. Phys. Lett.* **99**, 221105 (2011).

[13] R. Butté and N. Grandjean, *Nanophotonics* **9**, 569 (2020).

[14] C.H. Lin, J.Y. Wang, C.Y. Chen, K.C. Shen, D.M. Yeh, Y.W. Kiang, and C.C. Yang, *Nanotechnology* **22**, 025201 (2011).

[15] M. Arita, S. Kako, S. Iwamoto, and Y. Arakawa, *Appl. Phys. Express* **5**, 126502 (2012).

[16] S. Ichikawa, Y. Sasaki, T. Iwaya, M. Murakami, M. Ashida, D. Timmerman, J. Tatebayashi, and Y. Fujiwara, *Phys. Rev. Appl.* **15**, 034086 (2021).

[17] D.S.Y. Hsu, C.S. Kim, C.R. Eddy, R.T. Holm, R.L. Henry, J.A. Casey, V.A. Shamamian, and A. Rosenberg, *J. Vac. Sci. Technol.* **23**, 1611 (2005).

[18] A.F. Matthews, S.F. Mingaleev, and Y.S. Kivshar, *Laser Phys.* **14**, 631–634 (2004).

[19] M. Fujita, S. Takahashi, Y. Tanaka, T. Asano, and S. Noda, *Science* **308**, 1296–1299 (2005).

[20] J. Gérard and G. Panzarini, *Phys. Rev. B* **60**, 13276–13279 (1999).

[21] A. Meldrum, P. Bianucci, and F. Marsiglio, *Opt. Express* **18**, 10230 (2010).

[22] D. Timmerman, Y. Matsude, Y. Sasaki, S. Ichikawa, J. Tatebayashi, and Y. Fujiwara, *Phys. Rev. Appl.* **14**, 064059 (2020).

[23] N.A. Sanford, L.H. Robins, A. V. Davydov, A. Shapiro, D. V. Tsvetkov, A. V. Dmitriev, S. Keller, U.K. Mishra, and S.P. DenBaars, *J. Appl. Phys.* **94**, 2980 (2003).

[24] L. Sapienza, H. Thyrrestrup, S. Stobbe, P.D. Garcia, S. Smolka, and P. Lodahl, *Science* **327**, 1352–1356 (2010).

[25] J. Topolancik, B. Ilic, and F. Vollmer, *Phys. Rev. Lett.* **99**, 253901 (2007).

[26] D. Gerace and L.C. Andreani, *Opt. Lett.* **29**, 1897 (2004).

[27] N.V. Triviño, M. Minkov, G. Urbinati, M. Galli, J.F. Carlin, R. Butté, V. Savona, and N. Grandjean, *Appl. Phys. Lett.* **105**, 231119 (2014).

[28] N. Mann, A. Javadi, P.D. García, P. Lodahl, and S. Hughes, *Phys. Rev. A* **92**, 023849 (2015).

[29] S. Iwamoto, J. Tatebayashi, S. Kako, S. Ishida, and Y. Arakawa, *Physica E Low Dimens. Syst. Nanostruct.* **21**, 814–819 (2004).

[30] T. Iwaya, S. Ichikawa, M. Murakami, D. Timmerman, J. Tatebayashi, and Y. Fujiwara, *Appl. Phys. Express* **14**, 122002 (2021).

[31] T. Iwaya, S. Ichikawa, D. Timmerman, J. Tatebayashi, and Y. Fujiwara, *Opt. Express* **30**, 28853–28864 (2022).

[32] O. Painter, R.K. Lee, A. Scherer, A. Yariv, J.D. O'Brien, P.D. Dapkus, and I. Kim, *Science* **284**, 1819–1821 (1999).

[33] S. Strauf, K. Hennessy, M.T. Rakher, Y.S. Choi, A. Badolato, L.C. Andreani, E.L. Hu, P.M. Petroff, and D. Bouwmeester, *Phys. Rev. Lett.* **96**, 127404 (2006).

[34] Y. Yamamoto, S. Machida, and G. Björk, *Phys. Rev. A* **44**, 657 (1991).

[35] Y. Akahane, T. Asano, B. Song, and S. Noda, *Nature* **425**, 944 (2003).

[36] T. Asano, B.S. Song, Y. Akahane, and S. Noda, *IEEE J. Sel. Top. Quantum Electron.* **12**, 1123–1134 (2006).

[37] G.-L. Su, T. Frost, P. Bhattacharya, and J.M. Dallesasse, *Opt. Express* **23**, 12850 (2015).

[38] A. Takeo, S. Ichikawa, S. Maeda, D. Timmerman, J. Tatebayashi, and Y. Fujiwara, *Jpn J. Appl. Phys.* **60**, 120905 (2021).

[39] N.N. Ha, A. Nishikawa, Y. Fujiwara, and T. Gregorkiewicz, *J. Sci. Adv. Mater. Dev.* **1**, 220 (2016).

[40] N.V. Triviño, M. Minkov, G. Urbinati, M. Galli, J.F. Carlin, R. Butté, V. Savona, and N. Grandjean, *Appl. Phys. Lett.* **105**, 231119 (2014).

[41] J.P.P. Vasco and S. Hughes, *ACS Photonics* **5**, 1262–1272 (2018).

Chapter 5. Improved Q-factors of III-nitride-based photonic crystal nanocavities by optical loss engineering

5. 1 Introduction

In Chapter 4, to achieve high-Q III-nitride-based 2D-PhC cavities in the UV-visible range, we have investigated the degradation mechanism of Q-factors by reproducing experimentally introduced structural disorder into 3D-FDTD simulations. As a result, the calculated Q-factors considering the experimentally introduced degree of in-plane structural disorder well corresponded to experimental Q-factors, suggesting that the Q-factors of III-nitride-based 2D-PhC cavities have been dominantly limited by the structural disorder. Furthermore, we have designed 2D-PhC cavities that shows a high robustness against disorder, and reported that H*N* cavities, especially a H3-type cavity, shows a more robust stability of the Q-factor against structural disorder as compared to L*N* cavies.

Conventional well-known approach to achieve high Q-factors is to employ 1D-heterostructures formed by modulating air-hole radius or periodicity, which effectively confine light in the central of a defect by utilizing a controlled photonic band gap structure [1]. However, it is known that in-plane disorder strongly degrades the Q-factor of 1D-heterostructure nanocavities [2]. We calculated the Q-factor of a 1D-heterostructure considering structural disorder using the simulation method that we proposed in Chapter 4. With σ of 0.1, the calculated Q-factor was 1.1×10^4, which is much degraded as compared to the ideal Q-factor of several millions. For these reasons, employing 1D-heterostructures is not expected to be a successful approach for III-nitride semiconductors.

Recently, Ge *et al*. have focused on a 2D-heterostructure which supports a band-edge mode and observed a high Q-factor of ~15000 in the red spectral range using a silicon nitride film deposited on a quartz substrate [3]. Such 2D-heterostructures have a high possibility to show a better

robustness to in-plane disorder than 1D-heterostructures, in a similar way as 2D H*N* cavities show a better robustness to in-plane disorder than line-defect 1D-cavities [4].

In this chapter, we focus on two types of structure (H3 cavity and 2D-heterostructure) in order to achieve high Q-factors. We present the fabrication and optical characterization and discuss the dominant optical losses for III-nitride (GaN:Eu,O) -based 2D-PhC cavities in the visible range and demonstrate measures for suppressing such losses to achieve high Q-factors.

5. 2 Sample fabrication and characterization method

5. 2. 1 Material candidate for the sacrificial layer

To demonstrate 2D-PhC cavities with high Q-factors, an air-bridge structure is desirable for effective light confinement in a cavity by the high refractive index contrast between the GaN:Eu,O membrane and air-gap. However, standard wet-etching process is difficult to apply for III-nitride semiconductors because of the chemically stable nature.

So far, air-bridge structures have been realized by using unique techniques. Photoelectrochemical (PEC) etching techniques have been employed for either etching $In_xGa_{1-x}N$ sacrificial layers [5–7] or releasing active layers from 6H-SiC or Si substrates [8–10]. However, to attain a sufficiently large air-gap beneath the active layer, a thick $In_xGa_{1-x}N$ layer is required, that is technically challenging to achieve high crystalline and good surface morphology due to the large lattice mismatch between $In_xGa_{1-x}N$ and GaN. Besides, the relatively small etching selectivity of the PEC process frequently degrades the surface morphology of active layers [8], which leads to light scattering [11,12]. Furthermore, chemical solutions used for PEC etching methods such as HF and HCl can damage the $(000\bar{1})$ facets of III-nitride membranes [13], also result in a degraded surface morphology.

III-nitride-based 2D-PhC cavities on Si (111) substrate [14] or SiC layer on Si (001) substrate [15] have been reported using selective RIE etching processes. However, the thickness of the epitaxially grown layer corresponds to the thickness of the membrane, therefore it is limited to 200-300 nm. Consequently, this limitation typically results in low crystal quality in the active layers,

which in turn reduces the quantum efficiency and causes light scattering due to a high density of threading dislocations [16].

Arita *et. al* demonstrated an $In_xGa_{1-x}N/Al_xGa_{1-x}N$-QW-based membrane 2D-PhC cavities by selectively decomposing GaN layer at around 1000 °C utilizing the difference in thermal stability between GaN and $Al_xGa_{1-x}N$. In contrast to PEC etching processes, smooth $(000\bar{1})$ facets can be obtained using this method. However, in terms of crystal quality, a GaN-based membrane is generally preferred over an $Al_xGa_{1-x}N$-based membrane.

In this study, we choose $Al_xIn_{1-x}N$ as a sacrificial layer, that can be selectively etched using hot nitric acid [17]. Besides, the *a*-axis lattice constant completely matches that of GaN with the In composition of ~0.18. This allows for pseudomorphic growth, ensuring a high crystallinity in both the sacrificial layer and the active layer above it.

5. 2. 2 Crystal growth

The thickness of $Al_{1-x}In_xN$ layer should be thick enough (> ~600 nm) for a strong light confinement. However, it has been reported that although $Al_xIn_{1-x}N$ can be pseudomorphically grown on GaN when the thickness is ~50 nm or less, the crystalline degrades for thicker $Al_xIn_{1-x}N$ layers due to a decrease in the amount of incorporated In atoms [18]. Furthermore, it is known that surface morphology deteriorates due to In droplet and V-pits for thick $Al_xIn_{1-x}N$ layers [19–26].

To overcome these issues, we employed an original growth method as the temperature profile is illustrated in Fig. 5. 1. We first grew a 50-nm-$Al_xIn_{1-x}N$ layer, that is thin enough to maintain high crystalline and good surface morphology at a growth temperature of ~800 °C. An $Al_xGa_{1-x}N$ cap layer is grown to prevent the thermal decomposition of $Al_xIn_{1-x}N$ layer, and the temperature was raised to 1050°C to evaporate In droplets on the surface, which reportedly degrades crystalline and surface morphology of $Al_xIn_{1-x}N$ [19]. The thermal decomposition temperature of $Al_xGa_{1-x}N$ is higher than that of $Al_xIn_{1-x}N$, therefore In atom desorption from the $Al_xIn_{1-x}N$ layer is expected to be suppressed by the $Al_xGa_{1-x}N$ cap. Then, the growth of $Al_xIn_{1-x}N$ and $Al_xGa_{1-x}N$ cap is repeated until the desired film thickness is achieved.

In addition, to attain a thick $Al_xIn_{1-x}N$ layer with high crystallinity, the In composition has to be precisely controlled to ~0.18, otherwise dislocations are formed to minimize the system strain energy. In this study, the In composition was controlled by adjusting the growth temperature as parameter because the In composition is highly sensitive relative to growth temperature. The

equilibrium vapor pressure of In atom is much larger than that of Al [27,28], therefore high growth temperature leads to low In composition [29,30]. On the other hand, at a low growth temperature, the difference in the diffusion length of Al and In adatom induces a compositional inhomogeneity, resulting in alloy clustering [31]. Therefore, precise control of growth temperature is required to achieve an $Al_xIn_{1-x}N$ layer with low threading dislocation density and high crystallinity.

In composition of $Al_xIn_{1-x}N$ as a function of growth temperature is shown in Fig. 5. 2. Blue circles and red triangles depict data for samples grown on *c*-sapphire substrates and free-standing n-GaN substrates, respectively. With increasing the growth temperature, In composition decreases due to the evaporation of In atoms as previously reported [29,30]. Although the In composition greatly changes with temperature, when the lattice-match condition ($x \sim 0.178$) is satisfied, In composition becomes relatively insensitive and almost constant for a wide temperature range ($\Delta T \sim 12$°C). This result suggests that the In composition is spontaneously controlled to satisfy the lattice-match condition in order to minimize the system strain energy. Similar behavior is reported for $In_xGa_{1-x}N$ [32–34] and $Al_xGa_{1-x}N$ [35,36] grown on GaN or AlN, which is known as the compositional pulling-effect.

The surface of $Al_xIn_{1-x}N$ layer with different In composition observed using a Nomarski microscope are illustrated in Fig. 5. 3. When the In composition is around or larger than the lattice match condition, flat surfaces are appeared, however, many cracks are observed on the surface of $Al_{0.850}In_{0.150}N$, due to tensile strain.

(0004) 2θ-ω scanning profile of X-ray diffraction (XRD) measurement for $Al_{0.821}In_{0.179}N$ shows a single peak with a small FWHM of 0.0415 degrees, indicating that the In composition is highly uniform even the thickness is large [Fig. 5. 4 (a)]. On the contrary, the profile for $Al_{0.831}In_{0.177}N$ is broadened and appeared to be composed of several components, suggesting that lattice relaxation has occurred. From the observation that such a big difference is appeared even though the In compositions differ by only 0.002, it is implied that the In composition threshold is 0.178-0.179, and smaller In composition likely leads to lattice relaxation due to tensile strain. These results suggest that it is preferable to grow $Al_xIn_{1-x}N$ with In composition higher than 0.178-0.179 in order to suppress the dislocation formation and to achieve good surface morphology.

The ω scan profiles of XRD measurement for a 600-nm-thick $Al_{0.821}In_{0.179}N$ are plotted in Fig. 5. 4 (b). The FWHMs for ω scans are as small as 185 arcsec and 169 arcsec for (0004) and $(10\bar{1}5)$, respectively. Previously reported FWHM for (0002) ω scan profiles was 375 arcsec for a 250-nm-thick $Al_{0.81}In_{0.19}N$ [25], 232 arcsec for a 136-nm-thick $Al_{0.816}In_{0.184}N$ [25] and 208 arcsec for a

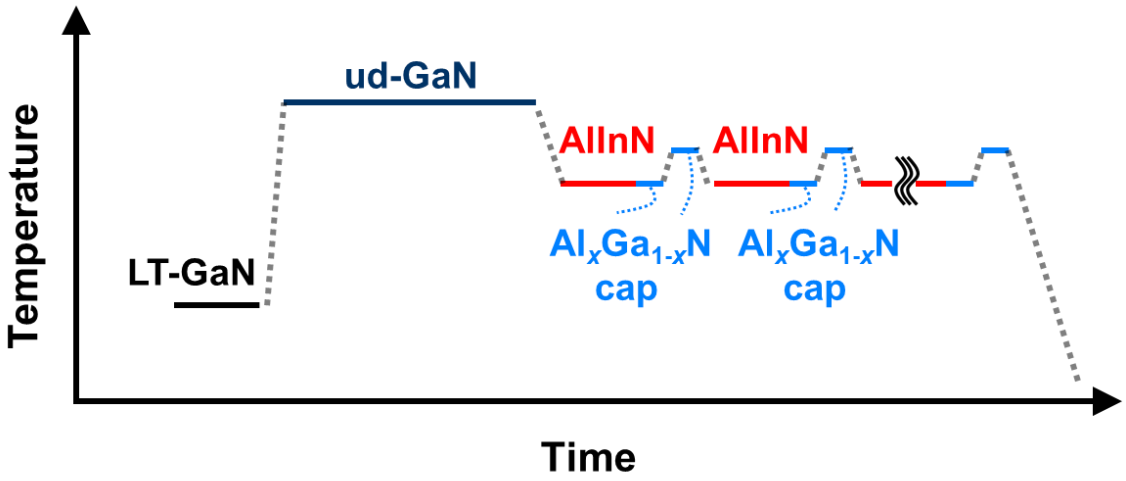

Fig. 5. 1 Temperature profile of growth of a thick $Al_xIn_{1-x}N$ layer.

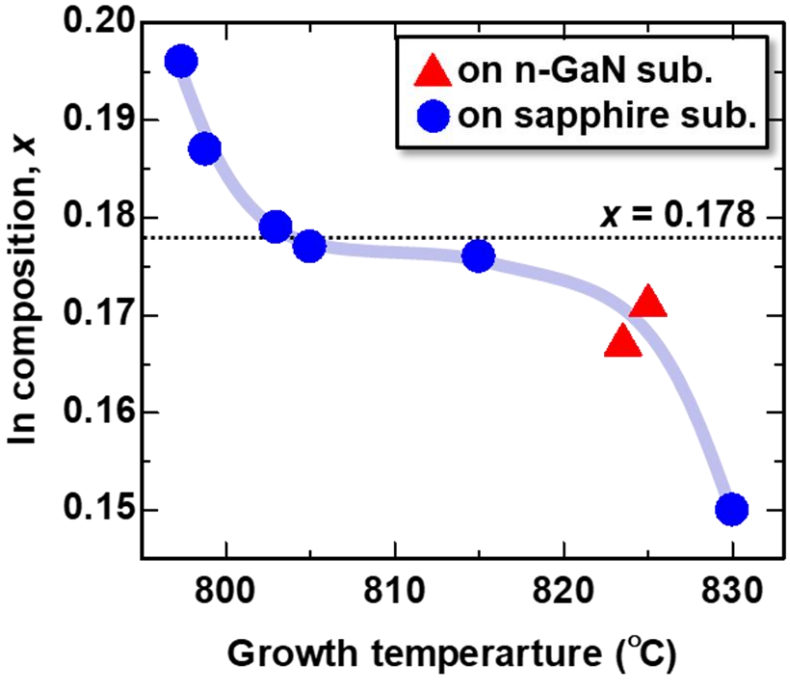

Fig. 5. 2 In composition of $Al_xIn_{1-x}N$ layers as a function of growth temperature.

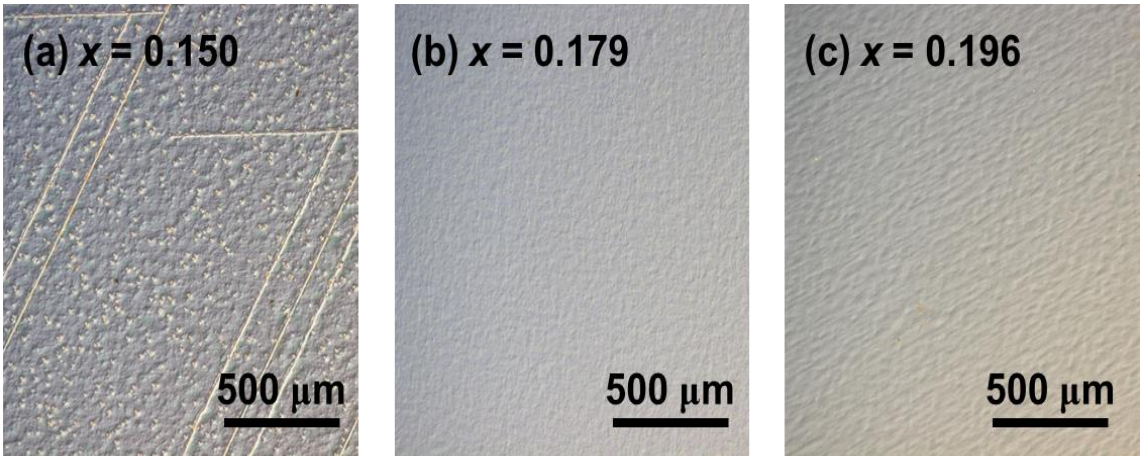

Fig. 5. 3 Surface of $Al_xIn_{1-x}N$ with In composition of (a) 0.150, (b) 0.179 and (c) 0.196 observed using a Nomarski microscope.

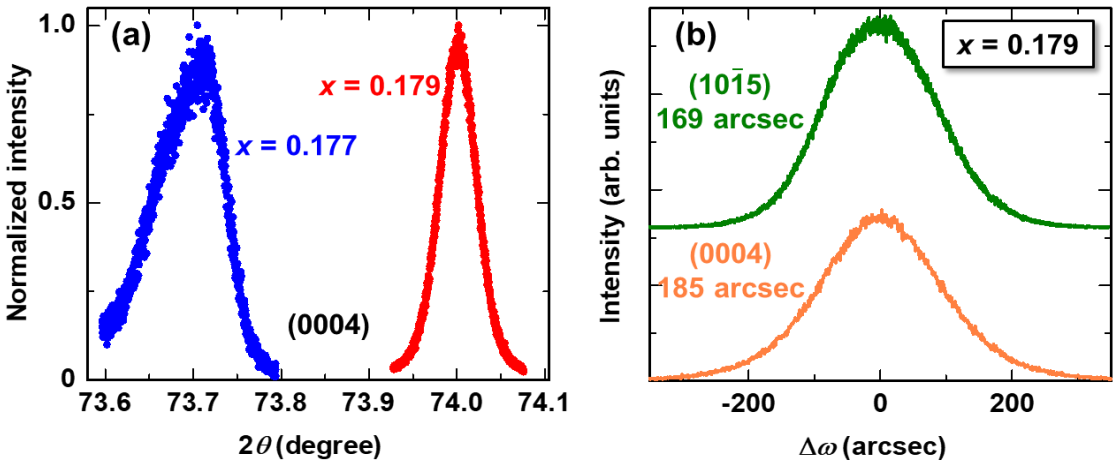

Fig. 5. 4 (a) (0004) XRD 2θ-ω scan profiles for the $Al_xIn_{1-x}N$ with In composition of 0.177 and 0.179. (b) (0004) and (10$\bar{1}$5) XRD ω scan profiles for a 600-nm-thick $Al_{0.81}In_{0.19}N$.

300-nm-thick $Al_{0.836}In_{0.164}N$ [22]. These results indicate that our growth method enabled reasonably low dislocation density and high uniformity of In composition, even the thickness is larger than previous reports.

Note that although few research has reported on the growth temperature dependence of In composition in $Al_xIn_{1-x}N$ grown by the OMVPE method [29,30], the In composition has been confirmed to monotonically decrease with increasing the growth temperature, without stabilizing around the lattice-match condition. We assume the reason that the compositional pulling effect was observed in this study is attributed to the high crystalline and high In composition uniformity of $Al_xIn_{1-x}N$ layers. In previous reports, continuously-grown $Al_xIn_{1-x}N$ layers thicker than 100 nm have been studied, which contain high dislocation density [19–26]

In addition to crystallinity, good surface morphology is vital to minimize optical losses caused by surface scattering and to achieve high Q-factors [11,12]. Atomic force microscope (AFM) image of the surface of a 600-nm-thick $Al_{0.820}In_{0.180}N$ is illustrated in Fig. 5. 5. Despite its considerable thickness, atomic steps are clearly observed with a small root-mean square (RSM) value of 0.14 nm. These results clearly indicate that In droplets are effectively evaporated by rising temperature, and the formation of V-pits are suppressed.

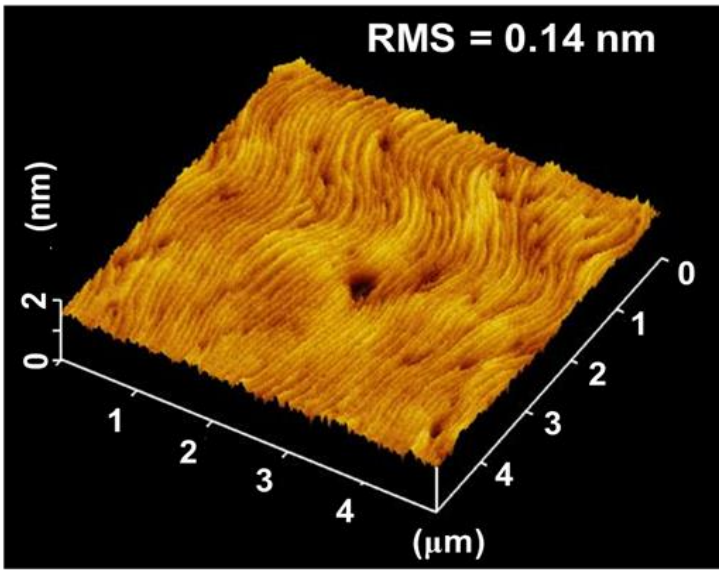

Fig. 5. 5 AFM image of a 600-nm-thick $Al_{0.80}In_{0.20}N$.

Using this growth method, sufficiently thick (~600 nm) $Al_xIn_{1-x}N$ layer with high crystallinity and surface morphology was attained, which is necessary to fabricate membrane-type 2D-PhC cavities with high Q-factors. The sample utilized for 2D-PhC cavity fabrication contains a low-temperature GaN buffer layer, a 2.7-μm-thick undoped-GaN, a 600-nm-thick $Al_{0.82}In_{0.18}N$ sacrificial layer, a 220-nm-thick Eu-doped GaN active layer and a 10-nm-thick GaN cap layer. We fabricated both H3 cavities and 2D-heterostructures on an identical sample.

5. 2. 3 Sample fabrication process

The fabrication process of a 2D-PhC is illustrated in Fig. 5. 6. (1) After growth of a sample, A 200-350-nm-thick SiO_2 layer was first evaporated as hard mask using the electron-beam (EB) evaporation method, and approximately 300-nm-thick EB resist (ZEP520A, Zeon Corp.) was spincoated subsequently. Triangular 2D-PhC patterns were defined on the resist by EB lithography at 125 kV (ELS-G125, ELIONIX INC.), and the resist was developed. (2) The 2D-PhC patterns were transferred to the SiO_2 mask by RIE (RIE-10NOU, Samco Inc.) with CHF_3/Ar gas. Then, GaN:Eu,O and $Al_xIn_{1-x}N$ layers were etched by inductively coupled plasma RIE with Cl_2 plasma (NE-750, ULVAC, Inc.). To form hexagonal air-holes with flat $\{1\bar{1}00\}$ sidewalls, the samples were chemically etched for 1 min at 85 °C in a tetramethylammonium hydroxide (TMAH) aqueous solution with a concentration of 13 wt.%. (3) Subsequently, the $Al_{0.82}In_{0.18}N$ sacrificial layer was selectively removed in hot nitric acid (2 mol/L) for 2~7 hours at 120 °C. (4) The SiO_2 hard mask was removed in buffered HF solution.

A bird's eye view SEM image of a fabricated air-bridge structure is shown in Fig. 5. 7 (a). The $Al_xIn_{1-x}N$ sacrificial layer is successfully removed by the selective wet-etching process leaving the GaN:Eu,O membrane structure. A cross-sectional view SEM image of a fabricated PhC structure exhibits vertically etched air-holes in GaN:Eu,O membrane [Fig. 5. 7 (b)]. However, the air-holes are not etched entirely vertically, but they show a certain degree (< 5 °) of tapering. This tapering occurs due to the small radii of air-holes [37] and the thick etching depth. Future optimization of RIE dry-etching (e.g., bias power, pressure) and TMAH-etching (e.g., etching time, concentration) would improve the verticality, enabling further high Q-factors.

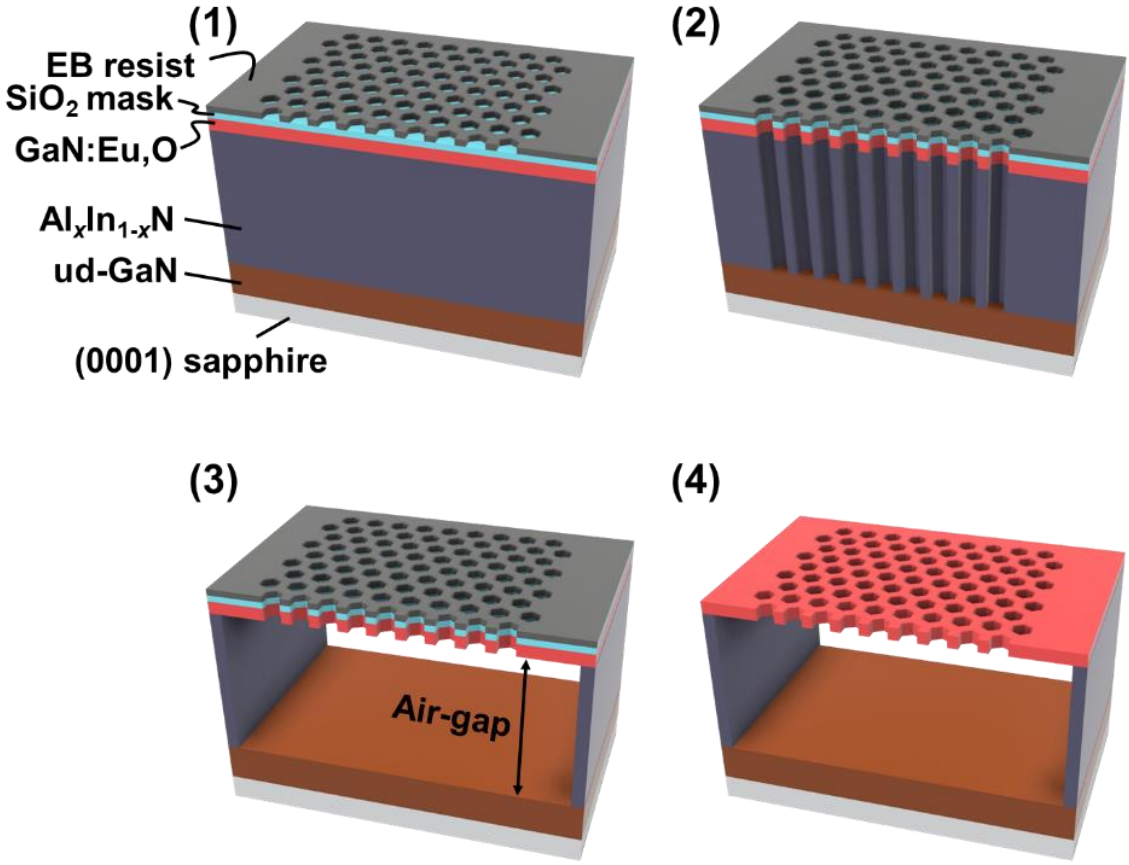

Fig. 5. 6 Fabrication process of a GaN:Eu,O-based 2D-PhC.

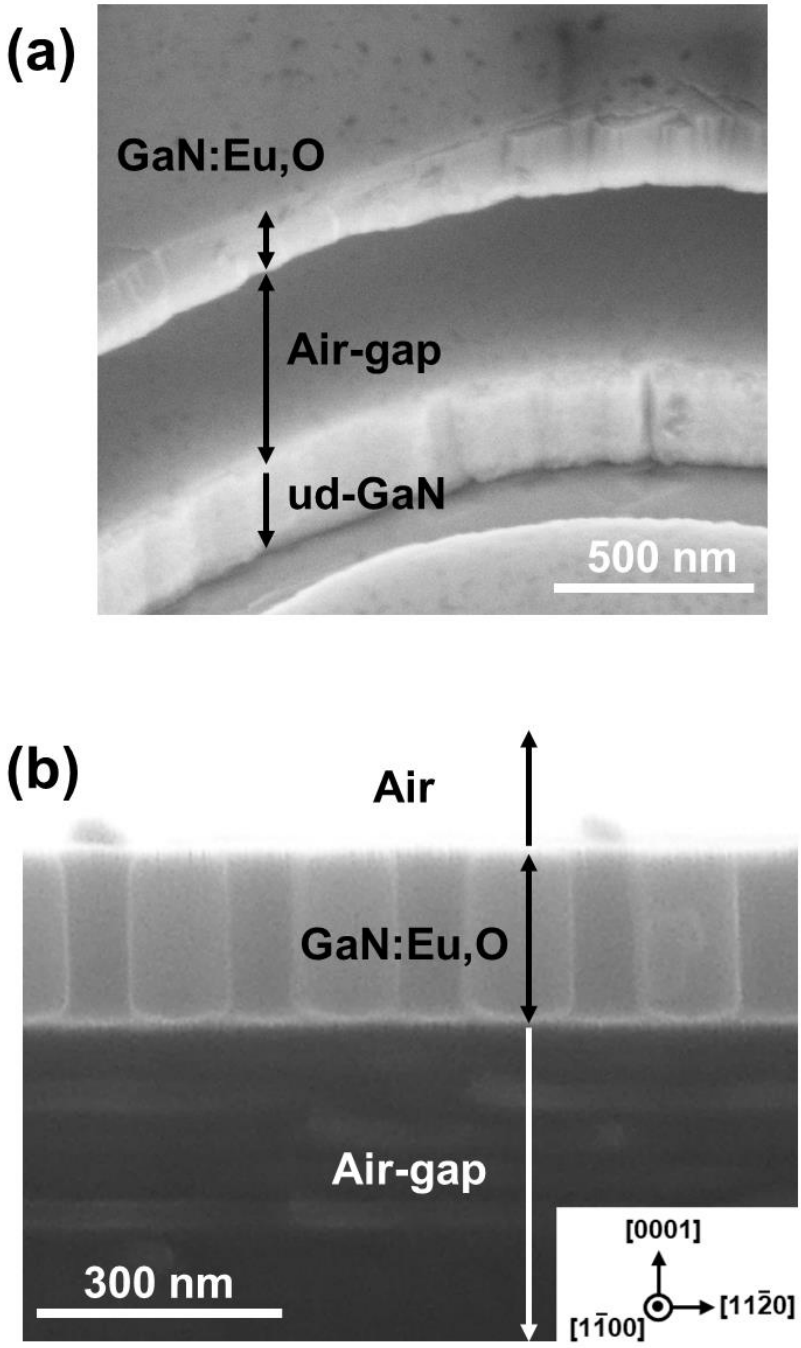

Fig. 5. 7 (a) A bird's eye view SEM image of a fabricated air-bridge structure. (b) A cross-sectional view SEM image of a fabricated 2D-PhC.

5. 2. 4 Sample characterization method

To evaluate the optical properties of 2D-PhC cavities, microscopic PL measurements were performed using the setup shown in Fig. 2. 2 (b). A continuous-wave He-Cd laser was used as excitation source. The laser was focused on the sample with a spot diameter of 1.6 μm through an objective lens (50×, NA = 0.42). The luminescence was collected by the same objective lens, dispersed by a 50-cm-spectrometer and detected by a Peltier-cooled CCD camera. The spectral resolution was about 0.02 nm.

A microscope with a spatial resolution of ~4 μm was used for spatial mapping of cavities. A He-Cd laser guided through an objective lens (40×, NA = 0.47) was used to excite samples with a spot diameter of ~3.2 μm. The luminescence was collected through the objective and was detected by a Peltier-cooled CCD camera on an 80-cm-spectrometer.

5. 3 Results and discussion (H3 cavities)

As discussed above, the experimental Q-factor (Q_{exp}) differs from Q_{id} that is purely determined by the light confinement characteristics of a non-disordered 2D-PhC cavity structure, following the formula:

$$Q_{exp}^{-1} = Q_{id}^{-1} + Q_{in}^{-1} + Q_{out}^{-1} + Q_{ba}^{-1} + Q_{sa}^{-1} + Q_{sc}^{-1}, \quad (5.1)$$

where Q_{out} corresponds to the losses due to out-of-plane (taper angle of sidewalls) structural disorder. Q_{ba} and Q_{sa} are related to bulk and surface absorption losses, respectively, and Q_{sc} denotes scattering losses due to surface roughness and threading dislocations. It is essential to identify each contribution in order to find solutions for achieving high Q-factors.

5. 3. 1 Structural characterization

Prior to the sample fabrication, we designed H3 cavity structures with the resonant wavelength tuned to match Eu^{3+} luminescence. We simultaneously modified both *r* and *a* because the resonant wavelength blue-shifts when the radius *r* is increased. The designed *r*/*a* ratio and *r* is in a linear relationship as shown in Fig. 5. 8 (a).

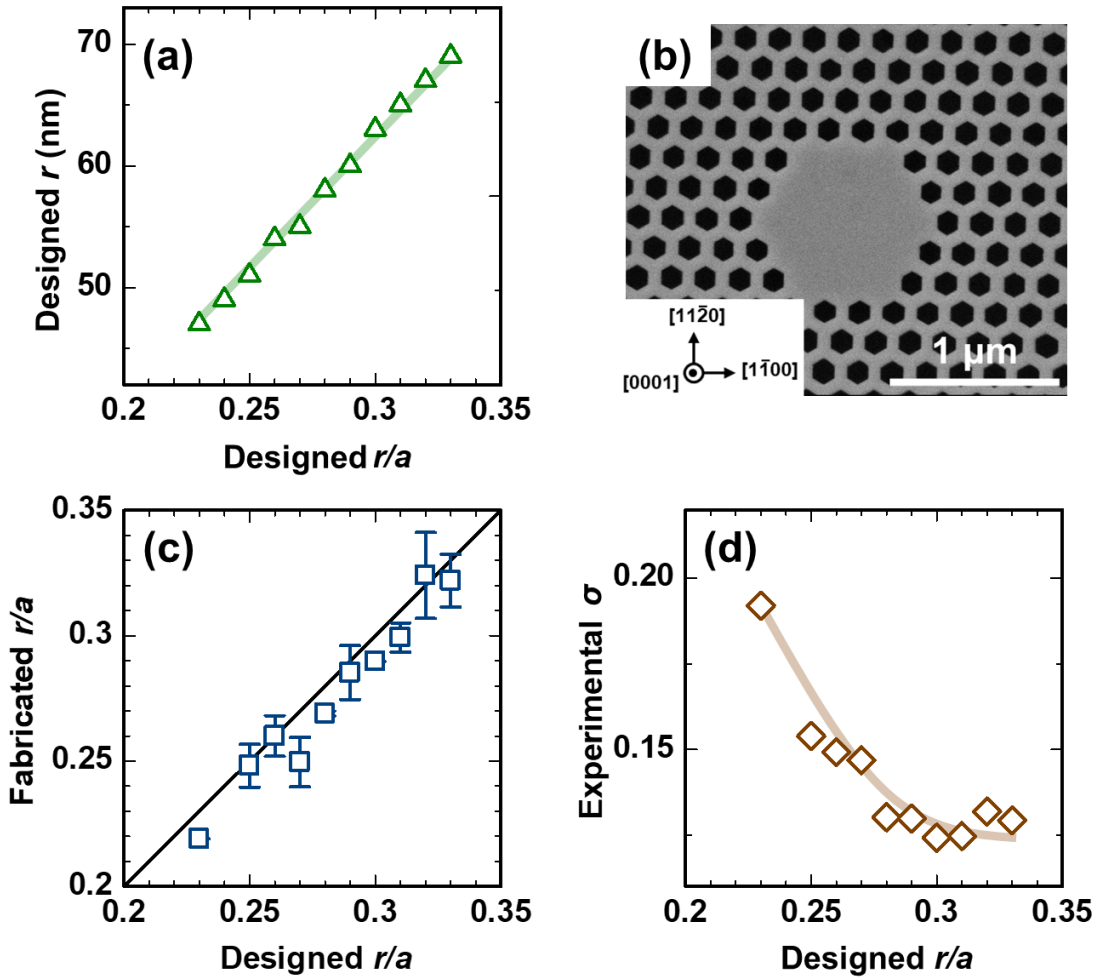

Fig. 5. 8 (a) Designed r of air-holes as a function of the designed r/a. (b) SEM image of a fabricated H3 cavity with r/a of 0.31. (c) Fabricated values of r/a and (d) experimentally introduced σ as functions of the designed r/a.

An SEM image of a fabricated H3 cavity with *a* of 209 nm, *r* of 65 nm and *r*/*a* of 0.31 is shown in Fig. 5. 8 (b). The fabricated *r*/*a* well matched with the designed *r*/*a* [Fig. 5. 8 (c)]. Although hexagonal air-holes with flat $\{1\bar{1}00\}$ sidewalls are obtained due to the TMAH-based etching process, in-plane structural disorder coming from variations in the hole radius is observed, which is known to degrade Q-factors [4,38–40]. We characterized the size-dependence of this degree of disorder for fabricated H3 cavities from SEM images. As depicted in Fig. 5. 8 (d), the degree of disorder (σ) becomes smaller for larger values of *r*/*a* because the absolute disorder value Δr is nearly constant (1.4-1.7 nm).

5. 3. 2 PL measurements

We performed PL measurements for H3 cavities with a variety of *r*/*a* to investigate the impact of the degree of disorder on the Q-factor. Due to the appropriately fabricated *r* and *a* (*r*/*a* value was varied from 0.23 to 0.33), the resonant wavelength of each H3 cavity was in the range from 618 to 629 nm and coupled with Eu^{3+} luminescence ($^5D_0 \rightarrow {}^7F_2$) [Fig. 5. 9 (a)], leading to strong enhancements of Eu^{3+} luminescence intensity. Two peaks appeared for each cavity corresponding to the fundamental mode of an H3 cavity with different optical polarization orientation. Although they are originally degenerated, they split due to in-plane-disorder [41].

The PL enhancement spectrum of an H3 cavity with *r*/*a* of 0.27 is plotted in Fig. 5. 9 (b). The resonant peaks are fitted with Lorentz curves, which are depicted with solid lines in Fig. 5. 9 (b). The resonant mode at the longer wavelength showed the highest Q-factor of 7900, which is ~1.5-times larger than the highest value of III-nitride-based 2D-PhC cavities in the visible ranges (Q ~ 5400 at ~ 624 nm [42]). This result supports our suggestion proposed in Chapter 4 that an H3 cavity is a promising structure for the realization of high Q-factors with III-nitride materials [4].

The resonant mode at the shorter wavelength showed a lower Q-factor (5200). To clarify the origin of the difference in Q-factors between the two modes, we investigated the polarization axis of each mode by PL measurement using a polarizer. The polarization-resolved PL intensity shown in Fig. 5. 9 (c) presents that each peak shows different polarization axis. Using FDTD simulations, we have confirmed that the H3 cavity fundamental mode splits into two modes polarized in the axis1 [0°, 60°, 120°, Fig. 5. 9 (d)] and axis2 [30°, 90°, 150°, Fig. 5. 9 (e)] direction of a hexagonal H3 cavity structure. Besides, the mode polarized in the axis1 typically shows a higher Q-factor in simulations, which may be due to a smaller interaction between the electric field and the

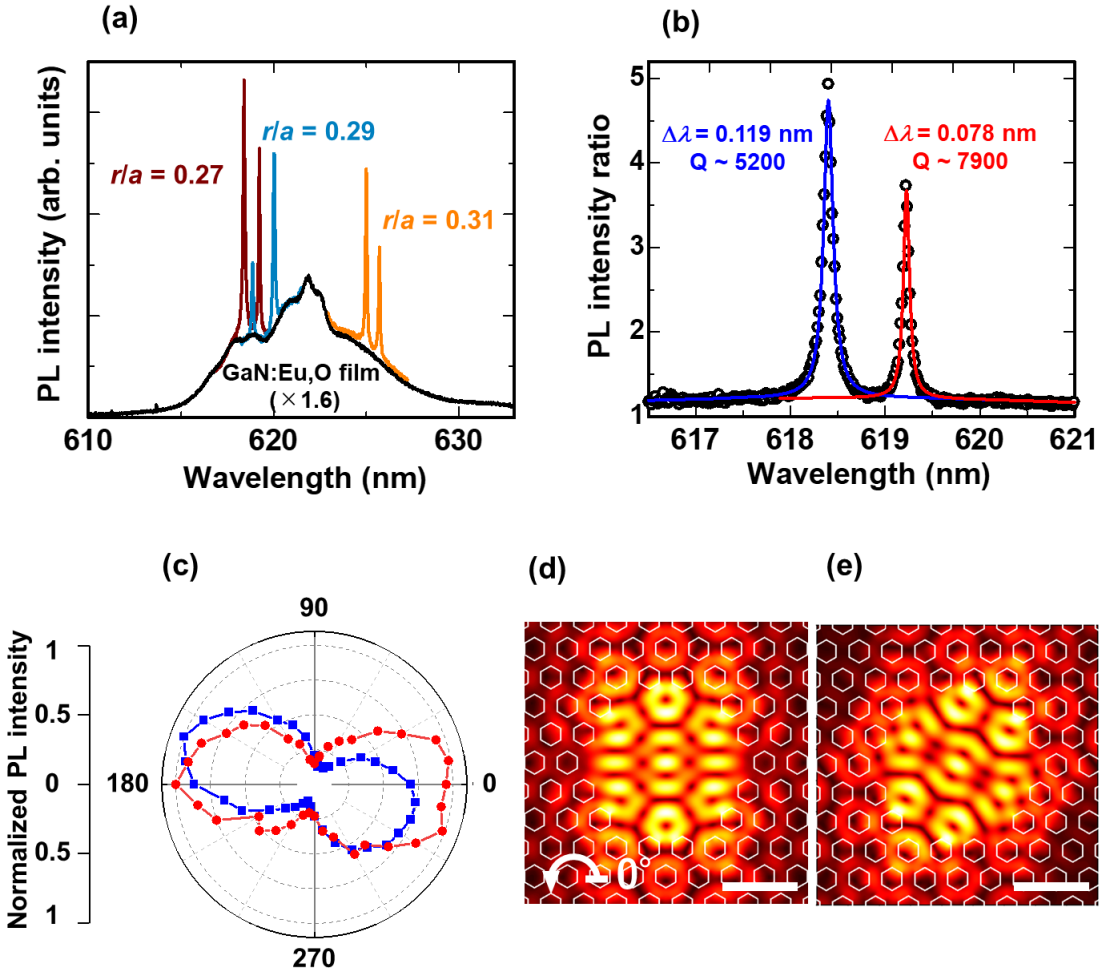

Fig. 5. 9 (a) PL spectra of H3 cavities with *r*/*a* values of 0.27, 0.29 and 0.31. The black line is a 1.6-times enlarged PL spectrum of an unpatterned GaN:Eu,O film. (b) PL intensity ratio of an H3 cavity with *r*/*a* of 0.27. The solid lines indicate the fitted Lorentzian curves of two peaks. (c) Full polarization-resolved normalized PL intensities of the resonant peaks shown in (b). Calculated electric field distribution for the fundamental modes of an H3 cavity polarized in the (d) axis1 [0 °] and (e) axis2 [150 °] of a hexagonal H3 cavity structure. The scale-bars correspond to 500 nm.

adjacent air-holes resulting in a smaller optical loss. These results suggest that the experimentally observed difference in Q-factors is due to the difference of the polarization orientation.

5. 3. 3 Dominant optical losses

Experimental Q-factors of the mode polarized in the axis1 for H3 cavities with different *r*/*a* values are depicted in Fig. 5. 10, and all cavities show a high Q_{exp} (>5800), with an average Q_{exp} of ~7000. Furthermore, we investigated the dominant optical loss limiting Q-factors of H3 cavities using the following relationship: $Q_{exp}^{-1} = Q_{id}^{-1} + Q_{in}^{-1} + Q_{other}^{-1}$ ($Q_{other}^{-1} = Q_{out}^{-1} + Q_{ba}^{-1} + Q_{sa}^{-1} + Q_{sc}^{-1}$). We calculated Q_{in} by introducing in-plane-disorder estimated from SEM images [Fig. 5. 8 (d)] into FDTD simulations, and calculated Q_{other} with above relationship.

In Fig. 5. 10, all determined Q-factors are given as a function of *r*/*a*. While Q_{id} decreases for larger *r*/*a*, Q_{exp} is almost constant over the whole range of *r*/*a*. Interestingly, Q_{other}, which represents out-of-plane disorder, scattering and absorption, slightly increases with *r*/*a*. If the scattering was the dominant contribution, it should give a nearly constant contribution with respect to *r*/*a* because it is mainly determined by surface morphology and threading dislocation density. Furthermore, the GaN:Eu,O material applied in this study shows a small bulk absorption coefficient (α ~ 3.9 cm^{-1} at 622 nm) [43]. This corresponds to an estimated Q_{ba} of ~ 6×10^4, following the relationship: $Q_{ba} = 2\pi n_{\text{eff}}/\alpha\lambda$, where n_{eff} indicates effective refractive index and is estimated as 2.31 [44]. Besides, we have confirmed that the ratio between $|E|^2$ confined in the PhC membranes and $|E|^2$ in the air-holes remains nearly constant (0.87-0.90) for values of *r*/a ranging from 0.23 to 0.33, therefore the *r*/a dependence of Q_{sa} can be safely neglected. Furthermore, we have conducted temperature dependent PL and found that the Q_{exp} is almost constant with respect to temperature, clearly suggesting that the absorption-related light loss is negligible. Thus, this trend suggests that Q_{other} is mostly determined by Q_{out} [45]. This is likely related to the fact that a smaller radius of air-holes results in a larger taper angle of sidewalls [37]. We believe that the large fluctuation in the Q_{other} is due to the un-uniformity of the taper angle of sidewalls. Especially, the taper angle of the nearest air-holes from the cavity should have the strong impact on Q-factors due to a relatively large overlap of the electric field and the sidewalls.

As a result of the high robustness of H3 cavities to in-plane disorder, the experimental Q-factor approaches the theoretical Q-factor and is the predominant limiting factor. It is thus

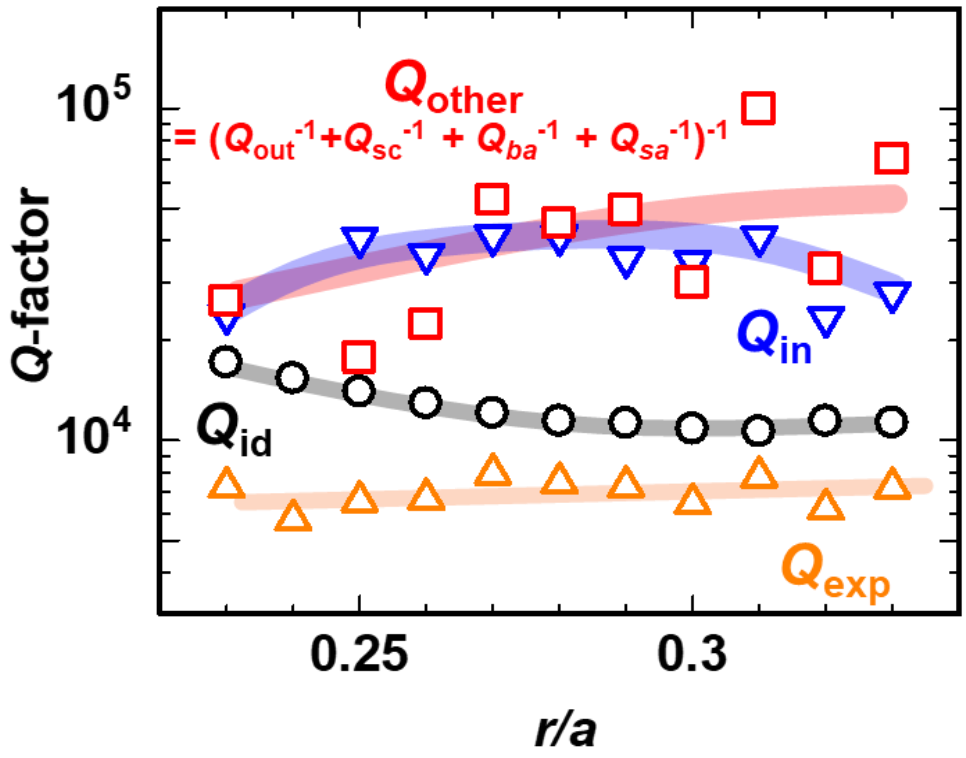

Fig. 5. 10 Q_{id}, Q_{in}, Q_{exp}, and Q_{other} as a function of r/a of H3 cavities. Q_{exp} depicts experimentally observed Q-factors. Q_{in} and Q_{id} were calculated using FDTD simulations while Q_{other} was derived from Eq. 5.1 ignoring absorption-related loss.

imminent to design cavities with larger Q_{id}, while maintaining the high Q_{in} of an H3 cavity.

5. 3. 4 Investigation on the origin of mode-splitting

To attain strong light-matter interactions, it is important to suppress the mode-splitting; otherwise, it decreases the polarization overlap between an optical mode and an emitter [46,47]. Furthermore, for laser applications, when the spectral spacing between the two split modes are shorter than the linewidth of Eu^{3+} emission, both modes can couple to Eu^{3+} and lead to an increase in the lasing threshold.

To suppress the mode-splitting and to attain strong light-matter interaction and low lasing threshold, it is important to minimize the degree of in-plane structural disorder. However, it is challenging to perfectly suppress structural disorder using present nano-fabrication techniques.

Similar mode-splitting behaviors for H*N* cavities have been reported [41,48–52]. Hennessy *et al*. demonstrated resonant wavelength tuning of H1 cavities after fabrication processes using the AFM nano-oxidation process [49]. However, in the case of III-nitride semiconductors, a large degree of disorder is randomly introduced, making it difficult to employ this technique where precise control of the orientation of resonant modes is required. Externally applied strain has been reported as effective in controlling the mode-splitting of H1 cavities [51], however, it may not be applicable for implementing devices based on 2D-PhC cavities.

Experimental and theoretical studies obtained in this research suggest that the mode-splitting of H3 cavities occurs due to the difference in the potentials between the two axes (axis1 and axis2). To compensate it, we designed H3 cavities with shifted air-holes; the twelve nearest neighboring air-holes around the centra defect (shown in red color) were shifted outwards as a schematic is illustrated in Fig. 5. 11 (a).

In order to investigate the impact of air-hole shift on the cavity mode-splitting, we conducted FDTD calculations for an H3 cavity (r/a = 0.3) with a shift value ranging from 0 to 0.15a. In-plane structural disorder with σ of 0.1 was introduced to reproduce the disorder-induced mode-splitting. As a result, all of the studied H3 cavities exhibited split fundamental modes. Calculated spectral spacing between split modes as a function of shift value of air-holes is plotted in Fig. 5. 11 (b). The spacing monotonically decreases with increasing the shift value. Although the mode-splitting is not perfectly suppressed, the shift of air-holes effectively reduces the difference in the potentials between the two axes.

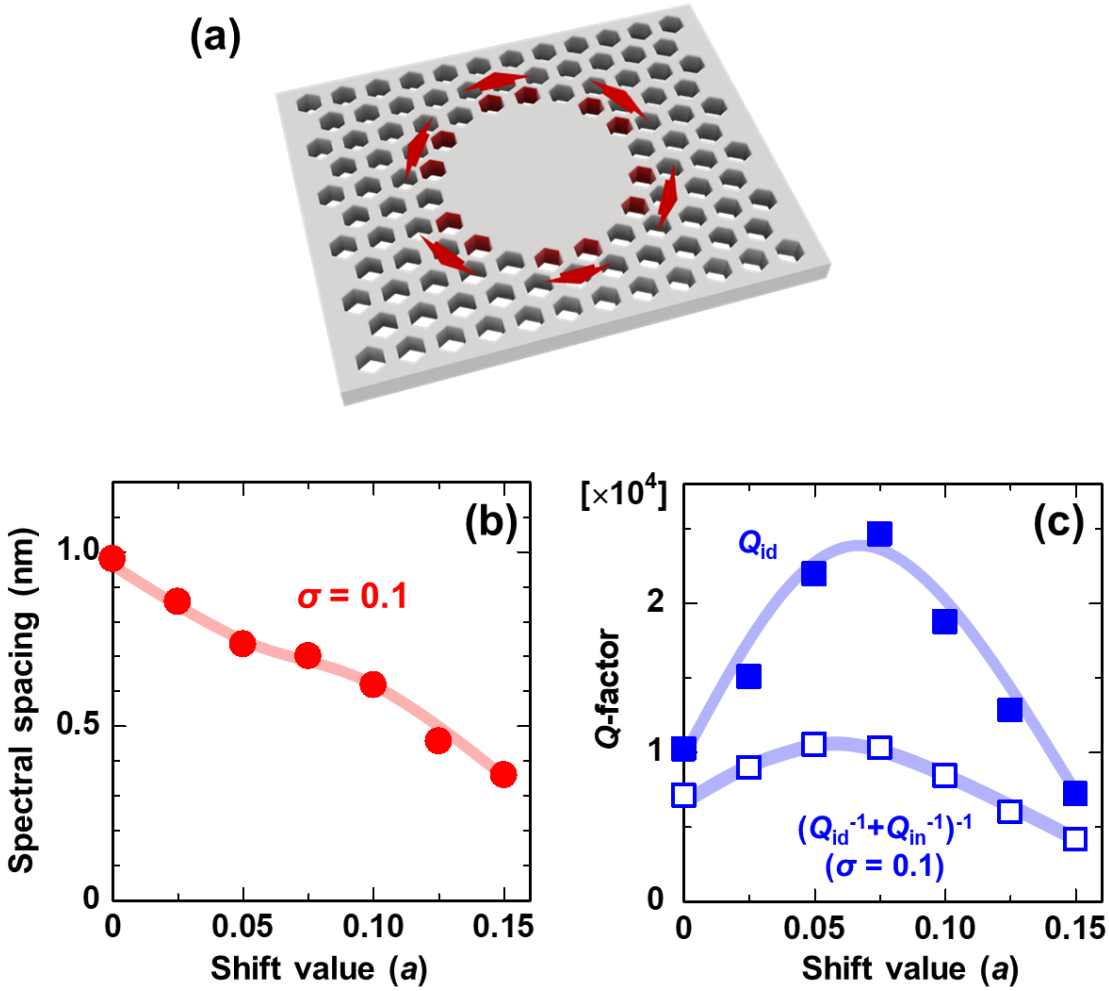

Fig. 5. 11 (a) Schematic of an H3 cavity with twelve nearest neighboring air-holes around the centra defect (shown in red color) shifted outwards. (b) Calculated spectral spacing between the split modes and (c) calculated Q-factors $[(Q_{id}^{-1} + Q_{in}^{-1})^{-1}]$ as a function of shift values of air-holes.

Calculated Q_{id} and Q-factors degraded with in-plane structural disorder $[(Q_{id}^{-1} + Q_{in}^{-1})^{-1}]$ are shown in Fig. 5. 11 (c). Q_{id} is increased with shifting air-holes, and is maximized at the shift value of $0.075a$ with a Q_{id} of 2.5×10^4, which is 2.1-fold larger than that of an H3 without air-hole shift. The Q_{id} is decreased again with further increasing the shift value.

As shown in Fig. 5. 11 (c), Q-factors strongly decrease by introducing in-plane structural disorder. However, H3 cavities with properly shifted air-holes exhibit reasonably higher Q-factors than that of an H3 without air-hole shift. These results suggest that the shift of air-holes effectively decrease the difference in the potentials between the two axes leading to a decreased spectral spacing between split modes. Moreover, it has a potential to improve Q_{id}. Further optimized cavity structural design, considering not only the shift of nearest neighboring air-holes but also shift of second or third nearest neighboring air-holes, is required to perfectly suppress mode-splitting while improving Q-factors. In addition, modulation of size (radii) of air-holes is expected to be effective.

5. 4 Results and discussion (2D-heterostructures)

5. 4. 1 Structural design

In order to achieve a high Q_{id} while simultaneously having a high robustness to in-plane disorder, we hereafter focus on 2D-heterostructures with reference to the research demonstrated by Ge *et al* [3].

To form a high-Q 2D-heterostructure, it is preferable to employ the band-edge mode at the K point of the first band (K1) because it supports a full in-plane band gap, and can be expected to have good light confinement (Fig. 5. 12). The inset in Fig. 5. 12 shows an out-of-plane-polarized magnetic field distribution at the K1 point, and the white lines indicate the outline of air-holes. The 2D-heterostructure we propose consists of ellipse shaped core, transition, and outer region, with air-hole radii of r_c, r_t, and r_o, respectively. By designing the radii as $r_c > r_t > r_o$, light in the shaded area in Fig. 5. 12 is well confined in the core region. As shown in Fig. 5. 13 (a), we defined the size of the regions by the number of air-holes in the major axis of the ellipse (N_c, N_t, and N_o), where the regions are described as; core region: $i^2 + j^2 \leq N_c^2$, transition region: $i^2 + j^2 \leq (N_c + N_t)^2$, and outer region: $i^2 + j^2 \leq (N_c + N_t + N_o)^2$. Integer i and j define the

layer number for x (major axis of the ellipse) and y (minor axis) direction, $x_{i+1} - x_i = a$ and $y_{i+1} - y_i = \sqrt{3}a/2$. We name this structure conventional heterostructure (CHS). In simulations, the CHS shows a great light confinement in the core region [Fig. 5. 13 (c)] and a high Q_{id} of 7.1×10^5 ($r_c = 0.27a$, $r_t = 0.23a$, $r_o = 0.20a$, $N_c = 14$, $N_t = 11$, $N_o = 6$), which is at least one order of magnitude larger than the reported Q_{id} for a similar 2D-heterostructure utilizing the Γ point of the first band [3], despite the number of air-holes constructing the PhC resonator is only 1/3-1/4 of that used in Ref. [3]. This high Q-factor is due to the strong light confinement at the K1 point, where the mode lies outside the light cone [53].

With the robustness to in-plane disorder in mind, we also designed another type of structure shown in Fig. 5. 13 (b), having a hexagonal defect consisting of 19 missing air-holes (identical to an H3 cavity) at the center. We expected this structure shows a better robustness because it has less air-holes in the core region that could lead to in-plane disorder. We name this structure defected heterostructure (DHS). DHS supports both the K1 band-edge mode and defect modes of an H3 cavity, such as the fundamental modes shown in Fig. 5. 9 (d) and (e). For the K1 mode, we found the electric field is well confined in the core region around the defect [Fig. 5. 13 (d)] showing a high Q_{id} of 1.1×10^5 ($r_c = 0.27a$, $r_t = 0.23a$, $r_o = 0.20a$, $N_c = 14$, $N_t = 11$, $N_o = 6$).

In the next step, we investigated the robustness to in-plane disorder for the K1 modes of CHS and DHS, and the H3 fundamental mode shown at the central of DHS by introducing in-plane disorder into simulations and changing the σ value.

In Fig. 5. 14, K1 modes in both CHS and DHS show higher Q-factors than the H3 fundamental mode even for large value of σ. Moreover, the K1 mode of DHS shows a slightly higher robustness against structural disorder than that of CHS. With a disorder of $\sigma = 0.13$, the K1 mode of DHS shows Q $[(Q_{id}^{-1} + Q_{in}^{-1})^{-1}]$ ~ 21000, which is 1.2-times larger than that of CHS (Q ~ 18000), and calculated values of Q_{in} as 25000 and 18000 for DHS and CHS, respectively. As abovementioned, a smaller number of air-holes is expected to give a higher robustness in DHS. These results suggest that the K1 mode of DHS is a promising mode in order to achieve high Q-factors using III-nitride materials.

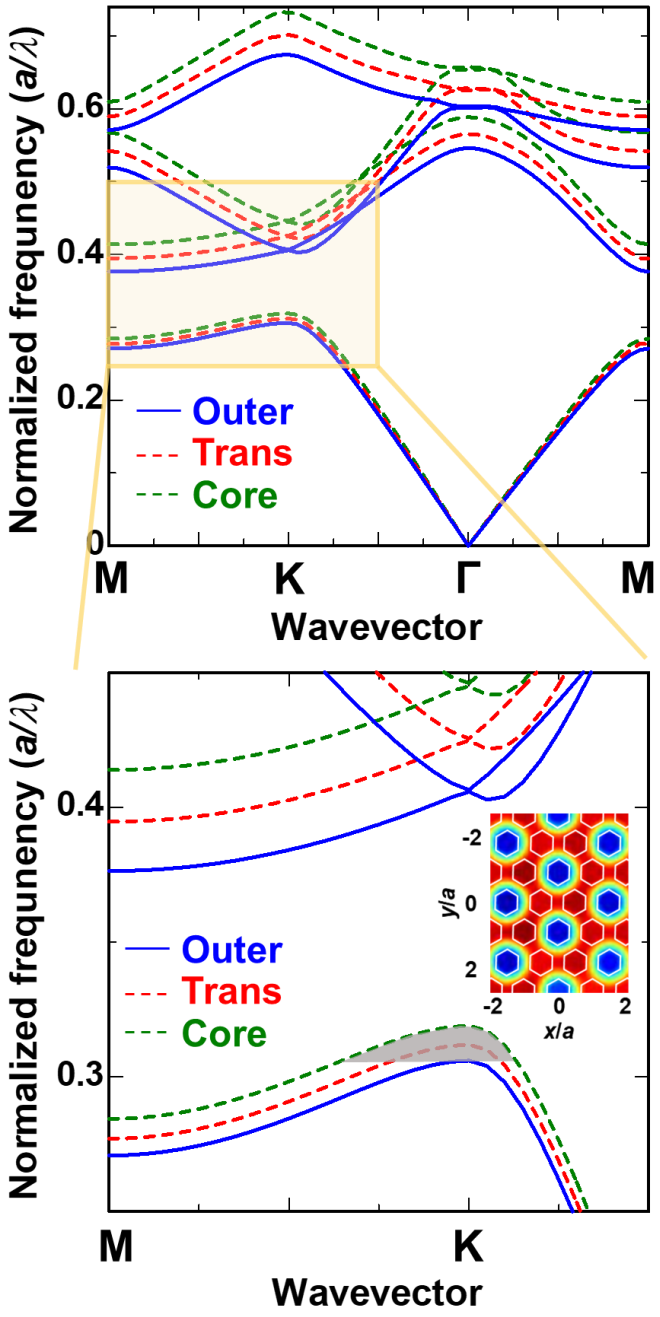

Fig. 5. 12 Calculated band diagram of a PhC in different layers (r_c = 0.38a, r_t = 0.36a, r_o = 0.34a). The bottom panel shows an enlarged diagram around the K point, and the shaded area indicates a region where the K1 mode in the core region is prohibited to couple with the same mode in the outer region. The inset shows a z-polarized magnetic field distribution at the K1 point, white lines indicate the outline of air-holes.

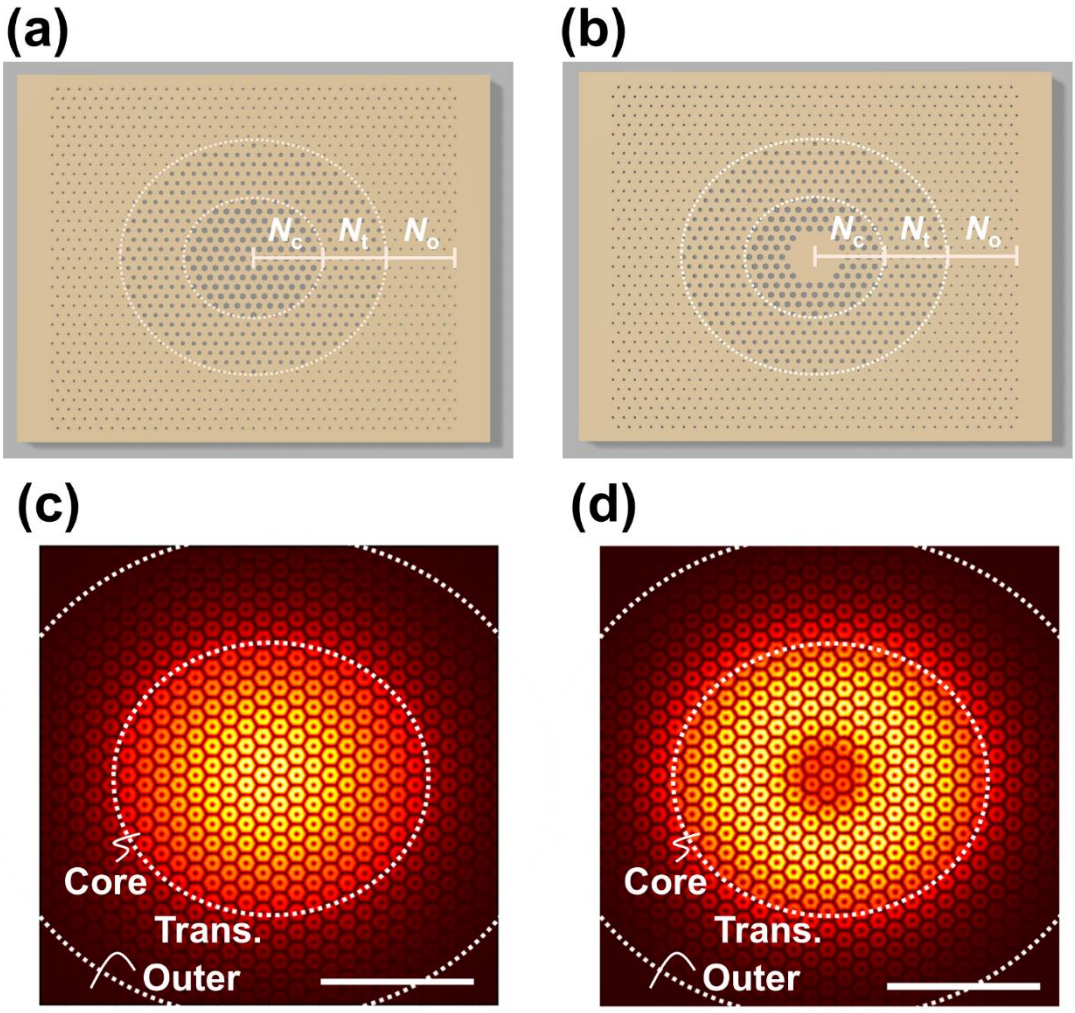

Fig. 5. 13 Schematic of a (a) CHS and (b) DHS, consisting of clad, transition, and outer layers. Calculated electric field distribution of K1 mode in (c) CHS and (d) DHS. The dot lines represent the boundaries between each range. The scale-bar corresponds to 3 μm.

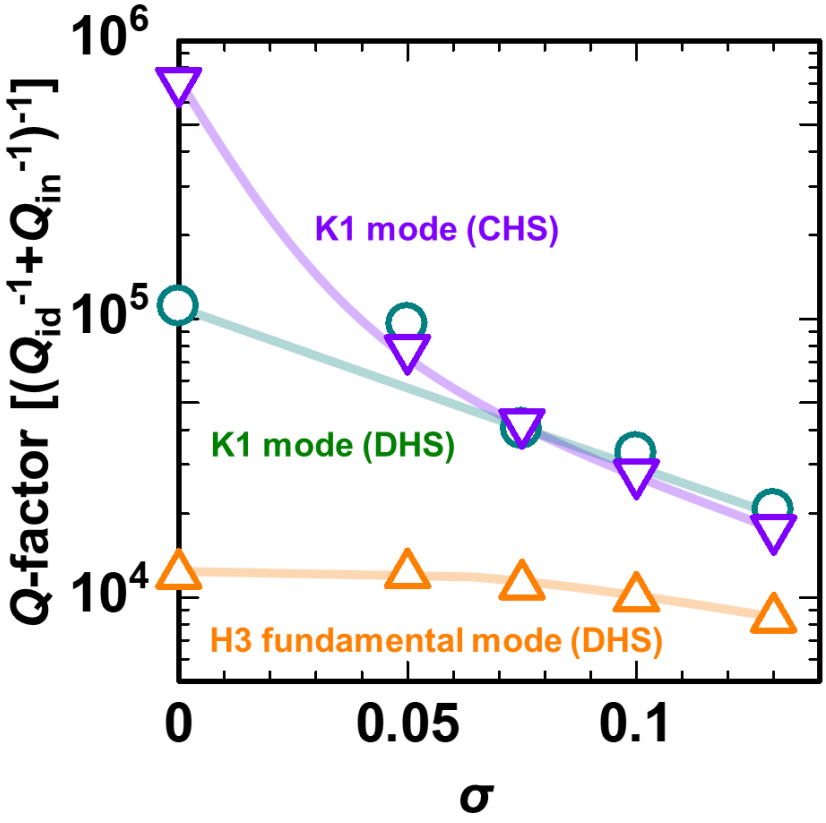

Fig. 5. 14 Calculated Q-factors $[(Q_{id}^{-1} + Q_{in}^{-1})^{-1}]$ for the K1 mode in CHS and DHS, and the fundamental mode of the H3 cavity in DHS, as a function of σ value.

5. 4. 2 Structural characterizations

Based on the simulation results, we fabricated a DHS (r_c = 0.27a, r_t = 0.23a, r_o = 0.20a, N_c = 14, N_t = 11, N_o = 6). The SEM image shown in Fig. 5. 15 reveals that air-holes have the same radii as designed, and the estimated disorder degree introduced to the core region is $\sigma \sim 0.13$.

5. 4. 3 PL measurements

Next, we conducted PL measurements for this sample at room temperature, PL spectra for DHS and GaN:Eu,O film are depicted in Fig. 5. 16 (a). The spectrum from a DHS shows many resonant peaks which originate from band-edge modes coupled to Eu^{3+} luminescence ($^5D_0 \rightarrow {}^7F_3$ transition). Because higher order band-edge modes appear at k-values somewhat away from the K point, modes appearing in the longer wavelength region correspond to higher order modes. The fundamental mode of the H3 cavity was not observed because it did not couple to Eu^{3+} luminescence.

At the shorter wavelength range (660−665 nm), four large peaks labelled as P_1^{1st}, P_2^{1st}, P_1^{2nd}, and P_2^{2nd} are clearly observed [Fig. 5. 16 (b)]. Because there are no resonant peaks for wavelengths shorter than P_1^{1st}, it can be identified as the fundamental K1 mode. In order to determine the origin of P_1^{1st}, P_2^{1st}, P_1^{2nd}, and P_2^{2nd}, we focus on the spectral spacing between each mode. Compared to the calculated spectral spacing between the fundamental and second order K1 mode (2.66 nm), the spacing between P_1^{1st} and P_2^{1st} (0.43 nm) is too small. On the contrary, the spacing between P_1^{1st} and P_1^{2nd} (2.17 nm), P_1^{1st} and P_2^{2nd} (2.64 nm) well match with the simulation result. Furthermore, the calculated spacing between the second and third order mode is 3.66 nm, which is much larger than that between P_1^{2nd} and P_2^{2nd} (0.47 nm). In addition to this, we conducted FDTD simulations taking into account the in-plane structural disorder to achieve a more profound insight of the mode assignments. The disorder in the core region was reproduced using the σ value of 0.13 which was derived from SEM observations, and for the transition and outer region, we applied σ values estimated based on the relationship between radii of fabricated air-holes and σ values that is shown in Fig. 5. 8 (d). As a result, we found that the first and second order modes exhibit mode-splitting as depicted in Fig. 5. 18 (a). The calculated spacings between P_1^{1st} and P_2^{1st} of 0.3 nm and that between P_1^{1st} and P_2^{2nd} of 2.28 nm well

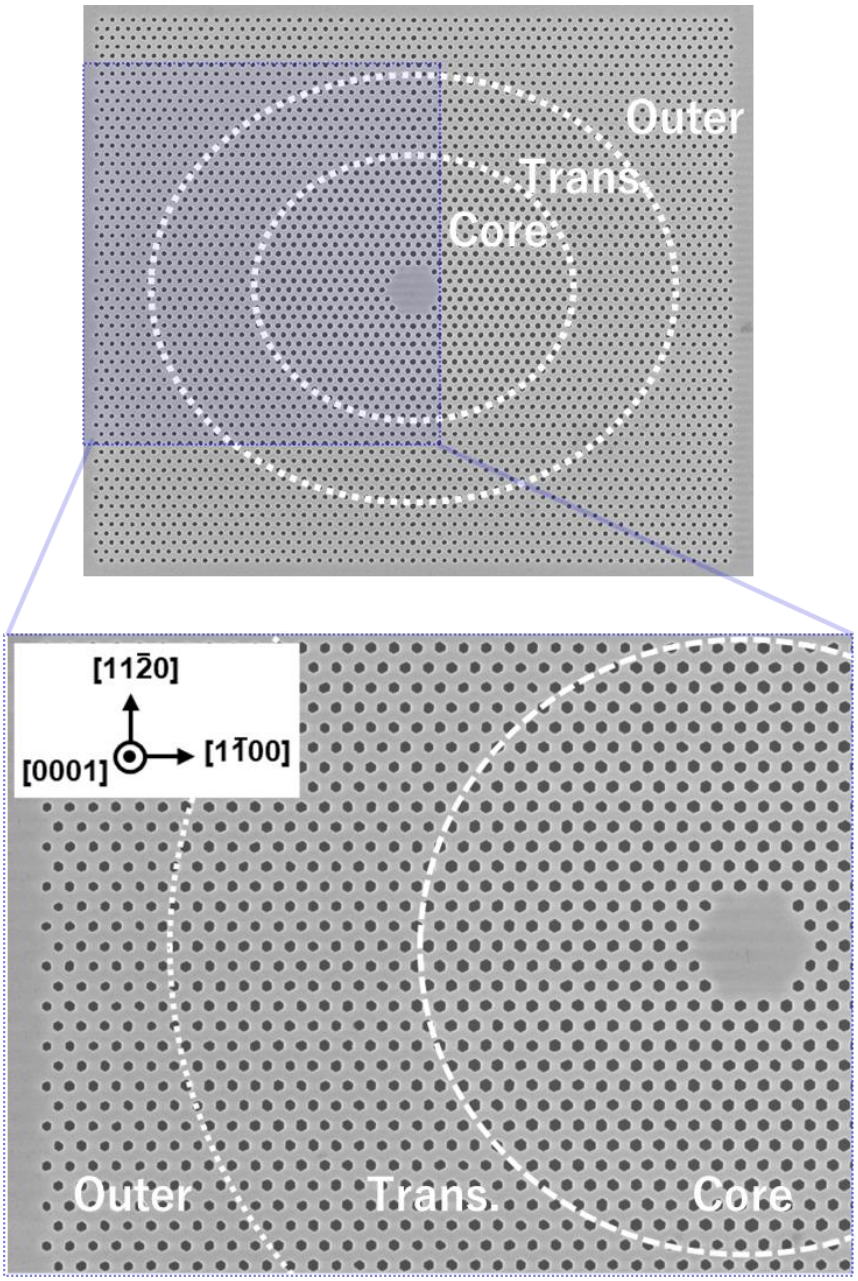

Fig. 5. 15 SEM image of a fabricated DHS (r_c = 0.27a, r_t = 0.23a, r_o = 0.20a, N_c = 14, N_t = 11, N_o = 6).

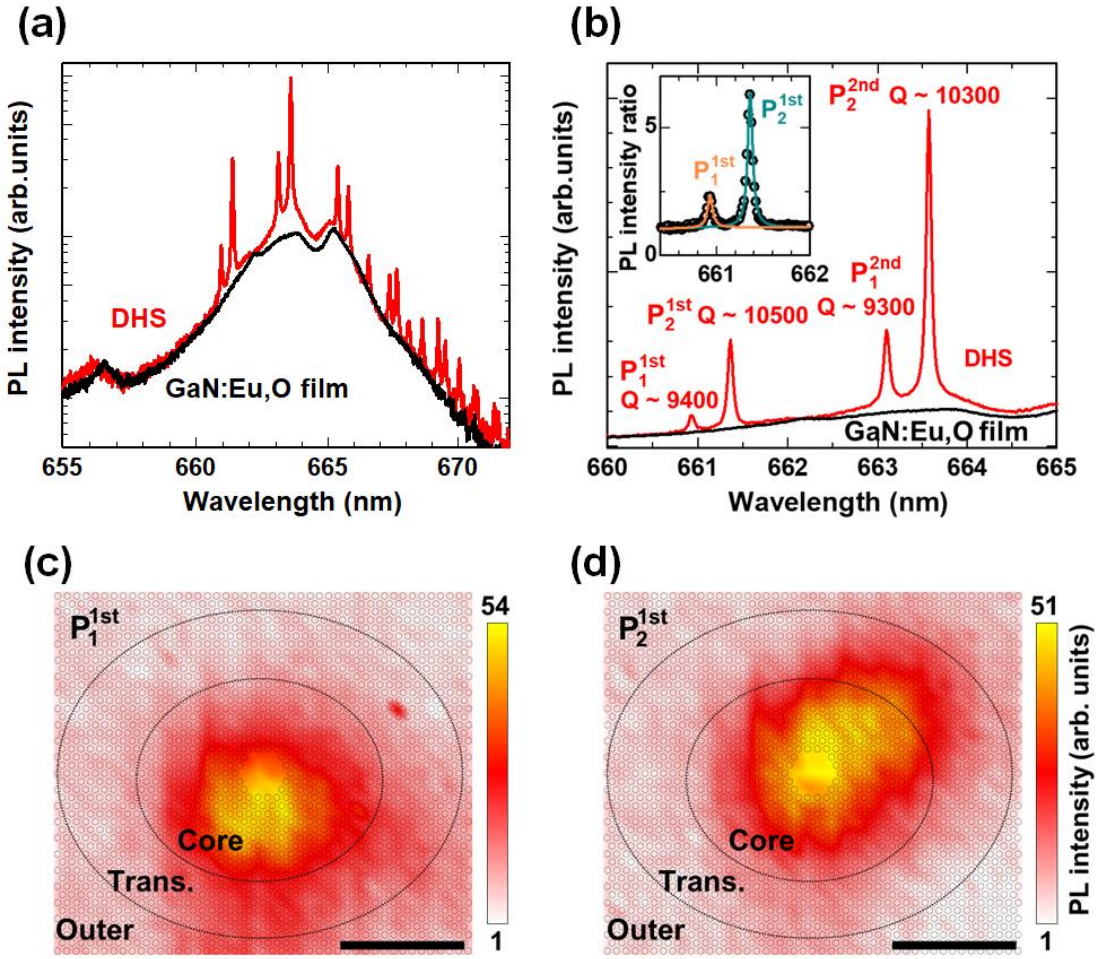

Fig. 5. 16 (a) PL spectra for a DHS and an unpatterned GaN:Eu,O film, the peaks correspond to the band-edge modes. (b) Enlarged PL spectra for a DHS and an unpatterned GaN:Eu,O film. The inset shows the PL intensity ratio, the solid lines indicate the fitted Lorentzian curves of P_1^{1st} and P_2^{1st}. Micro-PL spatial mapping of the (c) P_1^{1st} peak and (d) P_2^{1st} peak. The scale-bars correspond to 3 μm.

correspond to those of experimentally observed spacings of 0.43 nm and 2.17 nm, respectively. Thus, we conclude that P_1^{1st} and P_2^{1st} correspond to the fundamental K1 mode while P_1^{2nd} and P_2^{2nd} are the second order modes.

From micro-PL spatial mapping results for P_1^{1st} and P_2^{1st} [Fig. 5. 16 (c), (d)], it can be seen that each mode has its maximum PL intensity at a slightly different location. For this reason, we assume that these mode-splitting is caused by a field nonuniformity caused by in-plane disorder. We discuss the origin of this mode-splitting later in detail.

The determined Q-factors of each mode (P_1^{1st}-P_2^{2nd}) were 9400, 10500, 9300, and 10300, which surpass the highest Q-factor of an H3 cavity observed in this study. The inset in Fig. 5. 16 (b) ensures the accuracy of the Q-factor estimation because each peak is resolved by several pixels. From these results we confirmed that the K1 resonant mode of a DHS is a promising mode for achieving high Q-factors using III-nitride-based 2D-PhC cavities.

5. 4. 4 Dominant optical loss and a guideline towards further improvement of *Q*-factors

The value of Q_{exp} of P_2^{1st} (10500) matches well with the predicted value of 9400 from the simulations using the values of Q_{id} = 110000, Q_{in} = 21000 (σ = 0.13, Fig. 5. 14), and Q_{other} of ~20000 (r/a = 0.27, Fig. 5. 10), which suggests that Q_{exp} of the K1 mode in DHS is dominated by Q_{other} and Q_{in}. In order to improve Q_{exp} more, further improvement of taper angle and roughness of sidewalls is required to increase Q_{other}, for which we think the advancement of the wet-etching technique based on TMAH solutions plays a key role.

Further optimization of the cavity design (e.g., size of the central defect, number of layers) could lead to a further improvement of Q_{in}. Especially, N_c is reported to exhibit a significant impact on Q-factors [3], thus we calculate Q_{id} and Q_{in} as a function of N_c to establish cavity design guidelines towards further improvement of Q_{exp}.

As illustrated in Fig. 5. 17, Q_{id} (σ = 0) monotonically increases with N_c, as previously reported [16]. However, the Q-factor $\{(Q_{id}^{-1} + Q_{in}^{-1})^{-1}\}$ greatly degrades when structural disorder is introduced. Under the range of σ values of 0.12-0.19, which is experimentally introduced using our present nano-fabrication techniques [Fig. 5. 8 (d)], the Q-factor is almost constant with respect to N_c. It suggests that Q-factor is dominantly limited by Q_{in}. However, if σ can be suppressed to ~0.05, which almost corresponds to the absolute disorder value Δr of 1

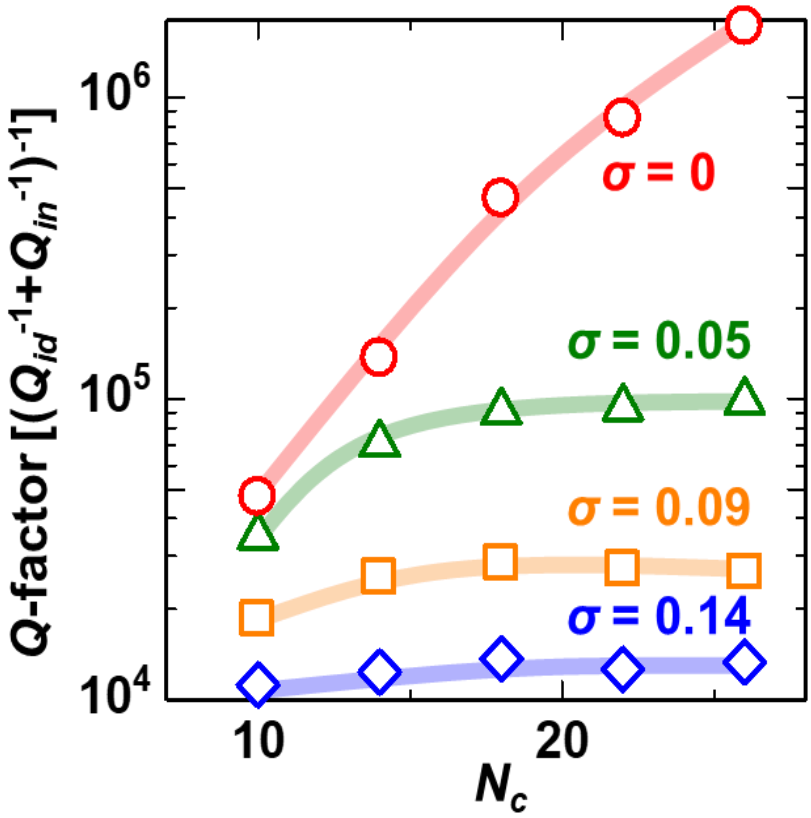

Fig. 5. 17 Calculated Q-factors $[(Q_{id}^{-1} + Q_{in}^{-1})^{-1}]$ for the K1 mode in DHS as a function of N_{core}.

nm, the Q-factor can be greatly increased with N_c. The N_c was 14 for the 2D-heterostructure which exhibited a Q-factor of 11500, therefore these results imply a minor improvement of nano-fabrication techniques is expected to further enhance Q_{exp} for III-nitride semiconductors.

We also note that by utilizing higher order band-edge modes it is possible to increase feature sizes in order to tune the resonant wavelength to the emission wavelength of a specific emitter, and improve Q_{other}, because Q_{other} depends on the *r* of air-holes.

5. 4. 5 Investigation on the origin of mode-splitting

As discussed above, it is important to suppress mode-splitting to attain strong light-matter interactions. In order to theoretically investigate the origin of mode-splitting for resonant modes of a DHS cavity, we conducted FDTD simulations taking into account the structural disorder using experimentally observed σ values. The calculated luminescence spectrum is illustrated in Fig. 5. 18 (a). The first and second order mode each split into two peaks, that well reproduces the experimental result including spacings between each mode as mentioned above. Calculated electric field distribution of the first order modes (P_1^{1st} and P_2^{1st}) are shown in Fig. 5. 18 (b), (c). The electric field is well confined in the core region, however, the nonuniform distribution indicates the presence of in-plane structural disorder induces Anderson localization. This result supports the experimental observation in the PL mapping, where the P_1^{1st} and P_2^{1st} exhibited their maximum intensities at distinct locations [Fig. 5. 16 (c), (d)].

Enlarged electric field distribution of the P_1^{1st} and P_2^{1st} modes are shown in Fig. 5. 19 (a) and (b), respectively. They reveal that each mode has similar circular distributions with electric field antinodes covering the area between a center air-hole and its six nearest neighboring air-holes. However, for each mode, the central air-holes within the circular electromagnetic field distribution were different. To gain a deeper understanding into the distinction between the two modes, we focused on the electric field directions of each mode as shown in Fig. 5. 19 (c), (d). It is clear that each mode is circularly polarized, but has opposite polarization direction; the P_1^{1st} is right-hand (RH) and the P_2^{1st} is left-hand (LH) circularly polarized. It is known that Bloch modes such as K1 mode are constructed by the combination of RH and LH modes, and they are originally degenerated at the same frequency [54,55]. These results confirm that the mode-splitting is a result of the lifted degeneracy caused by in-plane structural disorder.

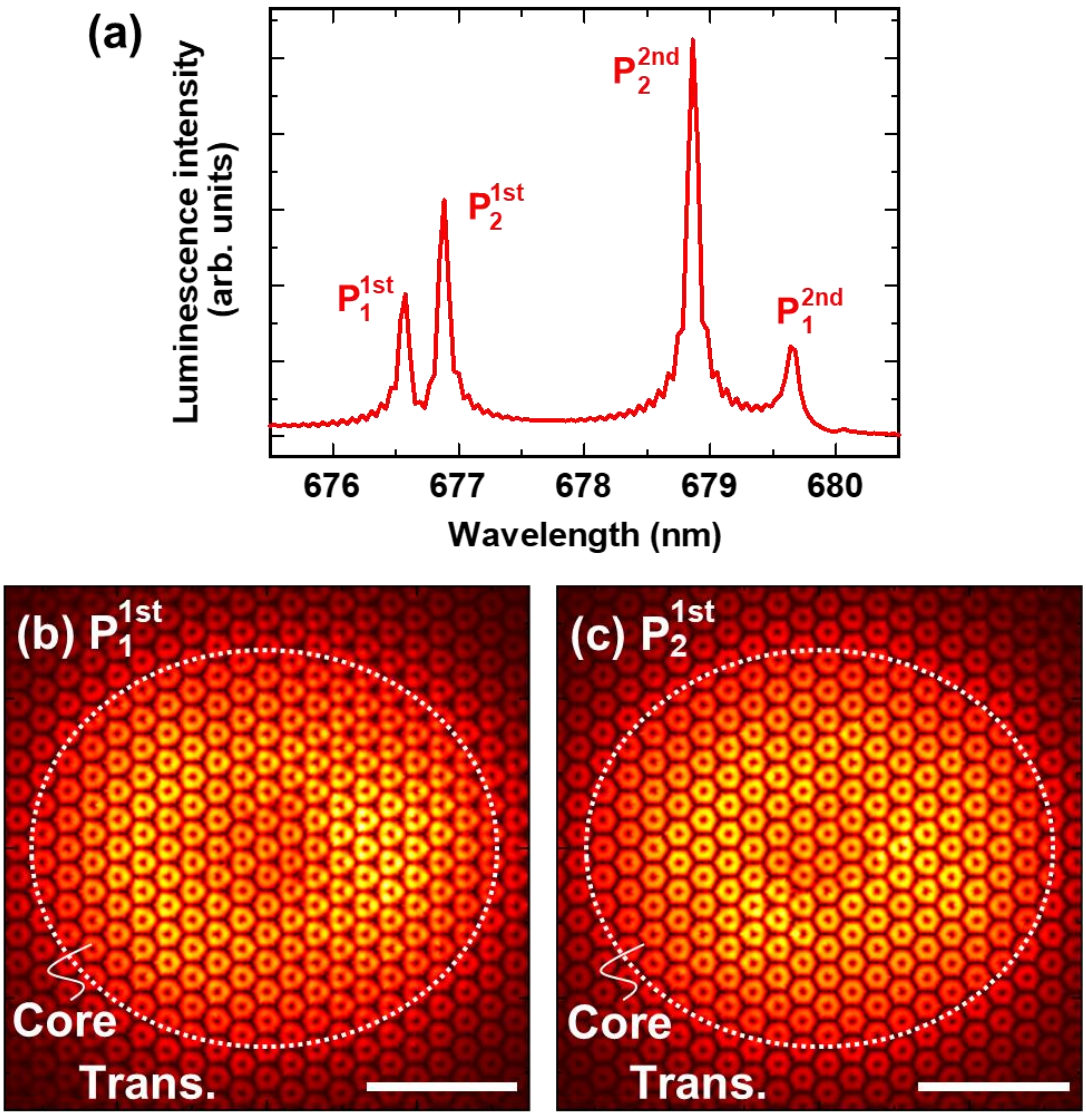

Fig. 5. 18 (a) Calculated luminescence spectrum of a DHS with in-plane structural disorder (r_c = 0.27a, r_t = 0.23a, r_o = 0.20a, N_c = 14, N_t = 11, N_o = 6). Calculated electric field distributions of (b) P_1^{1st} and (c) P_2^{1st} mode. The dot lines represent the boundaries between each range. The scale-bars correspond to 2 μm.

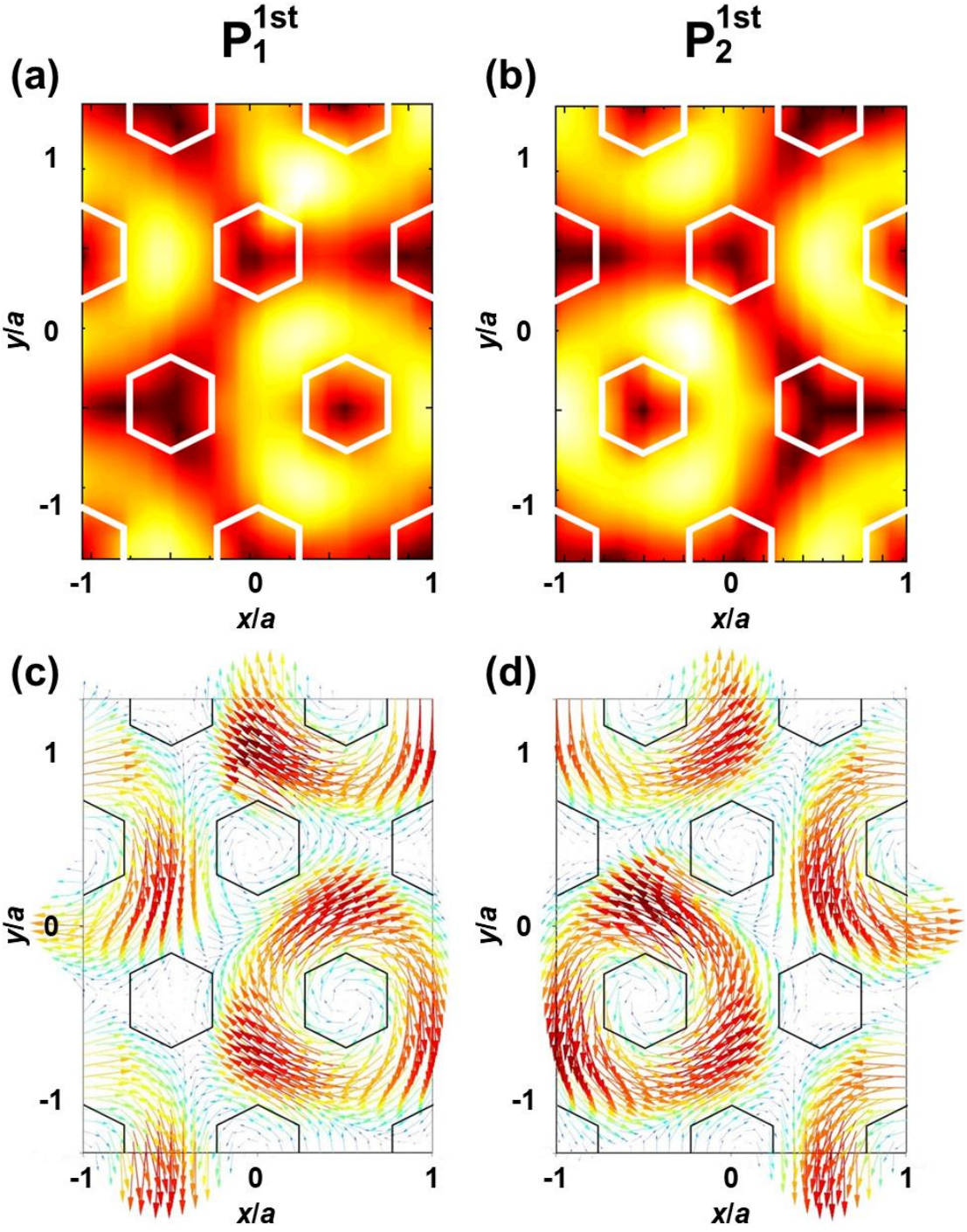

Fig. 5. 19 Enlarged electric field distribution of (a) P_1^{1st} and (b) P_2^{1st} mode in a DHS with structural disorder. Electric field directions of (c) P_1^{1st} and (d) P_2^{1st} modes.

To prevent the mode-splitting, the above-discussed AFM nano-oxidation processes [49] would be time consuming because of the relatively large cavity area of DHS. Besides, engineering of strain cannot solve the issue because of the complexity of the cause of mode-splitting. An alternative approach to prevent the rise in lasing threshold is to intentionally lift the mode degeneracy by introducing perturbation and increase the spectral spacing between two split modes large enough that only one of the modes couples to Eu^{3+} emission. A possible solution to intentionally lift the degeneracy is to employ PhC structures with low symmetricity.

5. 5 Summary

We have systematically analyzed the influence of various sources of optical losses in 2D photonic crystal nanocavities based on GaN in the red wavelength regime by a combination of FDTD simulations and experimental results. We found that for an H3-type cavity, which shows a good robustness against in-plane disorder, there is an influence of the hole radius due to limitations in the fabrication accuracy, however, the most important limitation for realizing even higher values of the Q-factor is the theoretical value of the design itself. Our best performing cavity reached a value Q = 7900, where the theoretical maximum is 12000. With this knowledge we designed 2D-heterostructure type of cavity, which is based on a band-edge mode with high theoretical Q-factor and a relatively high robustness to in-plane disorder. Using the cavity design, we realized a much higher experimental Q-factor of 10500, demonstrating the potential of this type of cavity.

The Q-factor of 10500 is the highest Q-factor in UV-visible range among the previously reported III-nitride-based micro-nanocavities including microdisk and 1D-nanobeam cavities to the best of our knowledge. Besides, the great design flexibility of the 2D-heterostructures makes them good candidates for applications for which high Q-factors are essential. Lasing in GaN:Eu,O was not observed in this study because the Q-factors were still low as compared to the required values for lasing (1.7×10^4–3.6×10^4). Future optimization of cavity design and improvement of nano-fabrication processes are expected to further enhance experimental Q-factors.

For applications where light-matter interactions are required, an H3 cavity is a more promising structure when compared to the 2D-heterostructures, because it possesses a large Q/V ratio. A further advancement of the structure design, for example in the shift and size modulation of air-holes, could improve the Q-factor more and open up a larger application potential.

These results show the potential for application of GaN:Eu,O-based light emitting devices, as well as 2D-PhC cavities based on other III-nitride materials in the visible regime, including low-threshold $In_xGa_{1-x}N$/GaN-QW-based lasers and wavelength conversion devices.

References

[1] B.S. Song, S. Noda, T. Asano, and Y. Akahane, *Nat. Mater.* **4**, 207 (2005).

[2] H. Hagino, Y. Takahashi, Y. Tanaka, T. Asano, and S. Noda, *Phys. Rev. B* **79**, 085112 (2009).

[3] X. Ge, M. Minkov, S. Fan, X. Li, and W. Zhou, *Appl. Phys. Lett.* **112**, 141105 (2018).

[4] T. Iwaya, S. Ichikawa, M. Murakami, D. Timmerman, J. Tatebayashi, and Y. Fujiwara, *Appl. Phys. Express* **14**, 122002 (2021).

[5] Y.S. Choi, K. Hennessy, R. Sharma, E. Haberer, Y. Gao, S.P. Denbaars, S. Nakamura, E.L. Hu, and C. Meier, *Appl. Phys. Lett.* **87**, 243101 (2005).

[6] C. Meier, K. Hennessy, E.D. Haberer, R. Sharma, Y.S. Choi, K. McGroddy, S. Keller, S.P. DenBaars, S. Nakamura, and E.L. Hu, *Appl. Phys. Lett.* **88**, 031111 (2006).

[7] T. Tajiri, M. Yoshida, S. Sosumi, K. Shimoyoshi, and K. Uchida, *Jpn. J. Appl. Phys.* **62**, SG1019 (2023).

[8] M. Arita, S. Ishida, S. Kako, S. Iwamoto, and Y. Arakawa, *Appl. Phys. Lett.* **91**, 051106 (2007).

[9] S. Sergent, M. Arita, S. Kako, K. Tanabe, S. Iwamoto, and Y. Arakawa, *Appl. Phys. Lett.* **101**, 101106 (2012).

[10] S. Sergent, M. Arita, S. Iwamoto, Y. Arakawa, S. Kako, S. Iwamoto, and Y. Arakawa, *Appl. Phys. Lett.* **100**, 121103 (2012).

[11] S. Sergent, M. Arita, S. Iwamoto, and Y. Arakawa, *Appl. Phys. Lett.* **100**, 121103 (2012).

[12] I. Rousseau, I. Sánchez-Arribas, K. Shojiki, J.F. Carlin, R. Butté, and N. Grandjean, *Phys. Rev. B* **95**, 125313 (2017).

[13] H.M. Ng, N.G. Weimann, and A. Chowdhury, *J. Appl. Phys.* **94**, 650–653 (2003).

[14] N. Vico Triviño, G. Rossbach, U. Dharanipathy, J. Levrat, A. Castiglia, J.F. Carlin, K.A. Atlasov, R. Butté, R. Houdré, and N. Grandjean, *Appl. Phys. Lett.* **100**, 071103 (2012).

[15] S. Blumenthal, M. Bürger, A. Hildebrandt, J. Förstner, N. Weber, C. Meier, D. Reuter, and D.J. As, *Physica Status Solidi C* **13**, 292–296 (2016).

[16] T.J. Puchtler, A. Woolf, T. Zhu, D. Gachet, E.L. Hu, and R.A. Oliver, *ACS Photonics*, **2**, 137 (2015).

[17] C. Xiong, P.R. Edwards, G. Christmann, E. Gu, M.D. Dawson, J.J. Baumberg, R.W. Martin, and I.M. Watson, *Semicond. Sci. Technol.* **25**, 032001 (2010).

[18] K. Lorenz, R. Gago, N. Franco, A. Redondo-Cubero, K. Lorenz, R. Gago, N. Franco, M.A. Di Forte Poisson, E. Alves, and E. Muñoz, *J. Phys. D Appl. Phys.* **43**, (2010).

[19] S. Zhang, B. Liu, J.Y. Yin, H.H. Sun, Z.H. Feng, and L.C. Zhao, *J. Phys. D Appl. Phys.* **44**, 075405 (2011).

[20] Q.Y. Wei, T. Li, Y. Huang, J.Y. Huang, Z.T. Chen, T. Egawa, and F.A. Ponce, *Appl. Phys. Lett.* **100**, 092101 (2012).

[21] G. Perillat-Merceroz, G. Cosendey, J.F. Carlin, R. Butté, and N. Grandjean, *J. Appl. Phys.* **113**, 063506 (2013).

[22] M. Miyoshi, M. Yamanaka, T. Egawa, and T. Takeuchi, *Appl. Phys. Express* **11**, 051001 (2018).

[23] M. Miyoshi, M. Yamanaka, T. Egawa, and T. Takeuchi, *J. Cryst. Growth* **506**, 40–44 (2019).

[24] Z.T. Chen, K. Fujita, J. Ichikawa, and T. Egawa, *J. Appl. Phys.* **111**, 053535 (2012).

[25] J.F. Carlin, C. Zellweger, J. Dorsaz, S. Nicolay, G. Christmann, E. Feltin, R. Butté, and N. Grandjean, *Phys Status Solidi B Basic Res.* **242**, 2326–2344 (2005).

[26] T.S. Oh, J.O. Kim, H. Jeong, Y.S. Lee, S. Nagarajan, K.Y. Lim, C.H. Hong, and E.K. Suh, J. Phys. D Appl. Phys. **41**, 095402 (2008).

[27] C.B. Alcock, V.P. Itkin, and M.K. Horrigan, *Can. Metall. Q.* **23**, 309–313 (1984).

[28] E.R. Buß, U. Rossow, H. Bremers, and A. Hangleiter, *Appl. Phys. Lett.* **104**, 162104 (2014).

[29] Y. Sakai, P.C. Khai, J. Ichikawa, T. Egawa, and T. Jimbo, *J. Appl. Phys.* **109**, 033512 (2011).

[30] J. Ichikawa, Y. Sakai, Z. Chen, K. Fujita, and T. Egawa, *Jpn. J. Appl. Phys.* **51**, 01AF07 (2012).

[31] E. Ahmadi, H. Chalabi, S.W. Kaun, R. Shivaraman, J.S. Speck, and U.K. Mishra, *J. Appl. Phys.* **116**, (2014).

[32] K. Hiramatsu, Y. Kawaguchi, M. Shimizu, N. Sawaki, Zheleva. T, R.F. Davis, H. Tsuda, W. Taki, N. Kuwano, and K. Oki, *MRS Internet J. Nitride Semicond. Res.* **2**, 11 (1997).

[33] M. Hao, H. Ishikawa, T. Egawa, C.L. Shao, and T. Jimbo, *Appl. Phys. Lett.* **82**, 4702–4704 (2003).

[34] S. Pereira, M.R. Correia, E. Pereira, K.P. O'Donnell, C. Trager-Cowan, F. Sweeney, and E. Alves, *Phys. Rev. B* **64**, 205311 (2001).

[35] H.Y. Lin, Y.F. Chen, T.Y. Lin, C.F. Shih, K.S. Liu, and N.C. Chen, *J. Cryst. Growth* **290**, 225–228 (2006).

[36] B. Liu, R. Zhang, J.G. Zheng, X.L. Ji, D.Y. Fu, Z.L. Xie, D.J. Chen, P. Chen, R.L. Jiang, and Y.D. Zheng, *Appl. Phys. Lett.* **98**, 2009–2012 (2011).

[37] K. Srinivasan, P.E. Barclay, and O. Painter, *Opt. Express* **12**, 1458 (2004).

[38] J.P.P. Vasco and S. Hughes, *ACS Photonics* **5**, 1262 (2018).

[39] S. Mookherjea, J.S. Park, S.H. Yang, and P.R. Bandaru, *Nat. Photonics* **2**, 90 (2008).

[40] S. Hughes, L. Ramunno, J.F. Young, and J.E. Sipe, *Phys. Rev. Lett.* **94**, 033903 (2005).

[41] A. Surrente, M. Felici, P. Gallo, B. Dwir, A. Rudra, G. Biasiol, and E. Kapon, *Appl. Phys. Lett.* **107**, 031106 (2015).

[42] S. Ichikawa, Y. Sasaki, T. Iwaya, M. Murakami, M. Ashida, D. Timmerman, J. Tatebayashi, and Y. Fujiwara, *Phys. Rev. Appl.* **15**, 034086 (2021).

[43] A. Takeo, S. Ichikawa, S. Maeda, D. Timmerman, J. Tatebayashi, and Y. Fujiwara, *Jpn. J. Appl. Phys.* **60**, 120905 (2021).

[44] R.E. Slusher, A.F.J. Levi, U. Mohideen, S.L. McCall, S.J. Pearton, and R.A. Logan, *Appl. Phys. Lett.* **63**, 1310–1312 (1993).

[45] Y. Tanaka, T. Asano, Y. Akahane, B.S. Song, and S. Noda, *Appl. Phys. Lett.* **82**, 1661–1663 (2003).

[46] A. Meldrum, P. Bianucci, and F. Marsiglio, *Opt. Express* **18**, 10230 (2010).

[47] D. Timmerman, Y. Matsude, Y. Sasaki, S. Ichikawa, J. Tatebayashi, and Y. Fujiwara, *Phys. Rev. Appl.* **14**, 064059 (2020).

[48] O. Painter and K. Srinivasan, *Opt. Lett.* **27**, 339 (2002).

[49] K. Hennessy, C. Högerle, E. Hu, A. Badolato, and A. Imamoğlu, *Appl. Phys. Lett.* **89**, 041118 (2006).

[50] M. Shirane, S. Kono, J. Ushida, S. Ohkouchi, N. Ikeda, Y. Sugimoto, and A. Tomita, *J. Appl. Phys.* **101**, 073107 (2007).

[51] I.J. Luxmoore, E.D. Ahmadi, B.J. Luxmoore, N.A. Wasley, A.I. Tartakovskii, M. Hugues, M.S. Skolnick, and A.M. Fox, *Appl. Phys. Lett.* **100**, 121116 (2012).

[52] T. Iwaya, S. Ichikawa, D. Timmerman, J. Tatebayashi, and Y. Fujiwara, *Opt. Express* **30**, 28853–28864 (2022).

[53] M. Minkov, D. Gerace, and S. Fan, *Optica* **6**, 1039 (2019).

[54] I. Moreno, J.A. Davis, I. Ruiz, and D.M. Cottrell, *Opt. Express* **18**, 7173 (2010).

[55] K. Chang, L. Fang, C. Zhao, J. Zhao, and X. Gan, *Opt. Express* **25**, 21594 (2017).

Chapter 6. Conclusions and future works

6. 1 Conclusions

In this thesis, we have investigated the *intrinsic* and *extrinsic* control of Eu^{3+} emission in GaN:Eu,O for wide applications including highly efficient LEDs, LDs and quantum information technologies.

For the *intrinsic* control of Eu^{3+} emission, we particularly focused on post-growth thermal annealing process to selectively form efficient luminescent sites with high excitation efficiencies. Selective formation of such sites is essential for even brighter and efficient GaN:Eu,O-based light emitting devices.

For the *extrinsic* control of Eu^{3+} emission, we mainly focused on 2D-PhC cavities, and presented studies to improve *Q*-factors considering experimentally introduced structural disorder. High-*Q* nanocavities would pave the way for wider potential applications such as LDs and quantum light sources.

In Chapter 2, we studied the impact of post-growth thermal annealing on the optical properties of GaN:Eu,O. The conventional growth temperature of GaN:Eu,O is relatively low (960°C) as compared to typical growth conditions for undoped GaN. This is because high temperature growth (> ~1000°C) results in a rough surface and limited Eu incorporation, as large amounts of Eu precipitates out as EuN. However, such a low temperature growth preferentially creates Eu clusters (OMVPE1 and OMVPE2) with low excitation efficiencies because of the limited diffusion length of Eu during growth. To dissociate such Eu clusters, we performed post-growth thermal annealing at high temperature.

As results, Thermal annealing at higher temperatures (≥ 1000°C) effectively drove the reconfiguration of luminescent sites. Using the CEES technique, we confirmed that the number of OMVPE1 and OMVPE2 remarkably decreased, while the number of sites with higher excitation efficiencies (OMVPE7, OMVPE8 and OMVPE-X) increased after annealing. Particularly, OMVPE-X, which exhibited an especially high excitation efficiency, was remarkably increased by

a factor of ~20 after annealing at 1100 °C. Because the OMVPE7, OMVPE8 and OMVPE-X centers can be excited efficiently, the sample annealed at 1100 °C exhibited up to a 5.1-times improved luminescence efficiency as compared to the as-grown sample. These results demonstrate the potential of improving the efficiency of GaN:Eu,O-based emitting devices using thermal annealing technique.

In Chapter 3, we intensely studied on the optical properties of a luminescent site (OMVPE-X) with an emission peak at ~2.004 eV which shows a strong emission under low excitation power region. This peak has been tentatively assigned as OMVPE8 so far because it is excited at the similar resonant excitation energy of OMVPE8. Based on the reported fact that OMVPE8 can be excited at the resonant excitation energies of OMVPE7 at an elevated temperature, we performed CEES measurements. As a result, OMVPE-X was not excited at the resonant energy of OMVPE7, suggesting that OMVPE-X is a different luminescent site from OMVPE-8. To gain further assurance of this suggestion, TR-PL measurements were conducted at 180 K. As it has been reported, we observed afterglow behavior of OMVPE8, where the PL intensity increases after an excitation laser pulse. Contrary to OMVPE8, emission from OMVPE-X monotonically decreased after the laser pulse with a single-exponential function. These results confirm that OMVPE-X is not a part of OMVPE8.

Then, we conducted temperature and excitation power dependent PL in order to investigate the detailed optical properties of OMVPE-X. OMVPE-X exhibited an increase in the PL intensity with the rise in temperature (< ~150 K), indicating that the local atomic structure of OMVPE-X stabilizes at elevated temperatures. Due to its thermally activated property, the thermal quenching ratio of the integrated PL intensity of OMVPE-X was smaller as compared to other luminescent sites. Furthermore, OMVPE-X demonstrated a predominant emission at low excitation power region, even though the existing ratio is as small as ~3%, indicating its quite high excitation efficiency. μ-LED displays are commonly utilized at low current injection density region, where GaN:Eu,O typically shows a relatively low quantum efficiency. Therefore, creation of Eu^{3+} luminescent sites with high excitation efficiencies such as OMVPE-X is critical to compete with trap levels associated with defects and impurities, in the carrier capture process and to enhance the quantum efficiency at low current injection density region.

Subsequently, we applied the annealing technique into LED fabrication process. When we continuously annealed a sample after the growth of GaN:Eu,O layer without carrying out it from

the reactor, the fabricated LED showed a good rectification property with a small series resistance. The good electrical property explained that the damage introduction to GaN:Eu,O active layer during the annealing process was well suppressed. The annealed LED demonstrated a stronger EL emission associated with OMVPE-X as compared to a conventional LED, especially at low current injection regime. This indicates that OMVPE-X shows a quite high excitation efficiency also under current injection. Due to this property, the annealed LED showed a reasonably higher EQE. We claim that OMVPE-X is a noteworthy luminescent site for even brighter and efficient GaN:Eu,O-based light emitting devices, and annealing is an effective method to selectively form such site with high excitation efficiencies towards even bright and efficient GaN:Eu,O-based LEDs.

In Chapter 4, to extrinsically control Eu^{3+} emission by utilizing outer optical cavities, we performed a study on design of nanocavities to achieve high *Q*-factors. Especially, we focused on 2D-PhC cavities, because high-*Q* 2D-PhC cavities have a potential to significantly modify the radiative probability of Eu^{3+} emission, which could lead to lasing in this material. However, *Q*-factors of III-nitride-based 2D-PhC cavities have been limited up to ~5000 in the UV-visible range. This is mainly due to the small device size designed for short wavelength range, and the chemical and physical stability that hinders accurate dry- and wet-etching process. In order to improve *Q*-factors of III-nitride-based 2D-PhC cavities, we reproduced experimentally introduced structural disorder in 3D-FDTD simulations and investigated the impact of such disorder on *Q*-factors.

L*N* and H*N* cavities, which are widely used cavities for a wide range of applications, were investigated to figure out suitable cavity structures which enable high *Q*-factors even with large degree of structural disorder. From SEM observation of a fabricated 2D-PhC with hexagonal air-holes, we concluded that the most dominant disorder for III-nitride-based PhCs is the shape variation of hexagonal air-holes. The experimentally introduced disorder was well reproduced in simulations, and the simulated *Q*-factors of 2D-PhC cavities with disorder was reasonably degraded as compared to ideal *Q*-factors. This numerical result well reproduced the tendency in actual experiments. Furthermore, we estimated the optical gain threshold, which is the minimum optical gain required for lasing, to study the impact of *Q*-factors on the lasing possibilities. As a result, the optical gain threshold was inversely proportional to *Q*-factors, clearly suggesting that the optical gain threshold is almost uniquely determined by *Q*-factors.

Large L*N* cavities (L7, L9) show high ideal *Q*-factors beyond 3×10^4, however, we revealed that their *Q*-factors saturate around $Q \sim 7000$ when structural disorder is introduced. In contrast to L*N* cavities, H*N* cavities demonstrated a high robustness to disorder. Particularly, H3 cavities achieved high ideal *Q*-factors, and maintained the high *Q*-factors even in the presence of structural disorder. To study the reason why H*N* cavities are more tolerant to disorder than L*N* cavities, we focused on the electric-field distribution of cavity modes. L*N* cavities showed a significant mode localization when disorder is introduced, which strongly limits *Q*-factors. Contrary to this, for H*N* cavities, the distribution of cavity modes did not greatly change even with disorder. For these reasons, we highlighted H3 cavity as a promising structure for the realization of high-*Q*-factors.

In Chapter 5, we fabricated H3 cavities to validate the simulation results and to explore the dominant optical loss that limits *Q*-factors with the aim of further enhancement. Besides, to study the experimental impact of structural disorder on *Q*-factors, we designed and fabricated H3 cavities with different *r*, because the degree of disorder strongly depends on *r*. We performed PL studies for the H3 cavities, and demonstrated a high average experimental *Q*-factor of 7000. The maximum *Q*-factor was 7900, which is reasonably higher than earlier reported values, confirming our suggestion that the H3 cavity is a promising structure to achieve high *Q*-factors. For an even improvement of *Q*-factors, we explored the dominant optical loss of H3 cavities through the combination of experimental and simulation studies. As a result, the designed *Q*-factor itself (12000) was derived as the most important limitation.

Based on this knowledge we designed 2D-heterostructure type of cavity. The 2D-heterostructure we propose consists of ellipse shaped core, transition, and outer region, with air-hole radii of r_c, r_t, and r_o, respectively. By designing the radii as $r_c > r_t > r_o$, light at a specific frequency is well confined in the core region. Through a proper cavity design, we found that high design *Q*-factors beyond 1.1×10^5 can be attained. With the robustness to in-plane disorder in mind, we introduced a hexagonal defect consisting of 19 missing air-holes at the center of 2D-heterosturcture. This cavity demonstrated a relatively high robustness to disorder because it has less air-holes in the core region that leads to structural disorder. Based on this design we realized a much higher experimental *Q*-factor of 10500. These results clearly suggest the high potential of this type of cavity, and even higher *Q*-factors are expected through a further optimization of design parameters.

6. 2 Future works

In this thesis, Eu^{3+} luminescence properties were greatly modified through the intrinsic and extrinsic control. Due to its distinctive properties of GaN:Eu,O such as the ultra-stable emission wavelength against for temperature and excitation conditions, it holds a great potential for wide applications. In this regard, we propose some ideas and corresponding methods to further enhance the luminescence efficiency of GaN:Eu,O and to explore its use in various device applications.

6. 2. 1 Combination of annealing techniques and high-*Q* 2D-PhC cavities

In this thesis, we have separately investigated on intrinsic and extrinsic control methods of Eu^{3+} emission. The combination of these achievements is expected to broaden the range of potential applications of GaN:Eu,O-based light emitting devices.

6. 2. 1. 1 Towards quantum light sources

In the field of quantum light sources such as single photon emitters, it is essential to keep the number of RE ions within a device sufficiently low. However, as discussed in Chapter 1, PL spectrum from a conventional GaN:Eu,O sample with a low Eu concentration on the order of 10^{18} cm^{-3} is primarily dominated by yellow luminescence originating from deep levels. To solve this issue, intrinsic control over the distribution of Eu^{3+} luminescent site is critical to effectively compete with defect levels in the free carrier capture process. However, as compared to carrier capture and recombination rate of defect levels [1,2], the radiative recombination rate of Eu^{3+} ions is significantly small, resulting in a low quantum efficiency. Therefore, high-*Q* nanocavities are necessary to enhance the radiative recombination probability of Eu^{3+} ions. In particular, an H3 cavity is promising to employ because of the high *Q*-factor and relatively small *V*, leading to a high Purcell factor.

6. 2. 1. 2 Towards lasers using GaN:Eu,O as an active layer

In this study, we have not observed lasing in GaN:Eu,O. This is partially because of the still limited *Q*-factors of nanocavities: the simulation results suggested *Q*-factors of no less than 20000 are required for lasing considering the optical gain of GaN:Eu,O at this stage. In addition to this, it is important to increase the optical gain to facilitate lasing. In these contributions, both of intrinsic control of Eu^{3+} emission and utilization of high-*Q* nanocavities are essential. In a theoretical aspect, the lasing condition is determined by the following equation [3];

$$N_{\mathrm{Eu}} D_0^{\mathrm{th}} \gamma_{\mathrm{sp}} > \gamma_{\sigma}, \tag{6.1}$$

where N_{Eu} is the number of active Eu^{3+} ions, D_0^{th} is the threshold inversion population, γ_{sp} is the spontaneous emission rate of atoms, and γ_{σ} is the dephasing rate (linewidth of atoms). A radiative rate in a system, which is proportional to the number of atoms in the excited state, is described as $N_{\mathrm{Eu}}(D_0^{\mathrm{th}} + 1)/2$. Simultaneously, an absorption rate of atoms is proportional to the number of atoms in the ground state, and is Expressed as $N_{\mathrm{Eu}}(1 - D_0^{\mathrm{th}})/2$. The net emission rate from a system is the difference between these two values, $N_{\mathrm{Eu}} D_0^{\mathrm{th}}$. Therefore, eq. (6. 1) suggests that lasing starts when the net emission rate exceeds the dephasing rate in a system.

To consider the requirement for lasing in GaN:Eu,O, we assume that only one type of Eu^{3+} luminescent site can contribute to lasing, and only one resonant mode couples to the site, for the simplicity. To satisfy the requirement for lasing shown in eq. (6. 1), the following things must be met: (i) Minimized dephasing rate (ii) Efficient population of Eu^{3+} ions into the excited state (iii) Augmented quantity of Eu^{3+} ions, and (iv) Elevated spontaneous emission rate.

To minimize the dephasing rate, it is crucial to decrease the linewidth of Eu^{3+} emission because the spectral linewidth Γ follows the well-known relation $\Gamma = \hbar/T_1 + \hbar/T_2$, where T_1 the spontaneous emission lifetime and T_2 the dephasing time. Thermal annealing effectively dissociated OMVPE1 and OMVPE2 with broad emission peaks, and led to a significant reduction in the linewidth of entire Eu^{3+} emission. However, the linewidth of each site was nearly unchanged even after annealing. The linewidth is determined by the effects of homogeneous broadening and inhomogeneous broadening. Homogenous broadening is typically influenced by the emission lifetime of atoms, which remained almost constant after annealing. In contrast, we anticipate that the inhomogeneous broadening can be effectively suppressed through local strain engineering, such as utilizing different substrates [4,5]. In addition, co-doping technique is important to form uniform local atomic structure suppressing inhomogeneous broadening [6].

A high excitation efficiency is crucial for efficient population of Eu^{3+} ions into excited states. We attribute that the limited optical gain in GaN:Eu,O to the presence of various types of luminescent sites. As discussed in Chapter 2, free carrier capture is a competing process with trap levels associated with impurities and defects, as well as other Eu luminescent sites. Consequently, for efficient excitation of a particular luminescent site, that site must have a high excitation efficiency. In this contribution, OMPPE-X is a promising luminescent site because of the high excitation efficiency. Although the existing ratio of OMVPE-X is still limited to several percent even after annealing at this stage, future optimization of growth and annealing conditions would lead to an increased abundance of OMVPE-X.

The spontaneous emission rate (γ_{sp}) of Eu^{3+} emission was not greatly modified by annealing treatment, thus optical resonators have to be employed to enhance γ_{sp} by the Purcell effect. Equation (4. 5) implies that γ_{sp} is almost proportional to Q/V ratio, however, N_{Eu} is typically proportional to V. Thus, the term involving V cancels out in eq. (6. 1), and the product of $N_{\mathrm{Eu}}\gamma_{\mathrm{sp}}$ is dominantly determined by Q. This result aligns with our FDTD simulation findings discussed in Chapter 4, indicating that the lasing threshold is purely determined by Q-factors [7,8]. In addition, it is critical to suppress mode-splitting, because it reduces the polarization overlap factor ξ^2 leading to a limited Purcell factor.

To sum up, it is essential to emphasize that both *intrinsic* control, which involves the selective formation of luminescent sites with high excitation efficiencies, and *extrinsic* control of radiative probability using high-Q cavities are vital to demonstrate lasing in GaN:Eu,O in the future.

We note that GaN:Eu,O grown on a semipolar $(20\bar{2}1)$ GaN template on a $(22\bar{4}3)$ sapphire substrate exhibits significantly increased concentration of OMVPE7 by a factor of ~140, as compared to that grown on a conventional (0001) sapphire substrate [9]. Due to this, PL and EL spectra for the $(20\bar{2}1)$ sample was dominated by the emission associated with OMVPE7. This is likely because of the promoted incorporation of oxygen for the growth on $(20\bar{2}1)$ [10]. These results indicate great potential to selectively form a luminescent site with a high excitation efficiency, despite the challenges associated with the growth of thick $Al_xIn_{1-x}N$ alloys, such as issues with crystal quality and surface morphology [11–13].

6. 2. 2 Annealing of GaN:Eu co-doped with different atoms

As discussed in Chapter 2 and Chapter 3, it is believed that pairs of donor-like defects and acceptor-like defects in GaN:Eu system enhance the efficiency of carrier capture and energy transfer to Eu^{3+} ions. Therefore, co-doping of different atoms has a good potential to form additional donor-like and/or acceptor-like defects and to enhance the Eu^{3+} luminescence efficiency. Several atoms (e.g., Si, Mg) have been studied as co-dopants to GaN:Eu system, and some kinds of luminescent sites with high excitation efficiencies have been reported. The experimental observation that site reconfiguration occurs by annealing at high temperatures implies that the formation energy of defect complexes strongly depends on the kind of luminescent site. Hence, thermal annealing of GaN:Eu co-doped with other dopants has a potential to generate luminescent sites with substantial excitation efficiencies.

Furthermore, formation energy of defects generally depends on the Fermi level unless they are in a neutral charge state. Therefore, co-doping of donors and acceptors can be an effective approach to modulate the Fermi level and the formation energy of a specific charged luminescent site and to increase its concentration. In semiconductors, free electrons and holes undergo Coulomb interaction with charged defects. Coulomb attraction between the defects and carriers increases carrier capture cross section, while Coulomb repulsion decreases it [14,15]. In this regard, the creation of charged defects through the co-doping of donors and acceptors is expected to enhance the carrier capture cross section.

6. 2. 3 Electrically driven 2D-PhC cavities

For the implementation of compact and efficient light emitting devices using GaN:Eu,O such as lasers and quantum light sources, current injection is essential for their operation. In particular, it is of great importance to design electrically driven nanocavities in order to maximize the luminescence efficiency of Eu^{3+}.

We have reported the fabrication of an electrically driven GaN:Eu,O-based microdisk cavity, and observed a whispering gallery mode under current injection [16]. To achieve the structure, a Si-doped $Al_xIn_{1-x}N$ layer was used as a sacrificial layer, and a SiO_2 spacer was utilized to isolate a microdisk cavity optically and electrically from an electrode. This cavity structure is more

compact as compared to GaN-based microdisks with a contact positioned on the top for probe access [17]. Furthermore, the microdisk is sandwiched between air-clads, thus higher light confinement effect is expected compared to microdisks utilizing $Al_xGa_{1-x}N$ cladding layers [18–20]. However, to increase *Q*-factors of microdisks, a relatively large-sized disk must be employed to suppress optical losses. This, in turn, leads to smaller spacings between each modes, which hinders single-mode lasing. The reduction of the number of modes has been reported using microgear and microtoroid structures [21–23]. However, it is technically challenging to fabricate III-nitride-based high-*Q* microgear cavity due to the anisotropic crystal structure. In addition, formation of electrode is an issue for microtoroid cavities. Besides, the footprint of the device inevitably increases to achieve high *Q*-factors.

In contrast, 2D-PhC cavities can offer both single-mode lasing and a high *Q*-factor. Furthermore, 2D-PhC cavities can be integrated into circuits alongside optical waveguides [24] and antennas [25,26] with small footprints, providing a great advantage for various device applications. Electrically driven lasers using 2D-PhC cavities have been reported using matured semiconductors such as $In_xGa_{1-x}As$ [27,28] and InP [29,30]. For the control of electrical conductivity, ion implantation technique has been typically utilized to introduce dopants. However, the activation of implanted dopants is challenging for III-nitrides, especially for p-type layers. Ion implantation introduces point defects, such as vacancies, interstitials, and their complexes, due to the energetic collision of ions. These defects can be partially recovered by thermal annealing, however, the activation efficiency of acceptors is still limited [31,32]. Recently, a high activation efficiency of Mg exceeding 70% was reported by utilizing UHPA technique [33]. However, it remains uncertain if this technique is suitable for industrial applications because of several issues, including costs and inclusion of impurities.

For these reasons, electrically driven III-nitride-based 2D-PhC cavities have been yet to be achieved to the best of our knowledge. To enable current injection while maintaining high *Q*-factors, electrodes must be poisoned at a distance from where the electromagnetic field is confined. However, the structure design should ensure that the current passes through inside the cavity (where the electromagnetic field is confined) to achieve a high Purcell effect.

Here, we propose a design of an electrically driven GaN:Eu,O-based 2D-PhC cavity by utilizing 2D-heterostructures (DHS). The layer structure is illustrated in Fig. 6. 1 (a). The sample is consisted of an ud-GaN layer, an n-GaN layer, an n-$Al_xIn_{1-x}N$ sacrificial layer, a GaN:Eu,O active layer and a p-GaN layer. Schematic of the proposed cavity structure is depicted in Fig. 6.

1 (b). The n-$Al_xIn_{1-x}N$ sacrificial layer is not entirely etched away beneath the membrane, leaving a pole to enable current injection into the active layer. The n-$Al_xIn_{1-x}N$ pole is positioned at the center of defect, where air-holes are absent. An n-electrode is placed on the n-GaN layer, where a mesa structure is formed. The DHS is surrounded by a p-electrode, which ensures uniform current injection into the active layer. To electrically isolate the DHS cavity, the membrane is physically separated from the surrounding structure, resulting in a relatively weak mechanical strength. As a solution, SiO_2 is introduced both to provide mechanical support for the DHS and to place the rest of p-electrode. To achieve small sheet resistance, introducing of an n-GaN layer between the n-$Al_xIn_{1-x}N$ and GaN:Eu,O layer should be effective. The carrier diffusion length in GaN:Eu,O is approximately 100 nm [34], which is comparable to the thickness of the 2D-PhC membrane, thus this layer structure enables electrical pumping of the GaN:Eu,O active layer.

As demonstrated in Chapter 5, electromagnetic field of the K1 mode in DHS is well confined in the core region. Consequently, the presence of the n-$Al_xIn_{1-x}N$ pole and p-electrode does not hinder the formation of the resonant mode. To further ensure a high Q-factor, it is effective to increase the size of the central defect in order for the n-$Al_xIn_{1-x}N$ pole not to interfere with the resonant mode. In addition, it is feasible to attain a resonant mode that confines the electromagnetic field in the transition region by appropriately designing the radii of air-holes in each region ($r_t > r_c, r_o$). Besides, DHS cavities can be designed with a high degree of flexibility, and high Q-factors is expected even when using a higher number of layers instead of just three. Using such structures, we can control where the resonant mode is confined to achieve high Q-factors.

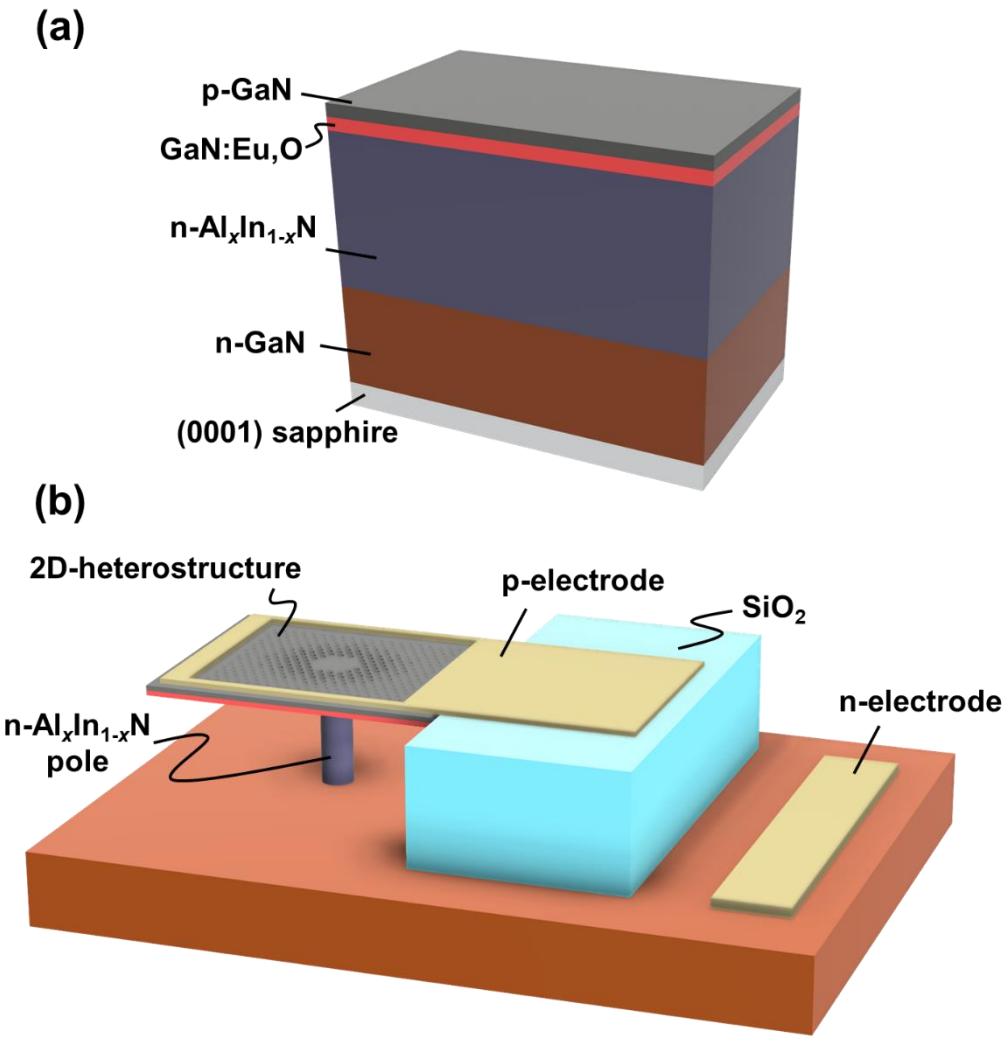

Fig. 6. 1 (a) Sample layer structure for an electrically driven 2D-heterostructure. (b) Schematic of an electrically driven 2D- heterostructure.

References

[1] M.A. Reshchikov and H. Morkọ, *J. Appl. Phys.* **97**, (2005).

[2] D. Timmerman, B. Mitchell, S. Ichikawa, M. Nagai, M. Ashida, and Y. Fujiwara, *Phys. Rev. B* **101**, 1–5 (2020).

[3] I. V. Doronin, A.A. Zyablovsky, E.S. Andrianov, A.A. Pukhov, Y.E. Lozovik, and A.P. Vinogradov, *Sci. Rep.* **11**, 1–10 (2021).

[4] N.T. Woodward, N. Nepal, B. Mitchell, I.W. Feng, J. Li, H.X. Jiang, J.Y. Lin, J.M. Zavada, and V. Dierolf, *Appl. Phys. Lett.* **99**, 122506 (2011).

[5] R. Wakamatsu, D.G. Lee, A. Koizumi, V. Dierolf, Y. Terai, and Y. Fujiwara, *Jpn. J. Appl. Phys.* **52**, 1–6 (2013).

[6] B. Mitchell, D. Timmerman, J. Poplawsky, W. Zhu, D. Lee, R. Wakamatsu, J. Takatsu, M. Matsuda, W. Guo, K. Lorenz, E. Alves, A. Koizumi, V. Dierolf, and Y. Fujiwara, *Sci. Rep.* **6**, 18808 (2016).

[7] T. Iwaya, S. Ichikawa, M. Murakami, J. Tatebayashi, and Fujiwara, *Journal of the Society of Materials Science* **69**, 721–726 (2020).

[8] T. Iwaya, S. Ichikawa, M. Murakami, D. Timmerman, J. Tatebayashi, and Y. Fujiwara, *Appl. Phys. Express* **14**, 122002 (2021).

[9] A. Takeo, S. Ichikawa, J. Tatebayashi, and Y. Fujiwara, *IWN 2022*, (2022).

[10] D.A. Browne, E.C. Young, J.R. Lang, C.A. Hurni, and J.S. Speck, *J. Vac. Sci. Technol. A* **30**, (2012).

[11] T. Wernicke, S. Ploch, V. Hoffmann, A. Knauer, M. Weyers, and M. Kneissl, *Phys Status Solidi B Basic Res*. **248**, 574–577 (2011).

[12] T. Wernicke, L. Schade, C. Netzel, J. Rass, V. Hoffmann, S. Ploch, A. Knauer, M. Weyers, U. Schwarz, and M. Kneissl, *Semicond. Sci. Technol.* **27**, (2012).

[13] B. Leung, D. Wang, Y.S. Kuo, and J. Han, *Phys Status Solidi B Basic Res*, **253**, 23–35 (2016).

[14] R.H. Bube, “Photoelectronic Properties of Semiconductors”, Cambridge University Press, (1992).

[15] K. Hoang, *Phys. Rev. Mater.* **5**, 034601 (2021).

[16] T. Taniguchi, D. Timmerman, S. Ichikawa, J. Tatebayashi, and Y. Fujiwara, *Opt. Lett.* **48**, 4590 (2023).

[17] Y. Mei, M. Xie, H. Xu, H. Long, L. Ying, and B. Zhang, *Opt. Express* **29**, 5598 (2021).

[18] F. Tabataba-Vakili, S. Rennesson, B. Damilano, E. Frayssinet, J.-Y. Duboz, F. Semond, I. Roland, B. Paulillo, R. Colombelli, M. El Kurdi, X. Checoury, S. Sauvage, L. Doyennette, C. Brimont, T. Guillet, B. Gayral, and P. Boucaud, *Opt. Express* **27**, 11800 (2019).

[19] Y. Tang, M. Feng, H. Zhao, J. Wang, J. Liu, X. Sun, Q. Sun, S. Zhang, and H. Yang, *Opt. Express* **30**, 13039 (2022).

[20] Y. Mei, M. Xie, T. Yang, X. Hou, W. Ou, H. Long, L. Ying, Y. Liu, G. Weng, S. Chen, and B. Zhang, *ACS Photonics* **9**, 3967–3973 (2022).

[21] M. Fujita and T. Baba, *Appl. Phys. Lett.* **80**, 2051–2053 (2002).

[22] D.K. Armani, T.J. Kippenberg, S.M. Spillane, and K.J. Vahala, *Nature* **421**, 925–928 (2003).

[23] T.J. Kippenberg, S.M. Spillane, and K.J. Vahala, *Appl. Phys. Lett.* **85**, 6113–6115 (2004).

[24]. J D Joannopoulos, R.D. Meade, J.N. Winn, M. Notomi, A. Shinya, S. Mitsugi, E. Kuramochi, and H.-Y. Ryu, *Opt. Express* **12**, 1551 (2004).

[25] E.R. Brown, E. Yablonovitch, and C.D. Parker, *J. Opt. Soc. Am. B*, **10**, 404 (1993).

[26] W. Withayachumnankul, R. Yamada, M. Fujita, and T. Nagatsuma, *APL Photonics* **3**, (2018).

[27] H.G. Park, S.H. Kim, S.H. Kwon, Y.G. Ju, J.K. Yang, J.H. Baek, S.B. Kim, and Y.H. Lee, *Science* **305**, 1444–1447 (2004).

[28] B. Ellis, M.A. Mayer, G. Shambat, T. Sarmiento, J. Harris, E.E. Haller, and J. Vučković, *Nat Photonics* **5**, 297–300 (2011).

[29] S. Matsuo, K. Takeda, T. Sato, M. Notomi, A. Shinya, K. Nozaki, H. Taniyama, K. Hasebe, T. Kakitsuka, 2 I Zh, V.M. Alferov, D.Z. Andreev, Y. V Garbuzov, E.P. Zhilyaev, E.L. Morozov, and V.G. Portnoi, *Opt. Express* **20**, 3773 (2012).

[30] S. Matsuo, T. Sato, K. Takeda, A. Shinya, K. Nozaki, H. Taniyama, M. Notomi, K. Hasebe, and T. Kakitsuka, *IEEE J. Sel. Top. Quantum Electron.* **19**, 4900311 (2013).

[31] J.D. Greenlee, T.J. Anderson, B.N. Feigelson, K.D. Hobart, and F.J. Kub, *Physica Status Solidi (A)* **212**, 2772–2775 (2015).

[32] B.N. Feigelson, T.J. Anderson, M. Abraham, J.A. Freitas, J.K. Hite, C.R. Eddy, and F.J. Kub, *J. Cryst. Growth* **350**, 21–26 (2012).

[33] H. Sakurai, M. Omori, S. Yamada, Y. Furukawa, H. Suzuki, T. Narita, K. Kataoka, M. Horita, M. Bockowski, J. Suda, and T. Kachi, *Appl. Phys. Lett.* **115**, (2019).

[34] D. Denier van der Gon, D. Timmerman, Y. Matsude, S. Ichikawa, M. Ashida, P. Schall, and Y. Fujiwara, *Opt. Lett.* **45**, 3973 (2020).

Appendix A. Investigation on the carrier dynamics in GaN:Eu,O using rate equations

A. 1. Introduction

As mainly discussed in Chapter 2, we observed that post-growth thermal annealing leads to a great luminescence intensity enhancement of GaN:Eu,O. We have suggested that the enhanced luminescence intensity is attributed to the luminescent site reconfiguration; OMVPE1 and OMVPE2 with low excitation efficiency decrease while OMVPE7, OMVPE8, and OMVPE-X, which have high excitation efficiencies, are formed. Excitation power dependent PL studies for the annealed GaN:Eu,O revealed that OMVPE-X shows a dominant emission under low excitation power region, and the PL intensity ratio decreases with increasing the excitation power due to the limited number of OMVPE-X. Furthermore, the derived QE was relatively low under low power excitation power, and was maximized under moderate excitation power, then decreased again under higher excitation power. We have suggested the possibility that non-radiative traps are closely related to the behavior of QE: under low excitation power, such traps efficiently capture carriers limiting the QE, and with increasing the excitation power, these traps become filled and the QE improves. Under further high excitation power, most of Eu^{3+} ions are in the excited states, lowering the QE.

For these experimental findings, theoretical studies using rate equations would provide a deeper and logical understanding of the carrier dynamics in GaN:Eu,O. Besides, we believe that such studies are effective to reveal the contributions of carrier capture rate and energy transfer rate to the excitation efficiency of Eu^{3+}. Furthermore, rate-equation analysis is critical to investigate the optimum drive condition of LEDs (e.g., pulse width, pulse frequency) and carrier distribution for laser applications.

So far, several reports have investigated the carrier dynamics in GaN:Eu,O using rate

equations [1–4]. Luminescence efficiency of GaN:Eu,O has been analyzed using rate equations [1,2], however, these analyses have not taken into account the effect that trap levels associated with impurities (defects) are filled under high excitation power region. Therefore, carrier dynamics, especially in the carrier capture, which is a competing process, has not been thoroughly investigated. For these reasons, we perform detailed rate-equation analysis taking account the effect of point defects that compete with Eu^{3+} ions for carrier capture.

A. 2. Rate equation

A schematic illustrating the carrier dynamics in GaN:Eu,O is shown in Fig. A. 1. Photon fluence of ϕ creates electrons and holes with concentrations of n and p, respectively. They form free excitons (FXs) with a concentration of N_{FX}. Subsequently they are captured by trap levels associated with impurities (defects) and Eu^{3+} ions of the luminescent site i, with concentrations of N_{d} and N_{t_i}, respectively, and capture rates of $1/\tau_{\mathrm{d}}$ and $1/\tau_{\mathrm{t}_i}$, respectively. The recombination energy of trap levels associated with Eu^{3+} ions is transferred to Eu^{3+} ions with a rate of $1/\tau_{\mathrm{ET}_i}$. Then, Eu^{3+} ions show luminescence with a rate of $1/\tau_{\mathrm{Eu}_i}$. The rate equations are given as follows:

$$\frac{\mathrm{d}n}{\mathrm{d}t} = \frac{\mathrm{d}p}{\mathrm{d}t} = \alpha\phi - \gamma np, \tag{A.1}$$

$$\frac{\mathrm{d}N_{\mathrm{FX}}}{\mathrm{d}t} = \gamma np - \frac{N_{\mathrm{FX}}}{\tau_{\mathrm{FX}}}. \tag{A.2}$$

α is the absorption coefficient and γ is the exciton binding coefficient. τ_{FX} is the lifetime of FXs, that can be written as

$$\frac{1}{\tau_{\mathrm{FX}}} = C_{\mathrm{cap,d}}(N_{\mathrm{d}} - N_{\mathrm{d}}^{*}) + \sum_{i} C_{\mathrm{cap,t}_i}(N_{\mathrm{t}_i} - N_{\mathrm{t}_i}^{*}) + \frac{1}{\tau_{\mathrm{FX_{rad}}}}, \tag{A.3}$$

with

$$C_{\mathrm{cap,d}} = \frac{1}{\tau_{\mathrm{cap,d}}} \cdot \frac{1}{N_{\mathrm{d}}}, \tag{A.4}$$

$$C_{\mathrm{cap,t}_i} = \frac{1}{\tau_{\mathrm{cap,t}_i}} \cdot \frac{1}{N_{\mathrm{t}_i}}, \tag{A.5}$$

where $\tau_{\mathrm{FX_{rad}}}$ is the radiative lifetime of FXs. The concentration of excited trap levels associated with impurities and defects (N_{d}^{*}), and Eu^{3+} ions ($N_{\mathrm{t}_i}^{*}$) are Expressed as following:

$$\frac{\mathrm{d}N_{\mathrm{d}}^{*}}{\mathrm{d}t} = C_{\mathrm{cap,d}}(N_{\mathrm{d}} - N_{\mathrm{d}}^{*})N_{\mathrm{FX}} - \frac{N_{\mathrm{d}}^{*}}{\tau_{\mathrm{d}}}, \tag{A.6}$$

$$\frac{\mathrm{d}N_{\mathrm{t}_i}^*}{\mathrm{d}t} = C_{\mathrm{cap,t}_i}(N_{\mathrm{t}_i} - N_{\mathrm{t}_i}^*)N_{\mathrm{FX}} - \frac{N_{\mathrm{t}_i}^*}{\tau_{\mathrm{t}_i}} - W_{\mathrm{ET}_i}N_{\mathrm{t}_i}^*\left(N_{\mathrm{Eu}_i} - N_{\mathrm{Eu}_i}^*\right), \tag{A.7}$$

$$W_{\mathrm{ET}_i} = \frac{1}{\tau_{\mathrm{ET}_i}} \cdot \frac{1}{N_{\mathrm{Eu}_i}}, \tag{A.8}$$

where τ_{d} and τ_{t} is the lifetime of trap levels associated with impurities (defects) and Eu^{3+} ions, respectively. The concentration of Eu^{3+} ions in the excited state ($N_{\mathrm{Eu}_i}^*$) is given by

$$\frac{\mathrm{d}N_{\mathrm{Eu}_i}^*}{\mathrm{d}t} = W_{\mathrm{ET}_i}N_{\mathrm{t}_i}^*\left(N_{\mathrm{Eu}_i} - N_{\mathrm{Eu}_i}^*\right) - \frac{N_{\mathrm{Eu}_i}^*}{\tau_{\mathrm{Eu}_i}} \tag{A.9}$$

with the lifetime of Eu^{3+} ions (τ_{Eu_i}). In the steady state under cw excitation, Eq. (A. 1), (A. 2), (A. 6), (A.7) and (A.9) can be written down as

$$N_{\mathrm{FX}} = \alpha\phi\tau_{\mathrm{FX}}, \tag{A.10}$$

$$N_{\mathrm{d}}^* = \frac{C_{\mathrm{cap,d}}N_{\mathrm{d}}N_{\mathrm{FX}}\tau_{\mathrm{d}}}{1 + \tau_{\mathrm{d}}C_{\mathrm{cap,d}}N_{\mathrm{FX}}}, \tag{A.11}$$

$$C_{\mathrm{cap,t}_i}(N_{\mathrm{t}_i} - N_{\mathrm{t}_i}^*)N_{\mathrm{FX}} = \frac{N_{\mathrm{t}_i}^*}{\tau_{\mathrm{t}_i}} + W_{\mathrm{ET}_i}N_{\mathrm{t}_i}^*\left(N_{\mathrm{Eu}_i} - N_{\mathrm{Eu}_i}^*\right), \tag{A.12}$$

$$N_{\mathrm{Eu}_i}^* = \frac{W_{\mathrm{ET}_i}N_{\mathrm{Eu}_i}N_{\mathrm{t}_i}^*\tau_{\mathrm{Eu}_i}}{1 + \tau_{\mathrm{Eu}_i}W_{\mathrm{ET}_i}N_{\mathrm{t}_i}^*}. \tag{A.13}$$

Equation (A.12) and (A.13) give

$$C_{\mathrm{cap,t}_i}\tau_{\mathrm{t}_i}(N_{\mathrm{t}_i} - N_{\mathrm{t}_i}^*)N_{\mathrm{FX}} = N_{\mathrm{t}_i}^* + W_{\mathrm{ET}_i}\tau_{\mathrm{t}_i}N_{\mathrm{t}_i}^*\frac{N_{\mathrm{Eu}_i}}{1 + \tau_{\mathrm{Eu}_i}W_{\mathrm{ET}_i}N_{\mathrm{t}_i}^*}. \tag{A.14}$$

With $A_i = C_{\mathrm{cap,t_i}}\tau_{\mathrm{t}_i}N_{\mathrm{FX}}$, $B_i = \tau_{\mathrm{Eu}_i}W_{\mathrm{ET}_i}$ and $C_i = W_{\mathrm{ET}_i}\tau_{\mathrm{t}_i}$,

$$A_i(N_{\mathrm{t}_i} - N_{\mathrm{t}_i}^*) = N_{\mathrm{t}_i}^* + C_iN_{\mathrm{t}_i}^*\frac{N_{\mathrm{Eu}_i}}{1 + B_iN_{\mathrm{t}_i}^*}. \tag{A.15}$$

Solving this equation leads to a quadratic equation:

$$N_{\mathrm{t}_i}^{*\,2}(B_i + A_iB_i) + N_{\mathrm{t}_i}^*\left(1 + C_iN_{\mathrm{Eu}_i} + A_i - A_iB_iN_{\mathrm{t}_i}\right) - A_iN_{\mathrm{t}_i} = 0. \tag{A.16}$$

The possible solution is

$$N_{\mathrm{t}_i}^* = -\frac{1 + C_iN_{\mathrm{Eu}_i} + A_i - A_iB_iN_{\mathrm{t}_i}}{2(B_i + A_iB_i)} + \frac{\sqrt{\left(1 + C_iN_{\mathrm{Eu}_i} + A_i - A_iB_iN_{\mathrm{t}_i}\right)^2 + 4(B_i + A_iB_i)A_iN_{\mathrm{t}_i}}}{2(B_i + A_iB_i)}. \tag{A.17}$$

Solving Eq. (A.3) as

$$\frac{\alpha\phi}{N_{\mathrm{FX}}} = C_{\mathrm{cap,d}}\frac{N_{\mathrm{d}}}{1 + \tau_{\mathrm{d}}C_{\mathrm{cap,d}}N_{\mathrm{FX}}} + \sum_i C_{\mathrm{cap,t}_i}(N_{\mathrm{t}_i} - N_{\mathrm{t}_i}^*) + \frac{1}{\tau_{\mathrm{FX_{rad}}}} \tag{A.18}$$

gives the solution of N_{FX}. Then, Eq. (A. 10), (A. 11), and (A. 13) leads the solution of τ_{FX}, N_{d}^*, and $N_{\mathrm{Eu}_i}^*$, respectively.

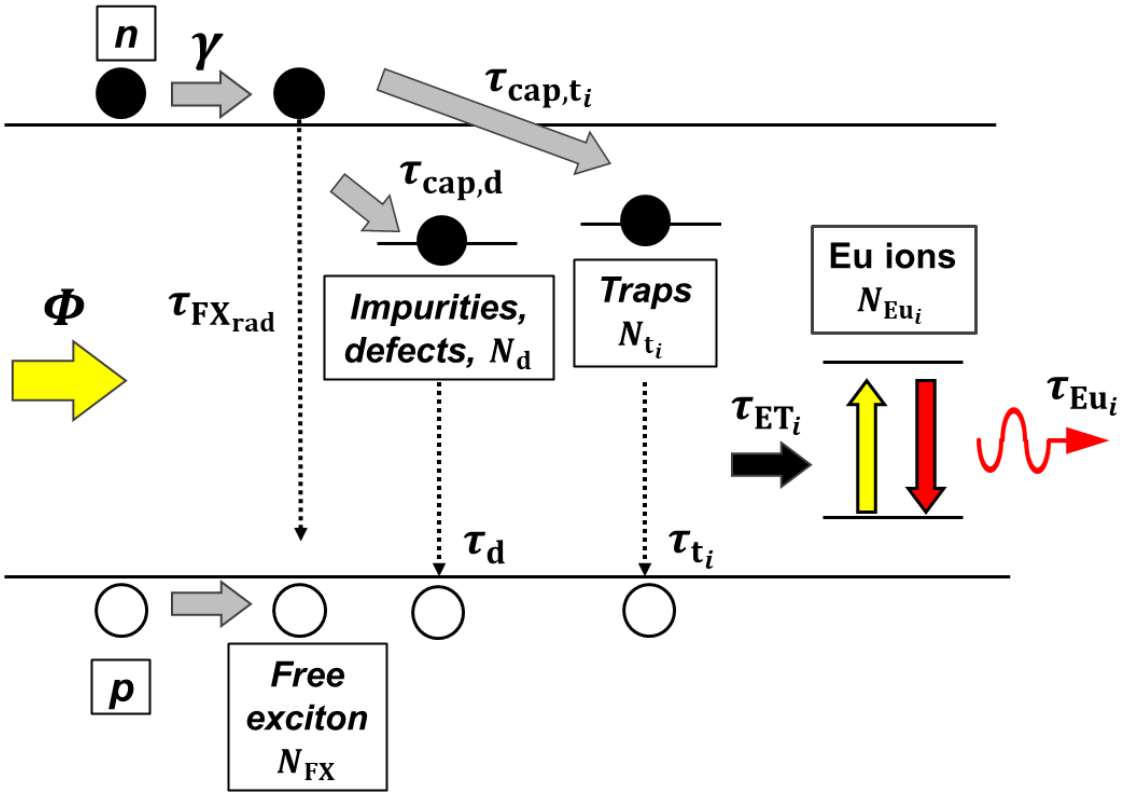

Fig. A. 1 Schematic of the carrier dynamics in GaN:Eu,O utilized for the rate equation analysis.

Emission intensity from Eu^{3+} ions of the luminescent site *i* is proportional to the $N^*_{\mathrm{Eu}_i}/\tau_{\mathrm{Eu}_i}$ product. Although τ_{Eu_i} encompasses radiative and non-radiative passes (e.g., back-transfer process to trap levels), we ignore such non-radiative processes for the simplicity.

A. 3. Number of excited states with respect to excitation power density

We used the parameter sets shown in Table A. 1 for the rate equation analysis. In the Set1, Eu1 has a larger carrier capture rate, that is ten times larger than the reported rate [5]. However, its abundance is lower than Eu2, which has smaller carrier capture rate, that is a hundred times smaller than that of Eu1. In the Set2, we increased the energy transfer rate of Eu1 by a factor of a hundred, while using the same parameters as in Set1.

The number of excited states using the Set1 is shown in Fig. A. 2 (a). It is obvious that the Eu1 is efficiently excited with a large excitation efficiency, suggesting that the carrier capture rate plays an important role in the excitation efficiency. Under low excitation power regime, Eu1 is dominantly excited, which aligns with experimental results. With increasing the excitation power, $N^*_{\mathrm{Eu}_1}$ starts to be saturated, and $N^*_{\mathrm{Eu}_2}$ quicky increases. This behavior also well corresponds to the experimental observations, where the relative luminescence intensity from OMVPE-X decreases while those of other luminescent sites increase with increasing excitation power.

The calculation result using the Set 2 demonstrates [Fig. A. 2 (b)] that the Eu1 is excited more efficiently compared to the Set1. These results clearly indicate that the energy transfer rate is an important factor in determining the excitation efficiency, alongside with the carrier capture rate.

The number of excited states using the Set1 is plotted in Fig. A. 3 (a) in logarithmic scale. The relative QE of Eu^{3+} emission calculated by dividing the number of excited Eu^{3+} ions by photon fluence is shown in Fig. A. 3 (b). Under low excitation power region that is depicted as the division (I) in Fig. A. 3 (b), the number of all excited states is linearly increased with excitation power. The QE is relatively low because the carriers are efficiently distributed to the trap levels associated with impurities and defects due to its large carrier capture rate. With increasing the excitation power [division (II)], most of these trap levels become filled, leading to carriers being distributed to Eu1,

Table A. 1 Parameter sets utilized for the rate equation analysis.

Parameters		**Set1**	**Set2**
Absorption coefficient (cm^{-1})	α	1.4×10^{5} [6]	
Number of states (cm^{-3})	N_{d}	1×10^{15}	
	N_{Eu_1} (N_{t_1})	1×10^{18}	
	N_{Eu_2} (N_{t_2})	9×10^{18}	
Recombination rate (s^{-1})	$1/\ \tau_{\mathrm{FX}_{\mathrm{rad}}}$	$1/(1.25\times10^{-10})$ [7]	
	$1/\ \tau_{\mathrm{d}}$	$1/(3\times10^{-5})$ [8]	
	$1/\ \tau_{\mathrm{t}_{1,2}}$	$1/(3\times10^{-5})$ [8]	
	$1/\ \tau_{\mathrm{Eu}_{1,2}}$	$1/(2.5\times10^{-4})$ [9]	
Carrier capture rate (s^{-1})	$1/\ \tau_{\mathrm{cap,d}}$	$1/(2.2\times10^{-12})$ [5]	
	$1/\ \tau_{\mathrm{cap,t}_1}$	$1/(8.5\times10^{-12})$	
	$1/\ \tau_{\mathrm{cap,t}_2}$	$1/(8.5\times10^{-10})$	
Energy transfer rate (s^{-1})	$1/\ \tau_{\mathrm{ET}_1}$	$1/(5\times10^{-6})$ [3]	$1/(5\times10^{-8})$
	$1/\ \tau_{\mathrm{ET}_2}$	$1/(5\times10^{-6})$ [3]	

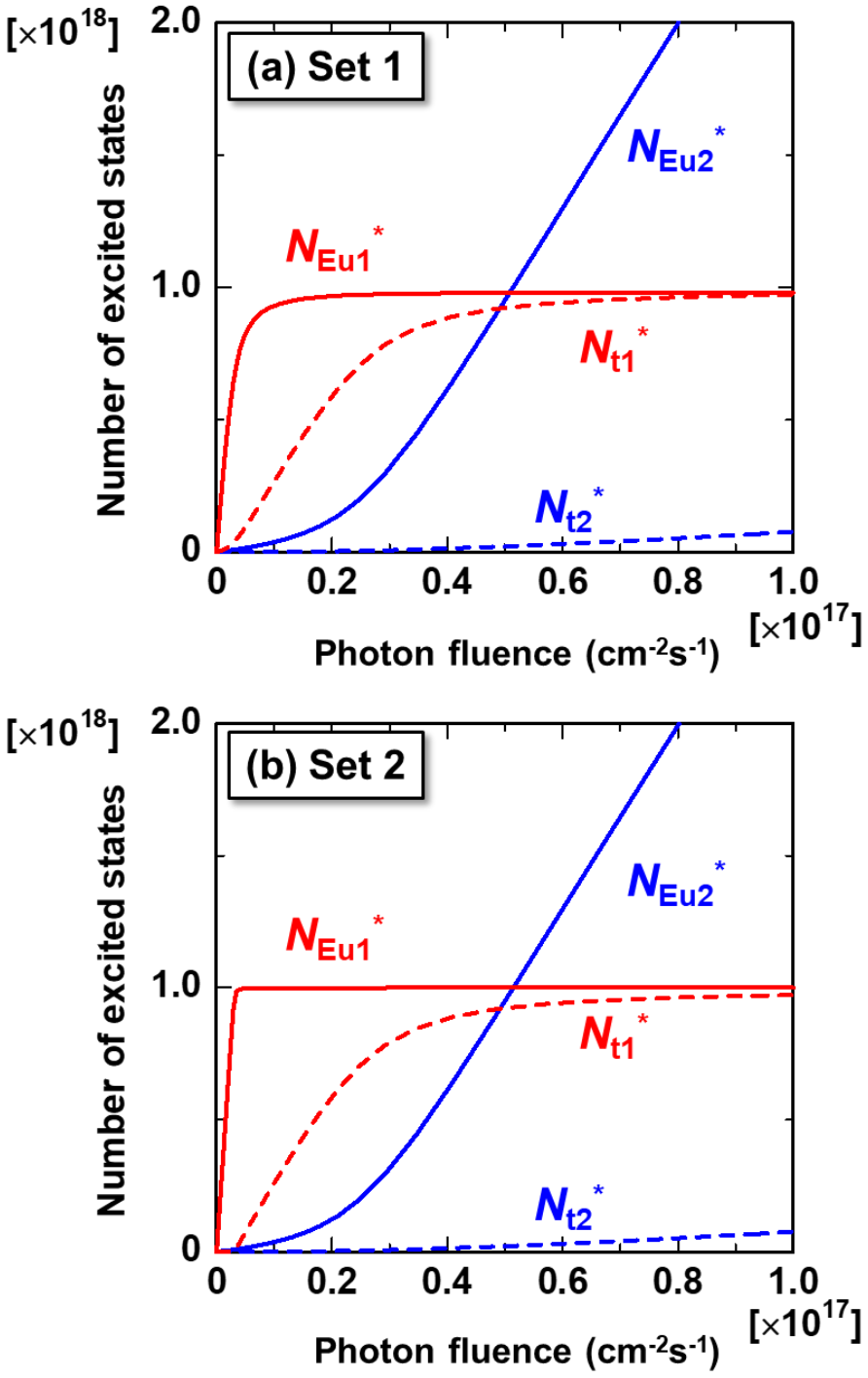

Fig. A. 2 Calculated number of excited states as a function of photon fluence for the (a) Set1 and (b) Set2.

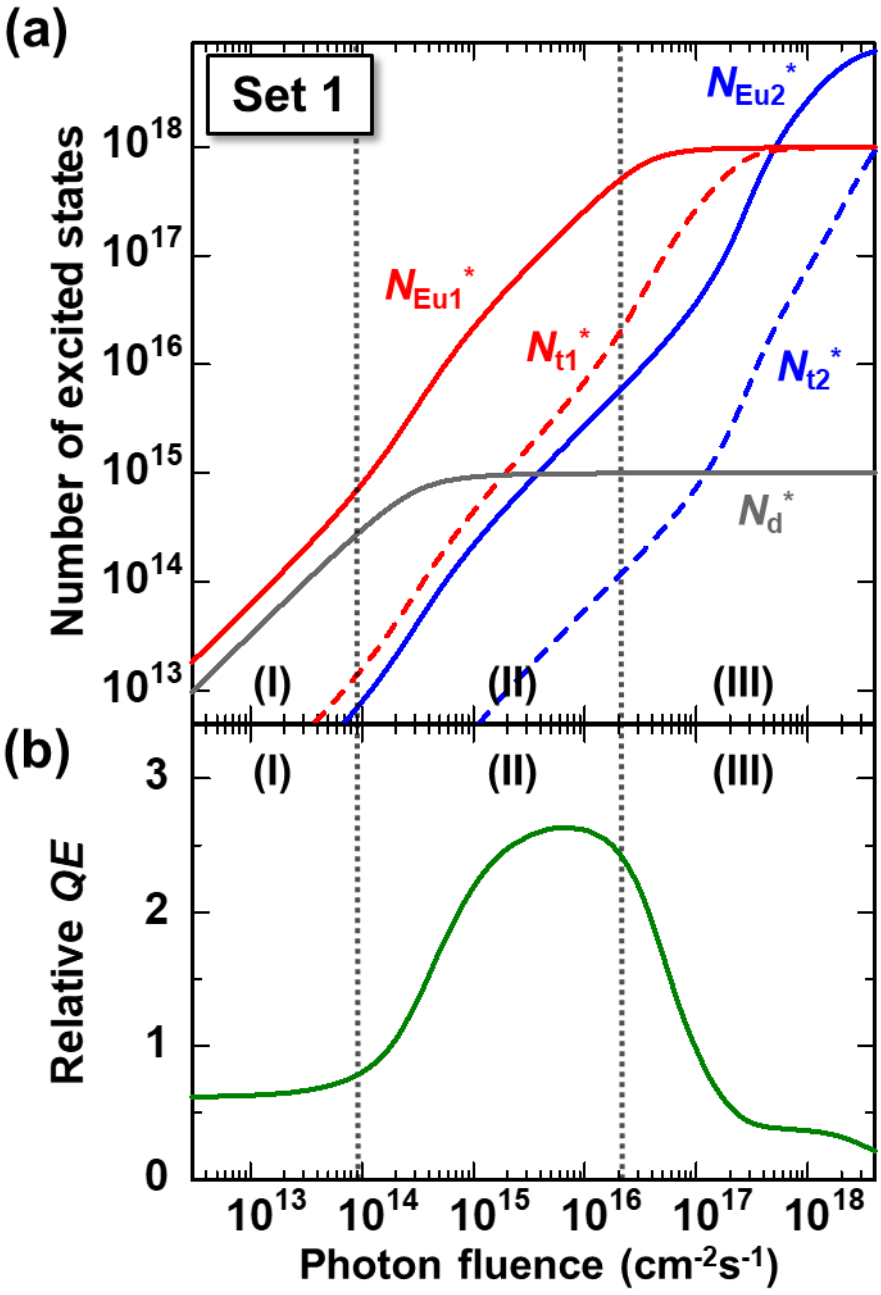

Fig. A. 3 (a) Calculated number of excited states as a function of photon fluence for the Set1. (b) Calculated relative quantum efficiency as a function of photon fluence for the Set1.

which has a larger carrier capture rate. In accordance with this, the QE quickly increases and reaches its maximum. At higher excitation power [division (III)], almost all the Eu1 become excited, resulting in a preferential carrier distribution to Eu2. However, the small radiative recombination rate of Eu^{3+} strongly limits the emission efficiency, which leads to a reduced QE.

These calculation results well correspond to the experimentally observed behavior of QE with respect to excitation power. This supports our suggestion that the QE is strongly influenced by the presence of trap levels of defects and impurities.

A. 4. Summary

We have investigated on the carrier dynamics in GaN:Eu,O using rate equations considering the effect of point defects. Eu^{3+} ions with large carrier capture rate and/or energy transfer rate were efficiently excited, indicating that these rates play an important role in the excitation process of Eu^{3+} ions. Furthermore, the calculated QE aligned with the experimental results, supporting our discussion on the behavior of QEs with respect to excitation power. The QE is limited under low excitation power region by trap levels associated with defects and impurities which have large carrier capture cross sections. When these defects become filled at higher excitation power, the QE quickly increases due to the efficient distribution of carriers to Eu^{3+} ions. Under further high excitation power, most of Eu^{3+} ions are saturated leading to a reduced QE.

References

[1] I.E. Fragkos, V. Dierolf, Y. Fujiwara, and N. Tansu, *Sci. Rep.* **7**, 16773 (2017).

[2] I.E. Fragkos, C.K. Tan, V. Dierolf, Y. Fujiwara, and N. Tansu, *Sci. Rep.* **7**, 14648 (2017).

[3] T. Inaba, T. Kojima, G. Yamashita, E. Matsubara, B. Mitchell, R. Miyagawa, O. Eryu, J. Tatebayashi, M. Ashida, and Y. Fujiwara, *J. Appl. Phys.* **123**, 161419 (2018).

[4] R. Wei, B. Mitchell, D. Timmerman, T. Gregorkiewicz, W. Zhu, J. Tatebayashi, S. Ichikawa, Y. Fujiwara, and V. Dierolf, *Phys. Rev. B* **100**, 81201 (2019).

[5] D. Timmerman, B. Mitchell, S. Ichikawa, M. Nagai, M. Ashida, and Y. Fujiwara, *Phys. Rev. B* **101**, 1 245306 (2020).

[6] J.F. Muth, J.D. Brown, M.A.L. Johnson, Z. Yu, R.M. Kolbas, J.W. Cook, and J.F. Schetzina, *MRS Internet J. Nitride Semicond. Res.* **4**, 502 (1999).

[7] J.P. Bergman, C. Harris, B. Monemar, H. Amano, and I. Akasaki, *Mater. Res. Soc. Symp. Proc.* **395**, 709–714 (1996).

[8] M.A. Reshchikov and H. Morkǫ, *J. Appl. Phys.* **97**, 061301 (2005).

[9] R. Wakamatsu, D.G. Lee, A. Koizumi, V. Dierolf, and Y. Fujiwara, *J. Appl. Phys.* **114**, 043501 (2013).

Appendix B. Investigation of the impact of ultra-high pressure annealing on the optical characteristics of GaN:Eu,O

B. 1 Introduction

In the main text, we have conducted thermal annealing at 100 kPa. As discussed in Chapter 2, luminescence intensity associated with Eu^{3+} monotonically increased with annealing temperature because atomic diffusion is promoted at higher temperatures, resulting in an effective conversion of luminescent sites. Further enhanced luminescence efficiency is expected by annealing at even higher temperatures, however, the surface morphology degrades due to thermal decomposition at temperatures beyond ~1200 °C at 100 kPa even with a mask. Ultra-high pressure annealing (UHPA) is a novel method that allows for high annealing temperatures by applying high pressures. This approach prevents significant thermal decomposition. In the research field of GaN, UHPA is intensely studied to recover damage introduced during Mg-ion-implantation process and to activate the Mg acceptors [1,2]. For Eu-ions-implanted GaN, UHPA has been reported to improve the crystallinity and enhance the Eu-related PL intensity [3–5]. In this chapter, we conduct UHPA to investigate the effect of annealing at an even higher temperature (1450 °C) on the properties of GaN:Eu,O grown using the OMVPE method.

B. 2 Experimental method

UHPA was performed at the institute of high pressure physics of the polish academy of sciences, in corporation with Prof. Boćkowski Michał. We used the same sample studied in Chapter 2 and Chapter 3 that a GaN:Eu,O active layer was grown on a 600-nm-thick $Al_{0.19}In_{0.81}N$ layer. To investigate the effect of SiO_2 mask on surface morphologies and luminescence properties, two

samples were annealed; one was capped by an 80-nm-thick SiO_2 mask, and the other was not capped. The samples were annealed in an UHPA chamber with nitrogen pressure of 1 GPa at 1450 °C for 30 minutes. Surface morphology was observed using a Nomarski microscope. For optical characterization, we conducted PL measurements under indirect and resonant excitation methods.

B. 3 Results and discussions

B. 3. 1 Surface morphology

Nomarski microscopy revealed that the surface morphology was significantly degraded by UHPA process [Fig. B. 1] whether with or without a SiO_2 mask, suggesting UHPA led to thermal decomposition. It has been reported that noticeable thermal decomposition occurs at high temperature (> ~1300 °C) even under high pressure [5,6]. In order to fully suppress thermal decomposition, optimization of the UHPA conditions is required, including annealing temperature and masks (e.g., using GaN powder as mask [6]).

In addition, after UHPA process, the color of the sample changed to blackish to the naked eyes, suggesting that crystal defects such as point defects and their complexes were incorporated into the sample at a fairly high density.

B. 3. 2 CEES measurements

To gain insight into the site distribution of Eu^{3+} ions, the CEES technique was performed at 10 K on the as-grown sample and the sample annealed at 1450 °C under 1 GPa without SiO_2 mask. The CEES results are shown in Fig. B. 2.

As it has been observed for the sample annealed at 1100 °C, OMVPE1 and OMVPE2 are almost disappeared for the UHPA sample, indicating that luminescent site reconfiguration took place during UHPA process [Fig. B. 2 (b)]. Although Jaroszynski *et al.* has reported that diffusion of Eu was not observed in SIMS measurements of GaN grown by ammonothermal method and treated with Eu implantation and UHPA process [5], this result ensures that Eu diffuses on an atomic scale during the UHPA process. However, in contrast to the sample annealed at 1100 °C, PL intensities from other sites did not increase that much from the as-grown state, with enhancement

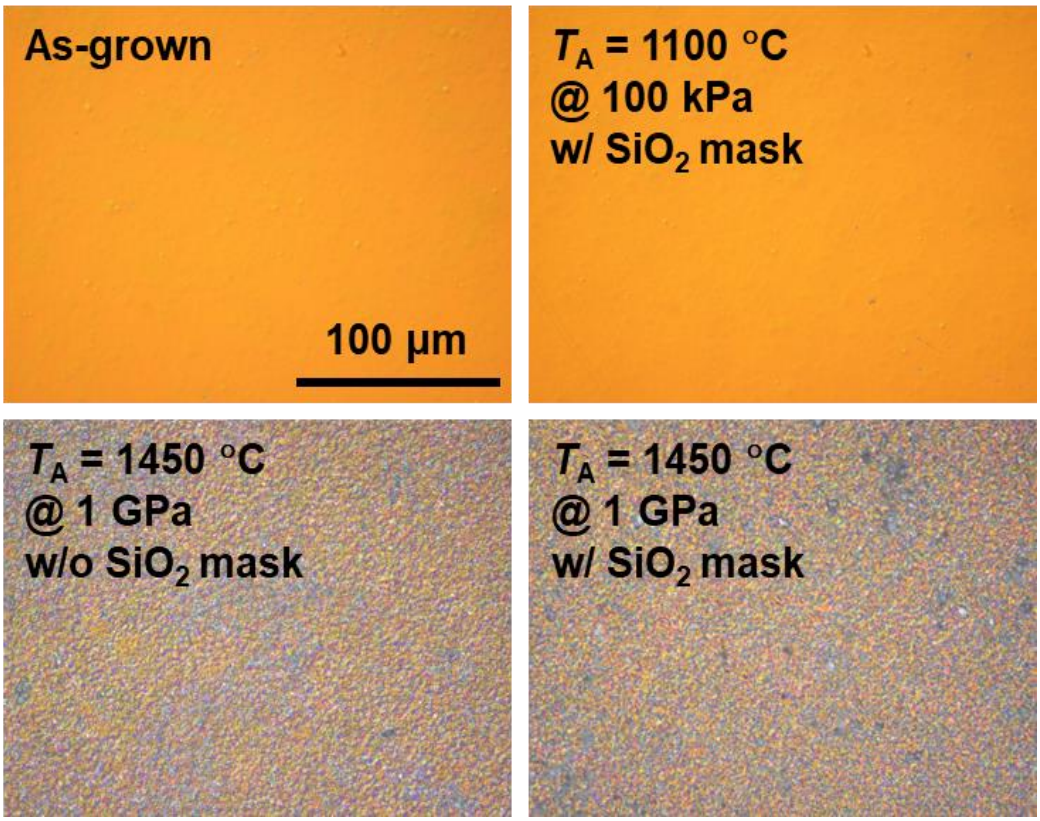

Fig. B. 1 Nomarski microscope image of the as-grown and annealed samples.

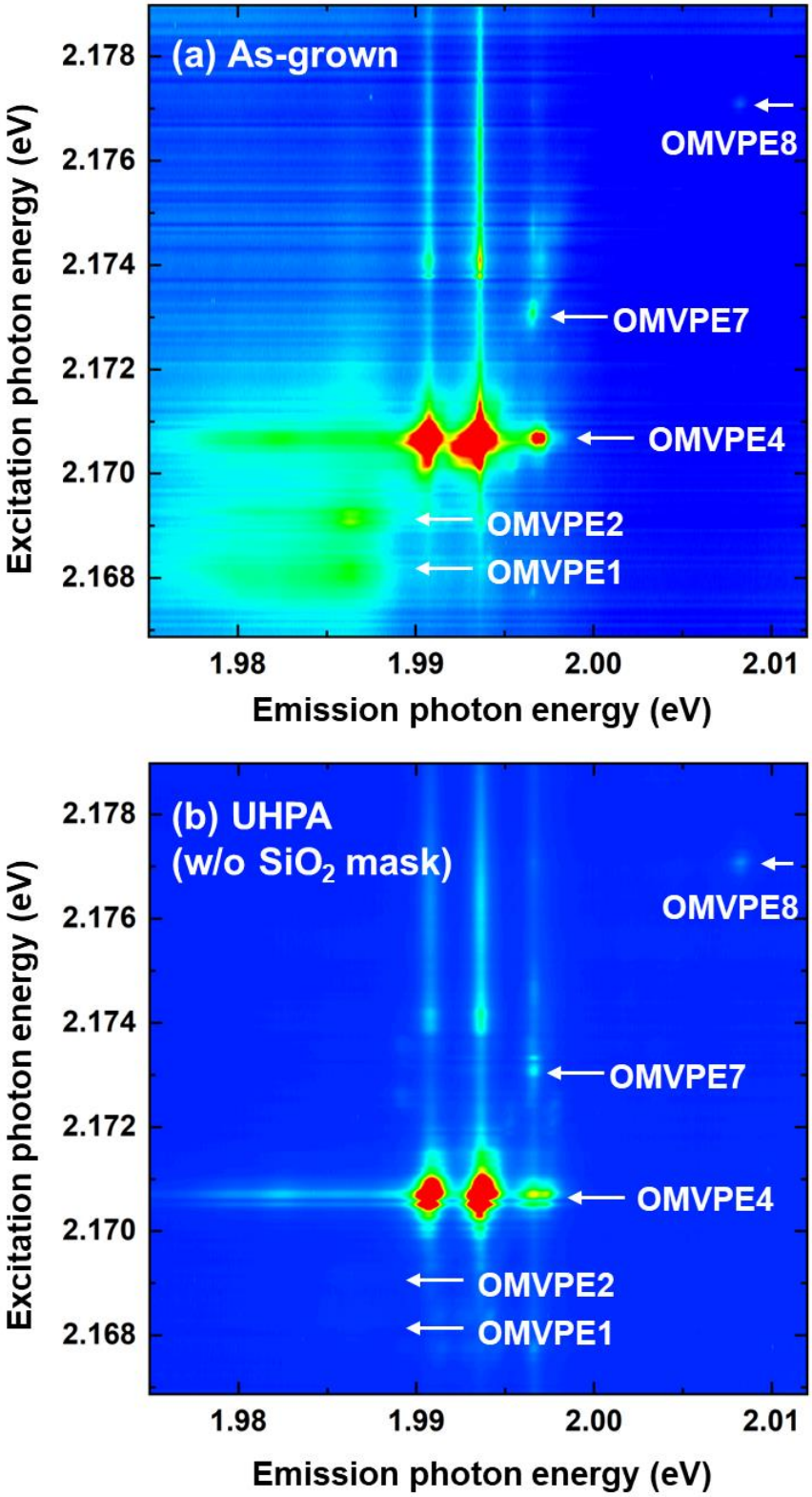

Fig. B. 2 CEES map measured at 10 K for the (a) as-grown sample and (b) sample annealed at 1450 °C under 1 GPa without SiO_2 mask.

factors of 1.2 for OMVPE4, 1.1 for OMVPE7 and 2.2 for OMVPE8. These results suggest a possibility that a portion of Eu^{3+} was inactivated with incorporation of a high density of defects by UHPA process.

B. 3. 3 PL measurements at room temperature

Subsequently, the samples were evaluated by PL spectroscopy at room temperature using a He-Cd laser. UHPA samples showed almost identical spectra whether with or without a mask, thus we will discuss optical properties of the sample annealed without a mask for the following experiments.

As shown in Fig. B. 3, the PL intensity is greatly decreased after UHPA, with the integrated PL intensity of Eu^{3+}-related emission (1.968-2.016 eV) decreasing by a factor of 0.1 as compared to the as-grown state. The inset in Fig. B. 3 shows a log-scale plot of the PL spectra. The as-grown sample and the sample annealed at 1100 °C show clear Eu^{3+} luminescence with negligible PL intensity associated with deep-level emission from defects in the GaN host, suggesting that free carriers are efficiently captured by Eu^{3+}-related trap levels. In contrast, the sample after UHPA process shows a strong luminescence originating from deep-levels, indicating that a high density of crystal defects was incorporated into the sample as mentioned above. The PL band maximum of the deep-level emission was estimated to ~2.28 eV. Substitutional carbon is often considered to be the main origin of yellow luminescence [7], however, it is reported that the carbon concentration remains small even after UHPA processes [2,5,6]. Therefore, V_{Ga}-related defects [8–14] such as V_{Ga}-$3H_i$ [14], Eu_{Ga}-V_{Ga} [5,13] are promising candidates for the origin of the yellow luminescence.

We note that Uedono *et al.* have reported that the sizes and concentrations of vacancy-type defects in Mg-implanted GaN decrease after UHPA process without the use of a capping layer, which is inconsistent with the above suggestion [2]. However, for GaN grown by ammonothermal method and implanted with Eu, it is also observed that the PL intensity of yellow band increases with annealing temperature [5]. Further investigation is required to identity the origin of the yellow band, however, we suggest a possibility that the likelihood of V_{Ga} depletion during UHPA process of GaN:Eu is relatively lower as compared to GaN doped with other dopants. GaN:Eu has been reported to contain more vacancy-type defects than undoped GaN, because Eu^{3+} has a large atomic covalent radius and prefers to have vacancies in its vicinity [15,16] .

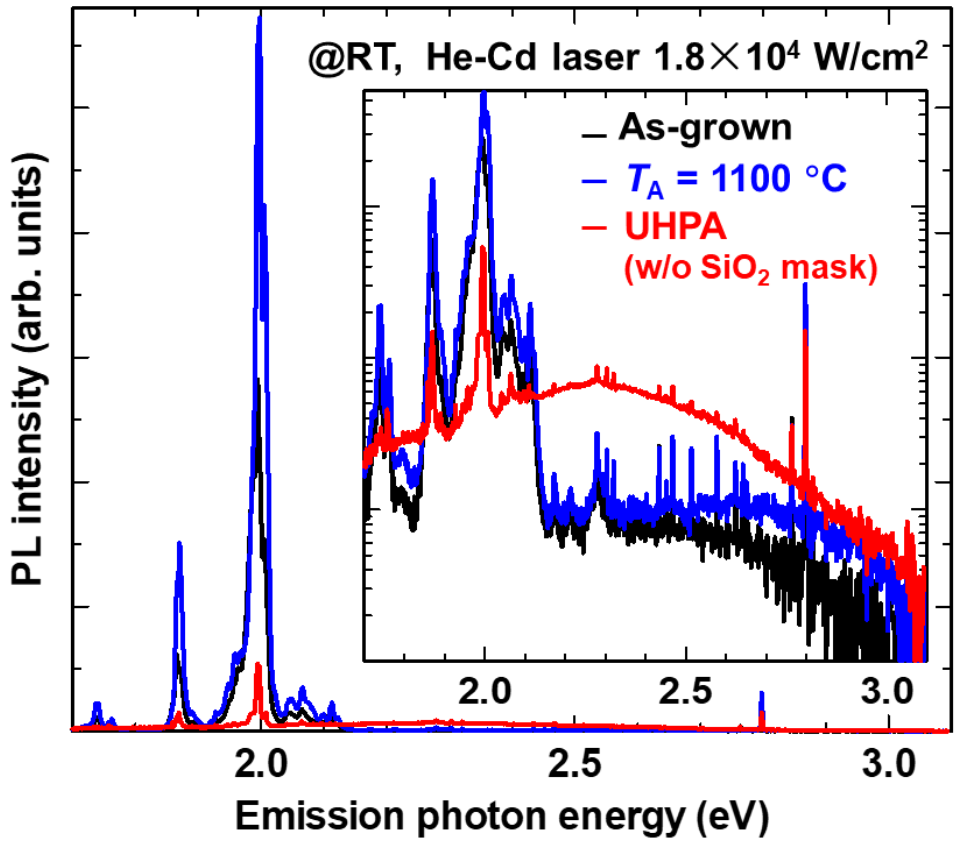

Fig. B. 3 PL spectra for the as-grown sample, sample annealed at 1100 °C at 100 kP (T_A = 1100 °C) and sample annealed at 1450 °C at 1 GPa (UHPA w/o SiO_2 mask), measured at room temperature. The inset shows a log-scale plot of the spectra.

B. 3. 4 PL measurements at cryogenic temperature

In order to mitigate the effect of defects on the Eu^{3+} luminescence properties, we conducted PL measurements at 10 K. PL spectra are plotted in Fig. B. 4. As shown in Fig. B. 4 (a), emission from deep-levels is well suppressed even for the UHPA sample, and the UHPA sample shows clear emission originating from Eu^{3+}. The integrated PL intensity ratios (1.968-2.016 eV) as compared to the as-grown sample were 1.6 for the sample annealed at 1100 °C and 0.90 for the UHPA sample. The decreased PL intensity of the UHPA sample is considered to be due to the incorporation of a high concentration of defects.

Enlarged PL spectra are displayed in Fig. B. 4 (b). As compared to the sample annealed at 1100 °C, the UHPA sample shows much narrower PL spectrum with decreased PL intensity from OMVPE1 and OMVPE2. Besides, the PL intensity of a peak on the shoulder of OMVPE7 (~1.998 eV), which is considered to be perturbed OMVPE7 [17–19], is greatly decreased after UHPA. Furthermore, the peak PL intensity of (unperturbed) OMVPE7 is higher for the UHPA sample as compared to the sample annealed at 1100 °C. In Fig. B. 5, PL spectra excited under indirect excitation and resonant excitation with a resonant excitation energy of OMVPE7 are plotted. It is clear that the spectrum excited under indirect excitation is very similar to that excited resonantly to OMVPE7. CEES mapping for the UHPA sample showed there still exists several different luminescent sites and the concentration of OMVPE7 did not increase much [Fig. B. 2], therefore these results indicate that OMVPE7 has a quite larger excitation efficiency as compared to other sites in the UHPA sample for some reasons. Further investigation on the optical properties of UHPA samples are required, however, it shows a potential to selectively excite one specific luminescent site for a variety of applications.

B. 4 Summary

In this chapter, we have investigated the impact of high temperature annealing (1450 °C) using UHPA method. As observed for samples annealed at 1000-1200 °C at 100 kPa, OMVPE1 and OMVPE2 were dissociated and converted into efficiently excited luminescent sites. Especially, OMVPE7 showed a distinguishable luminescence intensity, suggesting its quite high excitation efficiency in the UHPA sample. However, the surface morphology was significantly degraded, and

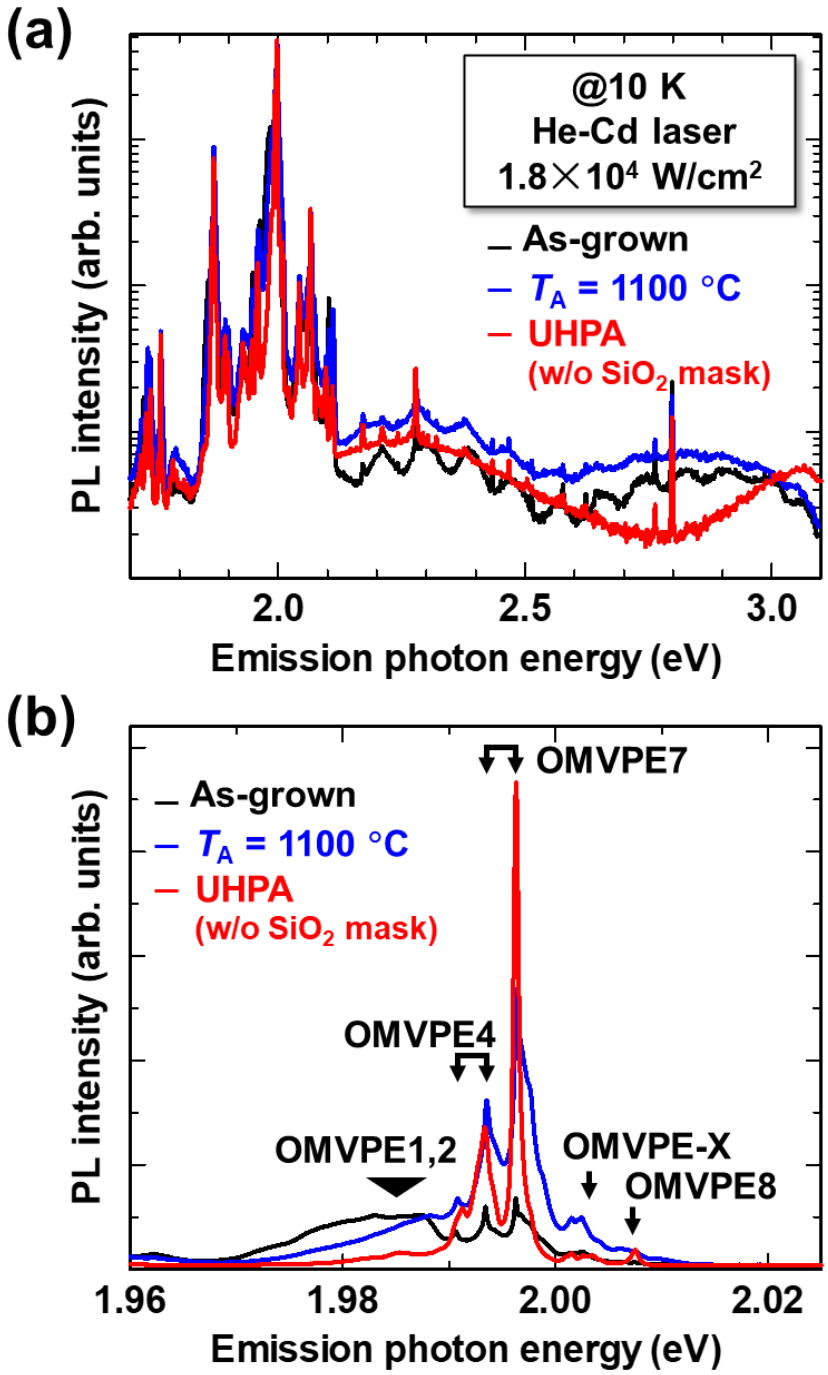

Fig. B. 4 (a) PL spectra for the as-grown sample, sample annealed at 1100 °C at 100 kP (T_A = 1100 °C) and sample annealed at 1450 °C at 1 GPa (UHPA w/o SiO_2 mask), measured at 10 K with (b) Enlarged PL spectra.

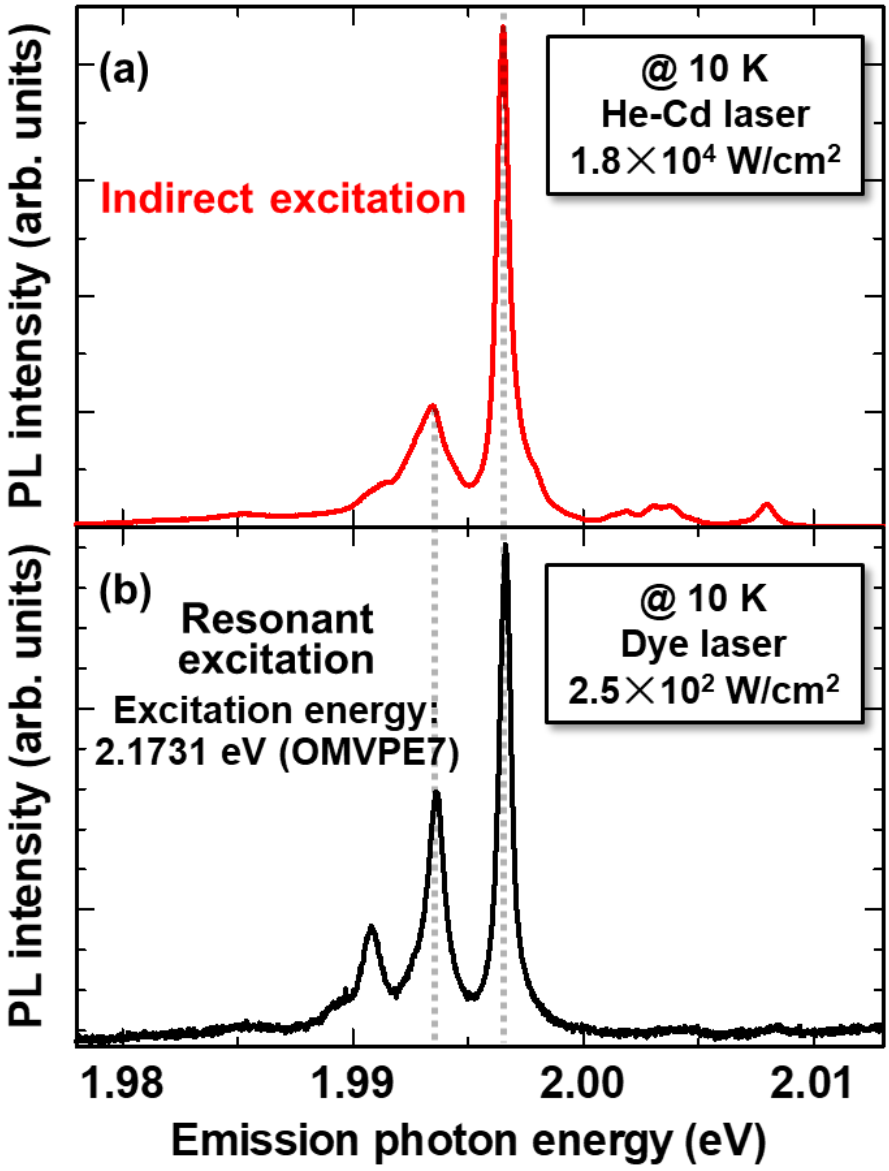

Fig. B. 5 PL spectra for the sample annealed at 1450 °C at 1 GPa without a SiO_2 mask, measured at 10 K under (a) indirect excitation and (b) resonant excitation with the resonant excitation energy of OMVPE7.

a high density of crystal defects was incorporated during the UHPA process, thus the annealing conditions must be improved for future applications.

References

[1] H. Sakurai, M. Omori, S. Yamada, Y. Furukawa, H. Suzuki, T. Narita, K. Kataoka, M. Horita, M. Bockowski, J. Suda, and T. Kachi, *Appl. Phys. Lett.* **115**, (2019).

[2] A. Uedono, H. Sakurai, T. Narita, K. Sierakowski, M. Bockowski, J. Suda, S. Ishibashi, S. F. Chichibu, and T. Kachi, *Sci. Rep.* **10**, 17349 (2020).

[3] D. N. Faye, M. Fialho, S. Magalhães, E. Alves, N. Ben Sedrine, J. Rodrigues, M. R. Correia, T. Monteiro, M. Boćkowski, V. Hoffmann, M. Weyers, and K. Lorenz, *Nucl. Instrum. Methods Phys. Res. B* **379**, 251 (2016).

[4] K. Lorenz, S. M. C. Miranda, E. Alves, I.S. Roqan, K. P. O'Donnell, and M. Bokowski, *Proc. SPIE* **8262**, 82620C (2012).

[5] P. Jaroszynski, E. Grzanka, M. Grabowski, G. Staszczak, I. Prozheev, R. Jakiela, F. Tuomisto, and M. Bockowski, *Appl. Surf. Sci.* **625**, 157188 (2023).

[6] K. Sierakowski, R. Jakiela, B. Lucznik, P. Kwiatkowski, M. Iwinska, M. Turek, H. Sakurai, T. Kachi, and M. Bockowski, *Electronics* **9**, 1380 (2020).

[7] T. Suski, P. Perlin, H. Teisseyre, M. Leszczyński, I. Grzegory, J. Jun, M. Boćkowski, S. Porowski, and T.D. Moustakas, *Appl. Phys. Lett.* **67**, 2188 (1995).

[8] R. Armitage, W. Hong, Q. Yang, H. Feick, J. Gebauer, E.R. Weber, S. Hautakangas, and K. Saarinen, *Appl. Phys. Lett.* **82**, 3457 (2003).

[9] K. Kuriyama, Y. Mizuki, H. Sano, A. Onoue, M. Hasegawa, and I. Sakamoto, *Solid State Commun*. **135**, 99 (2005).

[10] W. You, X. D. Zhang, L.M. Zhang, Z. Yang, H. Bian, Q. Ge, W. X. Guo, W. X. Wang, and Z. M. Liu, *Physica B* **403**, 2666 (2008).

[11] F. J. Xu, B. Shen, L. Lu, Z. L. Miao, J. Song, Z. J. Yang, G. Y. Zhang, X. P. Hao, B. Y. Wang, X. Q. Shen, and H. Okumura, *J. Appl. Phys.* **107**, (2010).

[12] S. O. Kucheyev, M. Toth, M. R. Phillips, J. S. Williams, C. Jagadish, and G. Li, *J. Appl. Phys*. **91**, 5867 (2002).

[13] K. Hoang, *Phys. Rev. Mater.* **5**, 034601 (2021).

[14] M. A. Reshchikov, D. O. Demchenko, D. Ye, O. Andrieiev, M. Vorobiov, K. Grabianska, M. Zajac, P. Nita, M. Iwinska, M. Bockowski, B. McEwen, and F. Shahedipour-Sandvik, *J. Appl. Phys.* **131**, (2022).

[15] A. Uedono, H. Bang, K. Horibe, S. Morishima, and K. Akimoto, *J. Appl. Phys.* **93**, 5181 (2003).

[16] W. Zhu, B. Mitchell, D. Timmerman, A. Uedono, A. Koizumi, and Y. Fujiwara, *APL Mater.* **4**, 056103 (2016).

[17] N. T. Woodward, N. Nepal, B. Mitchell, I. W. Feng, J. Li, H.X. Jiang, J. Y. Lin, J. M. Zavada, and V. Dierolf, *Appl. Phys. Lett*. **99**, 122506 (2011).

[18] J. D. Poplawsky, A. Nishikawa, Y. Fujiwara, and V. Dierolf, *Opt. Express* **21**, 30633 (2013).

[19] B. Mitchell, D. Timmerman, J. Poplawsky, W. Zhu, D. Lee, R. Wakamatsu, J. Takatsu, M. Matsuda, W. Guo, K. Lorenz, E. Alves, A. Koizumi, V. Dierolf, and Y. Fujiwara, *Sci. Rep*. **6**, 18808 (2016).

Appendix C. Investigation of the effect of post-growth thermal annealing on the optical characteristics of Tb and Tm doped $Al_xGa_{1-x}N$

C. 1. Introduction

In addition to GaN:Eu,O which has been discussed in the main text, III-nitride semiconductors doped with other RE elements hold great potential for a wide range of applications. For example, in the field of displays, the stability of emission wavelength exhibited by RE ions is advantageous because the emission originating from band-to-band transitions in semiconductors inevitably changes with temperatures, and in the case of certain semiconductors, with current injection level. In particular, as discussed in Chapter 1, the emission wavelength of green and red LEDs employing $In_xGa_{1-x}N$/GaN QWs undergoes a pronounced blueshift with increasing the current injection level, leading to a reduction in color gamut. Furthermore, the emission linewidth is typically broad due to several factors such as compositional fluctuations and well-width fluctuations. Tb-doped $Al_xGa_{1-x}N$ ($Al_xGa_{1-x}N$:Tb) has been focused as a good candidate to address these issues because it shows red (~620 nm), yellow (~580 nm), green (~550 nm) and blue (~490 nm) emission originating from the $^5D_4$-^7F_J (J = 3, 4, 5, 6) transition [1–4]. In addition, Tb-doped semiconductors are expected to be applied for white LEDs (WLEDs) because of the multiwavelength emission, which enables a large color rendering index, as compared to conventional WLEDs using $In_xGa_{1-x}N$ blue LEDs and yellow phosphors [5].

Besides, Tm-doped $Al_xGa_{1-x}N$ ($Al_xGa_{1-x}N$:Tm) has been explored as blue (~477 nm) and near-infrared (NIR) light (~800 nm) source [6–10]. Particularly, the emission wavelength of ~800 nm is attractive for various biomedical applications such as pulse oximeters [11,12].

Although LED operation of $Al_xGa_{1-x}N$:Tb and GaN:Tm [10] has been reported, the light output power still needs improvement for practical device implementation. As discussed in Chapter 2 and Chapter 3, we have demonstrated that post-growth thermal annealing is a powerful method to improve light output of GaN:Eu,O. In this chapter, we perform thermal annealing and investigate the impact on the optical characteristics of $Al_xGa_{1-x}N$:Tb and GaN:Tm.

C. 2. Tb doped $Al_xGa_{1-x}N$

C. 2. 1 Experimental method

First, we investigate the annealing effect on the optical characteristics of $Al_xGa_{1-x}N$:Tb. The sample was grown on (0001) sapphire substrates using the OMVPE method. Same as the growth of GaN:Eu,O, TMG, TMA, and NH_3 were used as precursors of Ga, Al, N, respectively. For the Tb-doped layer, tris-iso-propyl-cyclo-pentadienyl-terubium [$Tb(i\text{-}PrCp)^3$] was used. The growth was initiated with a low-temperature GaN buffer layer, followed by a 1.7-μm-thick undoped-GaN layer grown at 1180°C and at 100 kPa, and a 300-nm-thick ud-GaN layer grown at 960 °C and 10 kPa. Afterwards, a 400-nm-thick $Al_{0.48}Ga_{0.52}N$:Tb active layer was grown at 960 °C and 10 kPa and capped by a 20-nm-thick AlN. The Al composition was determined by the XRD reciprocal space mapping method. An 80-nm-thick SiO_2 was evaporated, and the sample was annealed at 1100 °C for 10 minutes in N_2 atmosphere at 100 kPa.

The fourth harmonic of a YAG laser (λ = 266 nm, pulse width = 200 ps) was used as an excitation source for PL measurements. Emission from the sample was detected by a cooled CCD camera equipped with a 50-cm-spectrometer. TR-PL signal was detected by a photon-counting system with a thermoelectrically cooled photomultiplier tube with laser repetition rate of 200 Hz.

C. 2. 2 Results and discussion

PL spectra for the as-grown sample and the sample annealed at 1100 °C measured at room temperature are plotted in Fig. C. 1. The annealed sample shows higher PL intensity, suggesting that thermal annealing is an effective method to improve the emission efficiency of $Al_xGa_{1-x}N$:Tb, as well as GaN:Eu,O. In the case of GaN:Eu,O, the enhanced luminescence efficiency was attributed

to the luminescent site reconfiguration, where sites with high excitation efficiencies were formed. However, the spectral shape of $Al_xGa_{1-x}N$:Tb emission is unchanged after annealing, suggesting that the distribution of luminescent site was not influenced by annealing.

In line with the luminescence mechanism proposed for GaN:Eu,O, where defects related to Eu^{3+} ions take place on carrier capture and energy transfer (Fig. 2. 1), the improved luminescence efficiency might be associated with following factors: (a) Enhanced radiative transition probability of Tb^{3+} ions (b) Enhanced carrier capture rate of defect related to Tb^{3+} ions (c) Enhanced energy transfer rate from defects to Tb^{3+} ions (d) Increased number of optically active Tb^{3+} ions.

To investigate the factor that improved the luminescence efficiency, TRPL measurements were conducted at room temperature. TRPL curves for the $^5D_4$-$^7F_5$ transition (554 nm) are shown in Fig. C. 2. In Fig. C. 2 (a), the initial fast decay components originate from deep-level emission from defects, and the slow decay components originate from Tb^{3+} emission. An earlier study has demonstrated that the lifetime of Tb^{3+} emission is constant in the temperature range of 15 K to room temperature [4]. This indicates that the effect of energy back transfer is negligibly small even at room temperature, and the lifetime of Tb^{3+} emission purely corresponds to the radiative lifetime. The decay curves were fitted using biexponential functions, and the lifetime was derived as 293±2 μs and 280±1 μs for the as-grown sample and the sample annealed at 1100 °C, respectively. The radiative lifetime remains nearly unchanged, suggesting that the radiative transition probability does not contribute to the enhancement of PL intensity.

With an improved temporal resolution, we also examined the rise time in TRPL measurements as shown in Fig. C. 2 (b). The almost identical PL curves indicate that the effective excitation cross section is unchanged after annealing. If the carrier capture and energy transfer rate has improved and/or number of optically active Tb^{3+} ions has increased, they would result in an enhanced effective excitation cross section. Therefore, the enhanced PL intensity was not caused by these factors.

When we applied the simple luminescence mechanism where defects related to RE ions take place on carrier capture and energy transfer to the investigation, the cause of the PL intensity enhancement could not be identified. Several other excitation mechanisms have been proposed for Tb^{3+} ions doped in $Al_xGa_{1-x}N$ [4,13,14], thus detailed analysis is required taking them into account.

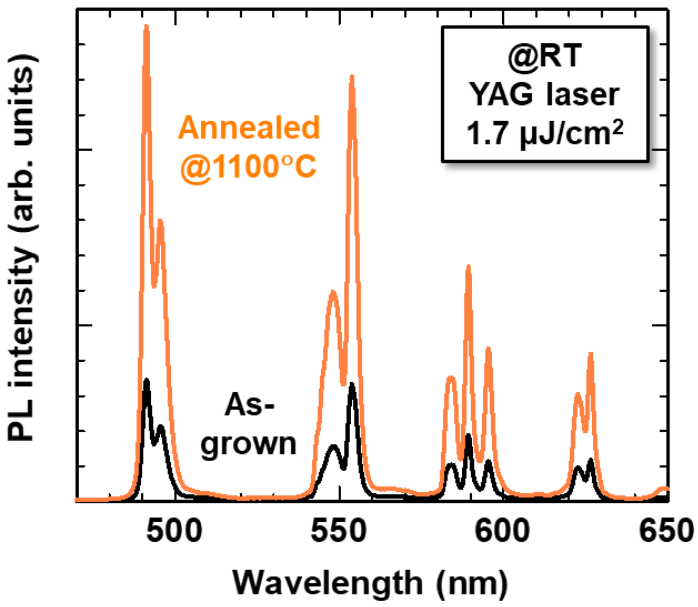

Fig. C. 1 PL spectra for the as-grown sample and the sample annealed at 1100 °C.

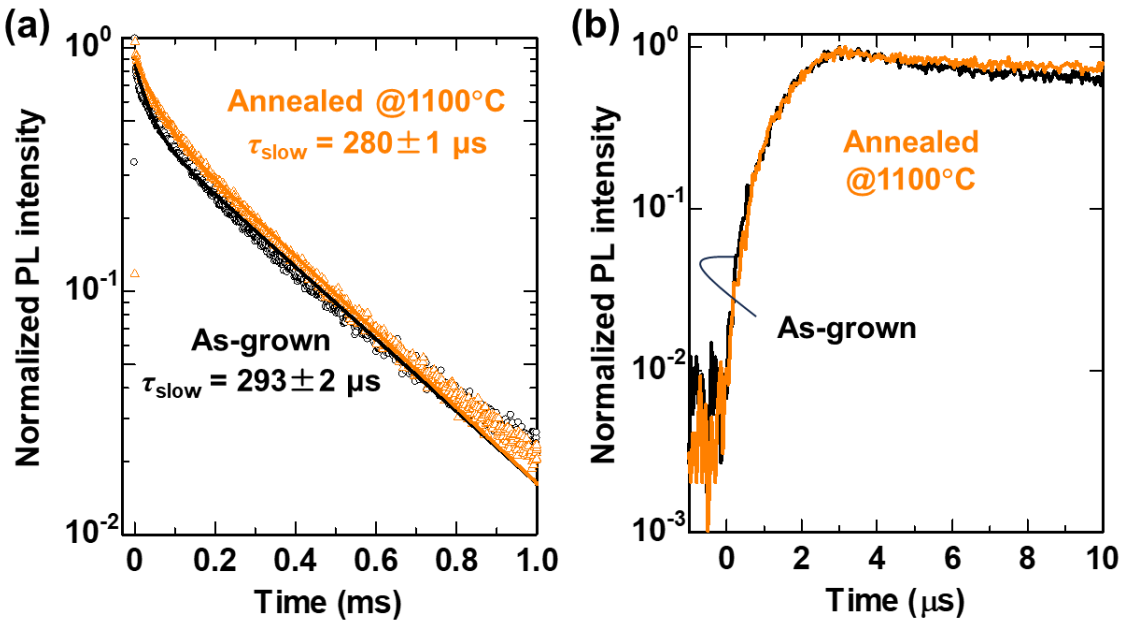

Fig. C. 2 TRPL curves measured with (a) low (b) high temporal resolution.

C. 3. Tm doped GaN

C. 3. 1 Experimental method

Then, we investigate the annealing effect on the optical characteristics of GaN:Tm. The sample was grown on (0001) sapphire substrates using the OMVPE method. Same as the growth of GaN:Eu,O and $Al_xGa_{1-x}N$:Tb, TMG, TMA, and NH_3 were used as precursors of Ga, Al, N, respectively. For the Tm-doped layer, tris-iso-propyl-cyclo-pentadienyl-thulium [$Tm(i\text{-}PrCp)^3$] was used. The growth was initiated with a low-temperature GaN buffer layer, followed by a 1.5-μm-thick undoped-GaN layer grown at 1180℃ and at 100 kPa. Afterwards, a 52-nm-thick GaN:Tm active layer was grown at 1030 ℃ and 10 kPa and capped by a 20-nm-thick AlN layer. An 80-nm-thick SiO_2 mask was evaporated, and the sample was annealed at 1050 °C for 10 minutes in N_2 atmosphere at 100 kPa.

C. 3. 2 Results and discussion

We conducted photoluminescence excitation (PLE) measurements at room temperature to study the optical characteristics. A laser-pumped plasma light source equipped with a monochromator was used as a wavelength tunable light source. Emission from the sample was detected by a cooled CCD camera equipped with a 50-cm-spectrometer.

PLE maps are illustrated in Fig. C. 3. At all the measured excitation wavelengths, the annealed sample exhibits a higher PL intensity associated with Tm^{3+}. This clearly indicates that post-growth thermal annealing also effectively improve the Tm^{3+} emission in GaN:Tm. When excited with energies below the GaN bandgap energy, the as-grown sample shows a strong emission from defect levels. This implies that the annealing process reduced the point defect concentration in GaN:Tm, and partially contributed to the improved Tm^{3+} luminescence efficiency.

C. 4. Summary

We applied post-growth thermal annealing processes to $Al_xGa_{1-x}N$:Tb and GaN:Tm, and observed

enhanced PL intensities associated with RE ions. In the case of GaN:Eu,O, the emission intensity enhancement was achieved by the luminescent site reconfiguration, where sites with high excitation efficiencies were preferentially formed by annealing. However, it is still not clear even if $Al_xGa_{1-x}N$:Tb and GaN:Tm have different types of luminescent sites. Further study of their optical properties would enable a detailed examination of the enhanced luminescence efficiency caused by annealing.

The obtained results imply that the annealing technique can be applied for various types of RE-doped semiconductor such as GaAs:Er [15], Si:Er [16], GaN:Er [17], and ZnO:Tm,Yb [18] to improve the light output and device performance. Future implementation of optical devices using RE-doped semiconductors is expected utilizing the annealing techniques.

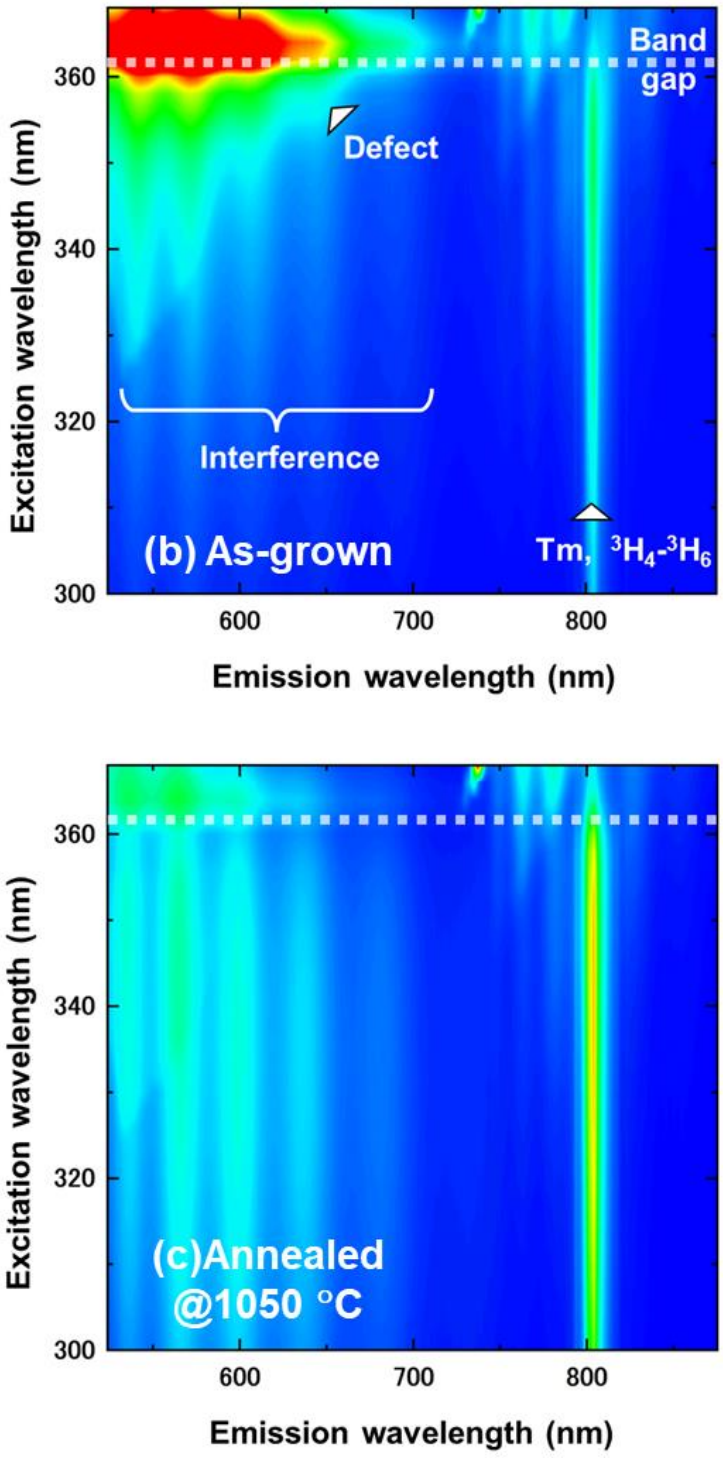

Fig. C. 3 PLE mas for (a) the as-grown sample and (b) the sample annealed at 1050 °C.

References

[1] H. Bang, S. Morishima, Z. Li, K. Akimoto, M. Nomura, and E. Yagi, Phys Status Solidi B Basic Res. 228, 319–323 (2001).

[2] A. Uedono, H. Bang, K. Horibe, S. Morishima, and K. Akimoto, J. Appl. Phys. 93, 5181–5184 (2003).

[3] H. Mendel, S.B. Aldabergenova, R. Weingärtner, G. Frank, H.P. Strunk, and A.A. Andreev, Opt. Mater. 28, 794 (2006).

[4] R. Komai, S. Ichikawa, H. Hanzawa, J. Tatebayashi, and Y. Fujiwara, J. Appl. Phys. 131, 073102 (2022).

[5] C. Braun, L. Mereacre, Z. Chen, and A. Slabon, Sci. Rep. 12, 1–7 (2022).

[6] J.H. Kim, M.R. Davidson, and P.H. Holloway, Appl. Phys. Lett. 83, 4746–4748 (2003).

[7] D.S. Lee and A.J. Steckl, Appl. Phys. Lett. 83, 2094–2096 (2003).

[8] U. Hömmerich, E.E. Nyein, D.S. Lee, A.J. Steckl, and J.M. Zavada, Appl. Phys. Lett. 83, 4556–4558 (2003).

[9] J. Takatsu, R. Fuji, J. Tatebayashi, D. Timmerman, A. Lesage, T. Gregorkiewicz, and Y. Fujiwara, J. Appl. Phys. 123, 1–6 (2018).

[10] S. Ichikawa, N. Yoshioka, J. Tatebayashi, and Y. Fujiwara, J. Appl. Phys. 127, (2020).

[11] K.K. Tremper, Chest 95, 713–715 (1989).

[12] J.E. Sinex, Am. J. Emerg. Med. 17, 59–66 (1999).

[13] D. De Graaf, S.J. Stelwagen, H.T. Hintzen, and G. De With, J. Non Cryst. Solids 325, 29–33 (2003).

[14] Y. Hakuta, T. Haganuma, K. Sue, T. Adschiri, and K. Arai, Mater. Res. Bull. 38, 1257–1265 (2003).

[15] K. Takahei and A. Taguchi, J. Appl. Phys. 74, 1979–1982 (1993).

[16] P.N. Favennec, H. L'Haridon, D. Moutonnet, M. Salvi, and M. Gauneau, Jpn J. Appl. Phys. 29, L524–L526 (1990).

[17] C. Ugolini, N. Nepal, J.Y. Lin, H.X. Jiang, and J.M. Zavada, Appl. Phys. Lett. 89, (2006).

[18] J. Tatebayashi, G. Yoshii, T. Nakajima, H. Kamei, J. Takatsu, D.M. Lebrun, and Y. Fujiwara, J. Appl. Phys. 123, (2018).

List of Publications

A. Full Length Papers and Letters

1. T. Iwaya, S. Ichikawa, M. Murakami, D. Timmerman, J. Tatebayashi, and Y. Fujiwara, "Investigation on suitable structure for laser oscillation in Eu-doped GaN with two-dimensional photonic crystal nanocavities", *Journal of the Society of Materials Science* **69**, 721 (2020).

2. S. Ichikawa, Y. Sasaki, T. Iwaya, M. Murakami, M. Ashida, D. Timmerman, J. Tatebayashi, and Y. Fujiwara, "Enhanced red emission of Eu,O-codoped GaN embedded in a photonic crystal nanocavity with hexagonal air holes", *Physical Review Applied* **15**, 034086 (2021).

3. D. Timmerman, T. Iwaya and Y. Fujiwara, "High-*Q* 1D rod-based nanocavities ", *Optics Letters* **46**, 4260 (2021).

4. T. Iwaya, S. Ichikawa, M. Murakami, D. Timmerman, J. Tatebayashi, and Y. Fujiwara, "Design considerations of III-nitride-based two-dimensional photonic crystal cavities with crystallographically induced disorder", *Applied Physics Express* **14**, 122002 (2021).

5. D. Timmerman, T. Iwaya and Y. Fujiwara, "Nanorod photonic crystal ring resonators", *Optics Express* **30**, 3488 (2022).

6. T. Iwaya, S. Ichikawa, D. Timmerman, J. Tatebayashi, and Y. Fujiwara "Improved *Q*-factors of III-nitride-based photonic crystal nanocavities by optical loss engineering", *Optics Express* **30**, 28853 (2022).

7. T. Iwaya, S. Ichikawa, D. Timmerman, J. Tatebayashi, and Y. Fujiwara,
   "Enhanced light output of Eu, O-codoped GaN caused by reconfiguration of luminescent sites during post-growth thermal annealing",
   Applied Physics Letters **122**, 032102 (2023).

8. T. Iwaya, S. Ichikawa, V. Dierolf, B. Mitchell, H. Austin, D. Timmerman, J. Tatebayashi, and Y. Fujiwara,
   "An efficiently excited Eu^{3+} luminescent site formed in Eu,O-codoped GaN",
   AIP Advances (Accepted).

9. T. Iwaya, S. Ichikawa, D. Timmerman, J. Tatebayashi, and Y. Fujiwara,
   "Demonstration of high reflective $Al_xIn_{1-x}N$/GaN distributed Bragg reflector in the red region",
   to be submitted.

10. S. Yamazaki, S. Ichikawa, T. Iwaya, J. Tatebayashi, and Y. Fujiwara,
    "Multiple color emission of Tb-doped $Al_xGa_{1-x}N$-based light-emitting diodes",
    to be submitted.

B. International Conferences

1. T. Iwaya, S. Ichikawa, M. Murakami, D. Timmerman, J. Tatebayashi, and Y. Fujiwara,
   "Strongly enhanced red emission from Eu-doped GaN in a two-dimensional photonic-crystal nanocavity",
   2020 International Conference on Solid State Devices and Materials,
   Online, E-2-04, (Sep. 2020), Oral.

2. T. Iwaya, S. Ichikawa, D. Timmerman, J. Tatebayashi, and Y. Fujiwara,
   "Demonstration of a GaN-based high-*Q* (7900) H3 photonic crystal cavity in the red region",
   International Conference on Nano-photonics and Nano-optoelectronics 2022,
   Yokohama, Japan, ICNN2-05, (Apr. 2022), Oral.

3. D. Timmerman, T. Iwaya, and Y. Fujiwara,
   "(Quasi-) 1D nanorod resonators",
   International Conference on Nano-photonics and Nano-optoelectronics 2022,
   Yokohama, Japan, ICNN2-06, (Apr. 2022), Oral.

4. T. Iwaya, S. Ichikawa, D. Timmerman, J. Tatebayashi, and Y. Fujiwara,
   "Improved *Q*-factors (> 10000) of III-nitride-based two-dimensional photonic crystal cavities in the red region",
   International Workshop on NITRIDE SEMICONDUCTORS 2022,
   Berlin, Germany, AT 177, (Oct. 2022), Oral.

5. D. Timmerman, T. Iwaya, and Y. Fujiwara,
   "GaN based (quasi-) 1D nanorod photonic resonators", **(Invited)**
   5th International Conference on Advanced Materials and Nanotechnology,
   Hanoi, Vietnam, I127, (Nov. 2022), Oral.

6. T. Iwaya, S. Ichikawa, D. Timmerman, J. Tatebayashi, and Y. Fujiwara,
   "III-nitride-based high-*Q* (>10000) two-dimensional photonic crystal nanocavities in the red region",
   International Conference on Nano-photonics and Nano-optoelectronics 2023,
   Yokohama, Japan, ICNN6-05, (Apr. 2023), Oral.

7. T. Iwaya, S. Ichikawa, D. Timmerman, J. Tatebayashi, and Y. Fujiwara,
   "Enhanced light output of Eu,O-codoped GaN caused by luminescent site reconfiguration during post-growth thermal annealing",
   The 32nd International Conference on Defects in Semiconductors,
   Rehoboth Beach, United States of America, (Sep. 2023), Oral.

8. T. Iwaya, S. Ichikawa, D. Timmerman, J. Tatebayashi, and Y. Fujiwara,
   "Enhanced luminous efficiency of Eu,O-codoped GaN due to luminescent site reconfiguration induced by high-temperature thermal annealing",
   (Best Student Award)
   14th International Conference on Nitride Semiconductors,
   Fukuoka, Japan, CH16-4, (Nov. 2023), Oral.

9. T. Iwaya, S. Ichikawa, D. Timmerman, J. Tatebayashi, and Y. Fujiwara,
   "Eu,O-codoped GaN-based high-*Q* two-dimensional photonic crystal cavities in the red region",
   2023 MRS Fall Meeting & Exhibit,
   Boston, United States of America, (Dec. 2023), Oral.

C. Domestic Conferences

1. T. Iwaya, S. Ichikawa, M. Murakami, J. Tatebayashi, and Y. Fujiwara,
   "Investigation on suitable structure for laser oscillation in Eu-doped GaN with two-dimensional photonic crystal nanocavities",
   67th Japan Society of Applied Physics Spring Meeting,
   Cancelled due to the COVID-19 pandemic., 13p-B401-1, (Mar. 2020), Oral.
2. T. Iwaya, S. Ichikawa, M. Murakami, J. Tatebayashi, and Y. Fujiwara,
   "Investigation on suitable structure for laser oscillation in Eu-doped GaN with two-dimensional photonic crystal nanocavities",
   81st Japan Society of Applied Physics Fall Meeting, Online, 10a-Z18-2, (Sep. 2020), Oral.
3. T. Iwaya, S. Ichikawa, M. Murakami, J. Tatebayashi, and Y. Fujiwara,
   "Impact of fabrication errors on laser oscillation in GaN:Eu-based photonic crystal cavities",
   39th Electronic Materials Symposium,
   Online, P2-22, (Oct. 2020), Short presentation and poster.
4. M. Murakami, S. Ichikawa, T. Iwaya, Y. Sasaki, J. Tatebayashi, and Y. Fujiwara,
   "Structural design of Eu-doped-GaN-based two-dimensional photonic crystal nanocavities and the optical characterization at low temperature",
   (Student Presentation Award)
   2nd The Society of Materials Science, Japan Committee on Semiconductor Electronics Meeting 2020, Online, 7, (Nov. 2020), Oral.

5. T. Iwaya, S. Ichikawa, M. Murakami, J. Tatebayashi, and Y. Fujiwara,
   "Investigation on suitable structure for the realization of high *Q*-factors using III-nitride-based two-dimensional photonic crystal cavities",
   (Student Presentation Award)
   3rd The Society of Materials Science, Japan Committee on Semiconductor Electronics Meeting 2020, Online, 1, (Jan. 2021), Oral.

6. T. Iwaya, S. Ichikawa, M. Murakami, J. Tatebayashi, and Y. Fujiwara,
   "Enhanced radiative transition rate of Eu ions doped in GaN modulated by radiation fields in two-dimensional photonic crystal nanocavities",
   68th Japan Society of Applied Physics Spring Meeting,
   Online, 17p-Z27-8, (Mar. 2021), Oral.

7. T. Iwaya, S. Ichikawa, M. Murakami, D. Timmerman, J. Tatebayashi, and Y. Fujiwara,
   "Fabrication and optical characterization of Eu-doped GaN-based high-*Q* H3 photonic crystal cavities",
   82nd Japan Society of Applied Physics Fall Meeting,
   Online, 10p-N101-13, (Sep. 2021), Oral.

8. T. Ishihara, S. Ichikawa, D. Timmerman, T. Iwaya, M. Ashida, J. Tatebayashi, and Y. Fujiwara,
   "Size dependence of quantum efficiency for Eu-doped GaN",
   82nd Japan Society of Applied Physics Fall Meeting,
   Online, 10p-N101-15, (Sep. 2021), Oral.

9. T. Iwaya, S. Ichikawa, D. Timmerman, M. Murakami, J. Tatebayashi, and Y. Fujiwara,
   "Fabrication and optical characterization of high *Q*-factor Eu-doped-GaN-based photonic crystal cavities",
   2nd The Society of Materials Science, Japan Committee on Semiconductor Electronics Meeting 2021, Online, 1, (Nov. 2021), Oral.

10. T. Ishihara, S. Ichikawa, D. Timmerman, T. Iwaya, M. Ashida, J. Tatebayashi, and Y. Fujiwara,
"Evaluation of quantum efficiencies of Eu-doped GaN micro-structure for realization of μ-LEDs",
(Student Presentation Award)
3rd The Society of Materials Science, Japan Committee on Semiconductor Electronics Meeting 2021, Online, 4, (Jan. 2022), Oral.

11. T. Iwaya, S. Ichikawa, D. Timmerman, J. Tatebayashi, and Y. Fujiwara,
"Demonstration of high-*Q* (>10,000) III-nitride-based photonic crystal cavities in the red region",
(Young Scientist Presentation Award)
69th Japan Society of Applied Physics Spring Meeting,
Aoyama Gakuin University, 22p-E202-14, (Mar. 2022), Oral.

12. T. Iwaya, S. Ichikawa, D. Timmerman, J. Tatebayashi, and Y. Fujiwara,
"Reconfiguration of local atomic structure around Eu^{3+} in Eu-doped GaN and enhanced luminous efficiency caused by thermal annealing",
(Student Presentation Award)
1st The Society of Materials Science, Japan Committee on Semiconductor Electronics Meeting 2022, Online, 4, (Aug. 2022), Oral.

13. T. Iwaya, S. Ichikawa, D. Timmerman, J. Tatebayashi, and Y. Fujiwara,
"Improved luminescence efficiency of Eu,O-codoped GaN due to a reconfiguration of luminescent sites caused by a post-growth annealing",
83rd Japan Society of Applied Physics Fall Meeting,
Tohoku University, 22a-C200-5, (Sep. 2022), Oral.

14. T. Iwaya, S. Ichikawa, D. Timmerman, J. Tatebayashi, and Y. Fujiwara,
"Introduction of 2D-hetero structures to improve the *Q*-factor of III-nitride-based photonic crystal resonators in the visible range", **(Invited)**
83rd Japan Society of Applied Physics Fall Meeting,
Tohoku University, 23a-C200-6, (Sep. 2022), Oral.

15. S. Yamazaki, S. Ichikawa, T. Iwaya, J. Tatebayashi, and Y. Fujiwara,
"Fabrication of LED using Tb-doped $Al_xGa_{1-x}N$ as an active layer and the optical/electrical characterization",
(Student Presentation Award)
1st The Society of Materials Science, Japan Committee on Semiconductor Electronics Meeting 2022, Online, 3, (Jan. 2023), Oral.

16. T. Iwaya, S. Ichikawa, D. Timmerman, V. Dierolf, H. Austin, B. Mitchell, J. Tatebayashi, and Y. Fujiwara,
"Luminescent properties of GaN:Eu,O annealed at high temperature under photoexcitation and current injection",
70th Japan Society of Applied Physics Spring Meeting,
Sophia University, 17p-B410-3, (Mar. 2023), Oral.

17. S. Yamazaki, S. Ichikawa, T. Iwaya, J. Tatebayashi, and Y. Fujiwara,
"Al flow rate dependence of optical and electrical properties for Tb-doped- $Al_xGa_{1-x}N$-based LEDs",
70th Japan Society of Applied Physics Spring Meeting,
Sophia University, 17p-B410-4, (Mar. 2023), Oral.

18. S. Yamazaki, S. Ichikawa, T. Iwaya, J. Tatebayashi, and Y. Fujiwara
"Demonstration of Tb-doped $Al_xGa_{1-x}N$-based light emitting diodes with high emission wavelength stability"
42nd Electronic Materials Symposium,
The KASHIHARA, (Oct. 2023), Short presentation and poster.

D. Awards

1. Student Presentation Award
3rd The Society of Materials Science, Japan Committee on Semiconductor Electronics Meeting 2020 (Jan. 2021).

2. Young Scientist Presentation Award
   69th Japan Society of Applied Physics Spring Meeting, (Mar. 2022).
3. Student Presentation Award
   1st The Society of Materials Science, Japan Committee on Semiconductor Electronics Meeting 2022 (Aug. 2022).
4. The Encouragement Prize for Article Presentations Abroad
   Association for the Advancement of Manufacturing & Technology (Oct. 2022).
5. Best Poster Presentation Award
   Osaka University Fellowship Quantum Leader Resources (QLEAR) Researcher exchange workshop (Mar. 2023).
6. Best Student Award
   14th International Conference on Nitride Semiconductors, (Nov. 2023).

E. Research Grants

1. Overseas Dispatch Assistance
   The Murata Science Foundation (Aug. 2020),
   (Declined due to cancellation of conference due to the COVID-19 pandemic.)
2. QLEAR Fellowship
   Osaka University Fellowship Quantum Leader Resources (QLEAR) (Apr. 2022).
3. Financial assistance for overseas travel
   Research Foundation for the Electrotechnology of Chubu (Oct. 2022).
4. Overseas Joint Research Support
   Osaka University Fellowship Quantum Leader Resources (QLEAR) (Oct. 2022).
5. International Exchange Grant
   Marubun Research Promotion Foundation (Oct. 2022).
6. Research Fellowships for Young Scientists (DC2)
   Japan Society for the Promotion of Science (Apr. 2023).

7. Financial assistance for overseas travel
   The Telecommunications Advancement Foundation (Sep. 2023).
8. International Exchange Grant
   Tateisi Science and Technology Foundation (Nov. 2023).
9. Grants for Researchers Attending International Conferences
   The NEC C&C Foundation (Nov. 2023).